Vrije Universiteit Brussel

Faculteit Wetenschappen en Bio-ingenieurswetenschappen
Vakgroep Fysica - Interuniversity Institute for High Energies

Search for High-Energy Neutrino Production in Short Gamma Ray Bursts with the IceCube Neutrino Observatory

Martin Casier

Proefschrift ingediend met het oog op het behalen van de academische graad van Doctor in de Wetenschappen.

Promotor: **Prof. Dr. Nick van Eijndhoven**

September 2015

Doctoral Examination Committee

Chair: Prof. Dr. C. De Clercq (VUB)
Promotor: Prof. Dr. Nick van Eijndhoven (VUB)
Secretary: Prof. Dr. S. Lowette (VUB)
Prof. Dr. J. D'Hondt (VUB)
Prof. Dr. G. Gentile (VUB)
Prof. Dr. F. de Proft (VUB)
Prof. Dr. D. Rijckbosch (UGent)
Prof. Dr. M. Tytgat (ULB)

A Raphaël, la mia fonte di vita

Abstract

The Universe is still full of not yet or not fully understood processes. Among all these phenomena, the *Gamma-Ray Bursts* (GRBs) are among the most impressive ones. The GRBs are the most luminous events known to occur in the Universe (L $\sim$ 10^{50} erg s^{-1}). These enormous explosions have been proposed as the solution of another Astroparticle Physics enigma: the origin of the ultra-high energy cosmic rays. GRBs could indeed be the cosmic accelerators responsible of the most energetic part of the Cosmic ray flux with particles reaching energies into the range of 10^{16}-10^{20} eV.

Physicists have devised several models to explain through which physical processes nature might be able to reach these kind of extremely high energies. One of the most popular models for GRBs is the so-called *Fireball Model*. All the models developed by physicists to describe the GRB phenomenon assume the creation of high-energy neutrinos ($E_\nu \sim 100\,\mathrm{TeV}$), which travel into the universe and should therefore be detectable on Earth.

Our analysis concentrates on a subclass of the GRBs: the short duration GRBs (SGRBs), defined by $T_{90} \leq 2\,\mathrm{s}$. This represents the first time that a neutrino analysis is performed on this subclass of GRBs. We have developed a dedicated analysis, with a new approach for the event selection and a specific statistical analysis. As most of previous works, no significant signal is found. Our computed limits on the neutrino flux disfavour much of the parameter space for the theoretical models for the production of neutrinos in SGRBs. The tension between observations and theoretical models is confirmed and enhanced.

Samenvatting

In ons heelal vinden dagelijks processen plaats die nog steeds niet volledig begrepen zijn. Een van de meest indrukwekkende gebeurtenissen zijn zogenaamde "gamma flitsen". Een gamma flits is de meest energieke, waargenomen, verschijning in het zichtbare heelal (L $\sim 10^{50}$ erg s^{-1}). Deze enorme explosies worden aangedragen als mogelijke oplossing voor een ander raadsel binnen de astrodeeltjesfysica: Wat is de oorsprong van de hoogenergetische kosmische deeltjes? Binnen de huidige modellen zijn gamma flitsen één van de mogelijke bronnen die in staat zijn deze hoogenergetische deeltjes met energieën tussen 10^{16}-10^{20} eV te produceren.

Natuurkundigen hebben verschillende scenario's uitgewerkt waarbij deze kosmische deeltjes versneld worden tot extreem hoge energieën. Een van de meest populaire modellen voor gamma flitsen is het zogeheten *Fireball Model*. De verschillende modellen die gamma flitsen beschrijven veronderstellen dat, naast de productie van hoog energetische kosmische deeltjes, ook hoog energetische neutrino's ($E_\nu \sim 100$ TeV) gecreëerd worden. Deze neutrino's reizen ongehinderd door ons universum en zouden dus op de aarde gedetecteerd moeten kunnen worden.

Onze analyse richt zich op een speciale klasse van de gamma flitsen, de kort durende gamma flitsen gedefinieerd door $T_{90} \leq 2$ s. Dit is de eerste neutrino analyse waarbij een dergelijke klasse binnen de gamma flitsen wordt bekeken. Hiervoor is een gerichte analyse ontwikkeld met een geoptimaliseerde signaal selectie en een specifieke statistische methode. Het resultaat van deze analyse is, zoals in eerdere analyses van gamma flitsen, dat er geen significant neutrino signaal van deze kort durende gamma flitsen is gevonden. De berekende limieten voor de neutrino flux sluiten een groot gedeelte van de parameterruimte binnen de verschillende theoretische modellen voor de neutrino productie van kort durende gamma flitsen uit. Het spanningsveld tussen de waarnemingen en de verscheidene theoretische modellen wordt hiermee bevestigd en versterkt.

Acknowledgments

A PhD thesis is undoubtedly a life experience and the result of years of work. Fortunately for me, this personal effort took place in an intellectually competitive environment composed of so many great people. Having the opportunity to perform this work within the IceCube Collaboration and especially at the Interuniversity Intstitute for High Energies (ULB-VUB) were two enormous advantages.

At the IIHE, I have found an amazing group of women and men that are not only great scientist or staff members but that are also wonderful persons. I would like to start to thank all the people that are allowing us to work in these great conditions: the administrative and computing staff. Thanks to all of you for the, often invisible, work that is of great support for the whole lab. Especially, I would like to express all my gratitude to Marleen Goeman which is an amazingly efficient person always ready to help but also a person with an enormous hart. Thanks also to Audrey Terrier for her kindness and her great work. With both of you, the IIHE has the best staff ever! How could I not thank Samir Amary that has always been there for solving and helping me with my uncountable problems with the cluster?! Thank you, Samir.

On a more scientific level, I cannot thank Nick van Eijndhoven enough for his advices, help, support and so much more that he gave me, as my supervisor, during these 4 years. Thank you Nick, I surely owe you a good whisky! I also want to thank all my colleagues whether professors or PhD students that have offered me so many useful discussions on scientific level but also so much fun and pleasure on a more personal aspect of our relations. Especially, I want to thank Lionel and Jan my two companions with whom I've shared so many intense moments; Geraldina, without you I think I would have never finished this thesis; Debanjan, for your eternal good mood that we miss since you've left; Elisa, for your kindness and your care; Thomas and David, your departure has left the lab so empty; Gwen, I will miss you and your never ending chats; but also Catherine, Isabelle, Aongus, Giuliano, Krijn and more recently Simona, Juanan, Jan, Kevin and Christoph. I wish all the best to this great team that is the IIHE!

The IceCube Collaboration is a wonderful international scientific community of more than 300 women and men which all deserve some level of thanks for their help and support during these years. I would like to thank more precisely the people of the GRB working group for their advices and help and especially Ignacio Taboada for his great support as group leader as well as Hans Dembinsky and Ryan Maunu who were two great reviewers of my work.

Ces quatre années furent aussi celle d'un tout autre engagement et d'un tout autre combat. Au-delà du travail qui m'a permis, dans les nombreux moments de doute qui émaillent le parcours d'un jeune doctorant, de m'échapper pour reprendre l'air et replonger de plus belle, ces années furent l'occasion de rencontres inoubliables, de moments forts et parfois durs. J'aimerais dire toute mon admiration pour Alain, qui au-delà d'avoir été un grand Président, m'a accordé tout de suite sa confiance totale. Je ne l'oublierai pas. Mes pensées vont bien sûr aussi à Marion et Fabienne qui m'ont accompagné quotidennement dans cette vie-là d'une manière admirable et c'est avec toute mon amitié que je veux les remercier. Merci évidemment aussi à Cécile, Arnaud et Michel pour ce bout de vie passé ensemble et ces longues réunions qui nous ont presque permis de faire changer le monde (enfin l'ULB, mais nous, on sait que si on a fait bouger l'ULB, le reste est simple). Un autre Michel a rejoint plus récemment cette bande un peu folle, qu'il sache qu'au-delà du plaisir personnel de l'avoir rencontré, je suis heureux et confiant de savoir qu'il tienne désormais une partie des rennes. Une pensée sincère également à Ahmed, qu'il sache que je le considère comme bien plus qu'un simple camarade de travail et qu'il soit remercié pour son coeur, ses investissements et ses combats. Merci enfin à Marc pour ces soirées sans fin à entremêler la bonne chaire et la lutte, brutale, des classes.

Plus personnellement, je veux remercier mes parents et ma soeur pour leur soutien et leur présence indispensable et sans faille depuis plus de 28 ans maintenant mais aussi Fio, Marc et Juju pour m'avoir accueilli avec tant de générosité et de fraternité (et pourtant...) dans la famille Jehotte-Brusco, ainsi bien sûr que toutes ces personnes qui m'entourent de leur présence, de leurs idées, de leur folie et parfois (voire souvent) de leur envie de refaire le monde ou plus simplement de faire la fête. Merci à Aline, Alizée, Caroline, Elie, Jerome, Julie, Laurent, Lise, Maia, Martin, Noémie, Thomas, Yannick et tous les autres que je ne peux nommer ici mais qui se reconnaîtront certainement. Simplement merci d'être toujours là et d'être vous. Une gargantuesque pensée bien sûr à François et à ses Frères, ainsi qu'à ces quelques Soeurs (il paraît qu'il faut bien), qui ont rendu ma vie ventripotente et généreuse jusqu'ici et dont le rôle est loin d'être fini car la chanson n'est pas finie et ne se finira jamais ! Enfin, merci à toi Raphaël, toi qui m'accompagnes depuis plus de 5 ans et demi, toi avec qui j'ai choisi de créer un nous, toi avec qui j'ai décidé de construire la suite de nos chemins ensemble, toi qui m'a fait et me fait encore découvrir tant de choses, toi qui m'apportes ce quelque chose qui rend la vie plus belle et surtout plus intense à vivre...

Ny Carquan, Ny Seuf !

Contents

È dunque l'universo uno, infinito, inmobile. Una, dico, è la possibilità assoluta, uno l'atto, una la forma o anima, una la materia o corpo, una la cosa, uno lo ente, uno il massimo ed ottimo...

⋆

Thus the universe is One, infinite, immovable. One - I say - is the absolute possibility, One is the act, One is the form or soul, One is the matter or body, One is the object, One is that which is, One is the maximum and otpimum...

Giordano Bruno,
De la causa, principio et uno, Dialogue V.

The Birth of Neutrino Astronomy

Since the very beginning of humankind, the sky and its shining points have been objects of extreme curiosity for human beings and have deeply passionated them. The nightly sky was so intriguing and so misunderstood that it could only be explained through supernatural processes. Most of early cultures throughout the world identified celestial objects with gods, divinities and spirits. Heavens were created... It became therefore of the utmost importance to perform methodical observations of this dark sky: understanding the sky was to understand the gods. The first astronomical observations were logically performed by priests or philosophers. Although their motivations were more based on religious principles, their observations have led to the first calendars and maps of the visible sky. As an example, the Warren Field calendar, believed to be based on the Moon phases, is to date the world's oldest known calendar, created as early as $\sim 8000\,\mathrm{BC}$ [1]. All these observations led to the birth of Astronomy which is now known as one of the oldest natural sciences in History.

Until the Renaissance, astronomy has been limited to the part of the electromagnetic spectrum which is visible by the naked eye. In 1610, Galileo Galilei[1] was responsible for the first breakthrough in astronomy: he decided to use the recently invented telescope to observe and study the Cosmos. Although many speculations and discussions about heliocentricism can be found as early as the 3rd century BC with Aristarchus of Samos[2], it is only in the 16th century that Nicolaus Copernicus[3] presented a geometric mathematical model of a heliocentric system. This model has finally been confirmed with Galileo's telescopic observations of the moons of Jupiter and the phases of Venus, ruling out the religious driven geocentricism. The use of astronomical instruments had changed dramatically, for the first time, the understanding of the Universe and had given to mankind the principal role pushing religion and believes into the background.

The visible light has remained our unique gateway to the Cosmos for centuries and actually, astronomers have used optical telescopes ever since. However, at the beginning of the 19th century, a revolution occurred with the discovery of infrared by William Herschel[4], quickly followed, at the other side of the spectrum, by the ultraviolet bands.

[1] Galileo Galilei ($\star$1564, †1642), Italian astronomer, physicist, philosopher, and mathematician.
[2] Aristarchus of Samos ($\star$310 BC, †230 BC), Greek astronomer and mathematician.
[3] Nicolaus Copernicus ($\star$1473, †1543), Prussian mathematician and astronomer.
[4] William Herschel ($\star$1738, †1822), German-English astronomer.

All along the 19th century, numerous discoveries have lead to a knowledge of almost all the bands of the electromagnetic spectrum. It is indeed only in the early nineteen hundreds that the gamma rays were added to the known spectrum. Meanwhile, the first technological applications were developed among which radio telescopes were built in the 1930's, followed by infrared and ultra-violet observations. These observations have broadened our view and have enhanced our knowledge of the Universe. Later, the launch of satellites enabled us to avoid the opacity of the atmosphere at certain wavelengths. This has widened even more our window of the Universe by adding X-rays and Gamma-rays to the observable spectrum. Nowadays, light, both visible and invisible, is thus used for observing cosmic objects and phenomena over an energy range of more than 18 orders of magnitude. But still, the principle has remained the same: observing electromagnetic radiation from cosmic sources.

Meanwhile, another important step in the development of astronomy was made: the discovery of cosmic rays. The unveiling of radioactivity had led to the idea that the observed natural ionisation of the air was caused by radiation from radioactive elements in the ground but the experimental observations were going to rule out this explanation... The first electrometers, devices to measure the rate of ion production, were developed and Theodor Wulf[5] showed that the radiation level was higher on the top of the Eiffel Tower than at ground level [2]. Two years later, an Italian physicist, Domenico Pacini[6] concluded after observing a radiation rate decrease underwater that [3]:

> « *A sizeable cause of ionisation exists in the atmosphere, originating from penetrating radiation, independent of the direct action of radioactive substances in the soil.* »

This first hint of the existence of an extraterrestrial source of radiation has lateron been confirmed by the famous balloon flights performed by Victor Hess[7] in the early 1910's which were rewarded with the Nobel Prize in Physics in 1936. Even though Robert Millikan[8] thought that the particles responsible for this radiation were photons, he invented the term "cosmic rays", still in use nowadays. It is finally in 1937 that Pierre Auger[9] concluded that, when penetrating into the Earth atmosphere, the high-energy primary cosmic-ray particles interact with air nuclei and initiate a cascade of secondary particles, including electrons, muons, hadrons and photons that reach ground level. This observation finally offered a complete explainable picture for these phenomena. The discovery of these cosmic rays has offered a complete new channel for observing the Cosmos and, although it was not realised at the time of their discovery, they created a brand new interdisciplinary field of research: Astroparticle Physics. The concept of a

[5] Theodor Wulf (⋆1868, †1946) German physicist.
[6] Domenico Pacini (⋆1878, †1934), Italian physicist.
[7] Victor Franz Hess (⋆1883, †1964), Austrian-American physicist.
[8] Robert Andrews Millikan (⋆1868, †1953), American experimental physicist.
[9] Pierre Auger (⋆1899, †1993), French physicist.

multi messenger approach for astronomy was born.

To discuss the last fundamental historical step for our field of research, we have to go back in time to the early 1930's. At this period, physicists were confronted with a big problem concerning beta decay. This interaction was indeed apparently breaking the law of energy and angular momentum conservations. As a way of circumventing this problem, Wolfgang Pauli[10] hypothesised the existence of a new undetectable particle that he called a "neutron". To distinguish this hypothetical particle from the actual neutron discovered in 1932 by Chadwick[11], Enrico Fermi[12] proposed the term "neutrino" the same year. A long hunt started to experimentally detect this neutrino, which ended in 1956 when Cowan[13] and Reines[14] published the detection, performed near a nuclear reactor, of a particle showing the theoretical predicted properties of a neutrino [4]. After this observational confirmation, many experiments were built to analyse the physical properties of this new particle. Even though some important caveats still remain, the understanding of neutrinos has now achieved a reasonable level.

Neutrinos are particles embedded in the Standard Model (SM) of Particle Physics and are part of the family of fermions. They are spin $\frac{1}{2}$ fermions that do not carry any electric charge nor magnetic moment. They therefore only interact through the weak force. Neutrinos appear in three flavour eigenstates ν_e, ν_μ and ν_τ which reflect the flavour of the charged lepton they couple to in the so-called charged-current (CC) interaction. The CC interaction is a weak interaction with an exchange of a $W^\pm$ boson. The exact mass of each neutrino is yet unknown but neutrino flavour oscillations have been observed indicating that these particles have a non zero mass with mass eigenstates different from the flavour eigenstates. Direct measurements indicate that the neutrino masses are of the order of $m_\nu \lesssim \mathcal{O}(1)\,\mathrm{eV}$ [5, 6]. Non-zero neutrino masses form an important fact pointing to the limitations of the SM and represent, up to now, the only experimental discovery beyond the Standard Model.

Neutrino properties are of great interest for astronomy. As they only interact weakly with matter and do not carry charge, they can travel in a straight line over very large distances without being absorbed by interstellar medium or deviated by galactic or intergalactic magnetic fields. Neutrinos could therefore be very interesting cosmic messengers if we can detect them on Earth and reconstruct their arrival direction. Since the sixties, considerable experimental efforts have been devoted to the development of neutrino detectors. As the discovery of radio waves or cosmic rays, neutrino astronomy opens a new gateway to the study of the Cosmos, giving

[10]Wolfgang Ernst Pauli (⋆1900, †1958), Austrian-Swiss theoretical physicist.
[11]Sir James Chadwick (⋆1891, †1974), English physicist.
[12]Enrico Fermi (⋆1901, †1954), Italian physicist.
[13]Clyde Lorrain Cowan Jr (⋆1919, † 1974), American physicist.
[14]Frederick Reines (⋆1918, †1998), American physicist.

us possibly access to as of yet invisible regions. Suggested by Bahcall[15] and Davis[16], the first detected extraterrestrial neutrinos were originating from the Sun and have been detected by the Homestake experiment [7] in 1968. Later, Kamiokande [8], followed by Super-Kamiokande, pioneered a new technique to observe solar neutrinos using water Cherenkov detectors. Unless previous experminents as Homestake which were looking for excesses of events, Cherenkov detectors are real-time experiments that provide information on the directionality and the energy of the neutrinos. It is in 1987 that the first extragalactic neutrinos were finally detected. That year, the supernova SN1987A exploded and 19 neutrino events detected by 3 different experiments definitively opened the entirely new branch of astronomy: neutrino astronomy.

In this context, the work described in this thesis is devoted to the detection of neutrinos from the most luminous and among the most energetic events in the Universe, *i.e.* Gamma Ray Bursts (GRBs). These cataclysmic events are intriguing and puzzling phenomena for the physics community and many of their physical features are still unknown or not yet fully understood. Moreover, they have been proposed as promising candidates for hosting the acceleration engines generating the most energetic cosmic rays. However the latest results point towards hard constraints for GRBs to be the principal source of Ultra High Energy Cosmic Rays. Meanwhile the first extra-galactic neutrinos have been detected by the IceCube Collaboration [9], no neutrino has yet been detected in correlation with any GRB. By analysing a specific subclass of GRBs, the short duration GRBs, with a newly developed method, we aim at to detect the first GRB neutrinos.

∴

This thesis is divided in three parts: Part I introduces the physical context in which our research is performed, Part II considers the hardware and software tools we use in this thesis for detecting the targeted neutrino signal and the last part, Part III, presents the actual performed analysis and its results. Part I is composed of two chapters. Chapter 1 is devoted to a general introduction of the cosmic ray physics and develops the interest in neutrino astronomy. Chapter 2 presents the physics behind the studied objects, the Gamma Ray Bursts. It presents the current state of knowledge about GRBs, starting with different observational facts and reviews the current theoretical status of these cataclysmic objects. The neutrino production and the expected flux on Earth are finally described as well as the latest results of neutrino searches from GRBs.

Part II opens with Chapter 3 giving a detailed presentation of the IceCube Neutrino Telescope as well as an introduction to neutrino detection in the South Pole ice and an overview of the traces left by the leptons travelling through the ice. The first level of data processing is presented in Chapter 4 which explains how we transform the

[15] John Norris Bahcall (⋆1934, †2005), American astrophysicist.
[16] Raymond Davis, Jr. (⋆1914, †2006), American chemist and physicist.

detected electric pulses into candidate muon tracks and how we tag, in a cpu efficient way, possible events of interest. We close this chapter with a discussion about the data simulations used in this thesis.

After having discussed all the necessary background information, we open the presentation of the innovative analysis we have performed in Part III. We start with Chapter 5 which is devoted to a presentation of the performed event selection: the method we have developed to select among the overwhelming background of atmospheric neutrinos and muons, the targeted signal neutrinos for our analysis. This event selection is performed in two steps. We first start with a newly developed observable that gives a quantitative way for describing the up(down) behaviour of a track. We then train a Boosted Decision Tree forest for achieving neutrino level. Chapter 6 concentrates on the innovative statistical analysis used in our thesis and finally a discussion of the results of our 4-years analysis is presented in Chapter 7.

Part I

High Energy Astrophysics

CHAPTER 1

Introduction

As so many discoveries in the past, the discovery of Cosmic Rays in the early 1910's has been totally unexpected and opened a new era in the study of the cosmos, leading to the birth of Astroparticle Physics. This new way of analysing the Universe merges the fields of particle physics and astronomy and is a versatile means of increasing our knowledge about the Universe. For now, it has probably raised more questions than providing answers, making it an exciting field of research. Moreover, the past years have seen the development of a new type of astronomy: neutrino astronomy, which is now slowly becoming a mature research discipline. Our analysis is devoted to this new detection method that we will apply in the hope of observing neutrinos from Gamma Ray Bursts.

The first Section of this Chapter is devoted to a brief presentation of the nature and the physics of Cosmic Rays. An important part concentrates on an essential element which is the acceleration mechanisms allowing to achieve the very high energies observed. The next section reviews in a nutshell the interest of neutrino astronomy and the last section describes the present analysis.

∴

1.1 Cosmic Ray physics

For centuries, humans were observing and analysing the sky through the only accessible channel: photons. First by using the visible light and then adding slowly other parts of the electromagnetic spectrum until today where we have built observatories on the Earth and in the sky that allow us to analyse the full electromagnetic spectrum. We now know that these different bands of observations are an unique tool to learn more about the Cosmos. The electromagnetic radiation is now not any more the only observation

channel we use.

As outlined in the before, it all started in the 1910's, when various physicists realised measurements of the the "natural ionisation" of the air. In particular, Victor Hess performed a series of high-altitude balloon flights in order to quantify the variation of the ionising radiation with altitude. This meticulous experiment confirmed previous hints that the ionising radiation increases with the altitude [10]. As Hess wrote it himself, only one conclusion could be drawn from these observations: "The results of the present observations are most easily explained by the assumption that radiation with very high penetrating power enters the atmosphere from above; even in its lower layers, this radiation produces part of the ionisation observed in closed vessels [...] Since there was neither a decrease at night or during solar eclipse, the Sun can hardly be considered as the source [...]." [10]. The discovered radiation has thus an extraterrestrial origin. These particles crashing into the atmosphere are now known as *Cosmic Rays* (CRs). Since the discovery of this phenomenon, hundreds of experiments have been dedicated to the study of these particles (for a historical review, see [11]).

1.1.1 Primary Cosmic Rays

Nowadays the massive efforts invested for studying the Cosmic Rays allow us to generally conclude that: (1) Cosmic Rays consist of atomic nuclei, (2) their flux is almost isotropic and (3) the spectrum follows an approximate power law over many decades in energy. As seen in Fig. 1.1, CRs span a remarkable wide range of energy (10^9 up to 10^{20} eV) and more than thirty orders of magnitude considering their flux.

The current state of knowledge about the features behind this spectrum attributes the origin of the cosmic rays with energies below 1 GeV to solar activity [13]. For somewhat higher energies, CRs are thought to be from galactic origin [14] and recent work [15] seems to confirm previous theoretical predictions [16, 17] that supernova remnants are important contributors to this component of the CRs. As can be seen in Fig. 1.1, the spectrum exhibits in this range a break around 10^{15} eV called the *Knee*, which origin is not yet fully understood. While these nuclei can reach us from the galaxy because their energy does not exceed the limit of containment by the galactic magnetic fields, this is not any more the case for higher energies. Therefore, the nuclei observed from the second break called the *Ankle*, around 10^{18} eV, are supposed to have been created in extragalactic sources [18]. This part of the spectrum is called the Ultra-High Energy Cosmic Rays (UHECRs). While their origin is suggested to be extra-galactic no compelling evidence points yet to specific sources. Finally the end of the spectrum is suggested to be suppressed because of the so-called GZK effect. Greisen, Zatsepin and Kuzmin have indeed predicted that there should be a strong attenuation in the energy spectrum of the CRs at $5 \cdot 10^{19}$ eV [19, 20]. Protons of higher energies will be destroyed on their journey through the universe because they have enough energy to interact with the cosmic background radiation through a delta resonance. The measurements at these energies are very rare, this effect is therefore still under debate. However, as suggested

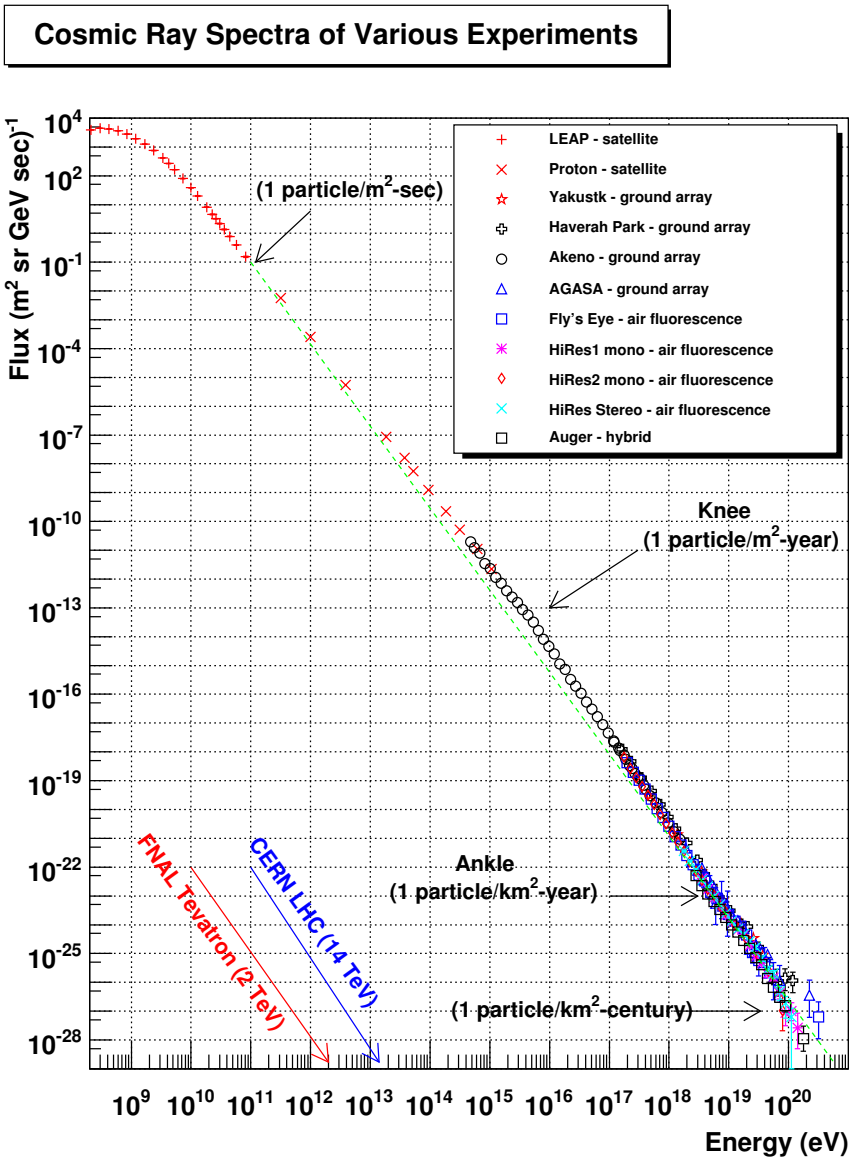

Figure 1.1: Measurements of the cosmic ray spectrum from several experiments. The observed spectrum shows only small deviations from an $E^{2.7}$ power law (shown as a dashed green line). While per-particle energies are well-measured, the distribution of the chemical composition of these particles is still under active investigation. From William Hanlon's (University of Utah) web site [12].

in Fig. 1.2, some observations seem to point to the existence of that effect.

In terms of composition, H and He form 85% and 12%, respectively of all CRs, with

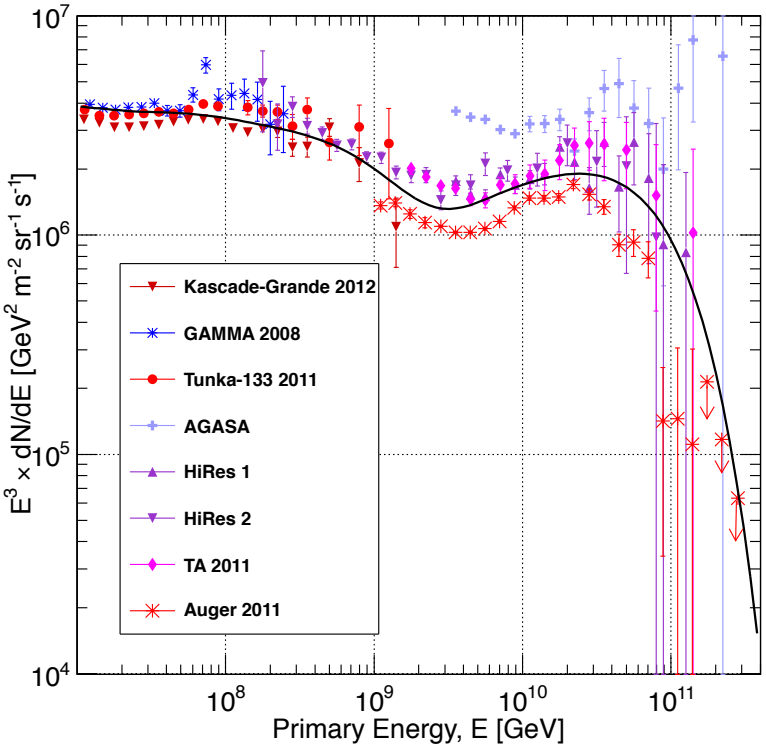

Figure 1.2: Ultra-High Energy Cosmic Ray fluxes measured with various giant air shower detectors. From [21].

contributions from heavier elements only at about 3% [22]. CR relative abundances follow closely those found natively in the Universe with the exception of elements Li, Be, B which are comparatively rarely produced by stars but are formed in CRs spallations with C and O nuclei.

Most of the observations realised on CRs are performed on Earth, which means that the experiments do not have directly access to the original CR particle. As depicted on the left part of Fig. 1.3, when a CR particle hits the Earth atmosphere, the primary nucleus initiates cascades of electromagnetic and hadronic interactions, creating lots of high energy secondary particles. Among these, the produced muons and neutrinos, which represent the biggest part of the flux at sea level (see right of Fig. 1.3), constitute an important background for the search of cosmic neutrinos. Distinguishing the Gamma Ray Burst neutrinos from these particles represents a hard challenge that is described in Chapter 5.

CRs are studied on Earth through the air showers they produce by observing directly the secondary produced particles or by detecting the Cherenkov or fluorescence

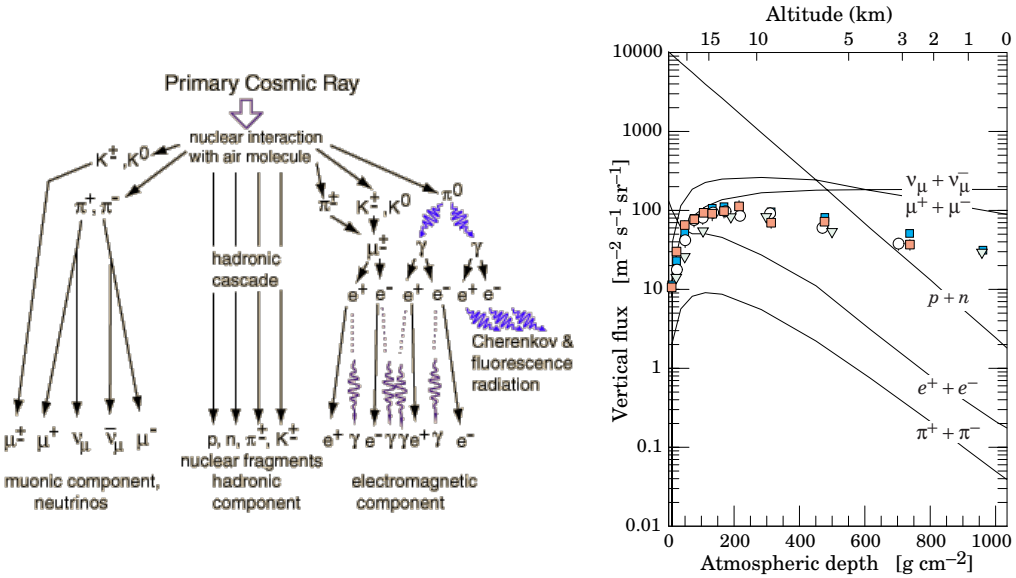

Figure 1.3: Left: Hadronic and electromagnetic cascades produced by the interaction of primary cosmic ray in Earth's atmosphere. Figure from the site of the Department of Physics and Astronomy of Georgia State University: http://hyperphysics.phy-astr.gsu.edu/hbase/hph.html. Right: Vertical fluxes of cosmic rays in the atmosphere with $E > 1\,\mathrm{GeV}$ estimated from the theoretical nucleon flux. The points show measurements of negative muons with $E_\mu > 1\,\mathrm{GeV}$. Figure from [23].

radiation emitted when these particles travel through the atmosphere. The first method involves particle detectors as e.g. scintillator arrays on the Earth surface or below it and the second involves photon detectors. One of the notable cosmic-ray experiments is the Pierre Auger Observatory [24] which is a "hybrid detector", meaning that it combines both techniques. This technique enlarges the instrument's effective area and improves the distinction between photon and hadron induced air showers. Among others the Pierre Auger Observatory, located in the southern hemisphere, is responsible for the great progress in composition studies of the CRs. Finally, it is to be noted that the IceCube Observatory also participates to such cosmic ray study through a dedicated instrument, called IceTop, composed of ice tanks on the surface of Antarctica.

As depicted in the previous paragraphs, though great progress has been achieved in the last decades, the physics of the CRs still contain a lot of open questions concerning their origin, their exact nature or about the acceleration mechanisms that achieve such high energies. In the next two sections, we will briefly review the most commonly accepted pictures for the origin of UHECR and the physics processes responsible for these high energies.

1.1.2 Possible sources of UHECRs

Obviously only the most energetic astrophysical objects could possibly produce these nuclei of energies higher than $10^9 - 10^{10}$ GeV. In this context, Hillas has developed a very simple argument for constraining the possible sources [25]. He argued that the accelerated particles must be confined in the accelerator by sufficiently strong magnetic fields, otherwise the nuclei would leave the accelerator before achieving the desired energy. The maximal energy is then obtained by imposing that the Larmor radius (the radius

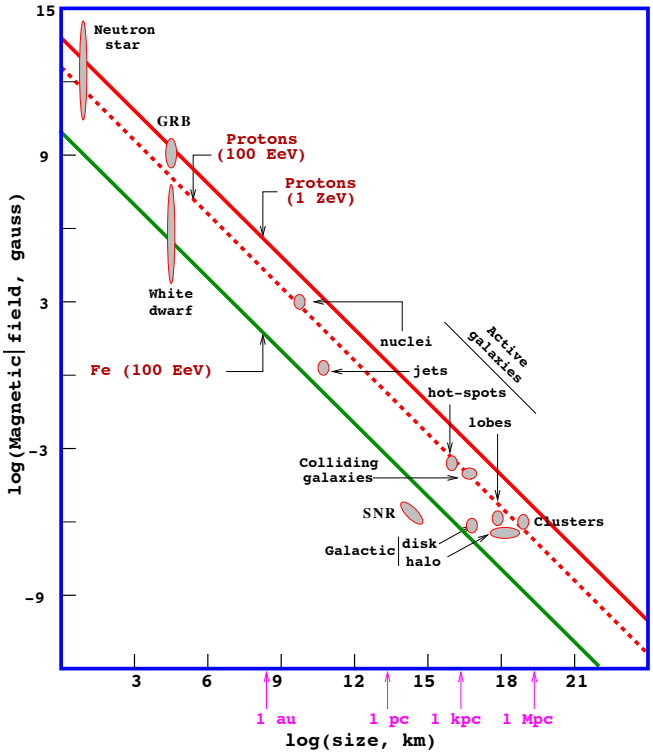

Figure 1.4: The Hillas plot. The magnetic field needed to contain a particle within a source long enough to obtain a given energy is a function of the size of the source and the species of the particle. The solid red line indicates the threshold for producing 10^{12} GeV protons; the dotted red line is the threshold for producing 10^{11} GeV protons; and the green line is the threshold for producing 10^{11} GeV iron nuclei. Figure modified from [25].

of the orbit of a charged particle moving in a uniform, perpendicular magnetic field) $R_L = E/(ZeB)$ fits inside the accelerator of size R_s. This directly yields the maximum energy that the source can provide:

$$E_{\max} = \Gamma ZeBR_s, \tag{1.1}$$

with e the electron charge, Z the atomic number, B the magnetic field intensity and where the Lorentz factor Γ has been introduced accounting for a possible relativistic bulk motion of the accelerated plasma, which is probably only needed for Gamma Ray Bursts (GRBs). The so-called "Hillas plot" is presented in Fig. 1.4. This straightforward argument does not account for details of acceleration mechanisms and therefore is not exact but it gives, with one simple calculation, generic constraints on the possible sources. Based on this criterion, GRBs emerge as very promising possible cosmic accelerators for the highest energy CRs.

GRBs are among the most violent events known in the Universe with energy releases of $\mathcal{O}(10^{51} - 10^{54}\,\mathrm{erg})$ and have been proposed by Waxman-Bahcall to be potentially the only source of UHECR in the Universe (see Chapter 2). They are divided in two sub-varieties, depending on their duration that varies from a fraction of a second to many minutes. Moreover, these objects are most of the time well-localised in space and in time, making them convenient objects to study and allowing for low background observations. A detailed presentation of these objects is given in Chapter 2.

1.1.3 Acceleration mechanisms

From the previous discussions, we know that we need acceleration processes that account for at least the two following energy considerations:

1. The obtained energy spectrum has to be a power-law in energy for all types of charged particles. The energy spectrum of cosmic rays of non-thermal sources has the form $\mathrm{d}N(E) \propto E^{-x}\,\mathrm{d}E$, with typical values of x in the range $2 - 3$.

2. The acceleration of cosmic rays has to reache energies of $E \sim 10^{20}\,\mathrm{eV}$.

Different acceleration mechanisms have been proposed during past decades. They can originate from processes as simple as multiple collisions of particles with clouds or more complicated involving hydrodynamic models and electromagnetism. The Fermi mechanism [26] is the most commonly admitted acceleration model for describing the origin of the high energy cosmic rays. It has been first proposed in 1949 by Enrico Fermi as a stochastic means by which particles could be accelerated to high energies through collisions with interstellar medium clouds. A detailed presentation and derivation of this mechanism can be found in [27]. We follow this reference and its computations in next sections.

1.1.3.1 Second order Fermi acceleration

The so-called "Second order Fermi acceleration" refers to the original version of Fermi's work. As illustrated in Fig. 1.5, it is based on charged particles that are reflected from "magnetic mirrors" associated with irregularities in the Galactic magnetic field. For an observer, the mirrors are assumed to move randomly with typical velocity V and Fermi showed that the particles gain energy stochastically in these reflections.

Following [27], we will now quantify the average energy gain per collision and derive the corresponding energy spectrum of the accelerated particles.

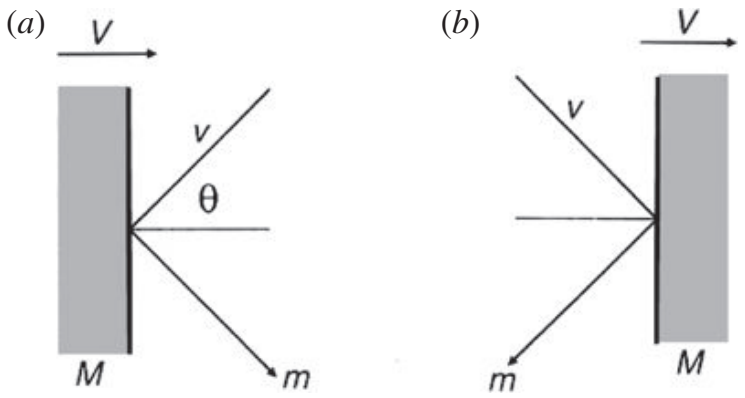

Figure 1.5: Collision between a particle of mass m and a cloud of mass M: (a) a head-on collision; (b) a following collision [27].

The mirror is taken to be infinitely massive and so its velocity is unchanged in the collision. The centre of momentum frame of reference is therefore that of the cloud moving at velocity V . The energy of the particle in this frame is given by the Lorentz transformation:

$$E_0' = \gamma(E_0 + V\,p_x), \tag{1.2}$$

where E_0 is the original energy of the particle in the observer frame, $p_x = p\cos\theta$ is the x-component of the momentum of the particle in that frame, and γ is the relativistic Lorentz γ factor, $\gamma = \left(1 - \frac{V^2}{c^2}\right)^{-\frac{1}{2}}$.

We know that in the CMS frame, the energy is conserved during the collision, $E_0' = E_1'$ while the momentum is inverted $p_x' \to -p_x'$. We therefore obtain the following energy after the collision back in the observer frame:

$$E_1 = \gamma\left(E_0' + V\,p_x'\right), \tag{1.3}$$

leading to

$$E_1 = \gamma^2 E_0\left(1 + \frac{V\,p_x}{E_0} + \frac{V\,p_x'}{\gamma E_0}\right). \tag{1.4}$$

Applying the Lorentz transformation for transforming the particle momentum in the CMS frame to the observer frame and rewriting the energy and the momentum terms, we obtain:

$$E_1 = \gamma^2 E_0\left(1 + \frac{2V\,v\cos\theta}{c^2} + \frac{V^2}{c^2}\right). \tag{1.5}$$

Expanding to second order in $\frac{V}{c}$, we get

$$\frac{\Delta E}{E_0} \equiv \frac{E_1 - E_0}{E_0} = \left(\frac{2V\, v \cos\theta}{c^2} + 2\frac{V^2}{c^2} \right). \tag{1.6}$$

This result has then to be averaged over all the possible values of the angle θ in the range 0 to π, which leads to (see [27])

$$\left\langle \frac{\Delta E}{E_0} \right\rangle = \frac{8}{3} \left(\frac{V}{c} \right)^2 \tag{1.7}$$

The average energy gain is proportional to $\left(\frac{V}{c}\right)^2$: the process is known as *second-order* acceleration owing to the value of the exponent. If we calculate the average time between collisions [27], an energy rate can be derived from previous equation

$$\frac{\mathrm{d}E}{\mathrm{d}t} = \frac{4}{3} \left(\frac{V^2}{cL} \right) E = \alpha E, \tag{1.8}$$

where L is the mean free path between cloud collisions, along the field lines.

Finally, it is then possible to find the energy spectrum $N(E)$ by solving a diffusion-loss equation in the steady state and considering this energy rate [27]. We also need to introduce the characteristic time for a particle to remain in the accelerating region, τ_{esc}. In so doing, one finds that

$$N(E)\mathrm{d}E \propto E^{-x}\mathrm{d}E, \tag{1.9}$$

where $x = 1 + (\alpha\tau_{\mathrm{esc}})^{-1}$.

Even though second-order acceleration succeeds in generating a power-law spectrum, it is not a completely satisfactory mechanism at least for two reasons:

- First, on account of the observed low cloud density and the very small random velocity of interstellar clouds in the galaxy compared to the velocity of light, the energy gain, α is very low.
- Second, the mechanism fails to explain the observed value of 2.7 for the exponent in the power-law spectrum: the value of the exponent is determined by the uncertain value of the combination $\alpha\tau_{\mathrm{esc}}$. It would be surprising if the mechanism of acceleration in very diverse types of sources were such that the product of τ_{esc} and the rate of energy gain conspired to give the same value of x.

1.1.3.2 Diffuse shock acceleration in strong shock waves

In the late 1970s a new version of the Fermi mechanism associated with particle acceleration in strong shock waves has been developed, often referred to as "diffusive shock acceleration". The key feature of this process, as we will see in the next paragraphs,

is that the acceleration is first order in the shock velocity and automatically results in a power-law spectrum with energy spectral index $x \approx 2$. This mechanism has been discovered independently by a number of different authors (see for example the work of Bell [28]).

Before we discuss first-order Fermi acceleration, it is convenient to formulate the Fermi mechanism in a different and simpler way, valid for both the second- and first-order versions. For this purpose, let us define two constants β and P as follows: βE_0 is the average energy gain of the particle after one collision, with E_0 the energy before the collision, and P is the probability that the particle remains, after one collision, inside the acceleration region. After n collisions, we then have $N = N_0 P^n$ particles with energies $E = E_0 \beta^n$. Eliminating n in these equations, we obtain $\frac{\ln(N/N_0)}{\ln(E/E_0)} = \frac{\ln P}{\ln \beta}$ and hence, we have

$$\frac{N}{N_0} = \left(\frac{E}{E_0}\right)^{\frac{\ln P}{\ln \beta}}. \tag{1.10}$$

Since this value of N is $N(\geq E)$ since this is the number which reach energy E and some fraction of them continue to be accelerated to higher energies, this leads again to a power-law energy spectrum of the form:

$$N(E)\mathrm{d}E \propto E^{-1+\left(\frac{\ln P}{\ln \beta}\right)}\mathrm{d}E \tag{1.11}$$

We obtain again the expected power-law and the parameters P and β can be translated into the ones that were found for the Fermi second-order mechanism.

The advantage of the first-order acceleration mechanism is that it yields an energy gain that is linear in $\left(\frac{V}{c}\right)$, a condition that would make the acceleration process more effective, especially at relatively high values of V. This set-up will occur when the relativistic particles collide with strong shock waves (e.g., like those produced in GRBs, active galactic nuclei, etc.), which can reach supersonic velocities (10^3 times the velocity of an interstellar cloud). The dynamics of high-energy particles in the vicinity of a strong shock wave are illustrated in Fig 1.6.

Performing the same reasoning as in the previous section for a complete acceleration cycle, we can work out the average energy of the particle after one collision, β. Owing to the turbulence behind the shock and the irregularities in front of it, the particle velocity distribution is isotropic in the frames of reference where the interstellar gas is at rest on either side of the shock. Consequently, there is a complete symmetry when a high-energy particle crosses the shock from downstream to upstream or from upstream to downstream. In both types of crossing, the particle gains energy given by (see again [27] for a detailed derivation):

$$\left\langle \frac{\Delta E}{E} \right\rangle = \frac{4}{3}\frac{V}{c} \tag{1.12}$$

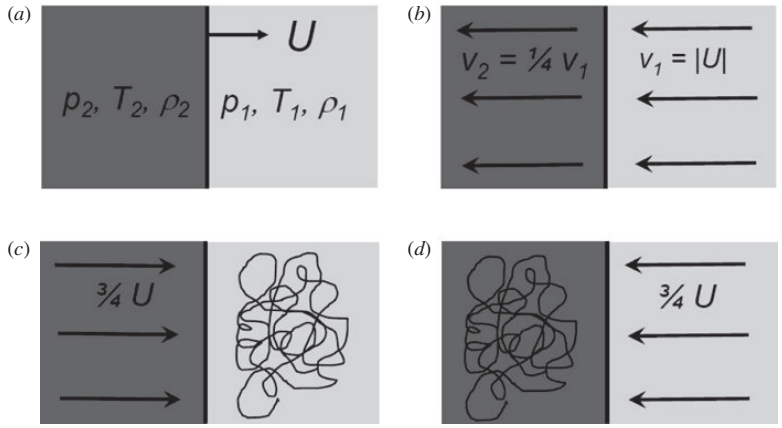

Figure 1.6: The dynamics of high-energy particles in the vicinity of a strong shock wave. (a) A strong shock wave propagating at a supersonic velocity U through stationary interstellar gas with density ρ_1 , pressure p_1 and temperature T_1 . The density, pressure and temperature behind the shock are ρ_2 , p_2 and T_2 , respectively. (b) The flow of interstellar gas in the vicinity of the shock front in the reference frame in which the shock front is at rest. In this frame of reference, the ratio of the upstream to the downstream velocity is, for a fully ionised plasma, $v_1/v_2 = 4$. (c) The flow of gas as observed in the frame of reference in which the upstream gas is stationary and the velocity distribution of the high energy particles is isotropic. (d) The flow of gas as observed in the frame of reference in which the downstream gas is stationary and the velocity distribution of high energy particles is isotropic. From [27].

leading to

$$\beta = 1 + \frac{4}{3}\frac{V}{c}, \tag{1.13}$$

in one round trip.

We are then only left with P, which is related to $P_{\rm esc}$, the particle escape probability from the shock. Following Bell's argument and using kinetic theory, one obtains

$$P_{\rm esc} = \frac{4}{3}\frac{V}{c} \tag{1.14}$$

Replacing these two parameters in Eq. (1.11), we finally obtain the desired spectrum

$$N(E)\mathrm{d}E \propto E^{-2}\mathrm{d}E. \tag{1.15}$$

Incorporation of other ingredients as non-diffusive transport properties allows the spectral index to reach up to ~ 2.5.

1.2 Neutrino Astronomy : a new window on the Universe

As briefly discussed in the previous section, the origin of the UHECRs is still an open question in Astroparticle Physics. Unfortunately, observing directly the cosmic rays for detecting their related sources is non trivial. The intergalactic and galactic magnetic fields are indeed responsible for curving all the charged particles travelling through them and make therefore direct correlation of CR to any astrophysical sources impossible except for very nearby objects or for the most energetic cosmic rays.

That is why, using neutral particles as photons or neutrinos is a much more promising approach. They would indeed not be affected by magnetic deviations. If the acceleration mechanisms involve hadronic components, neutrinos and gammas will be produced (see Section 2.5). However, most of these photons will interact with matter or background radiation before arriving on Earth and those that survive will be difficult to distinguish from the bulk of observed emission from the accelerator. Moreover, as the line of sight to very distant objects may be obscured by interstellar dust, part of these photons will also be blocked on their way to the Earth. However, the neutrinos do not suffer from all these drawbacks. They are indeed only interacting weakly and their mean free path is therefore much larger than for other particles. Neutrinos can thus reach Earth totally unimpeded. These considerations are depicted in Fig. 1.7.

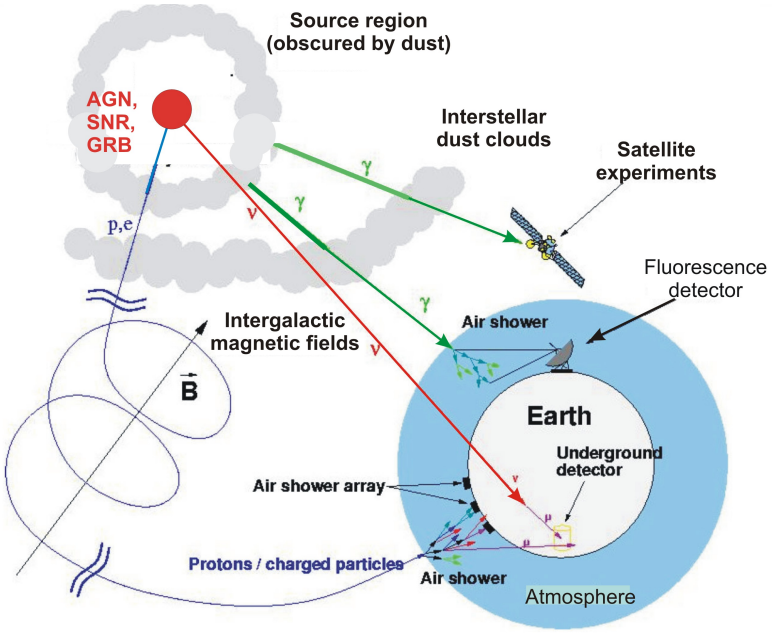

Figure 1.7: Illustration of the possible observation channels of distant objects. From [29].

However, this enormous advantage in their propagation to the Earth is also an important disadvantage for detecting them. To illustrate this, remember that the neutrino cross section with normal matter for a neutrino of energy E_ν in the GeV range is given by:

$$\sigma_{\nu N} \sim 10^{-38} \frac{E_\nu}{1\,\mathrm{GeV}}\,\mathrm{cm}^2\,\mathrm{nucleon}^{-1}. \tag{1.16}$$

The interaction between a neutrino and a nucleon is therefore a very rare process and requests the use of huge detectors in order to increase the chance of such a process. Another option is of course to observe over a very long period of time (or to stack as much as possible observations) to increase the statistics.

For a long time, this new channel for astronomy has therefore only been postulated but no astrophysical neutrinos had never been detected. Today, using three years of the data of the full detector, IceCube has proven that it is possible. The IceCube Collaboration has identified 37 neutrino candidate events rejecting a purely atmospheric explanation at 5.7 σ [9]. Unfortunately, no hypothesis test yet yielded statistically significant evidence of clustering or correlations of these neutrinos with known astrophysical sources. One thing is however sure now, neutrino astronomy has started!

1.3 The present analysis

As indicated in last section, astrophysical neutrinos have now been detected for the first time in history but they have not yet been correlated to any known astrophysical sources. On the other hand, the origin of the Ultra-High Energy Cosmic Rays is still under debate and remains unknown albeit an impressive effort has been devoted to that field of research. Different astrophysical objects emerge as promising candidates among which we find Gamma Ray Bursts. GRBs are distant sources, which were discovered accidentally by military satellites recording their flashes of high-energy electromagnetic radiation [30]. GRBs are observed to have a well defined localised position and a well define duration, which, as mentioned before, allows us to reduce the background in analysing this kind of data.

The aim of this thesis is to perform an original analysis on neutrinos emitted from short duration GRBs (SGRBs). We have decided to split the dataset in long and short GRBs in the hope that the optimisation of the statistical method only for SGRBs can result in a neutrino detection in relation with a GRB or in stringent upper-limits on the neutrino flux. Our approach consists of analysing, for the first time, four full years of IceCube data (from May 13th, 2011 to May 18th, 2015) and to develop a new procedure for the selection of relevant neutrinos hidden in background data. This procedure is performed in two steps: a precut is first applied based on a newly developed method combining the information of different track reconstructions and a final selection is then realised through a "Boosted Decision Tree" procedure. This event selection turns to be more efficient than the classical procedure used until now in GRB analysis in the IceCube

Collaboration. Finally specific statistical tools exploiting the physical properties of the SGRBs are developed leading to very competitive sensitivities. More over, as no prompt neutrinos (neutrinos emitted during the gamma flash of the GRB) have been detected so far either by IceCube or by Antares [31, 32, 33, 34], we have worked out an analysis that is sensititive to earlier or later burst of neutrinos.

CHAPTER 2

Gamma Ray Bursts

As mentioned in the previous Chapter, Gamma Ray Bursts (GRBs) are promising candidates for the origin of the UHECRs. Moreover, these extreme phenomena open a great number of questions which remain still unanswered. The launch of new satellites (e.g. Fermi and Swift, see [35, 36, 37] for a general presentation), has given access to very useful pieces of information that opened a new era towards understanding these events. In this Chapter, we will present the history of the discovery of GRBs and present the current theoretical perception of these cataclysmic events. This presentation is based on [38, 39, 40].

The first section will be devoted to a general overview of the actual status of knowledge of GRBs and to the history of their discoveries. The experimental data obtained with the satellites BATSE, BeppoSAX, Swift and Fermi as well as their implications on the understanding of GRBs will, in turn, be presented in more detail in the second section. The third and the fourth sections will focus on the physics related to GRBs. We will present in the third section the most accepted model for the origin of the γ-rays and for the other wavelength photons, the so-called *Fireball Model* originally proposed by Paczyński and Goodman [41, 42] and developed later, among others, by Shemi and Piran [43]. We will also present the generally accepted models for accelerating particles inside jets of relativistic outflows, which is a general characteristic of these phenomena [38, 39]. We will then briefly review the possible candidates of progenitors in the fourth section.

The two last sections will finally present the neutrino production in GRBs: Section 2.5 will present the neutrino flux expected from GRBs, based on the actual most popular model, the Waxman-Bahcall model [44, 45, 46]. Section 2.6 will then close this chapter presenting the efforts made by the IceCube collaboration in this field of research.

∴

2.1 General overview

Within the physics community GRBs have been known for a long time and are still puzzling. As outlined by Gomboc [47], they are extremely complex phenomena related to many fields of (astro)physics: they emit photons from radio wavelengths to gamma-rays, as well as non-electromagnetic particles like protons, neutrinos or even gravitational waves ; they seem to be related to the late stages of stars and, due to their enormous luminosities, they are also of great interest for cosmological studies.

GRBs are sudden, intense and non-repetitive flashes of gamma-rays, with mainly a non-thermal spectrum[1] peaking at $E_\gamma \sim 100\,\mathrm{keV}-1\,\mathrm{MeV}$, which outshines all the other sources of γ-rays in the sky. These brief events are occurring at an average rate of a few per day throughout the Universe. They are the most luminous and among the most energetic events in the Universe: the measured γ-ray fluence implies indeed, if it is emitted isotropically, that GRBs release a total energy of one solar rest mass, $M_\odot c^2 \sim 10^{54}\,\mathrm{ergs}$[2]. Moreover, GRBs last from $10^{-3}\,\mathrm{s}$ to about $10^3\,\mathrm{s}$, meaning that this huge quantity of energy is released in a few seconds, leading to an isotropic luminosity of $\sim 10^{51}\,\mathrm{ergs/s}-10^{57}\,\mathrm{ergs/s}$. This amount can be compared to another type of cataclysmic events, the *Supernovæ*. In this case, the total observed energy output is of the order of $\sim 10^{51}\,\mathrm{ergs}$ but is detected over timescales of weeks to months! Actually, GRBs are the most concentrated and brightest electromagnetic explosions in the Universe.

Despite their particular luminosity and keeping in mind that the Earth atmosphere is basically non-transparent to γ-rays, the discovery of the GRBs only took place in the late 1960s. They were accidentally discovered in 1967 by the USA military Vela satellites monitoring the "Outer Space Treaty" that forbade nuclear tests in space. It was soon realised that these detected gamma-ray flashes were not coming from the Earth direction but originated from outside the Solar System, leading to a new extremely puzzling cosmic phenomenon [30]. The official announcement of this wonderful by-product of the military mission has only been announced some years later by Klebesadel *et al.* [30] and was quickly confirmed by Russian observations [49] and by the IMP-6 satellite [50]. These extreme events challenged the theorists and in 1974, only one year after the publication of the GRB discovery, there were already 15 models developed and by 1992 more than a hundred.

For a long time, the origin of GRBs has remained a complete mystery. The first significant step forward came from the results of the *Burts and Transient Source Expermient* (BATSE) detector on the Compton Gamma Ray Observatory, launched in 1991. The interested reader can find a complete summary of these results in [51]. The all-sky survey from BATSE obtained the positions of $\sim$ 3000 GRBs and indicated an

[1] The Fermi GBM experiment has confirmed previous indications from BATSE of the presence of an underlying thermal component [48].

[2] As we will see later, the emission is actually not isotropic and leads to a total energy release of $10^{54} \times \frac{\Omega_\gamma}{4\pi} \sim 10^{51}$ ergs, where Ω_γ is the solid angle into which the gamma-rays are beamed.

isotropic distribution, ruling out a galactic origin for these events and hence strongly suggesting that GRBs appear at cosmological distances [52]. These gigantic distances imply an enormous quantity of energy, which, from the fast time variability of the fluxes, must arise in a small volume and in a very short time. The current interpretation is that a great amount of gravitational energy is released by a cataclysmic stellar event, e.g. the core collapse of a massive star or the merger of two heavy compact cores, like neutron stars or black holes. Most of this energy will escape in the first few seconds through thermal neutrinos and probably also through gravitational waves. This release of energy will then lead to the formation of an ultrarelativistically expanding fireball [41, 42, 43] containing $e^+ - e^-$ pairs, photons and relatively fewer baryons (mostly protons). This optically thick hot plasma expands due to the radiation pressure overcoming the gravitational forces [53].

While not all observed features are understood, there is an overall agreement between the observations and the *Fireball model* [38]. According to this model the γ-rays are produced when the kinetic energy of this ultrarelativistic flow is dissipated. As the observed burst spectra are principally non-thermal, this conversion of kinetic energy to radiation must occur in an optically thin region due to interactions with the external medium (e.g. the ISM [54]) or to an internal process with internal shocks inside the flow itself [55, 56, 57].

A last important contribution of BATSE is, as we will discuss in more detail later, the confirmation of earlier hints [58] that GRBs separate in two categories of different durations [59]: the short GRBs (SGRBs) with $T_{90} \lesssim 2\,\mathrm{s}$ and the long GRBs (LGRBs) with $T_{90} \gtrsim 2\,\mathrm{s}$[3].

For almost thirty years GRBs were only observed in prompt γ-rays, which made it impossible to perform an accurate position determination and hence maintained the mystery around their site of origin. In 1997, a major development has been achieved with the detection of X-ray afterglow [60] counterparts of GRBs by the Italian-Dutch satellite BeppoSAX [61]. This allowed follow up observations by other satellites or ground based instruments and the detection of optical [62, 63] and even radio [64] signals. These studies yielded sufficient accurate position determinations and hence opened the way to the identification of candidate host galaxies in almost all cases and enabled optical redshifts to be measured and the extragalactic origin of GRBs to be confirmed [65, 66, 67]. Within the host galaxies there is evidence that long duration GRBs arise within star-forming regions, and there is evidence that they follow the star formation rate [38]. The detections of these counterparts, sometimes over timescales of many months or even several years (for radio waves) after the γ emission, led to the identification of the existence of a GRB *afterglow*: lower-energy, long-lasting emission

[3] T_{90} is defined as the time needed to accumulate from 5% to 95% of the fluence in the $50 - 300\,\mathrm{keV}$ band.

in the X-ray, optical and radio wavelengths, as shown for example in Fig. 2.1[4] . The analysis of these afterglows, which had been predicted by the fireball mechanism [68], has provided strong confirmation for this generic model, as described in [69, 70, 71, 72]. BeppoSAX also contributed to the characterization of a new class of sources called X-ray flashes (XRF) [73] very likely representing softer GRBs.

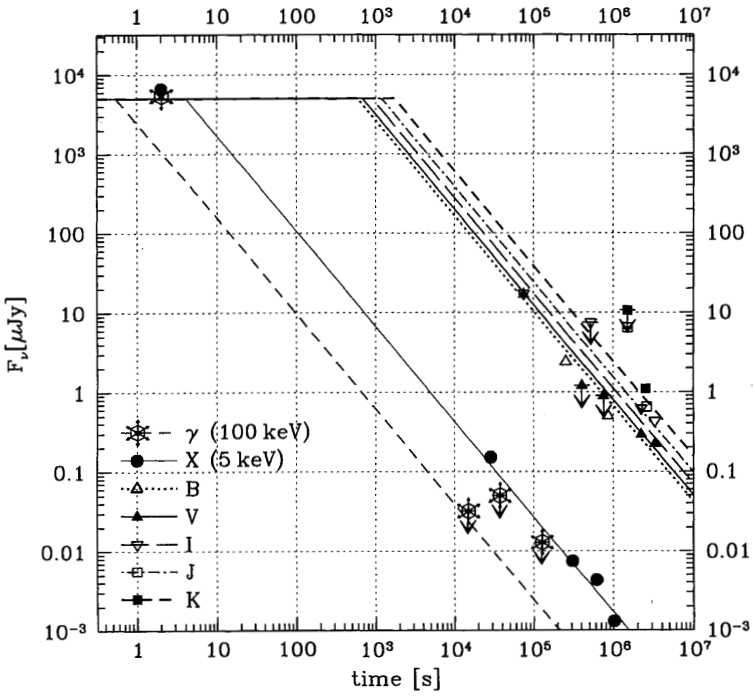

Figure 2.1: The afterglow light curves of GRB 970228 from gamma-rays to near-infrared. The lines indicate the prediction for a relativistic blast wave [69].

Finally, the launch of the Swift and the Fermi satellites respectively in 2004 and 2008, has opened the third era in GRBs studies [40]. Swift [35] has a wide-field imaging camera that detects bursts at a rate of $\sim 90\,\mathrm{yr}^{-1}$, providing positions with arcminute accuracy. The spacecraft then autonomously reorients itself for sensitive X-ray and UV/optical observations of the afterglow. Fermi is composed of two wide-field instruments : the Gamma-ray Burst Monitor (GBM) [36] and the Large Area Telescope (LAT) [37]. The GBM detects bursts in the gamma-ray band (a few keV to $\sim$ 30 MeV) at a rate of $\sim 300\,\mathrm{yr}^{-1}$ with an angular error of $\sim 10\,^{\circ}$. On the other hand, LAT observes bursts in the largely-unexplored high-energy gamma-ray band (20 MeV to more than 300 GeV)

[4]GRBs are named based on the following convention : GRB YYMMDD, where Y,M and D are respectively the year, the month and the day of their observation. In case more than one GRB appears on the same date, a letter is added following the order of the alphabet, e.g. GRB 110824B, is the second observed GRB of the August 24th, 2011.

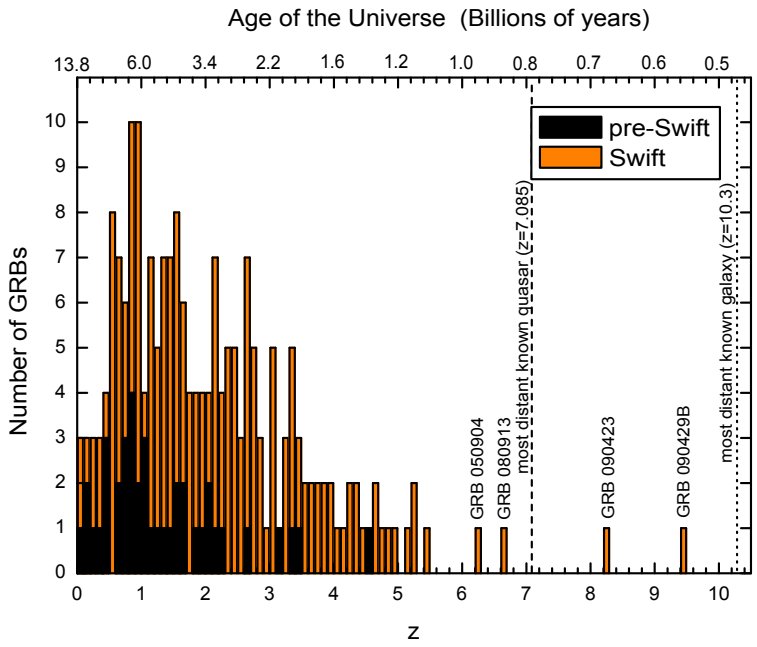

Figure 2.2: GRB redshift distribution. Due to the higher sensitivity and the rapid response time of Swift in comparison to e.g. BeppoSAX, and follow-up campaigns, the redshift distribution of pre-Swift and Swift GRBs are different: average redshift of the Swift GRBs is larger of a factor ~ 2 compared to previous data. This figure was obtained from [47].

at a rate of $\sim 10\,\mathrm{yr}^{-1}$. Combined, the two missions are improving our understanding of all aspects of GRBs, including the origin of short bursts, the nature of bursts coming from the explosion of early stars in the universe and the physics of the fireball outflows that produce the gamma-ray emission. As seen in Fig. 2.2, Swift also opened a new dimension in the redshift window due to improved equipment and response time.

2.2 Observational facts

As mentioned before, GRBs are short, unexpected and principally non-thermal bursts of γ-rays. However a wide diversity of bursts has been observed. It is therefore almost impossible to summarize all the features of these objects. Following the general classification of Piran [74], we will concentrate on their principal characteristics.

2.2.1 Burst duration

The "typical" duration of GRBs is $\mathcal{O}(10\,\mathrm{s})$ but can vary from the millisecond scale to thousands of seconds, as can be seen in Fig. 2.3. The separation between long ($T_{90} \gtrsim 2\,\mathrm{s}$)

and short ($T_{90} \lesssim 2\,\mathrm{s}$) bursts is clearly visible. It is important to note that, as explained by Kouveliotou *et al.* [59], this separation is not an instrumental artifact of BATSE but is a real physical property. Actually, both subpopulations are isotropically distributed as expected from two physics subpopulations of extragalactic sources. One generally considers that the fraction of SGRBs is $\sim 30\%$ and $\sim 70\%$ for LGRBs.

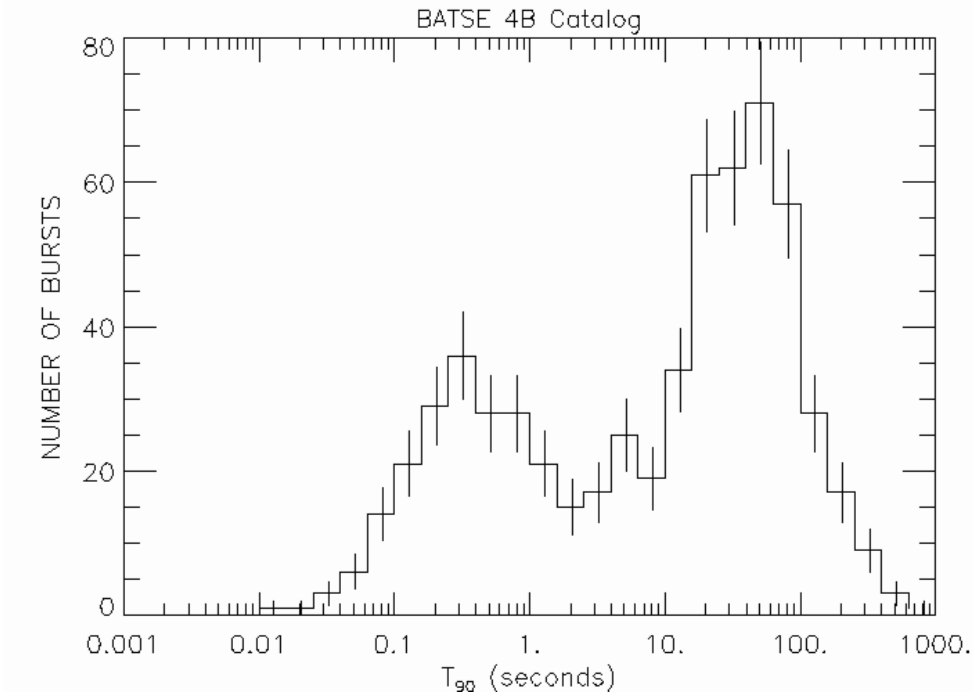

Figure 2.3: Distribution of T_{90} for 1234 GRBs in the BATSE 4B Catalog. From [75].

It has been postulated that this separation into two subpopulations has also been found in the distribution of the spectral hardness ratio. The hardness ratio (HR) of a burst is defined as the fluence in the channel $100 - 300\,\mathrm{keV}$ divided by the fluence in the channel $50 - 100\,\mathrm{keV}$. This has been suggested by Qin *et al.* [76] with the data of the fourth BATSE (4B) catalog as shown in Fig. 2.4. Qin *et al.* have shown that, while the hardness ratio and the duration are correlated for the entire set of the 4B catalog, they are not at all correlated within any of the two subclasses. To confirm the intrinsic existence of these two populations, they considered various other separations of T_{90} to make a division between short and long bursts and found them always correlated, clearly confirming the existence of the two classes of GRBs, when separating at 2s.

Moreover, the existence of two populations seems to be confirmed in the light of the difficult question of the *progenitor* candidates of GRBs. As we will discuss in Section 2.4,

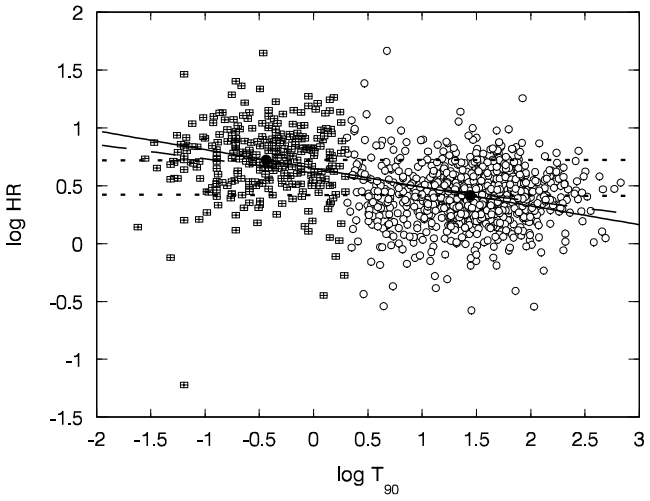

Figure 2.4: Distribution of $\log HR$ versus $\log T_{90}$ of the 1179 GRBs from the 4B catalog [59] with available T_{90} values and fluences in the two considered channels, where T_{90} is in units of s. The open circles represent the long GRBs and the squares, the short ones. The solid line is the regression line of the total sample, while the two dotted lines are the regression lines for the two subsamples. Filled circles represent the two data points standing for the average values of the two quantities for the two classes respectively. The dashed line is a straight line connecting these two data points.

the commonly accepted picture is that LGRBs and SGRBs have a different origin. This different origin could possibly lead to different neutrino timing signatures and therefore we have decided to restrict our study in this thesis to only one of the subpopulations: the short duration Gamma Ray Bursts.

2.2.2 Temporal structure and variability of the GRB light curves

As outlined in [39], the light curves of the prompt GRB emission are greatly diverse (see, e.g. Fig. 2.5): from smooth, fast-rise and quasi-exponential decay, through curves with several peaks, to highly variable curves with many peaks [51]. The pulse distribution is complex [77], and the time structure can provide clues for the geometry of the emitting regions [78]. However, only $\sim$ 80% of the bursts show substantial substructure in their light curves [38].

The variability of the prompt emission of the bursts is measured through the observable δt, which is determined by the width of the peaks. δt is much shorter (in some cases by more than a factor of 10^4) than the duration of the bursts. Based on empirical correlations between δt and the isotropic luminosity of GRBs, Fenimore and Ramirez-Ruiz [79] suggested that it can be used as distance measures for the bursts that

do not have a known redshift (see also [80]).

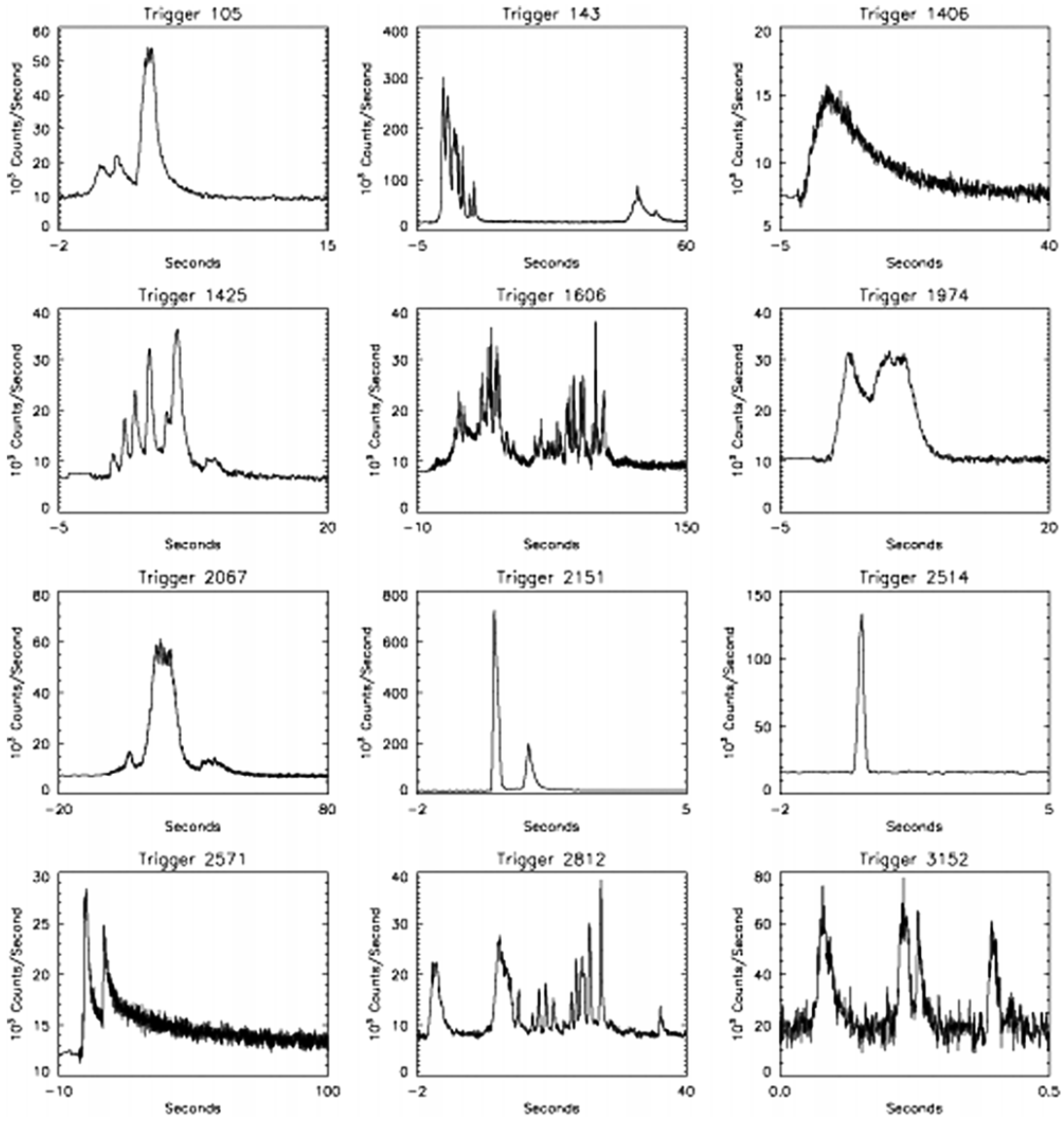

Figure 2.5: Diversity of gamma-ray light curves observed by BATSE [39].

2.2.3 Characteristics of the GRB photon emission

As already mentioned, the photon emission from GRBs consists of a prompt emission and an afterglow component. The prompt emission is characterized by a peak at $E_\gamma \sim 100\,\mathrm{keV}-1\,\mathrm{MeV}$ with a high energy tail as wel as a lower energy component. On the

other hand, the afterglow is a lower energy counterpart and contains radiation of X-rays, UV/Optical photons and even radio waves. We will sketch, in the following, the principal features of these spectra and the theoretical aspects will be discussed in Section 2.3.

For a long time the GRB prompt emission was considered as a non-thermal spectrum [38, 47, 74]. As we will see further, the picture is apparently more complex. Generally, it is important to note that the spectrum varies strongly from one burst to another. However, Band *et al.* [81] succeeded in fitting an excellent phenomenological broken power law (see Fig. 2.6), the so-called *Band function*, with a typical break energy, $(\alpha - \beta)E_0 \sim 200\,\mathrm{keV}$, and power law extensions down into the X-ray, and up into the 100 MeV to GeV ranges, given by :

$$\frac{\mathrm{d}N_\gamma}{\mathrm{d}E} = N_0 \times \begin{cases} \exp(-\frac{E}{E_0})\, E^\alpha & \text{for} \quad E \leq (\alpha-\beta)E_0 \\ [(\alpha-\beta)E_0]^{\alpha-\beta}\, \exp(\beta-\alpha)\, E^\beta & \text{for} \quad E \geq (\alpha-\beta)E_0, \end{cases} \tag{2.1}$$

where N_γ is the number of photons, E the photon energy, E_0 the break energy, α and β are respectively the low-energy and high energy spectral indices and N_0 a constant parameter of the fit. As emphasised by Band *et al.*, there is no specific theoretical model that predicts this spectral shape. Still, this three-parameter function fits most of the observed bursts.

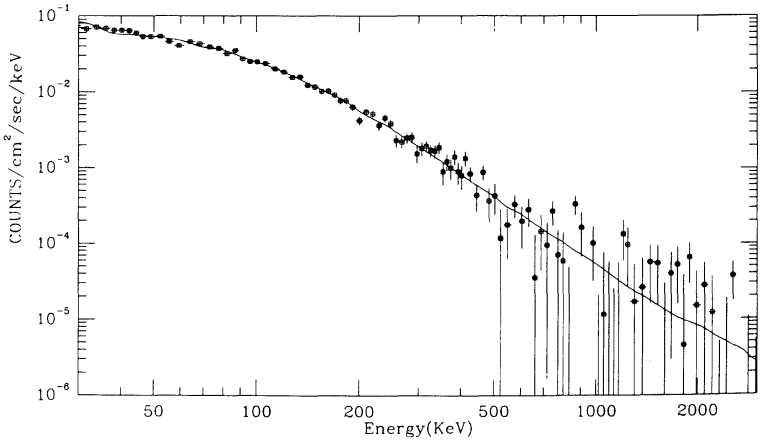

Figure 2.6: Spectrum of GRB 911127 fitted with the Band function [81].

Nowadays, recent investigations indicate that a thermal component is also present [48, 82, 83], confirming previous suggestions made by Mészáros *et al.* [84]. This thermal component was detected in the spectrum of e.g. GRB110721A, one of the brightest bursts observed by the Fermi Gamma-ray Space Telescope. Its prompt emission spectrum exhibited significant deviations from a single Band spectrum [82]. The time-resolved spectrum is characterised by two spectral peaks as shown in Fig. 2.7: the first one can be modelled by a blackbody spectrum while the second one is given by

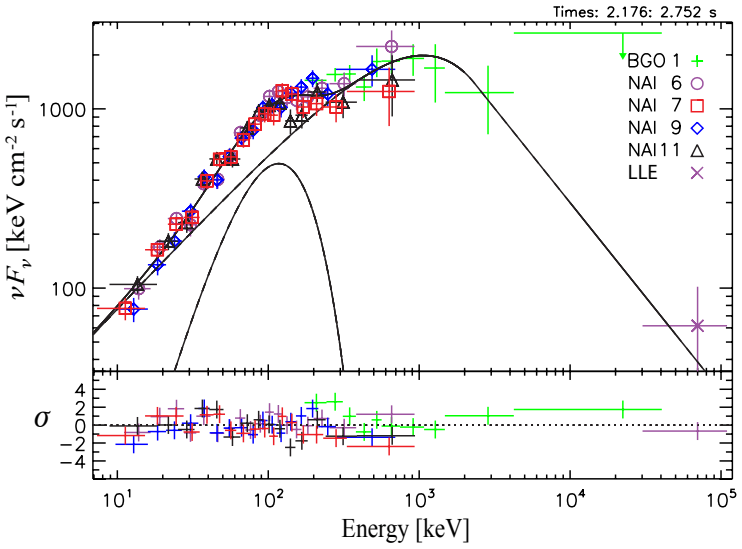

Figure 2.7: Time resolved spectrum for the time bin $2.2 - 2.7$ s after the GBM trigger of GRB 110721A. The spectrum is best modeled using a blackbody spectrum ($kT \sim 100keV$) and the Band function ($E_{\rm peak} \sim 1$ MeV). From Iyyani *et al.* [82].

a Band function.

The afterglow is on the other hand characterised with a much simpler spectrum. The spectrum of the afterglow component of GRBs is seen as a succession of different power laws of the type $F_\nu \propto \nu^{-\tilde{\alpha}}$.

Beamed explosions

The beaming of the GRB explosions is an important factor for the estimation of the total energy release of the objects. A first indication that the GRB emission is not isotropic but collimated was found in the analysis of GRB 990123. The inferred isotropic energy of this GRB was determined to be 4.5×10^{54} ergs [47], which is more than a solar rest mass. This presented a serious problem for all the stellar mass model of GRBs. This problem can be solved if the emission is beamed. In this case indeed, the energy release is given by: $E_{\rm iso} \times \frac{\Omega_\gamma}{4\pi} \sim E_{\rm iso} \times \frac{\theta_j^2}{8\pi}$, where Ω_γ is the solid angle into which the gamma-rays are beamed and $\theta_j << 1$ rad, the half-opening angle of the jet.

The next decisive indication was the observation of a simultaneous break or steepening of several wavelengths curves. A classical example of this effect was found in GRB 990510 [85, 86], as shown in Fig. 2.8.

Such a break is explainable if the emission is highly relativistic (see Section 2.3) and

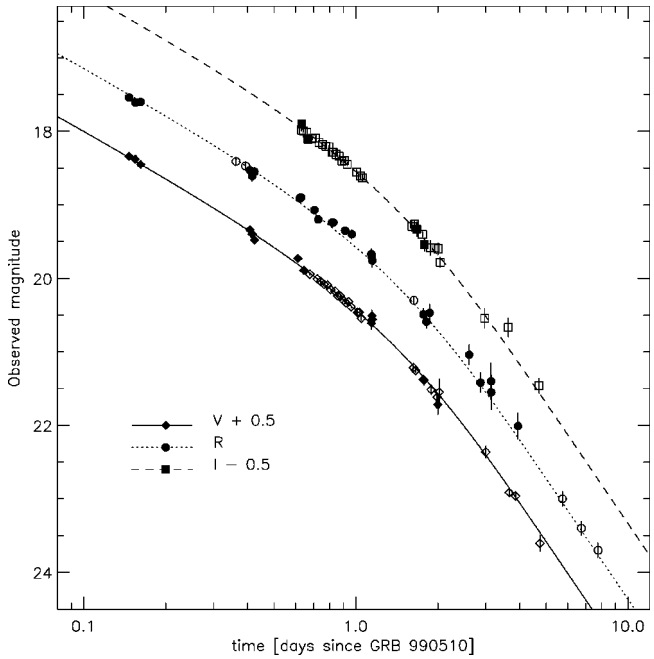

Figure 2.8: Observed light curves of the optical afterglow of GRB 990510 in three filters. From Piran [38].

beamed, as illustrated in Fig. 2.9. In this case, the emission from relativistic material moving with Lorentz factor Γ, is beamed within an angle of $\theta_b \sim 1/\Gamma$. This means that an observer only sees the emission from this patch. Radiation that would be emitted from an other area would never arrive at the observer. But the ejecta are moving through the interstellar medium and slow down, and the angle θ_b is therefore increasing. As long as $\theta_b < \theta_j$, the observer can not distinguish between spherical and collimated outflow. However, when $\theta_b > \theta_j$, the observers "see" the edges of the cone and receive less light than in the isotropic case [87, 88, 89, 90] . This causes a faster decaying light curve. The steepening in the light curve is seen simultaneously in all wavelengths. The typical LGRBs inferred jet opening angles are $\theta_j \sim 5° - 10°$, which limit the emitted energy from $10^{53} - 10^{54}$ ergs to about 10^{51} ergs [91, 92].

Finally, beamed emission implies that, if the directions of the jets are isotropic, the number of GRB events in the Universe is in fact much larger than we can detect, since we can observe only those that accidentally point in our direction.

2.2.4 Association with Supernovæ

As the total energy emitted in a GRB is of the same order as the energy liberated during a supernova (SN) explosion, it has been tempting to relate these two phenomena

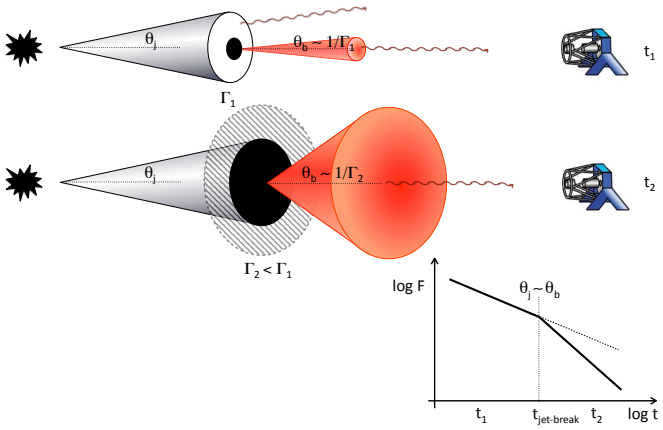

Figure 2.9: Achromatic steepening of the light curve is expected if relativistic outflow is beamed in a narrow angle θ_j. When ejecta slow down $\theta_b > \theta_j$ and the observer 'misses' the emission from the dashed area, which causes the light curve to decay more steeply. From Gomboc [47].

[93]. However, as already mentioned, the period during which this energy is released is totally different: a few months for SN and a few seconds for the GRBs. Moreover, the SN outflow is non-relativistic and thermalised, while the GRB outflow is relativistic and emission is principally non-thermal.

It was therefore a surprise when one has observed a connection between GRB 980425 and SN1998bw [94, 95]. The first really unambiguous supernova signature (SN2003dh) was detected in GRB 030329, firmly establishing the GRB-SN associations [96, 97] : several days after the GRB, the optical afterglow spectrum exhibited an emerging change from a classic GRB power law spectrum to include more and more SN features. One can now firmly say that, at least, some long GRBs are associated with supernova explosions. This association between SN and GRBs has been confirmed by Swift on February 18th, 2006, when connecting SN2006aj to GRB 060218 [98]. This association provided a considerable amount of new information on the connection between SN and GRBs [40].

More generally, the GRB-SN connection is, if not a confirmation, at least a strong indication, that some LGRBs are related to the late stage of massive stars.

2.3 Theoretical framework: the Fireball Model

The physics involved in the GRB phenomenon is quite complicated and there are still many caveats and unexplained features. However, as already discussed before, there is

convincing evidence that GRBs are the visible part of catastrophic energy release in stellar massive objects. It is believed that the LGRBs are almost surely associated to the "death" of a massive star, *i.e.* the collapse of its core (the so-called *collapsar* model) [99, 100]. The picture is less settled yet for the SGRBs, but there are some observational confirmations [101, 102, 103] that SGRBs would be associated with compact binary mergers [41, 104], two neutron stars colliding (NS-NS) or a neutron star with a black hole (NS-BH). In both cases, the liberated gravitational energy is converted, on time scales of milliseconds and inside a volume of $\mathcal{O}(10\,\mathrm{km}^3)$, into free energy. However, the generic evolution of the explosion after the initial energy injection is most probably independent of the progenitor. The "inner engine" would only have some influence on the variability of the light curves of the GRB [105, 106].

We will now present the global ingredients that are needed for explaining GRBs and concentrate on the most generally accepted model: the Fireball Model [41, 42, 43]. This model is matter dominated and magnetic fields do not play a dominant role apart from being partially responsible for giving rise to the formation of the two back to back jets. Other models, magnetic dominated, are also discussed by the community. For details on these models, please refer to [107, 108, 109].

2.3.1 Generally accepted picture

The generally accepted picture of GRBs involves a stellar mass object which undergoes a catastrophic event, releasing $\sim M_\odot c^2$ energy in a very compact region. The principal result of this is the conversion of a big fraction of that energy into thermal neutrinos and into gravitational waves, while a significantly smaller fraction $(10^{-2} - 10^{-3})$ goes into a hot fireball consisting of $e^\pm$, γ-rays and baryons [39]. The fireball is transparent to the gravitational waves and, beyond several interaction lengths, also to the neutrinos. This would then lead to an undetected prompt emission of $\sim 10^{53}$ ergs composed of thermal $\nu_e\bar{\nu}_e$ with typical energies of $10 - 30\,\mathrm{MeV}$ and of gravitational waves of $10^2 - 10^3\,\mathrm{Hz}$ [39]. The rest of the energy, still $\sim 10^{50} - 10^{52}$ ergs, is trapped in the fireball which can be matter or magnetic dominated (see the above discussion).

The fireball outflow is moving at highly relativistic velocities (see Section 2.3.2.1). Since the flow was initially optically thick (see Section 2.3.2.1), it undergoes an adiabatic expansion and cools down. At large distance, $\sim 10^{11}\,\mathrm{m}$ of the inner engine, it becomes optically thin and the γ-rays escape: a GRB is seen! These photons only carry a fraction of the energy, the rest will collide with the surrounding medium at larger distances of $\sim 0.01 - 1\,\mathrm{lyr}$, producing electromagnetic radiation of lower energies : the *afterglow*. A general picture of this behavior is given in Fig. 2.10.

As already discussed in Section 2.2.3, the γ prompt emission could also be composed of thermal emission inside the generic fireball model as proposed by several of authors [41, 42, 43, 53]. This thermal γ emission could, in some scenarios, be so bright that

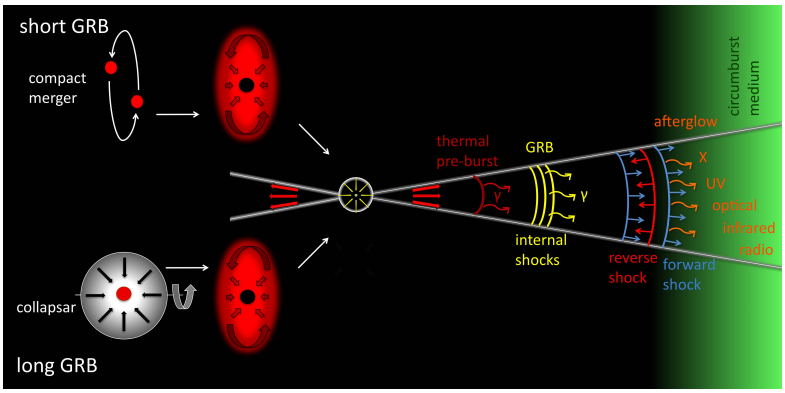

Figure 2.10: Left - Progenitor models for short and long GRBs. Right - Production sites of photons in the fireball model. From Gomboc [47].

it would even outshine the non-thermal γ emission produced by internal shocks in the 100 keV−1 MeV range [110].

2.3.2 Relativistic flows: indications and effects

As we will see below, highly relativistic outflows with a Lorentz Factor, $\Gamma \geq 100$, are a necessary ingredient of GRBs. We will then briefly review the principal impacts of these high velocities on the hydrodynamics of the outflows.

2.3.2.1 Compactness problem

The first hint for the necessity of relativistic motion in GRBs arises with the so-called *Compactness problem*. The short time variability detected in the GRB light curves, δt, implies, due to causality, small source size: $D \leq \delta t \cdot c$. Such a compact object with that large luminosity would be opaque to its own radiation, because of $e^{\pm}$ pair creation ($\gamma\gamma \rightarrow e^{\pm}$) and would consequently highly suppress the radiation with energy above 0.5 MeV ($m_e c^2 = 0.511$ MeV). We would also observe an unique thermal spectrum. As (most of) the GRB prompt spectrum is non-thermal and exhibits high energy tails above 1 GeV, a contradiction appears. This problem is solved by considering that the flow expands highly relativistically.

To explain this, let us make a very rough derivation of the optical depth for the photons inside the flow. The optical depth is given by: $\tau_{\gamma\gamma} \sim f_e n_\gamma \sigma_T D$, where f_e is a numerical factor denoting the average probability that one photon will collide with another whose energy is sufficient for pair creation, n_γ, the photon density, σ_T, the Thomson cross-section and D, the size of the source. For an isotropic emission[5] of energy, $E_{\rm iso}$, the photon density of a typical photon energy of $\bar{E}_\gamma \sim 1$ MeV is given by:

[5] A beamed emission does not change the physical conclusions of the reasoning.

$n_\gamma \sim \frac{E_{\rm iso}}{E_\gamma D^3}$. This leads to an optical depth of:

$$\tau_{\gamma\gamma} \sim 10^{15}\,{\rm s}^2 \times f_e \left(\frac{E_{\rm iso}}{10^{51}\,{\rm ergs}}\right)\left(\frac{1\,{\rm MeV}}{\bar{E}_\gamma}\right)\left(\frac{0.01\,{\rm s}}{\delta t}\right)^2, \tag{2.2}$$

which is totally incompatible with a (at least partially) non-thermal GRB prompt spectrum. One can avoid this problem when the flow expands relativistically, with Lorentz factor Γ. The relative angle at which photons collide is hence less than Γ^{-1} and the threshold for pair production is highly diminished. This condition yields

$$\Gamma \gtrsim 10^2 \left[\left(\frac{E_\gamma}{10\,{\rm GeV}}\right)\left(\frac{E_t}{1\,{\rm MeV}}\right)\right]^{1/2}, \tag{2.3}$$

in order for photons of energy E_γ to escape annihilation against target photons of energy $E_t \sim 1\,{\rm MeV}$ [111].

2.3.2.2 Relativistic time effects

We will develop here some tools that we will need in the next sections, following the developments made by Piran in [38]. Consider a relativistic flow expanding at velocity v with $\Gamma >> 1$ in the direction of the line of sight of an observer. Let us calculate the arrival time difference Δt_R at an observer of two photons emitted respectively at distance R_1 and R_2 from the source and at time t_1 and t_2, see Fig. 2.11. We have

$$\begin{array}{rcl} \Delta t_R & = & \frac{R_2-R_1}{v} - \frac{R_2-R_1}{c} \\ & \approx & \frac{R_2-R_1}{c(1-\frac{1}{2}\Gamma^{-2})} - \frac{R_2-R_1}{c} \\ & \approx & \frac{R_2-R_1}{2c\Gamma^2}. \end{array} \tag{2.4}$$

We can then associate an "observer time difference"[6] $\frac{\Delta R}{2c\Gamma^2}$ with the distance $\Delta R = R_2 - R_1$. In case the first photon is emitted at the centre of source (*i.e.* $R_1 = 0$), this provides a typical radius R related to the burst duration.

Consider now two photons emitted at the same time but from different parts of the same spherically relativisticaly expanding shell, moving at angle θ relative to the line of sight of the observer, as sketched in Fig. 2.12. The time delay of these two photons for the observer will be $\Delta t_{\rm ang} = R(1-\cos\theta)/c$. The radiation is beamed at an angle $\sim 1/\Gamma$ and $\Gamma >> 1$, hence

$$\Delta t_{\rm ang} \approx \frac{R}{2c\Gamma^2}. \tag{2.5}$$

The coincidence $\Delta t_{\rm ang} \sim \Delta t_R$ will be of importance for later.

[6] This reasoning yields for a flow moving at constant velocity, v, whereas, a numerical factor of order 8 has to be added [38] in case the velocity v is not constant.

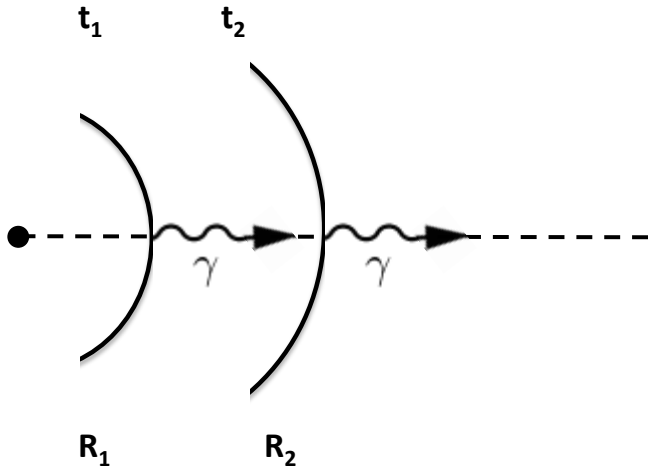

Figure 2.11: Sketch of the definition of the "observer time".

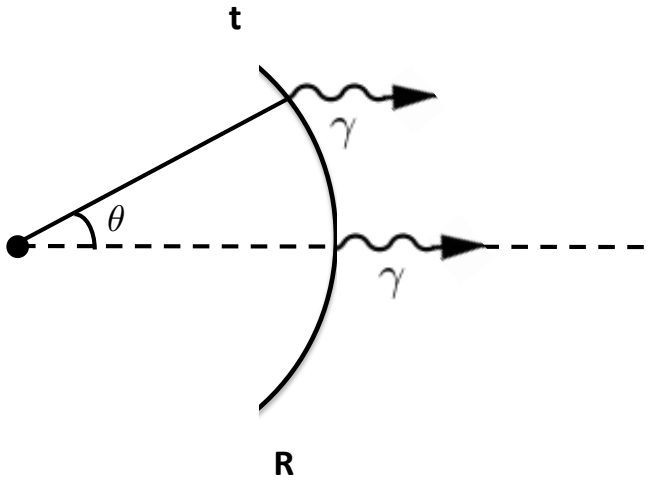

Figure 2.12: Sketch of the definition of the $\Delta t_{\rm ang}$.

2.3.3 The thermal component of the prompt photon emission: the Photosphere

Up to now we have discussed an optically thick outflow. Let us now discuss the moment when the object begins to radiate. We therefore introduce the photospheric radius, *i.e.* the radius from which the outflow becomes optically thin, given by [112]:

$$r_{ph} \simeq 6 \times 10^{11} L_{51}\, \eta_2^{-3}\, \mathrm{cm}, \tag{2.6}$$

where L_{51} is the luminosity in 10^{51} ergs unit and η_2 indicates that the baryon loading is given in unit of 10^2. As indicated by [41, 42, 43], the expected spectrum of the

photosphere is logically a black-body emission. This emission is promising to explain the hard Band spectrum below $E_p \sim \mathcal{O}(100\,\mathrm{keV})$, typically the νF_ν peak of the γ-ray spectrum. Moreover dissipation of the kinetic energy at or below the photosphere, by shocks or other mechanisms such as neutron-proton decoupling and interactions [113, 114, 115] could even enhance thermal radiation for moderately baryon-loaded fireballs.

As we already discussed in Section 2.2.3 it seems that for some GRBs, e.g. 090902B, this thermal photospheric emission is dominant in the spectrum [116]. In other Fermi observed bursts the addition of a photospheric component seems to improve the fits, although thermal emission is not dominant [117].

2.3.4 Dissipative fireballs and shocks as origin of the non-thermal component of the prompt photon emission

We still have to face the last problem for our generic fireball : "how to obtain the non-thermal part of the GRB spectrum?" For this, we need to find a mechanism that will, after the flow has become optically thin, re-convert the kinetic energy of the flow into random radiation in an efficient way. A generic process that can achieve this is *shock* wave acceleration [53, 54, 55, 118, 119, 120]. Such shocks are essentially unavoidable as the fireball runs into the external medium, producing a blast wave but they can also arise inside the flow itself. They will be collisionless, *i.e.* mediated by chaotic electric and magnetic fields rather than by binary particle interactions[7]. Through the Fermi mechanism [26], the (internal) shocks provide an acceleration mechanism to ultra-relativistic energies for the particles inside the outflow [121, 122, 123, 124], see Section 1.1.3. The so-created relativistic electrons will then produce non-thermal radiation via (1) the synchrotron and (2) Inverse Compton (IC) processes. The synchrotron radiation is likely responsible for (a part of) the keV-MeV band of the prompt emission and for the afterglow. The IC is the leading model for the higher energy part of the prompt emission. Beside these two natural mechanisms, there are several alternative models for the prompt emission. For a complete discussion on these the reader is referred to [39].

2.3.4.1 Internal versus External Shocks

We have now two candidates that could be responsible for the prompt emission part of the GRBs : the internal and the external shocks. The former take place when a faster-moving shell of matter overtakes a slower-one. On the other hand, the external shocks are a consequence of the collision of the flow with the surrounding material. This would hence be the analog of a supernova remnant. We will restrict ourselves to show in the following paragraphs that the external shocks cannot produce the variability we detect in the light curves of the GRBs [125]. For a complete discussion of the spectrum of the

[7]These kind of shocks are known from interplanetary experiments and as inferred in supernova remnants and in active galactic nuclei (AGN) jets.

GRBs including the afterglow, please refer to, e.g. [38, 39].

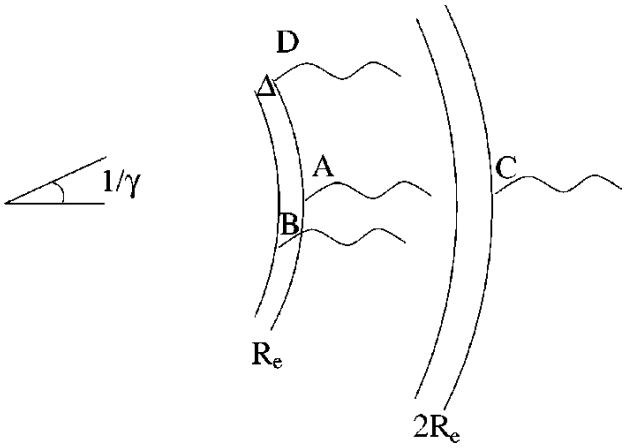

Figure 2.13: Different time scales from a relativistic expanding shell in terms of the arrival times (t_i) of various photons: $\Delta t_{\rm ang} = t_D - t_A$, $\Delta t_R = t_C - t_A$ and $\Delta t_\Delta = t_B - t_A$ for a relativistic expanding flow with Lorentz factor Γ. From Piran [38].

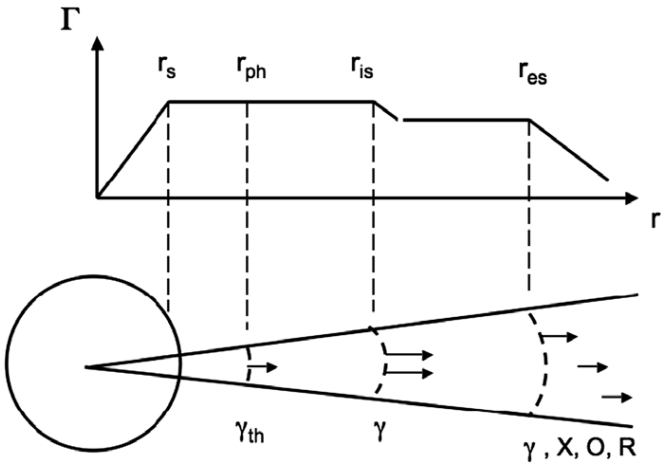

Figure 2.14: Jet Lorentz factor schematic behaviour and examples of nominal locations of the saturation radius r_s which refers to the radius beyond which the Lorentz factor becomes constant, the photospheric radius r_{ph}, the internal shock radius r_{is} and external shock r_{es}. The photosphere produces thermal γ-rays, the internal shock/dissipation region produces the non-thermal γ-rays and the external shock region produces the afterglow. From Mészáros [39].

Considering Fig. 2.13, let us calculate the arrival time difference between the photons produced at the various locations indicated. The difference between points A

and C is Δt_R of Eq. (2.4) and is hence equal to $R_e/2c\Gamma^2$. The difference between A and D is $\Delta t_{\rm ang}$ of Eq. (2.5) and hence also equals $R_e/2c\Gamma^2$. Finally, if the shell thickness is Δ, a photon emitted in A will arrive at the observer at a time $\Delta t_\Delta = \Delta/2c\Gamma^2$ before a photon emitted in B. All these ingredients indicate that the emissions from different angular points are smoothed on a time scale of $\Delta t_{\rm ang}$. Therefore if $\Delta t_\Delta \leq \Delta t_{\rm ang}$, the burst will be smooth with a width of $\Delta t_{\rm ang} \sim \Delta t_R$. It turns out that for external shocks, $\Delta \leq R_e$ [125], which excludes the external shocks as a cause of the prompt emission. The external shocks are a perfect candidate for explaining the smooth long-lasting afterglow.

Following the timescale discussed so-far, there is only one possibility for having variable light curves: $\Delta t_\Delta \geq \Delta t_{\rm ang}$. This would lead to a GRB duration of Δt_Δ and a variability time scale of $\Delta t_{\rm ang}$. As explained by Piran [38], this can easily be achieved in an internal shock scenario. This discussion finally leads to the schematic behavior seen in Fig. 2.14.

2.3.4.2 Prompt GeV emission

The origin of $\gtrsim 100\,\mathrm{MeV}$ prompt radiation from GRBs has been intensely debated in recent years. In the context of the internal shock mechanisms, the IC scattering is the leading model to produce the hard power law component [126, 127]. In such a mechanism the keV synchrotron photons are boosted by the surrounding relativistic electrons via the Inverse Compton mechanism. However, the time delay observed between the different energy bands (see Fig. 2.15) is longer than what is possible in the IC processes.

Alternative mechanisms could also generate γ-rays of $\gtrsim 100\,\mathrm{MeV}$ such as synchrotron radiation from protons and $\gamma\gamma \to e^+e^-$ pair cascades [129] or photohadronic interactions and associated cascades radiation [130, 131]. These hadronic models could account for the time delay.

2.4 Possible progenitors

After reviewing the experimental observations and the theoretical framework, we will discuss, in this section, the possible progenitors of the GRBs. Remember that this discussion is decoupled from the description of the GRB explosion itself. But remember also that all the theory we developed above needs an "inner engine" to release the necessary energy. We will now try to remove the mystery around this "inner engine". Inevitably, more than a hundred models have been proposed over the years for explaining the origin of GRBs. Most of these were abandoned as new data became available and new discoveries were made, but a few have survived. We will discuss, in the following, the two currently most popular models: the so-called collapsar and compact binary merger models.

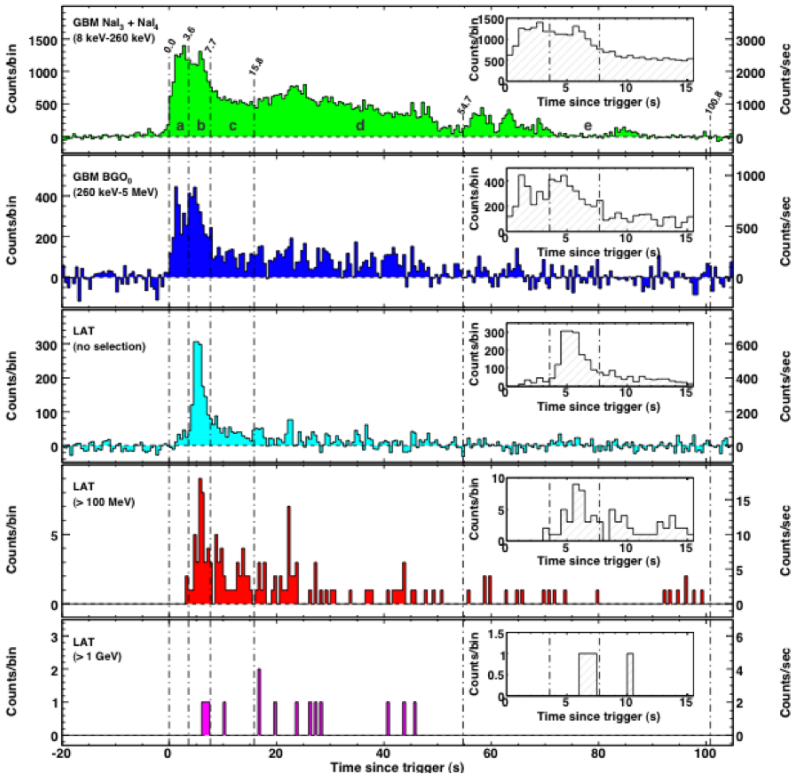

Figure 2.15: Light curves of GRB 080916C with the GBM (top two panels) and LAT (bottom three panels). The high energy LAT emission is delayed relative to the lower energy GBM emission. From Abdo et al. 2009 [128].

2.4.1 The Collapsar Model

As we already outlined in Section 2.2.4, a connection between core collapsing SN and GRBs exists and hence it may be said that (at least some) long GRBs are caused by the collapse of massive stars. As indicated by Woosley [132], a good candidate for the collapsar model is a massive, rapidly rotating Wolf-Rayet star [133], which has lost its hydrogen envelope, has a core with about $10M_\odot$ and is the size of the Sun. When the nuclear fusion reactions taking place in the core stop, the core collapses to a black hole (BH) of a few $M_\odot$ surrounded by a massive accretion disk. The material surrounding the BH, that is in the equatorial plane, can not directly fall into the BH because of the very large angular momentum. This is not the case along the rotation axis : the material can undergo almost free-fall. This rarifies the region around the rotation axis and creates a so-called "low density funnel" in the envelope. As explained by Gomboc in [47], if enough energy is injected into this region, it is able to push material along the rotation axis for as long it takes to cross the star, typically a few $\sim 10\,\mathrm{s}$, and the outflow eventually breaks through the star's surface. Numerical simulations [99] show that in

this case the outflow is collimated by the pressure from the stellar mantle, and gains high Lorentz factors as it breaks through the surface, forming a collimated, relativistic outflow or a jet. Magnetic fields will enhance the collimation effect as well.

Only a few GRBs showed a direct connection to SN, however it is believed that all LGRBs are caused by the core collapse of a massive star. An easy way to verify this theory is to look to the host of the LGRBs. If our interpretation is correct, the LGRBs should take place in active star forming regions, because massive stars have a short lifetime of $\sim 10^7$ yr. This implies that they reach their ends while star formation in their vicinity is still active and before they can move far from their birth places. And, indeed, host studies of LGRBs indicated that they arise in star forming regions.

2.4.2 Compact binary mergers

As proposed by Eichler [104], binary systems of two neutron stars (NS-NS) or a neutron star and a black hole (NS-BH) are two candidates for Compact binary merger models. It is believed that they are the "inner engines" of the short GRBs. The merger process starts with the two NS to spiral around each other[8], emitting gravitational waves so that the distance between the two objects decreases [134]. This phase can last for "only" $\sim 10^6$ yr to about $\sim 10^9$ yr. When the NS are at a few radii of each other, the tidal forces distort the objects, and they finally merge (see Fig.2.16), creating a similar "inner engine" as in the collapsar model, *i.e.* a low-mass black hole surrounded by a massive accretion disk.

This scenario has again an impact on the possible places where to find SGRBs. The merging process is supposed to be "quick", so, as for the LGRBs, we should find again some SGRBs inside galaxies in star forming regions. However, it is known that NS can experience substantial kicks, sending the NS far away from the star forming regions and even sometimes out of their galaxies. SGRBs should then also be detected outside of these regions. This is indeed what has been observed.

2.5 Neutrino production in the Fireball

As we already mentioned, the physical conditions of the fireball model should lead to acceleration of particles [135, 136], among which are protons, through the well-known Fermi mechanism [26] up to energies of $\gtrsim 10^{20}$ eV (for the prompt phase). It has been confirmed by studies of the Ultra-High Energy Cosmic Rays (UHECR) that the spectrum is consistent with the Fermi acceleration mechanism (possibly of protons in cosmological GRBs [44]). A natural counterpart of these protons are neutrinos of $\sim 10^{14}$ eV created by the decay of photo meson produced pions in interactions between the fireball γ-rays and the accelerated protons.

[8]The merger of a NS and a BH follows the same picture but is more complicated.

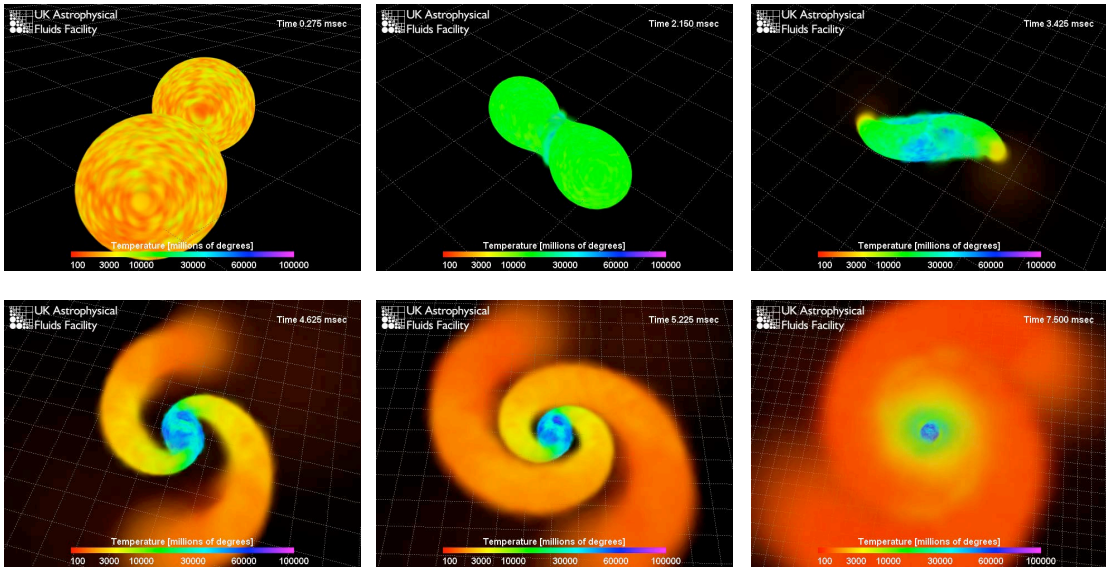

Figure 2.16: Snapshots of a simulation of the merger of two neutron stars (each neutron star has $1.4\,M_\odot$ and $\sim$ 30 km diameter). Initially, they are less than 10 km apart, and moving at around $= 0.2c$. As the two stars spiral into each other, they become deformed, and finally touch. When they merge, the matter reaches $T \sim 10^{11}$ K. A few percent of the matter is ejected in the form of spiral arms, which cool rapidly. The whole merger process takes only a few ms. The grid in the images has a spacing of 30 km intervals. Credit: simulation by Stephan Rosswog, visualization by Richard West, http://www.ukaff.ac.uk/movies/nsmerger/

As we explained in previous sections, the models of photon production in the GRBs comprise three phases. This would lead to non-thermal neutrino production during the precursor phase [137], the prompt phase [45, 46] and the afterglow [138]. A sketch of the possible spectra is given in Fig 2.17.

Generally, neutrinos can be produced through $p\,p$ collisions or $p\,\gamma$ collisions. The $p\,\gamma$ channel is the most favoured one for the prompt and the afterglow phase [45, 46, 138]. However, Paczyński and Xu also discussed [57] the possibility that the γ-rays would be produced by the decay of neutral pions, which are produced in $p\,p$ collisions once the kinetic energy is dissipated through internal collisions. This would then lead to a possible neutrino burst of ~ 30 GeV due to the decay of the charged pions. In the more classic synchrotron emission or inverse compton scattering, the proton density is too low to efficiently induce $p\,p$ collisions. However, the prompt phase could contain neutrinos partially produced by $p\,p$ collisions.

Collisions between sufficiently energetic protons and photons lead to pion production,

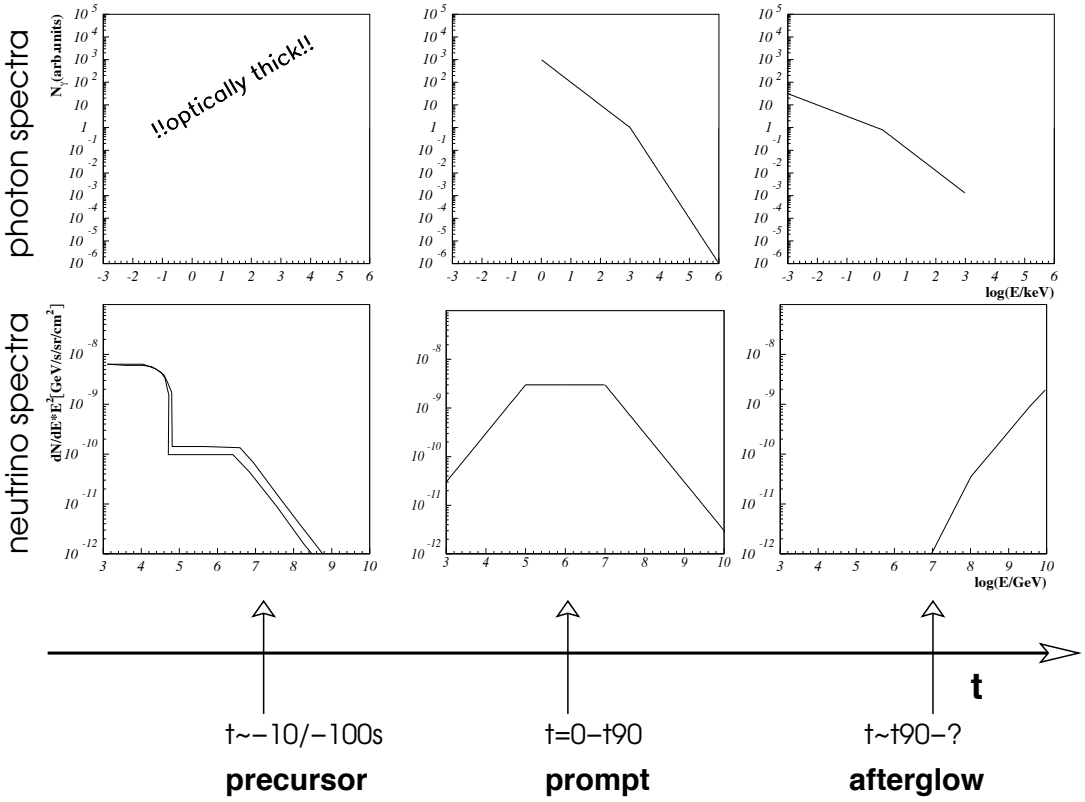

Figure 2.17: Sketch of the different neutrino and photon production scenarios during the three phases of a GRB. Details of the models can be found in the text. From [75].

mainly through the Δ resonance. These pions will then decay and produce photons, electrons, positrons and neutrinos. The process can be sketched as follows:

$$\begin{aligned} p + \gamma \to \Delta^+ \quad &\to \quad \pi^+ \quad + n \\ &\hookrightarrow \quad \mu^+ + \nu_\mu \to e^+ + \nu_e + \bar{\nu}_\mu + \nu_\mu \\ &\to \quad \pi^0 \quad + p \\ &\hookrightarrow \quad \gamma\,\gamma \end{aligned} \tag{2.7}$$

If we could distinguish the photons from π^0 decay, it would enable us to estimate the related neutrino flux. However, these gammas have sufficiently high energies that most interact with the extragalactic background radiation before reaching the Earth [139].

In order for the photon-proton interaction to produce the pions, they should have enough energy to create a Δ particle. In the co-moving frame, this translates by the

following condition for the proton energy:

$$E'_p \geq \frac{m_\Delta^2 - m_p^2}{4E'_\gamma}, \tag{2.8}$$

which transforms in the observer frame as:

$$E_p \geq 1.4 \times 10^{16} \frac{\Gamma_{2.5}^2}{E_{\gamma,\,\mathrm{MeV}}}\,\mathrm{eV} \equiv E_p^{th}. \tag{2.9}$$

Here, E'_p (E'_γ) and E_p (E_γ) are respectively the proton (photon) energy in the co-moving frame and in the observer frame, $\Gamma_{2.5}$ is the bulk Lorentz factor in $10^{2.5}$ units and $E_{\gamma,\,\mathrm{MeV}}$ refers to the photon energy given in MeV units.

By kinematics, we can consider that the mean fraction of energy that is transferred from the initial proton to the π^+'s and the π^0's, $\langle x_{p\to\pi}\rangle$, roughly represents 20%. The energy of each neutrino should therefore be given by:

$$E_\nu \sim \frac{1}{4}\langle x_{p\to\pi}\rangle E_p \geq 7 \times 10^{14} \frac{\Gamma_{2.5}^2}{E_{\gamma,\,\mathrm{MeV}}}\,\mathrm{eV}, \tag{2.10}$$

where the factor $\frac{1}{4}$ comes from the fact that there are 4 final leptons produced by the π^+ decay each carrying approximately the same amount of energy. The astrophysical uncertainties on the models allow us to consider these approximations sufficiently adequate.

Note that, as seen in Eq. (2.7), only muon and electron neutrinos are produced with a ratio $(\nu_e : \nu_\mu : \nu_\tau) = (1 : 2 : 0)$. As expected from oscillations and confirmed by Becker in [75], this partition will equalise to $(1 : 1 : 1)$ on Earth.

Before discussing in more detail the different neutrino spectra, it is important to address the question of the timing of photon and neutrino emission. The environment of the astrophysical shock is crucial but remains largely unknown. It is therefore postulated that the neutrinos are not exactly emitted at the same time as the photons but it is typically still assumed that the neutrinos are emitted during a similar time duration interval as the photons. This explains why, in neutrino searches for flaring sources, the search time windows are often taken larger than the time window of the observed photons.

2.5.1 Precursor neutrinos

As explained above, the precursor phase is mostly optically thick and neutrinos should be produced by shock-accelerated protons interacting with thermal X-rays. The low energy part of the neutrino spectrum arises from neutrino production in $p\,p$ collisions and at $E_\nu > 10^5$ GeV, neutrinos should originate from proton-photon interactions [137]. Razzaque *et al.* indicate that the total neutrino spectrum is obtained by assuming that a fraction of the fast proton spectra are converted into neutrinos:

$$\frac{\mathrm{d}\Phi_\nu}{\mathrm{d}E_\nu} = \frac{1}{4\pi d_L^2} \cdot \begin{cases} \int f_{pp} \cdot M_\nu(E_p) \frac{\mathrm{d}\Phi_p}{\mathrm{d}E_p} & \text{for} \quad E_p < E_p^{th} \\ \frac{f_\pi}{4} \frac{\mathrm{d}\Phi_p}{\mathrm{d}E_p} & \text{for} \quad E_p > E_p^{th}, \end{cases} \tag{2.11}$$

where d_L is the luminosity distance, f_{pp} is the proton-proton efficiency, f_π is the fraction of protons converted into pions and the neutrino multiplicity $M_\nu(E_p)$, through pion decay, in the pp interactions is given in [140]. The $\frac{\mathrm{d}N_p}{\mathrm{d}E_p}$ spectra are derived in [137] assuming a classic E_p^{-2}-shaped spectrum. As already explained, at this stage the medium is optically thick, so neutrino detection from precursor GRBs would be crucial for constraining the models and would lead to alert the photon experiments before the actual GRB occurs.

2.5.2 Prompt neutrinos

The derivation of the prompt neutrino spectrum will follow the developments made in [141, 75] and any interested reader can find there all the details about the presented calculations. As explained above, the neutrinos will be produced through proton-photon interactions through the Δ resonance. This process needs that the energy of the center of mass of the $p\gamma$ system is larger than the Δ rest mass. Hence, $E_p \cdot E_\gamma = \text{constant}$[9] and, as the proton and the neutrino energies are directly proportional, this implies that the photon and neutrino energy are inversely proportional, $E_\nu \propto E_\gamma^{-1}$ and therefore the neutrino energy spectrum will trace the broken power law based on the Band function and the neutrino flux is given by:

$$\frac{\mathrm{d}\Phi_\nu}{\mathrm{d}E_\nu} = \Phi_0 \cdot \begin{cases} \left(\frac{E_\nu}{E_\nu^b}\right)^{-\alpha-2} & \text{for} \quad E_\nu < E_\nu^b \\ \left(\frac{E_\nu}{E_\nu^b}\right)^{-\beta-2} & \text{for} \quad E_\nu^b < E_\nu \leq E_\nu^s. \end{cases} \tag{2.12}$$

The neutrino break energy E_ν^b is related to the break energy in the photon spectrum E_γ^b (see Eq. (2.1)) through the previous equation and is given:

$$E_\nu^b = \frac{(m_\Delta^2 - m_p^2) \cdot \Gamma^2}{4 \cdot (1+z^2) \cdot E_\gamma^b}, \tag{2.13}$$

where an explicit dependence on redshift, z, has been introduced. In the observer frame, this leads to:

$$E_\nu^b = 7.5 \times 10^5 \cdot (1+z)^2 \, \frac{\Gamma_{2.5}^2}{E_{\gamma,\,\mathrm{MeV}}^b} \,\mathrm{GeV}. \tag{2.14}$$

At higher energies, a second break E_ν^s will appear in the neutrino spectrum because the highest energy pions (and even muons) may lose energy due to synchrotron emission before decaying to neutrinos. The high-energy tail of the neutrino spectrum is therefore suppressed and is steepened by tan additional spectral index of 2,

$$\frac{\mathrm{d}\Phi_\nu}{\mathrm{d}E_\nu} \propto \left(\frac{E_\nu}{E_\nu^b}\right)^{-\beta-2} \left(\frac{E_\nu}{E_\nu^s}\right)^{-2} \quad \text{for } E_\nu \geq E_\nu^s. \tag{2.15}$$

[9] This equation is only true at the threshold. However, for higher values, the relation with the gamma spectrum holds.

The value of this second energy break is connected to the pion synchrotron loss time and depends on the neutrino flavour. We are only interested in this thesis in muon neutrinos, and in that case, we have:

$$E^{s}_{\nu_\mu} = \frac{10^8}{1+z}\,\epsilon_e^{1/2}\,\epsilon_B^{-1/2}\,\frac{\Gamma^4_{2.5}\cdot t_{\nu,-2}}{L^{1/2}_{\gamma,52}}, \tag{2.16}$$

where ϵ_e is the fraction of internal energy converted to electrons, ϵ_B the fraction of the internal energy carried by the magnetic field, $t_{\nu,-2}$ the GRB light curve time scale fluctuation in 10^{-2} s and $L_{\gamma,52} = L_\gamma/10^{52}$ erg/s the γ-ray luminosity of the GRB.

All these ingredients lead then to the well known Waxman-Bahcall flux as presented in Fig. 2.18. In this thesis, we provide constraints on neutrino flux models of the form:

$$\frac{\mathrm{d}\Phi_\nu}{\mathrm{d}E_\nu} = \Phi_0 \begin{cases} E_\nu^{-1}\varepsilon_b^{-1} & \text{for} \quad E_\nu < \varepsilon_b \\ E_\nu^{-2} & \text{for} \quad \varepsilon_b \le E_\nu < 10\varepsilon_b \\ (10\varepsilon_b)^2 E_\nu^{-4} & \text{for} \quad 10\varepsilon_b \le E_\nu \end{cases}, \tag{2.17}$$

where ε_b is the first break energy and $10\,\varepsilon_b$ refers to the second break. This model is based on updated Waxman-Bahcall calculations accounting for more recent measurements of the UHECR flux [142] and typical gamma break energy [143] in accordance with the original prescription from Waxman and Bahcall [45]. The neutrino break energies are obtained through measurement of the average gamma-ray spectral break [143] and an assumed typical bulk Lorentz factor of $\Gamma \sim 300$.

The only part we still have to address is the normalisation factor Φ_0 of Eq. (2.17). For this, we consider two approximate extreme cases of the expected neutrino flux in the context of GRBs being the leading source of the UHECRs. The neutrino flux normalisation Φ_0 is constraint through measurements of the of the cosmic ray flux [142]. Two options are then possible: (1) the protons responsible for the neutrinos production of Eq. (2.7) are confined and the UHECRs are determined by the neutrons that are produced and will β-decay back in protons further away from the GRB or (2) protons can escape freely the fireball. The first option induce that for each cosmic ray particle, three neutrinos are present whereas the second option predict fewer neutrinos accompanying each UHECR particle. For the first option, we refer to Ahlers *et al.* [144] and the second is the original proposition of Waxman and Bahcall [45].

2.5.3 Neutrinos from the afterglow

The afterglow neutrinos will be produced when the internal shock waves of the fireball collide with the ISM and produce external shocks. Waxman and Bahcall [138] predict the acceleration of ultra high-energy protons ($E_p > 10^{20}$ eV) in reverse, middle relativistic shocks. They conclude that a significant neutrino flux should appear in the afterglow phase through proton-photon interactions and should be detectable for

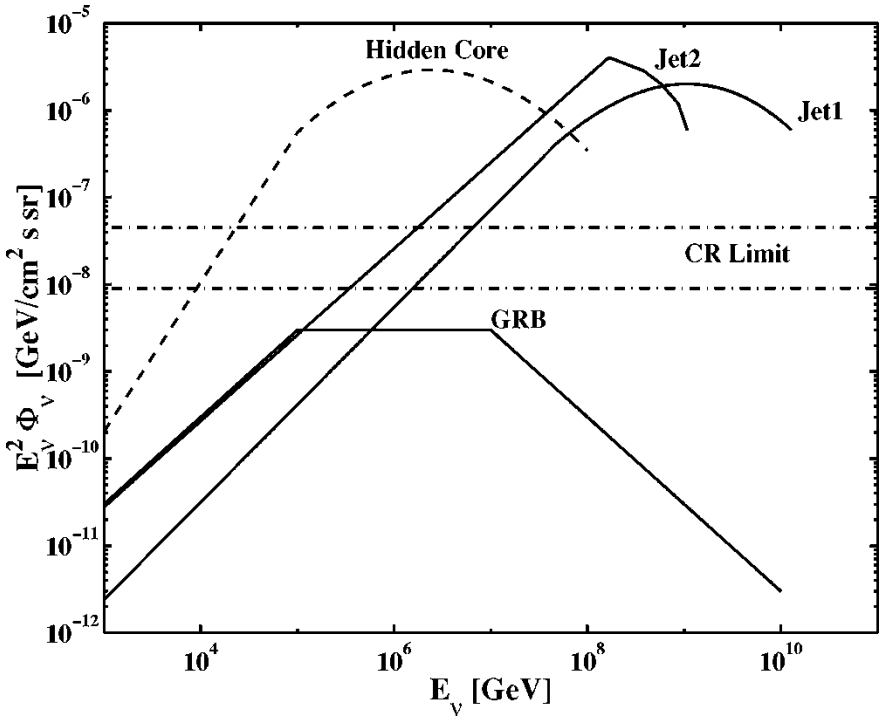

Figure 2.18: Comparison of muon neutrino intensities (ν_μ and $\bar{\nu}_\mu$ combined) predicted by different models with the upper bound implied by cosmic ray observations. The dash-dotted lines give the upper bound calculated by Waxman and Bahcall [46] corrected for neutrino energy loss due to redshift and for possible redshift evolution of the cosmic-ray generation rate. The lower line is obtained assuming no evolution, and the upper line assuming rapid evolution similar to the evolution of the quasi-stellar object (QSO) luminosity density. The AGN jet model predictions are labeled "Jet1" and "Jet2", and the dashed line represents the AGN hidden-core conjecture, which produces only neutrinos and to which the upper bound does not apply. From [46].

experiments as IceCube.

Provided that synchrotron losses of protons and pions can be neglected in that environment and supposing a fermi E_p^{-2} spectrum from the proton energy, the neutrino spectrum is given by [138]:

$$\frac{\mathrm{d}\Phi_\nu}{\mathrm{d}E_\nu} = \Phi_0 \cdot \begin{cases} E_\nu^{-1} & \text{for} \quad E_\nu < E_\nu^b \\ E_\nu^{-5/2} & \text{for} \quad E_\nu > E_\nu^b, \end{cases} \tag{2.18}$$

where E_ν^b is the neutrino break energy and is fixed by Waxman and Bahcall to $E_\nu^b = 10^8$ GeV and the normalisation factor Φ_0 is calculated by assuming that UHECRs are

produced by GRBs, implying that the power in UHECRs is comparable to the electromagnetic output from GRB and is given by

$$\Phi_0 = 10^{-10}\,\mathrm{GeV\ cm^{-2}\,s^{-1}\,sr^{-1}}. \tag{2.19}$$

The neutrino flux is expected to be strongly suppressed at energies $E_\nu > 10^{10}\,\mathrm{GeV}$, since the protons are not expected to be accelerated to energies $E_p \gg 10^{20}\,\mathrm{eV}$.

2.6 GRB neutrino searches with IceCube

In this last section, we will concentrate on the detection of these GRB neutrinos and principally on the efforts performed by the IceCube Collaboration.

First of all, despite the fact that IceCube has observed cosmic neutrinos [9], it is important to note that no correlation between these cosmic neutrinos and GRBs has ever been detected so far [31, 32, 145, 146]. In its two last publications on this subject [32, 34], the IceCube Collaboration has, for the first time, determined very stringent constraints on the production of prompt neutrinos in GRBs. In [32], we have

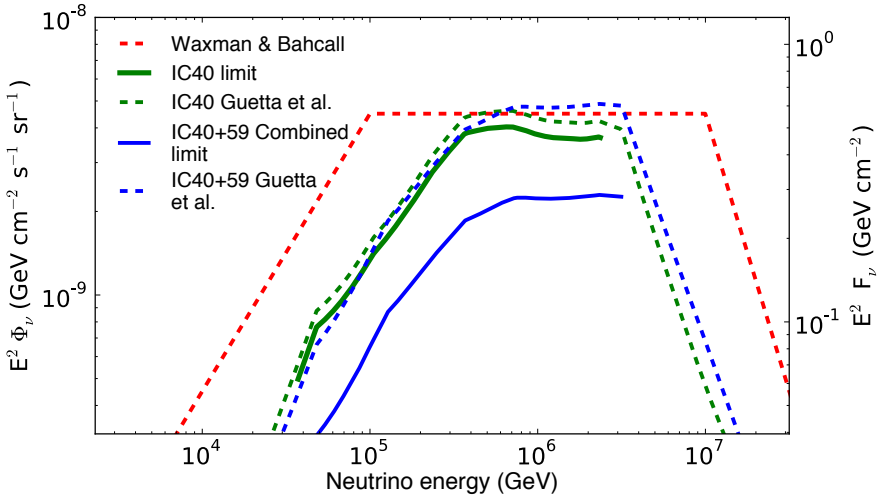

Figure 2.19: Comparison of experimental upper limits with predictions based on observed gamma-ray spectra. The summed flux predictions normalized to gamma-ray spectra [145, 147, 148] is shown in dashed lines; the cosmic ray normalized Waxman-Bahcall flux [45] is also shown for reference. The normalisation to the gamma ray fluxes shown is slightly modified [145] from the original calculation [147]. Φ_ν is the average neutrino flux at Earth, obtained by scaling the summed predictions from the bursts in the sample (F_ν) by the global GRB rate (here 667 bursts/year [31]). From [32]. The results shown are given for the best Δt interval of Fig. 2.21.

indicated that, based on different models, the neutrino spectrum is at least a factor 3.7 below the predictions. It has therefore been claimed that either "the GRBs are not the only sources of cosmic rays with energies exceeding 10^{18} eV or that the efficiency of neutrino production is much lower than has been predicted", see Fig. 2.19. This derived constraint has even been improved in [34] where four years of data is used and where only one single neutrino candidate event correlated with a GRB. Based on doubly-broken power spectrum models, the exclusion contours for such models are presented in Fig. 2.20.

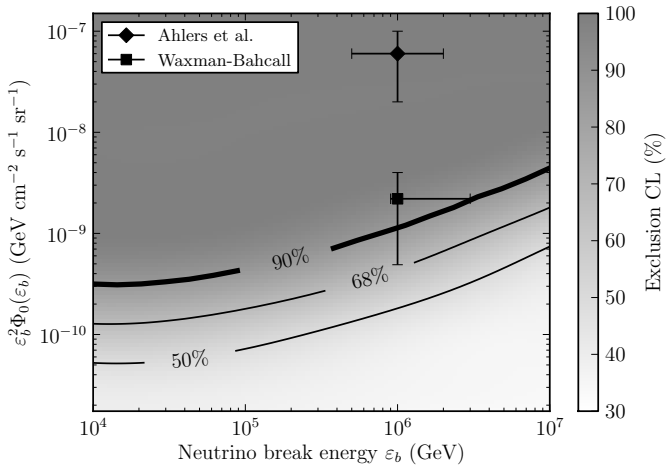

Figure 2.20: Constraint on generic doubly-broken power law neutrino flux models given by Eq. 2.17 as a function of first break energy ϵ_b and normalisation Φ_0. From [34].

A model independent analysis has also been performed in [32] and does not change the physical implications, see Fig. 2.21.

Since the publication of these IceCube data, extensive work has been performed on the model predictions for neutrinos in GRBs. See for a very interesting and recent example [150]. The currently existing upper limits are essentially derived for a prompt neutrino flux, this leaves therefore still room for precursor or afterglow neutrinos. The general conclusions of all these efforts is that GRBs could still be an excellent candidate for the origin of UHECR.

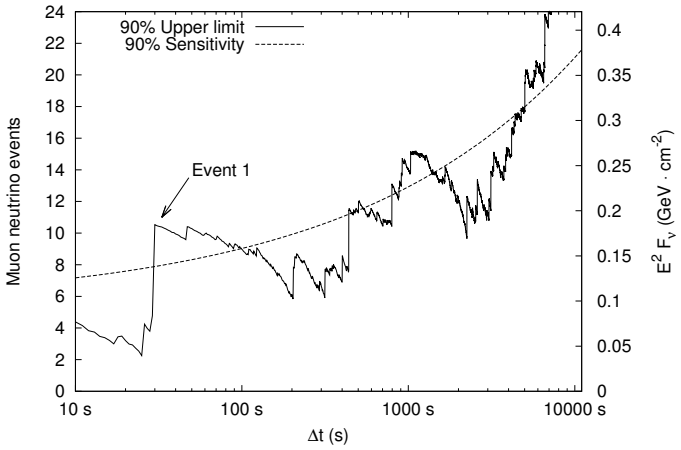

Figure 2.21: Upper limits on an E^{-2} power-law muon neutrino flux, calculated using the Feldman-Cousins method [149] from the results of the model-independent analysis. The left y-axis shows the total number of expected ν_μ events while the right-hand vertical axis (F_ν) is the same as in Fig. 2.19. A time window of Δt implies observed events arriving between Δt seconds before the burst and Δt afterward. The variation of the upper limit with Δt reflects statistical fluctuations in the observed background rate, as well as the presence of individual events of varying significance. The event at 30 seconds (Event 1) is consistent with background and believed to be a cosmic-ray air shower. From [32].

Part II

Hardware and Software Tools

CHAPTER 3

The IceCube Observatory

Neutrinos have much smaller interaction cross sections than all other particles and are hence difficult to detect. It is therefore essential to build very large detectors to collect cosmic neutrinos in statistically significant numbers. It had already been postulated in the 1970s that a cubic-kilometer detector was needed to observe cosmic neutrinos [151] and newer estimates have not changed these exigent sizes [152]. The only possible way to achieve this requirement is to take advantage of a natural transparent medium such as deep ocean water or glacial ice. This was the motivation for building the IceCube project that transforms $1\,\mathrm{km}^3$ of deep ultra-transparent ice into a particle detector at the South Pole [152, 153].

In the first section, we will describe in detail the detection principle of the neutrinos and the physics behind this principle. We will show that IceCube detects indirectly the neutrinos through the light trace created by a charged lepton travelling in the ice.

The second section will be devoted to a description of the ice characteristics that play a crucial role in the understanding of the detector. We will then present, in Section 3.3, the IceCube Observatory and its instrumentation. We will describe the data acquisition system and the different triggers and filters that are used to differentiate interesting events. Finally, Section 3.4 will concentrate on describing the signatures left by the particles inside the detector.

∴

3.1 Neutrino detection

IceCube is a Cherenkov telescope that detects neutrinos through the Cherenkov light produced by the charged current induced lepton travelling in the ice at a speed exceeding

the speed of light in this medium. We will first describe the interactions of the neutrinos and then explain the Cherenkov radiation production.

3.1.1 Neutrino interactions

Most of the neutrinos that cross the IceCube detector will stream through it without leaving any trace, even at very high energies. IceCube will only detect the few that interact in (or close to) the detector. Neutrinos entering the Antarctic ice can only interact with a nucleon (N) or an electron. As the neutrino-electron cross-section is, for almost the complete energy range, much smaller than the neutrino-nucleon one (for a recent review, see [154]), we will only consider the latter in the following.

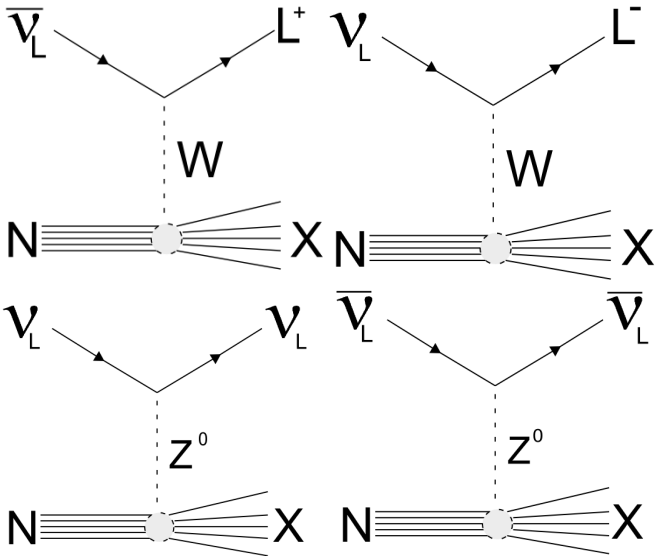

Figure 3.1: Feynman diagrams of the charged current (above) and the neutral current (below) interactions of a neutrino on a nucleon, N.

As sketched in Fig. 3.1, a neutrino can interact with an nucleon of ice nucleus by charged current (CC) interaction where a $W^{\pm}$ is exchanged or a neutral current (NC) interaction where a Z^0 is exchanged:

$$\text{(a)} \quad \nu_l + N \rightarrow l + X$$

$$\text{(b)} \quad \nu_l + N \rightarrow \nu_l + X$$

The CC interaction creates a charged lepton: $e^{\pm}$ for a primary electron neutrino, $\mu^{\pm}$ for a primary muon neutrino or $\tau^{\pm}$ for a primary tau neutrino. As we will see in Section 3.4, the signatures of these secondary particles travelling through the ice are different. When the secondary charged lepton is traversing the ice, it will emit Cherenkov radiations

and hence leave a specific light trace in the detector, allowing flavour determination of the leptons. The NC interaction does not lead to a specific track in the ice but creates a hadron shower leading to the detection of a cascade. This mechanism is important because it is responsible for energy losses.

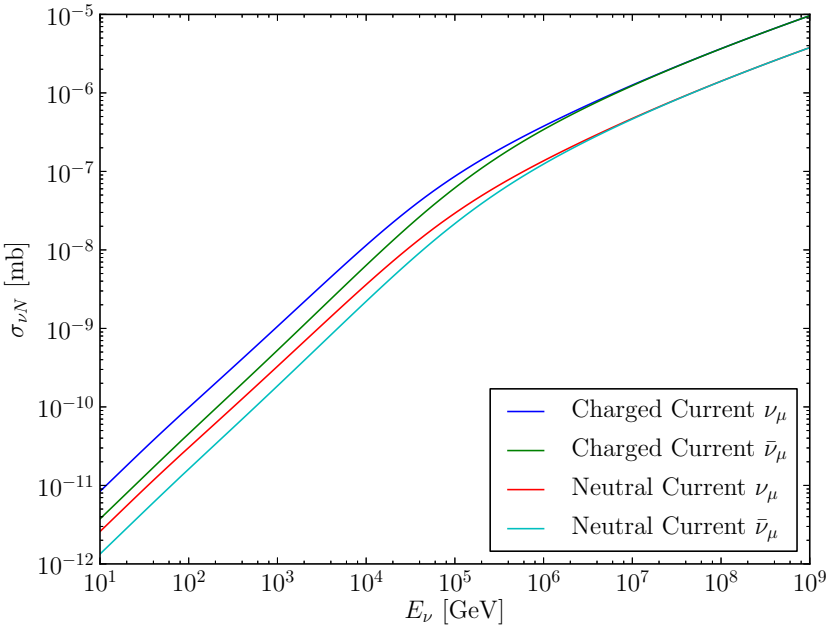

Figure 3.2: Neutrino-nucleon cross section for muon neutrinos as a function of neutrino energy. Only charged current (CC) interactions produce muons which can be detected. However, neutral current (NC) interactions must be accounted for in losses while propagating neutrinos through the Earth. At low energies ($E_\nu \ll M_w^2/2M_N$) the cross section is proportional to E_ν , while at higher energies ($E_\nu \gg M_w^2/2M_N$) the interaction is damped by the W-boson propagator and the cross section becomes proportional to $E^{0.363}$. Above $\sim 10^6$ GeV the contribution from valence quarks becomes negligible compared to sea quarks so that the neutrino and anti-neutrino cross sections become equal [155]. From [156].

Both the CC and NC interaction cross sections are energy-dependent and increase with the neutrino energy, as shown in Fig. 3.2, so the Earth becomes opaque to the highest energy neutrinos. Consequently, IceCube is forced to look to these very energetic neutrinos from the horizon or above. At low energies ($E_\nu \ll M_w^2/2M_N$) the cross section is proportional to E_ν, while at higher energies ($E_\nu \gg M_w^2/2M_N$) the cross section becomes proportional to $E_\nu^{0.363}$[155].

As IceCube detects the trace left by the lepton traversing the ice in the aim of finding back the direction of the initial neutrino, it is important to note that there exists an angle between the incoming neutrino direction and the produced muon direction. This angle is energy dependent and is given by [157]:

$$\Delta\theta \text{ [rad]} \sim \sqrt{\frac{1\,\text{GeV}}{\pi E_\nu}}, \text{ for } E_\nu > 10\,\text{GeV}. \tag{3.1}$$

The median deviation is $\sim 1°$ for neutrino energies of $\sim 1\,\text{TeV}$. We therefore can consider that the neutrino and the muon are almost collinear at the energies concerning our analysis.

3.1.2 Cherenkov radiation

As shown by Pavel Čerenkov in 1937 [158], a charged particle emits light when it travels through a dielectric medium with a velocity greater than the speed of light in this medium. Due to an asymmetrical polarisation of this traversed medium which leads to a varying electric dipole momentum, light is emitted along the track of the particle with an opening angle θ, with $\cos(\theta) = \frac{c}{vn} = \frac{1}{\beta n}$, where n is the refractive index of the medium. Fig. 3.3 sketches this effect and shows the so-called Cherenkov cone.

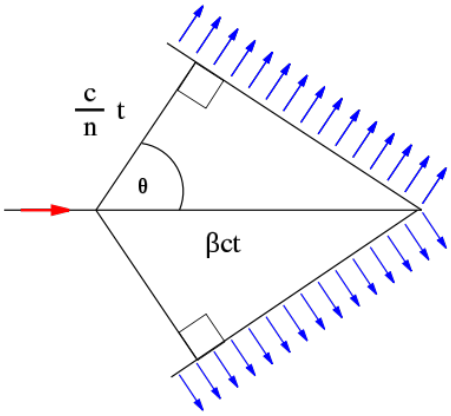

Figure 3.3: Production of the Cherenkov cone of light at angle θ by a charged particle travelling into a medium at a velocity higher than the speed of light in that medium.

The intensity of the Cherenkov photons is given by the Frank-Tamm formula [159]:

$$\frac{\mathrm{d}E}{\mathrm{d}x} = \frac{\mu q^2}{4\pi}\omega\left(1 - \frac{1}{\beta^2 n^2}\right)\mathrm{d}\omega, \tag{3.2}$$

where μ is the permeability and n the refraction index of the medium, q is the electric charge of the particle moving in the medium and ω is the angular frequency of the Cherenkov radiation. The intensity of the Cherenkov photons decreases therefore with larger wavelengths (see Fig. 3.8).

3.2 Ice properties

This section is devoted to an analysis of the properties of the South Pole ice and the impact on the detection of the Cherenkov light produced by the various particles. The current discussion is based on [160], where the interested reader can find all the detailed information.

To detect the Cherenkov light emitted by the charged particles, the medium has to be as transparent as possible. The Antarctic ice is the most transparent medium for wavelengths from 200 nm to 400 nm [160] and is therefore an excellent medium for our detector. Understanding the propagation of the photons in this medium is crucial to be able to reconstruct correctly the directions of the particles. The propagation of the photons directly depends on their speed but also on effective scattering length and the absorptivity of the medium (see Fig. 3.4) they are travelling in. The two sharp peaks visible in this figure are created by a significant dust layer in the ice at ~ 2000 m depth very likely originating from the Toba eruption which happened about 75000 years ago in the vicinity of Indonesia.

The ice of the South Pole has developed over a period of 165 000 years [161] and has a thickness of 2820 m [160]. The ice is composed of horizontal layers with various concentrations of dust that can be correlated to the different climate changes and volcanic eruptions which took place during the history of the Earth [162]. The absorption of the photons is described by the absorption length λ_a or by the absorptivity b_a with $b_a = 1/\lambda_a$ and is defined as the distance at which the survival probability drops to 1/e. For the South Pole ice and for wavelengths between 200 nm and 500 nm, the absorption length is of $\lambda_a \sim 100$ m, which is similar to the string spacing and much larger than the spacing between the optical modules of IceCube (see Section 3.3.1) on a given string.

The scattering of the photons on microscopic scattering centers, such as submillimeter-sized air bubbles and micron-sized dust grains is well described by the Mie theory [160, 163]. We define an effective scattering length λ_e by adopting the definition of the transport mean free path, which is the length scale over which randomisation occurs, in the limit of many scatters, when scattering is not isotropic, which is given by:

$$\lambda_e = \frac{\lambda_s}{1 - \langle \cos\theta \rangle}, \tag{3.3}$$

where θ is the scattering angle, the mean value of its cosine is $\langle \cos\theta \rangle \sim 0.94$ [160] and λ_s is the geometric scattering length, *i.e.* the average distance between scatters. For the South Pole ice, this gives an effective scattering coefficient of $b_e \sim 0.05 - 0.04$ and hence $\lambda_e \sim 20 - 25$ m.

The ice properties are crucial for both the simulation and reconstruction algorithms of IceCube. Different models of these are used by the IceCube collaboration, more details can be found in [164].

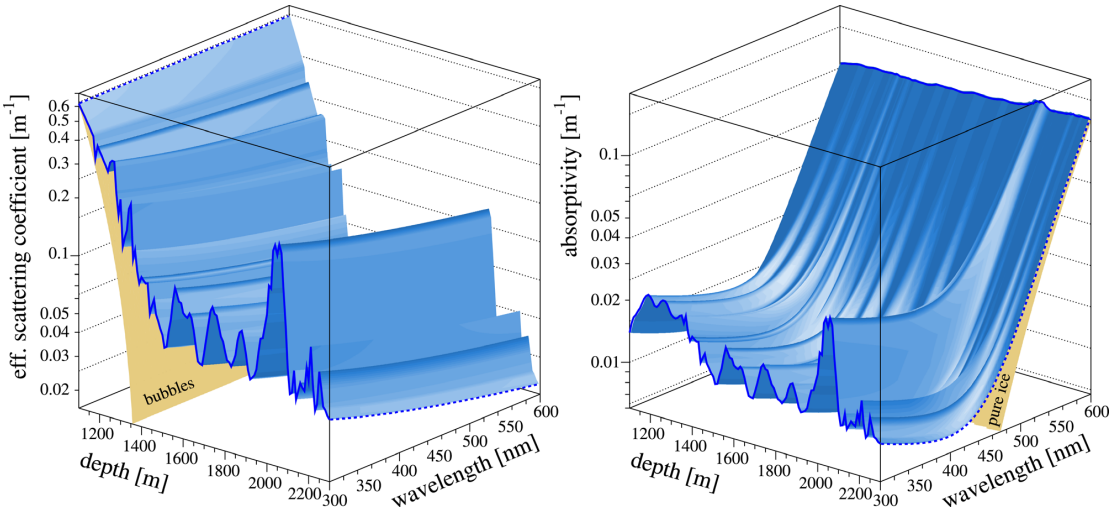

Figure 3.4: Maps of optical scattering and absorption coefficients for deep South Pole ice from [160]. These coefficients are the reciprocal of, respectively, the scattering and the absorption length. The depth dependence between 1100 and 2300 m and the wavelength dependence between 300 and 600 nm (left) for the effective scattering coefficient and (right) for absorptivity are shown as shaded surfaces, with the bubble contribution to scattering and the pure ice contribution to absorption superimposed as (partially obscured) steeply sloping surfaces. The dashed lines at 2300 m show the wavelength dependences: a power law due to dust for scattering and a sum of two components (a power law due to dust and an exponential due to ice) for absorption. The dashed line for scattering at 1100 m shows how scattering on bubbles is independent of wavelength. The slope in the solid line for absorptivity at 600 nm is caused by the temperature dependence of intrinsic ice absorption.

3.3 The IceCube Neutrino Telescope

The IceCube Telescope [153] is a large-scale neutrino observatory buried in the ice at the geographical South Pole. The construction began in 2004 and has been finished in December 2010. This work was only possible in the summer seasons at the Pole, being unique periods where the weather allows the deployment of the experiment. The construction has therefore lasted about 6 years. Data has been taken during all of the construction phase, offering the possibility to test the detector and to perform first analyses.

The general design of IceCube is based on its precursor, the Antarctic Muon And Neutrino Detector Array (AMANDA) experiment [166]. The global observatory is composed of two different parts. The first one is located in the deep ice, representing the in-ice part of IceCube including the *DeepCore* low-energy extension. The second

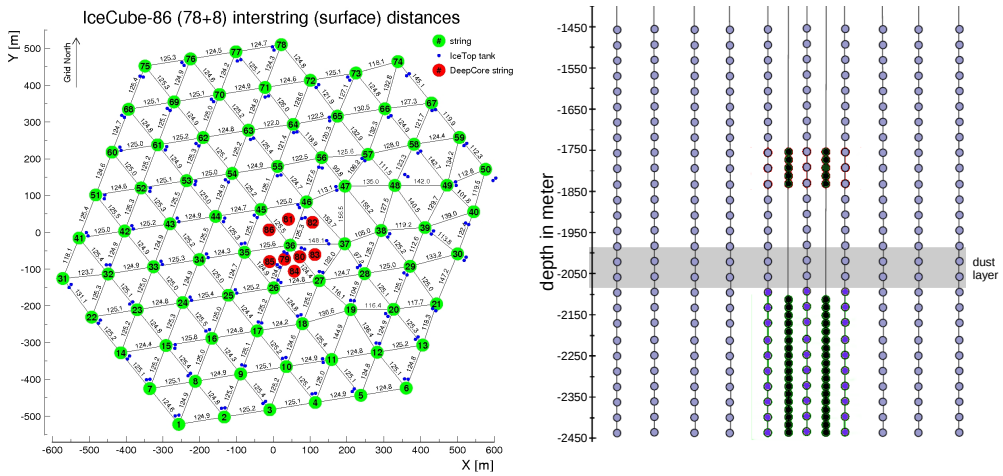

(a) (b)

Figure 3.5: (a) IceCube top view: the surface geometry of the complete IceCube Observatory. Green and Red circles stand for the location of the in-ice strings whereas the blue circles indicate the IceTop surface array tanks. (b) Side view, not to scale: DeepCore DOMs (black dots) are instrumented denser than DOMs on standard strings (blue dots) and elude the dust layer (gray band). From [165].

one is the surface array *IceTop*.

For IceCube, 86 "holes" of 2500m depth located as depicted in Fig. 3.5 have been drilled into the Antarctic ice, using techniques developed especially for this experiment. After a hole was drilled, a vertical cable called a *string* has been deployed in every hole. Each of the 78 standard IceCube strings are instrumented every 17m from 1450m to 2450m with a total of 60 photomultipliers and read-out units called Digital Optical Modules (DOMs) that detect the light emitted by the particles in the ice (see Section 3.3.1 for more details on the DOMs). For the 8 DeepCore strings, the 10 first DOMs are spaced every 10m between 1750m and 1850m and the 50 others are spaced every 7m from 2100m until 2450m. This specific spacing has been chosen so that these DOMs are in the most pure regions of the ice. Furthermore, the smaller spacings of the DeepCore DOMs provide a lower energy threshold for track reconstruction, as explained later on. In total IceCube comprises 5160 DOMs. Fig 3.6 shows a visual representation of IceCube, including DeepCore, IceTop and its precursor AMANDA-II.

IceCube's surface array, IceTop, detects air showers with an energy threshold of about 300 TeV [153] and studies the physics of cosmic rays and their composition. It consists of 160 frozen water tanks containing 2 DOMs each (*i.e.* a high gain and a low gain one). At each location of an IceCube string two IceTop tanks have been positioned. This thesis will only concentrate on data from the in-ice part, from now referred to as IceCube, and

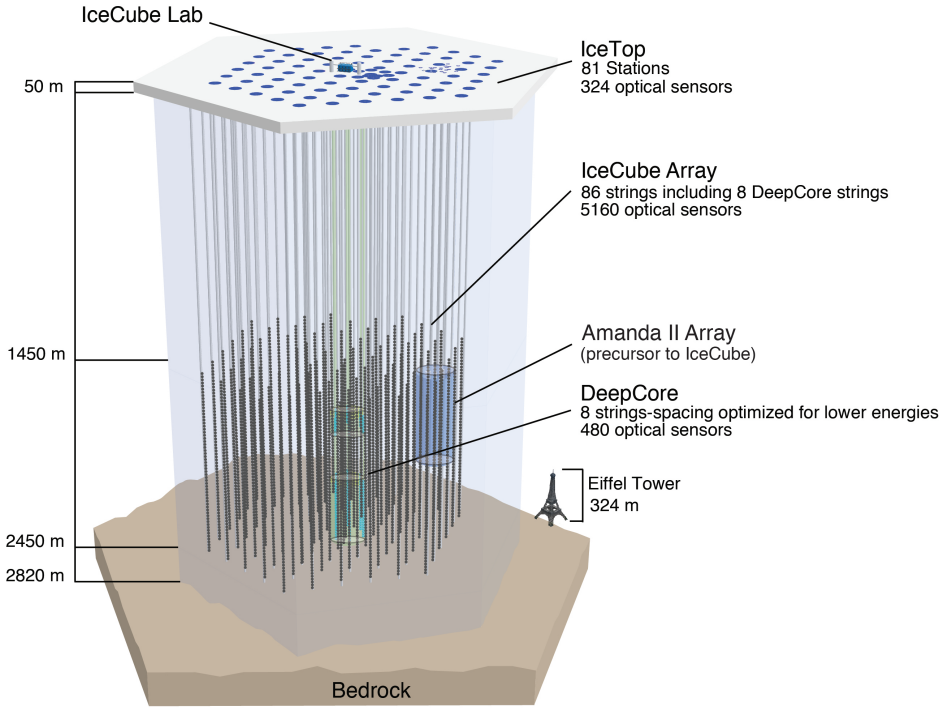

Figure 3.6: Schematic of the IceCube Observatory, including the low-energy extension DeepCore and the surface detector IceTop. The precursor of IceCube, AMANDA-II [166] is also shown. The Eiffel Tower is depicted for scale.

not from IceTop.

3.3.1 The digital optical modules

In this section, we will present a summary of the properties of the DOMs of IceCube. Interested readers can find more information in [167, 168, 169].

3.3.1.1 Composition and operation

Each DOM is composed of two different parts, as shown in Fig. 3.7. The lower part is composed of a 25 cm (10 inch) Photo-Multiplier Tube (PMT) and the upper part contains all the electronics needed for collecting and digitising the voltage pulses from the PMT. These components are housed in a glass sphere of 13 mm of thickness capable to resist to the up to 650 atm pressure during freeze-in and 300 atm pressure after freeze-in created by the ice at the bottom of the detector. The embedded electronics of the DOMs work from room temperature (for testing) to -55° C. It is also important to note that the DOMs are of course totally inaccessible after deployment. A reliability requirement

of 90% DOM survival after 15 years has been set, which is the same as for components of satellites. As we will discuss in the next paragraph, the DOMs need a high voltage to work correctly. This high voltage is supplied by a Cockroft-Walton power supply. The output voltage is digitally controlled and may be adjusted from the surface. Needing less than 300 mW, the power-supply is low-power. The entire DOM operates on a power of 5 W.

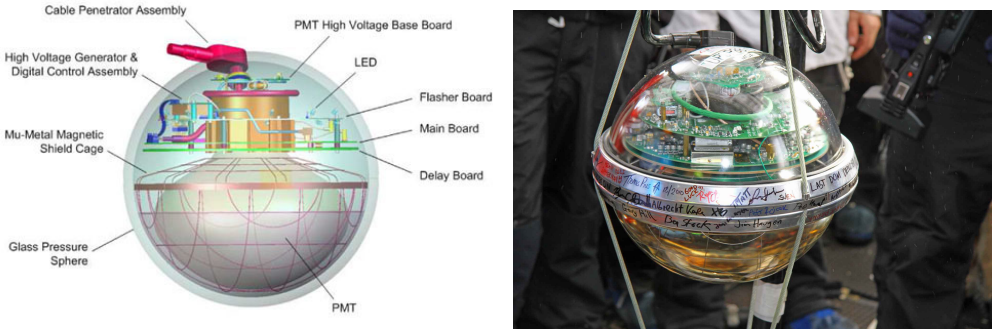

(a) (b)

Figure 3.7: (a) Schematic view of an IceCube DOM from [153] (b) Photo of the last DOM deployed at Pole in December 2010.

The requirements for the electronics of the PMTs were rather stringent because they have to record the arrival of most of the photoelectrons with a timing resolution of less than 5 ns and the dark noise rate have to be below 500 Hz. The PMTs chosen (Hamamatsu R7081-02) are composed of a bi-alkali photo-cathode and 10 dynode stages which produce a gain of about 10^7 for voltages between 1300 V and 1500 V. The quantum efficiency of the PMT, which refers to the probability of an incident photon producing a photoelectron[1] (PE), is 25% at 420 nm. The PMTs are sensitive for a range of wavelengths between 300 nm and 600 nm because of the "transparency" of the glass spheres (see Fig. 3.8). Their dark noise rate is about 300 Hz.

As seen on the block diagram of the DOM mainboard, shown in Fig. 3.9, the PMTs are connected to the mainboard through transformers, which are responsible for the digitalisation of the PMT output waveform. Two transformers, controlled by the Field Programmable Gate Array (FPGA), coexist in the DOM mainboard: the Fast Analog Digital Converter (FADC) and the Analog Transient Waveform Digitisers (ATWD). The FADC is a commercial digitiser recording the PMT waveforms at a rate of 40 MHz for signal of about 6.4 μs. The 40 MHz rate is obviously a limiting factor compared to the required timing resolution of several nanoseconds, therefore the ATWDs are used. They have a much better timing precision and dynamic range. They sample the waveforms at a rate of 300 MHz but only for 422 ns, after which they need 29 μs to digitise and clear.

[1] A photoelectron refers to the ejected electron after a Cherenkov photon hits the photo-cathode.

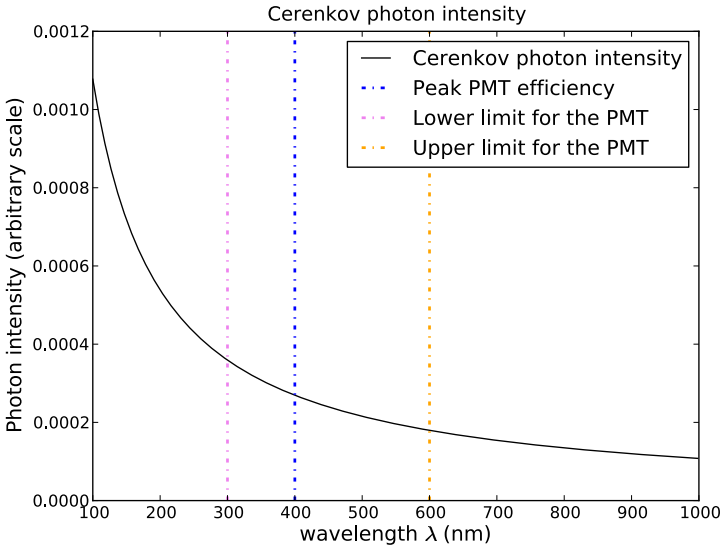

Figure 3.8: The intensity of the Cherenkov photons in function of the wavelength λ following Eq. (3.2). The purple and orange vertical lines indicate the sensitivity range for the IceCube PMT while the blue vertical line indicates the peak quantum efficiency for these PMT. From [170].

This dead time justifies the existence of two ATWDs which are working in alternation. In the rare case of three or more simultaneous pulses in 29 μs, only the first two are saved and the others are lost. The ATWDs are composed, as seen in Fig. 3.9, of 4 different channels. The three first channels amplify the signal by a factor of 16, 2 and 0.25 respectively, the last channel is used for calibration and monitoring.

If the PMT output current detected by the FADC exceeds a threshold value (fixed at 1/4 PE in IceCube), the digitised waveform is stored to be sent to the surface. In view of the noise rate, the produced data rate is too high to handle. Therefore, and also for reducing the ATWD dead time, a local coincidence condition is imposed before sending information to the surface. Until early 2009, IceCube required a Hard Local Coincidence (HLC) condition. This condition implies that the waveforms of the DOMs will only be read out when two nearest neighbour or next-to-nearest-neighbour DOMs see a signal within a 1 μs coincidence window. The local coincidence condition suppresses most of the noise hits and limits the rate to 3 to 15 Hz, depending on the DOM's depth, the muon flux and the ice properties. From 2009, IceCube started taking data also for Soft Local Coincidence (SLC), which is a misleading name since actually no coincidence requirement is imposed. In this case, not the full waveform is read out and sent to the surface but only the peak value and the values of the two adjacent FADC time bins, which obviously reduces dramatically the data volume for these signals. Obviously these

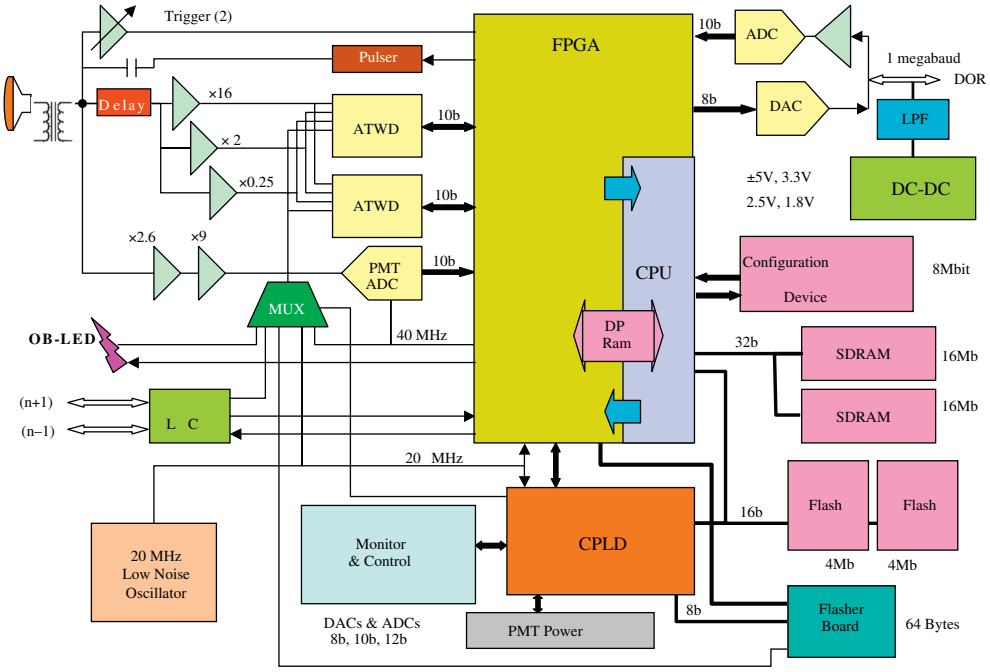

Figure 3.9: Block diagram of the DOM mainboard. The PMT, FADC and ATWDs, CPU and FPGA, 20 MHz clock, flasher board and supporting electronics are visible. From [168].

SLC hits cannot participate in forming a trigger (see next section) but they are used in some of the reconstructions to obtain a better energy estimate for the event.

DOM Launching and communication are coordinated by an on-board CPU that communicates with the other on-board electronics through the FPGA. Finally, each DOM also contains a 20 MHz oscillator for precision time-keeping and a "flasher" composed of 12 LEDs mounted around its edges. These flashers are used for calibration issues and also for measuring *in situ* the propagation of the light inside the ice and the timing between different DOMs [171].

3.3.1.2 Calibration

Obviously calibration of the DOMs is a very important aspect of IceCube's performance. Three observables are crucial in terms of precision measurements: (1) timing and (2) signal response calibrations are required to obtain consistent waveforms in view of reconstructing correctly the physical pulses occurring in the PMT and (3) geometry calibration is fundamental for achieving precise reconstructions of the muons travelling through the detector.

As mentioned before, each DOM comprises a 20 MHz oscillator responsible for time calibration inside the DOM. A general calibration for all IceCube DOMs is obtained through a GPS-discipled rubidium clock which fixes an IceCube Time (ICT) with a precision of ± 10 ns. The clock is located in the IceCube Laboratory (ICL) which communicates with and powers all the 5160 DOMs by cable. Once per second, a timing calibration procedure called Reciprocal Active Pulsing calibration (RAPCAL) is used to measure each DOM's clock offset and drive rate with respect to ICT. For the ATWDs the sampling rate (300 MHz) is faster than the internal clock rate (20 MHz). The timing precision is then obtained using the fourth channel and is subject to further correction using the ICT. Calibration of the PMT and digitiser responses are realised through a program called DOMcal which is runned periodically on the DOMs' CPUs. During the different construction phases of IceCube, this code was run monthly but it has since been found that an annual periodicity was sufficient.

Finally, the geometry of the DOMs has been controlled during deployment of the different DOMs. These initial controls lead to a precision of the location of each DOM of 0.5 m. A precision measurement is then obtained by running specific flasher runs using the previously described on-board flashers, where the transmit-receive time intervals are measured in view of deriving the position of the DOMs. Finally a location precision of the order of 10 cm is obtained.

3.3.2 The data acquisition system

The Data Acquisition System (DAQ) [168] controls the detector and the triggers. The DAQ is composed of a specific computer for each string called DOMHub. The DOMHub provides the needed power and receives the data sent by the DOMs of the controlled string. The DAQ is responsible for identifying from all the transmitted HLC and SLC readouts, the potential physics events.

When a DOMHub receives a waveform from a DOM, it sends it to the trigger system. The trigger system continuously scans the data trying to fulfil one of the trigger conditions (see section below) to form a detector trigger. When a trigger occurs, longer readout windows are opened 4 μs before and 6 μs after the trigger window to capture early or late light. If multiple trigger windows overlap, then all of the data from the time intervals are saved as a single event. After 6 μs during which no trigger condition is satisfied, the event data is finalised and packaged into a data bundle called *frame*. These frames then continue to the Processing and Filtering (PnF) system, a small computing cluster ($\sim$ 20 servers) that performs fast reconstructions and event selections on the triggered DAQ events, reducing the 1 TB/day raw data stream to approximately 100 GB/day [172] for transmission to the North over satellite.

The IceCube software trigger looks for clusters of HLC DOM triggers in time and/or space, using the timestamps and known DOM positions. In order to operate efficiently, the trigger operates on a combined time-sorted hit stream from all DOMs.

3.3.2.1 Triggers

Most of the triggers look for a certain multiplicity of HLC hits within a given time window. Some of them add to this time requirements and/or geometry conditions of the hits. Triggers can be assigned to operate on different "DOM sets", such as all in-ice DOMs, DOMs within the DeepCore sub-array, or IceTop DOMs. We will list below all the in-ice triggers that were in use during the data taking periods related to this thesis [172]. A summary of all the trigger conditions is to be found in Table 3.1 where the passing rate of each of them is indicated.

Simple Multiplicity Trigger. The Simple Multiplicity Trigger (SMT) is the most important trigger of IceCube. Two versions exist: the SMT 8 and the SMT 3. The SMT looks for 8, respectively 3, HLC hits within a time window of 5 μs, respectively 2.5 μs, without any spatial condition. The SMT8 is used for the regular IceCube DOMs, whereas the SMT3 is exclusively used for DeepCore. As long as the multiplicity condition is satisfied, the trigger window is extended.

Volume and String Triggers. The SMT is too restrictive if the particle has low-energy or if it is travelling vertically in the detector. Two triggers relaxe the SMT requirements imposing some topological conditions. The *volume trigger* defines a fixed size cylinder ($r = 175\,\text{m}$ and $h = 75\,\text{m}$) around each hit DOM and searches for 4 HLC hits in that volume in a time window of 1 μs, see Fig. 3.10, which offers the opportunity to look for lower energy particles. The *string trigger* relaxes the requirements even more by searching for 5 HLC hits within a length of 7 adjacents DOMs along a single string in a 1.5 μs time window. The latter obviously profits from the small spacing between DOMs on one and the same string, but consequently only works for (nearly) vertical tracks.

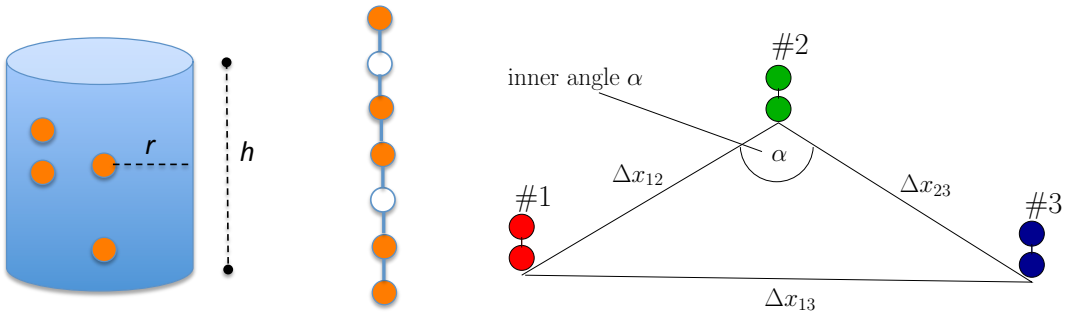

(a) Schematic representation of the volume trigger (HLC hit DOMs are darkened).

(b) Schematic representation of the string trigger.

(c) Parameters defining a SLOP trigger 3-tuple (from Ref. [4])

Figure 3.10: Topological triggers of IceCube. From [172].

Slow Particle Trigger. The Slow Particle Trigger (SLOP) is used for detecting

hypothetical subrelativistic heavy particles such as magnetic monopoles. As the speed of these particles is of the order of $v \sim 0.001\,c - 0.01\,c$, the previous time windows are much too short. The trigger operates in several stages. HLC hits, which by design come in at least pairs along a string, are cleaned to avoid multiple muon hits by removing pairs that are too close in time ($\Delta t < T_{\text{pro}} = 2.5\,\mu\text{s}$). Then, triplets of pairs within a time window of maximum $500\,\mu\text{s}$ are formed. The geometry of each 3-tuple formed must satisfy track-like conditions: the obtuse inner angle of the triangle formed must be larger than $\alpha_{\text{min}} = 140°$, and the "velocities" along the triangle sides must be consistent. Specifically, the normalised velocity difference $v_{\text{rel}} = 3(v_{12}^{-1} - v_{23}^{-1})/(v_{12}^{-1} + v_{23}^{-1} + v_{13}^{-1})$, with $v_{ij} = \Delta x_{ij}/\Delta t_{ij} \leq v_{\text{rel}}^{\text{max}} = 0.5$. Fig. 3.10 shows the geometry parameters of the 3-tuple. Finally, the number of track-like 3-tuples must be greater than or equal to $N_{\text{tuple}} = 5$.

Other Triggers. Other special-purpose triggers exist; the most notable is the fixed-rate trigger (FRT) that triggers at a given rate and simply reads out 10 ms of data from the full detector. This is useful as a minimum-bias sample and for studies of DOM noise.

Table 3.1: Trigger requirements for the IceCube DAQ and passing rates.

Trigger	DOM set	N HLC hits	Time window [μs]	Topology	Rate [Hz]
SMT-8	in-ice	8	5	-	2100
SMT-3	DeepCore	3	2.5	-	250
Volume	in-ice	4	1	Cylinder of $r = 175\,\text{m}$ and $h = 75\,\text{m}$	3700
String	in-ice	5	1.5	7 adjacents DOMs on one single string	2200
SLOP	in-ice	$N_{\text{tuple}} = 5$	$T_{\text{prop}} = 2.5$ $T_{\text{max}} = 500$	$\alpha_{\text{min}} = 140°$ $v_{\text{rel}}^{\text{max}} = 0.5$	12
FRT	all	-	-	-	0.003

3.3.2.2 Processing and Filtering

As explained above, the "raw" DAQ data output is still too massive, $\mathcal{O}(1\,\text{TB/day})$, to be sent to the North by satellite. The Tracking and Data Relay Satellite System (TDRSS) bandwidth allocated to the IceCube experiment is limited to 105 GB/day. The IceCube Collaboration therefore developed the PnF system that scans the DAQ raw data to look for interesting events and sends this subset of data to the North. The details of filters and the reconstructions are discussed in detail in Chapter 4 and the use of these observables for the analysis are presented in Chapter 5. This section is devoted to a presentation of the operational aspects of the PnF system.

The filters are a first analysis stage (called Level 1) that marks various types of interesting physics events at the South Pole Station. There exists as many filters as dedicated searches (muon, low-energy, cascades, ...). The filters are run by the PnF system, which first calibrates and cleans the data and then searches for events containing characteristics which are relevant for the corresponding filter stream. The PnF system performs some fast first-guess reconstruction algorithms with some loose "quality cuts" that throw away the "non-interesting" data. However, with the arrival of more and more efficient computing hardware the online reconstructions at the Pole become also more elaborate. This obviously results in cleaner online event samples.

When an event passes at least one filter, the full waveforms and reconstruction results are sent to the North. For the other events, only the reconstructions are transmitted. Note however, that no data is lost since all obtained signals are recorded on storage devices at the Pole and shipped by plane to the North at the start of the Austral summer.

3.4 Event signatures

As we already discussed above, IceCube detects neutrinos by observing the energy loss and Cherenkov radiations of the secondary particles. In the CC interactions, the created leptons carry an average of 50% (for $E_\nu \sim 10\,\mathrm{GeV}$) to 80% for higher energies, of the original neutrino energy. The energy that remains is transferred to the nuclear target, which will be released through hadronic showers. Both the charged lepton and the shower will produce Cherenkov radiation. Depending on the lepton type, the topology of the events left in the detector is totally different and IceCube can distinguish each of them separately:

- The muons travel through the detector emitting Cherenkov light which create a track ;
- The electrons and the tau's loose their energy through showers that can not be distinguished from the hadronic showers from the nuclear target, creating a single cascade ;

Note that a neutrino which undergoes a NC interaction transfers a fraction of its energy to the nucleon, producing a hadronic shower. This will then leave a cascade signature in the ice. For very energetic events the tau neutrinos can provide very distinct signatures, as outlined hereafter.

3.4.1 Muon tracks

As indicated above, muons travel through the detector and leave a clear distinguishable track. Nevertheless, a muon also looses energy when it traverses the ice. The

possible mechanisms are: ionisation, pair production, bremsstrahlung and photo-nuclear interactions. The energy loss as a function of the traveled distance x is given by [173]:

$$-\frac{\mathrm{d}E}{\mathrm{d}x} = a(E) + b(E)E, \tag{3.4}$$

where $a(E)$ represents the ionisation losses and is known as the Bethe-Bloch function

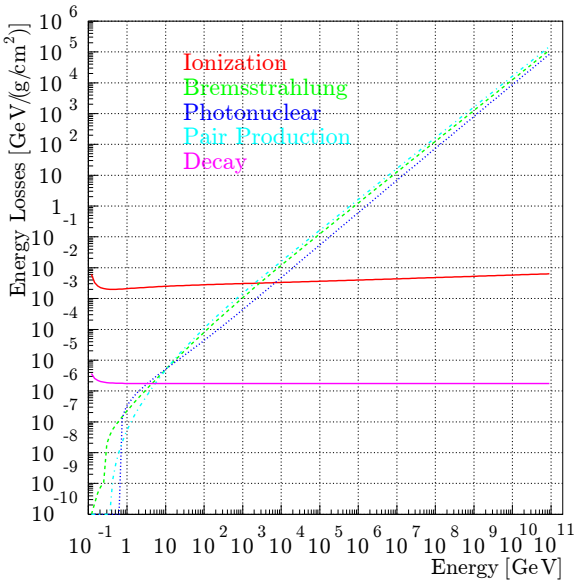

Figure 3.11: Average muon energy losses in the ice. The four types of losses are shown. At low energies, the ionisation process dominates and is weakly dependent on energy while at higher energies, the bremsstrahlung, photo-nuclear and pair production mechanisms are dominant and are proportional to the muon energy. From [173].

[174] and $b(E)$ accounts for the sum of the pair production, bremsstrahlung and photo-nuclear effects. The various components of the muon energy loss in ice are shown in Fig. 3.11.

If we consider the functions a(E) and b(E) to be only weakly depending on energy and assume the initial energy of the muon to be E_0, we find that the traveled distance is:

$$x \approx \frac{1}{b} \ln\left(1 + \frac{b}{a}E_0\right) \tag{3.5}$$

For example, at TeV energies, muon tracks can be up to 10 kilometres long, which offers clearly the opportunity to IceCube to detect these muons. A sketch of the muon signature is given in Fig. 3.12.

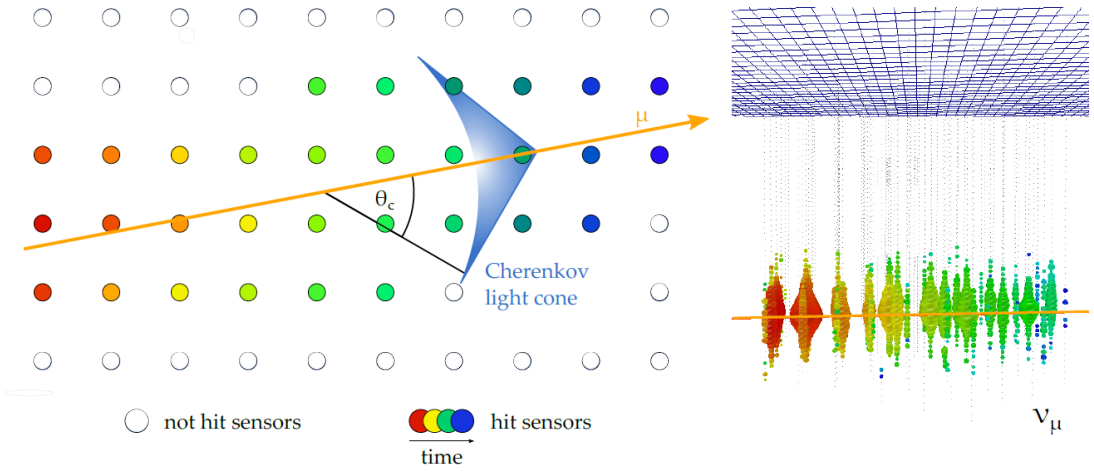

Figure 3.12: Example of a track left by a muon. Left : Sketch of a muon travelling through a detector similar to IceCube, from [175]. Right : Real event observed by the IceCube Collaboration.

This signature offers the opportunity to determine accurately the muon direction, and hence the neutrino direction. This is of course a key point for developing neutrino astronomy. On the other hand, because the track is not totally contained in the detector, the energy estimation becomes more difficult. More over, the background of atmospheric μ and ν_μ is very large and complicates the determination of astrophysical muon neutrinos.

3.4.2 Cascades

Cascades can be created by the CC interaction induced hadronic shower of a ν_e or a ν_τ and by a NC interaction of any neutrino type. The electrons created by the CC interaction of a ν_e will loose almost instantaneously their energy through an electromagnetic shower, resulting in a nearly spherical signature, as sketched in Fig. 3.13. This cascade also contains the hadronic shower of the nuclear target and is indistinguishable from the electron signature. Due to the short lifetime of a τ, a specific track is in general not observed leading also to a cascade signature. However, a specific signature is discussed hereafter.

In the situation of a cascade signature, the energy of the incoming ν can be much more precisely determined because the event is contained. It is also to be noted that the background of atmospheric ν_e is significantly lower and that there are basically no atmospheric ν_τ. Finally, it is important to know that even if these cascades are nearly spherical, they are not isotropic. The light is preferentially emitted at the Cherenkov angle, resulting in a possible direction determination which obviously is less accurate than for track like events.

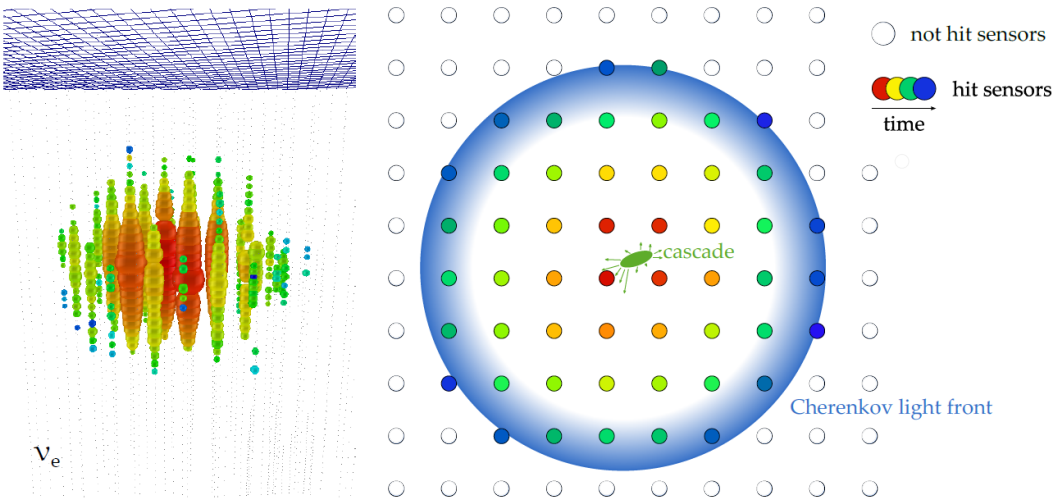

Figure 3.13: Example of a signature left by an electron. Right : Sketch of an electron cascade left in a detector similar to IceCube, from [175]. Left : Real event observed by the IceCube Collaboration.

3.4.3 Double Bang, Lollipop and Sugar Daddy

Depending on its energy and its decaying mode, the ν_τ can create many different signatures in the detector. At high energies ($E_\tau \geq$ PeV), the CC created τ will have a long track (of about hundred meters) and can then create a very specific and unique signature: the "double bang" (branching ratio of 82%). This topology is composed of two cascades: the first is the hadronic shower from the nuclear target at the interaction point of the ν_τ and the second at the decay point of the τ.

If one of these two cascades happened outside the detector, only the τ track and one blob will be recordered. This topology is called the "lollipop" signature. In 18% of the cases, the τ also can disintegrate in a muon, which will then leave a more luminous track in the detector and not a cascade. This specific signature is called the "sugerdady".

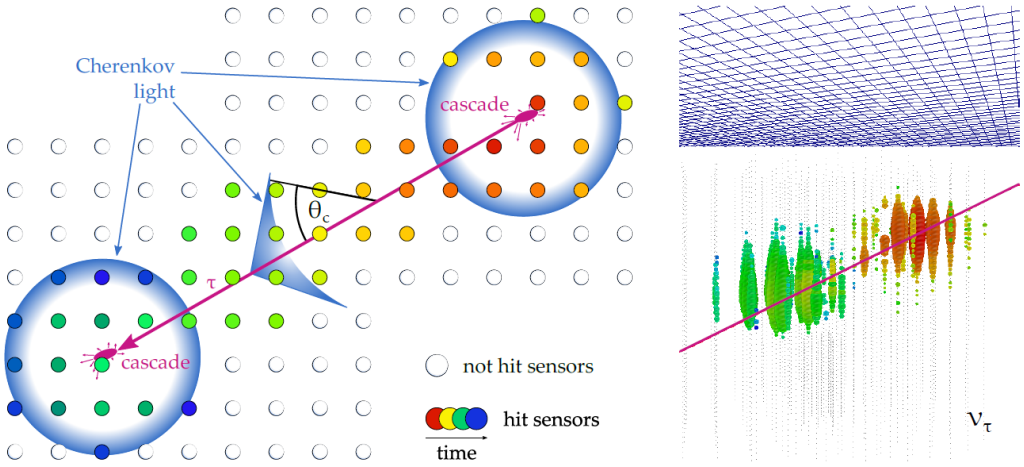

Figure 3.14: Example of a track left by a tau. Left : Sketch of a tau signature, the so-called "Double Bang", in a detector similar to IceCube, from [175]. Right : Simulated event as it would appear in the IceCube detector.

CHAPTER 4

Event Filtering and Processing

We have left the previous Chapter with an operational description of the Processing and Filtering system which aim is to transform raw data into physical quantities. This Chapter will now describe the complete processing chain starting from the individual DOM readouts to the full event reconstruction. For our analysis searching for muon tracks in the detector, this means that we are investigating the original angle and eventually energy of the incoming muon. Only after that, we will be able to potentially associate certain neutrinos to GRBs. The processing is therefore a necessary step before the actual analysis can be performed.

The first section of this Chapter is devoted to a discussion about the creation of the pulse series starting from individual hits in the DOMs. We will discuss the different aspects of that construction. We then present, in Section 4.2, the different filters that tag physics events between all the detected muons. The next section concentrates on a very important aspect: the track reconstruction. This is obviously a key feature for all analyses. Finally, we conclude this Chapter with a discussion on the various simulations that have been applied for developing our analysis and how they have been used.

∴

4.1 Pulse series construction

The construction of the pulses that will be used in the reconstruction algorithms is based on two important steps. First the waveforms that are generated by the PMTs have to be extracted and calibrated to obtain physical values like absolute hit time and number of recorded photo-electrons and then the noise hits have to be subtracted from the pulse series. We refer to the first step as Waveform Construction and the second

consists of a so-called cleaning procedure.

But first of all it is to be kept in mind that an initial check concerns of course the DOM itself. Some DOMs are "bad" for a short period of time, meaning that it has bad surface communication, power problems, *etc.* Most of them have been found to exhibit this behaviour only very occasionally since their deployment and very few have broken during operation. For IC86, $\sim$ 100 DOMs on a total of 5160 are marked bad for HLC coincidences but $\sim$ 20 can still be used for SLC launches. Of course the data from these bad DOMs is not used for any further step.

4.1.1 Waveform construction

The first step is to calibrated correctly the waveforms. Each capacitor in the ATWD (see Section 3.3.1.1) has an offset (pedestal voltage), which must be measured separately for each ATWD by setting the voltage to zero and measuring the remaining charge. Once it is known, it can be subtracted from every measurement to obtain a physical value of the deposited charge. This is realised by DOMcal (see Section 3.3.1.2). Unfortunately this is not the only effect that affects the measurement. The ATWD is indeed inductively coupled to the anode of the PMT with a transformer. Therefore it introduces droop in the trailing edge of the waveform. This effect is also corrected for and we finally obtain an exploitable waveform.

The last step is then performed by an algorithm called WaveDeform [176] which unfolds the calibrated waveforms into series of reconstructed pulses. As the shapes of the calibrated waveforms are dominated by the ATWDs and the FADC, their shaping functions (see Fig. 4.1) are used as templates to form a basis for decomposing the waveforms. The pulse amplitudes and times of arrival events are found by finding a set of pulses that combine linearly to provide a good fit to the FADC and the three ATWD channels simultaneously. To achieve this, the algorithm has a DOM response template which predicts the voltage as a function of time for a pulse at a given time and amplitude. The feature extraction algorithm identifies upward slopes in the calibrated waveform as initial guesses for the time and amplitude of pulses. Then it uses an iterative unfolding algorithm to find the best match between the templates and the observed waveform. The algorithm terminates when it achieves the minimal possible error. A threshold is fixed as a minimal gain obtained at each iteration to avoid too long processing but achieving still a good representation of the real waveform and allowing a physical interpretation of the reconstructed pulses. An example of the performance of WaveDeform is given in Fig. 4.2.

4.1.2 Pulse series cleaning

The final step before using the pulses for physics analyses is to eliminated the noise hits which could reduce the quality of the future reconstructions. Remember that there is a time window of at least 10 μs during which all HLC and SLC readouts are stored.

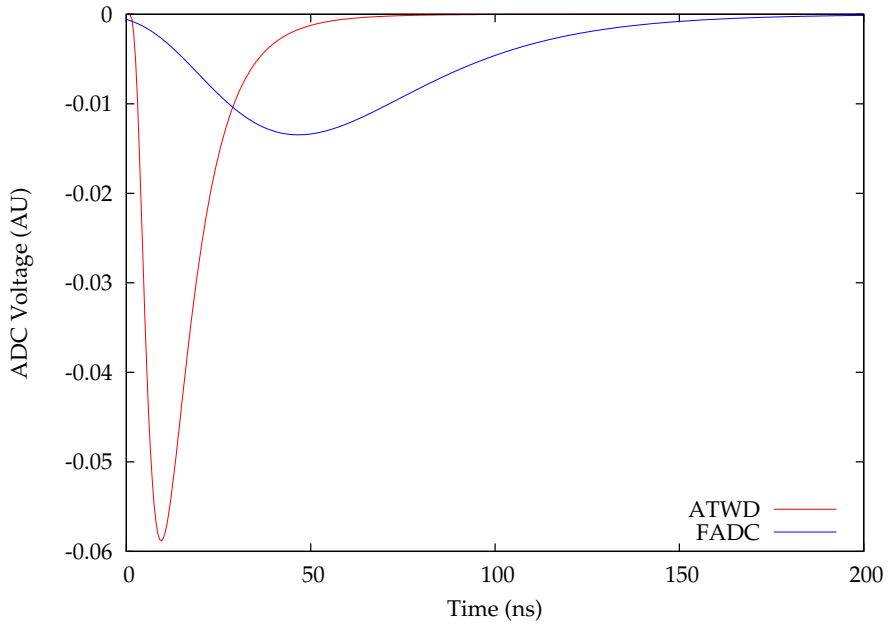

Figure 4.1: ATWD and FADC shaping functions. PMT pulses are elongated to ensure that each pulse covers several digitiser bins. The signal is widened more for the FADC because of its lower sampling rate. The highest-gain ATWD channel is shown here; there are small differences for lower-gain ATWD channels due to differences in amplifier chains. From [176].

There are therefore often noise hits present unrelated to the muon which triggered the event. Different cleaning procedures exist in IceCube. In this thesis, we have chosen to apply the so-called HiveSplitter cleaning [177].

HiveSplitter cleaning provides a classic hit-cleaning that is based on the hexagonal description of the detector. This enables a more precise steering of the parameters and a more powerful cleaning process than the usual generic approaches. The employed algorithm isolates hits, which do not have neighbouring hits occurring within a certain distance within a certain time window, and removes them. Because noise hits predominantly occur randomly and show up as isolated hits in the detector array, while physics hits occur in a clustering fashion, this algorithm is excellently suited for noise-cleaning.

4.2 Filters

We have presented how the pulses are constructed and cleaned. We now review different IceCube filters. As previously explained, a large number of different filters with specific physical objectives exist and we will only present, in the following, the filters that are used in our analysis.

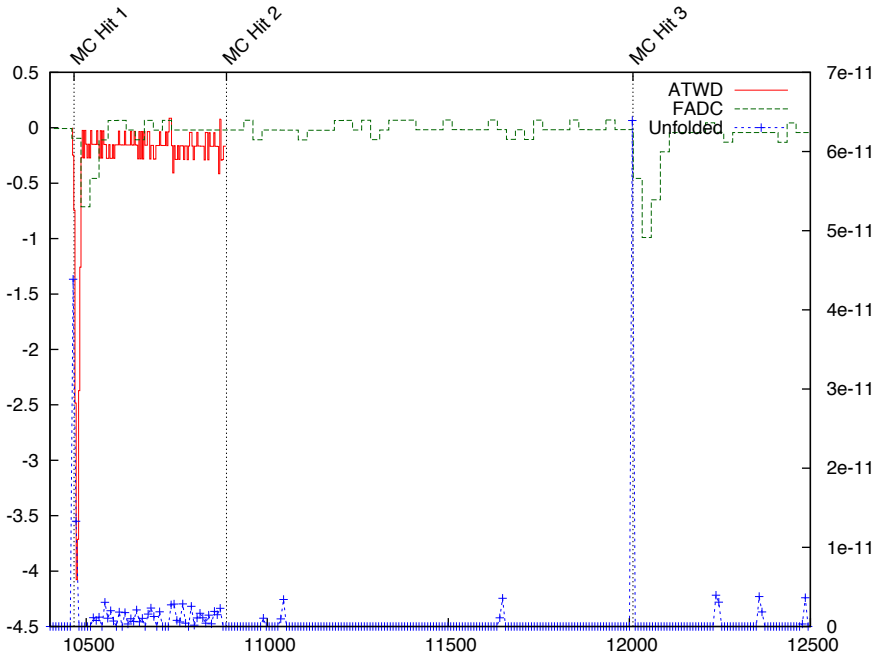

Figure 4.2: Simulation of the response of the WaveDeform algorithm. From [176].

4.2.1 The Muon Filter

The muon filter aims to provide a sample of muons to be used for analyses over the whole sky. The sky will be divided in different zenith regions as reconstructed by the initial LineFit (LF) (see Section 4.3.1.1). After a base cut is applied according to the LineFit results which reduce the data before performing a more cpu time consuming reconstruction, the events are divided into different regions of the sky using the reconstructed zenith from a non-iterative log likelihood fit seeded with the LineFit results (see section 4.3.2.1), called Pole Muon LogLikeliHood Fit (PoleMuonllhFit). Different cuts in the reconstructed track quality of the PoleMuonllhFit and total charge are made in each region.

The list of the applied selection is given in Table 4.1, where a up-going muon is defined based on the PoleMuonllhFit zenith angle with $180° \geq \theta_{\text{Zenith}} \geq 78.5°$ and the opposite for an down-going, NChan is the number of lit DOMs, Q_{tot} the integrated charge and LogL the value of the minimised loglikelihood (see Section 4.3.2.1).

4.2.2 The Extremely High Energy Filter

The EHE Filter aims at collecting energetic events with as less bias as possible. To achieve this, a selection on the total number of detected photo-electrons (NPE) is

Table 4.1: Selections applied for the Muon Filter.

Base Cut	$\theta_{\text{Zenith, LF}} > 70° : \text{NChan} \geq 8$ $\theta_{\text{Zenith, LF}} \leq 70° : \text{NChan} \geq 10$
Up-going muon	$\text{Logl}/(\text{NChan - 3}) \leq 8.7$
Down-going muon	$\theta_{\text{Zenith, PoleMuonllhFit}} > 60° : \log_{10}(Q_{\text{tot}}) \geq (3.9 * \cos(\theta_{\text{Zenith}}) - 0.5) + 2.6$ $\theta_{\text{Zenith, PoleMuonllhFit}} \leq 60° : \log_{10}(Q_{\text{tot}}) \geq (0.6 * \cos(\theta_{\text{Zenith}}) - 0.5) + 2.6$

performed as follows:

$$\log_{10}(\text{NPE}) \geq 3. \tag{4.1}$$

4.2.3 The Cascade Filter

The cascade filter is designed to select cascade like events based on the shape and source speed of a distribution of light in the detector. Based on the SPE0 (see Section 4.3) zenith angle, the sky is divided in two regions and specific selections are then applied to these regions.

The applied selections are presented in Table 4.2, where v is the LineFit speed defined in Section 4.3.1.1, $\mathcal{L}_{\text{reduced}}$ the cascade reduced log-likelihood value (which is the final minimised loglikelihood divided by the number of degrees of freedom, which is approximately equal to the number of DOMs participating in the event) calculated using the "Pandel" PDF parameterisation (see Section 4.3.2.1) and I_R is the tensor of inertia eigenvalue ratio. An effective tensor of inertia is calculated based on the distribution of hits in the detector and given by the ratio of the smallest eigenvalue to the sum of the three eigenvalues:

$$I_R = \frac{I}{I_1 + I_2 + I_3} \tag{4.2}$$

Table 4.2: Selections applied for the Cascade Filter.

cos(zenith) < 0.20 ("up" region)	$\mathcal{L}_{\text{reduced}} < 11.75$
cos(zenith) ≥ 0.20 ("down" region)	$\mathcal{L}_{\text{reduced}} < 9.5$ $I_R > 0.1$ $v < 0.12\,\text{m/ns}$

4.2.4 The DeepCore Filter

The DeepCore filter tries to identify and reject down-going atmospheric muons by using the power of a 3 string layers thick veto area around the DeepCore fiducial volume.

The filter begins by selecting SMT3 events. The DeepCore fiducial volume is defined as followed (see Fig. 3.6):

- Bottom 22 DOMs on strings 25, 26, 27, 34, 35, 36, 37, 44, 45, 46, 47, 54 and 1
- Bottom 50 DOMs on strings 79-86

The remaining in-ice DOMs are part of the veto region. The DeepCore filter selects hits in the fiducial volume and calculates a centre of gravity (COG). Next, the filter assumes that hits in the veto region are due to direct photons from passing particles. Then the speed of a hypothetical particle traveling from an individual hit in the veto region to the COG is calculated. Should the calculated speed of a veto region hit be close to that of the speed of light, 0.25 to 0.4 m/ns, then that hit is tagged as a "VetoWindowHit". This speed calculation is done for all hits (after hit cleaning) in the defined IceCube veto region, and events that contain more than one "VetoWindowHit" are excluded. Events that have an empty veto region hit series pass the filter automatically.

4.3 Track reconstructions

We have previously explained how IceCube records the data and we have just described how the pulse series are constructed and cleaned but we still have to present how the IceCube software reconstructs the characteristics of the particles that have produced the various DOM signals. The parameters which will be chosen, e.g. the topology (cascade or track), the energy, the direction or the interaction point depend on the type of analysis that is performed. In this work, we only concentrate on the muon tracks left in the detector and not on other signatures since for our analysis we need a well defined track direction. In this context we describe below the relevant track reconstructions for our analysis and also the energy reconstruction.

4.3.1 First estimation algorithms

The likelihood reconstructions discussed in next section need an initial track hypothesis to start the minimisation. The initial track is derived from first guess methods, which are fast analytic algorithms that do not require an initial track.

4.3.1.1 LineFit

The first reconstruction performed is called LineFit [178]. It reconstructs the tracks based on an assumption that does not take into account the geometry of the Cherenkov cone: it assumes that the generated light wave travels along with the muon as a wavefront at a speed $\overrightarrow{v}$. This is unphysical but has the advantage of providing an analytical solution to the χ^2 minimisation of a plane wave hitting a series of DOMs. Moreover, because of its processing speed, LineFit can be run on all events that are recorded by the DAQ. LineFit is also of importance because it provides a seed track to be used by other more elaborate reconstruction c.q. fitting algorithms that require a

seed track.

Assuming that an event has a total number of N_{hits} hit signals with each hit DOM having position $\vec{r_i}$ and being hit at time t_i, we can write an equation for χ^2 as follows:

$$\chi^2 = \sum_{i=1}^{N_{\text{hits}}} (\vec{r_i} - \vec{r} - \vec{v}t_i)^2 \,, \tag{4.3}$$

where $\vec{r}$ is the reconstructed position of the muon and $\vec{v}$, the reconstructed velocity vector. The solution of the χ^2 minimisation is given by:

$$\vec{r} = \langle \vec{r_i} \rangle - \vec{v}\langle t_i \rangle \text{ and } \vec{v} = \frac{\langle t_i \vec{r_i} \rangle - \langle \vec{r_i} \rangle \langle t_i \rangle}{\langle t_i^2 \rangle - \langle t_i \rangle^2} \tag{4.4}$$

As the particles are supposed to travel through the ice almost at light speed, the LineFit speed v is used as quality parameter of the reconstruction.

4.3.1.2 IceDWalk

A detailed presentation of the original version of the Direct walk algorithm can be found in [178]. It is a pattern recognition algorithm based on selected hits, which were most likely caused by direct photons. An updated version[1] has recently been developed using more physics driven observables and criteria. The procedure is composed of 7 steps:

1. Construction of Track Elements (TE), a straight line connecting two HLC hits.
2. Association of the selected hits to the TE, based on the time residuals.
3. Construction of Track Candidates (TC) which are TEs which fulfil certain quality criteria concerning the associated hits.
4. Clustering of TC into jets when their directions are within a certain maximum angular distance.
5. Merging of the jets when their directions are within a certain maximum angular distance.
6. Quality ordering of the merged jets to provide one or more final candidate.
7. Quality selection of the merged jets to provide finally one or more constructed tracks.

The different types of DOMs (standard IceCube, DeepCore, and InIce, respectively referred as IC, DC and I) are treated separately in IceDWalk, which means that for events with various DOMs firing, direct walk tracks of different reconstructions quality may be produced.

[1] See http://www.iihe.ac.be/ ice3/ncfsdoc/IceDwalk.html

The procedure starts by selecting the straight line between any two hit HLC DOMs at distance d, which are hit with a time difference :

$$|\Delta t| < \frac{d}{c_{\text{vac}}} + 30\,\text{ns}, \text{ with } d > 50\,\text{m}. \tag{4.5}$$

The known positions of the DOMs define the track element direction (θ, ϕ). The vertex position (x, y, z) is taken at the center between the two DOMs and the time at the vertex t_0 is defined as the average of the two hit times. The next step is dedicated to the counting of the *associated hits*. Let us define the time residual as the difference between the observed time when the DOM was hit by a photon t_{obs} and by the geometry expected arrival time t_{geo}, given by:

$$t_{\text{res}} \equiv t_{\text{obs}} - t_{\text{geo}}, \tag{4.6}$$

where t_{geo} is the hit time expected for a "direct photon", a Cherenkov photon that travels undelayed directly from the muon to a DOM without scattering and is given by (see Fig. 4.3):

$$t_{\text{geo}} = t_0 + \frac{\hat{p} \cdot (\overrightarrow{r_i} - \overrightarrow{r_0}) + d\,\tan(\theta_c)}{c}. \tag{4.7}$$

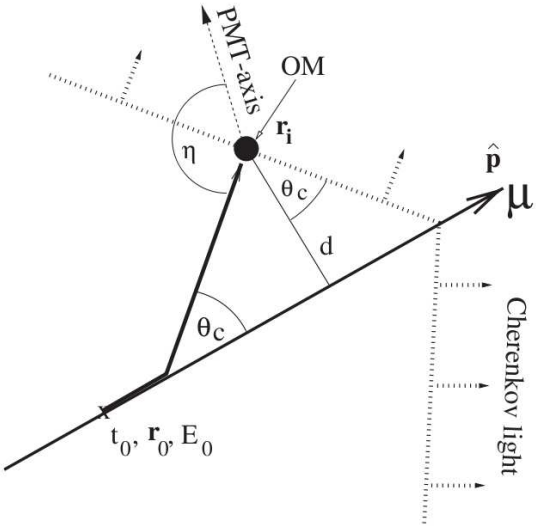

Figure 4.3: Sketch showing the the Cherenkov cone and the definition of the variables used in the reconstructions. From [178].

A hit is then considered as associated to a track element if it fulfils the following two conditions:

$$t_{\text{min}} < t_{\text{res}} < t_{\text{max}} \qquad \text{and} \qquad \frac{d_{\text{hit}}}{\lambda_{\text{scat}}} < F, \tag{4.8}$$

where the time difference intervals are specific for each DOM type, λ is the effective scattering length for various detector locations (above, in or under the dust layer), F

is again DOM type specific and d_{hit} is the distance traveled by the Cherenkov photon from the track to the hit position.

These TE become then a TC if they pass the following two conditions:

$$n_{\text{ax}} > 0 \qquad \text{and} \qquad Q_{\text{TC}} \geq 0.8\, Q_{\text{max}}, \tag{4.9}$$

with n_{ax} is given by $n_{\text{ax}} = n_{\text{am}} + n_{\text{ah}} + n_{\text{ahlc}}/n_{\text{ah}} + 2 \cdot (n_{\text{as}} - 1)/n_{\text{as}}$ and where n_{am}, n_{ah}, n_{ahlc}, n_{as} refer respectively to the number of associated modules, hits, HLC hits and strings. The definition of the track quality factor, Q_{TC} is given by:

$$\begin{aligned} Q_{\text{TC}} \equiv & 2 \cdot n_{\text{ax}} \left(\frac{\text{sp}(x)}{\max(x) - \min(x)} + \frac{\text{sp}(|x|)}{\max(|x|) - \min(|x|)} \right) \\ & - \left(\frac{\text{sp}(x) - \text{sp}^{\text{exp}}(x)}{\text{sp}(x)} + \frac{\text{sp}(|x|) - \text{sp}^{\text{exp}}(|x|)}{\text{sp}(|x|)} + \frac{|\text{median}(\delta t)|}{\text{sp}(\delta t)} \right), \end{aligned} \tag{4.10}$$

where, x is the projected hit position on the track with respect to the track reference point r_0 of Eq. 4.7, $\text{sp}(x) = \langle |x - \text{median}(x)| \rangle$ is the spread of the associated hit positions and $\text{sp}^{\text{exp}}(x)$ is the expected spread of the hits given a uniform hit distribution along the track between the maximum and minimum x values. The first two fractions are the contribution to the track quality of the spread of the hit pattern compared to the maximum spread one can reach based on the most distinct hits. Deviations of the spread from a uniform hit distribution along the track are subtracted. The Q_{TC} is then used to define the norm of the momentum of the TC as such serves as a weight for the jet momentum after clustering of the TC's and later on merging of the jets (see hereafter).

The track candidates passing the above condition are then clustered into jets when their directions are within a cone of 15°. In addition a TC must be within 20 m distance of the jet starting TC in order to get clustered. The latter criterion prevents clustering of (nearly) parallel track candidates crossing the detector at very different locations (e.g. muon bundles). The average of all the position r_0 and time t_0 values of the constituent TCs of the jet will provide the position and the time (*i.e.* reference point) of the jet. The jet total momentum consists of the vector sum of the momenta of the constituent TCs. This implies that the Q_{TC} quality numbers of the various TCs define a weight for each track in the construction of the jet direction. In addition it means that the total jet momentum represents the sum of the Q_{TC} of the constituent TCs weighted by the opening angles between the various TCs. As such, each jet is given an absolute quality indicator defined as:

$$\langle Q_{\text{TC}} \rangle = \frac{|p_{\text{jet}}|}{N_{\text{TC}}}, \tag{4.11}$$

where N_{TC} indicates the number of TCs in the jet. This jet quality indicator is further refined using also the number of hits and DOMs associated to the jet as:

$$Q_{\text{jet}} = \frac{\langle Q_{\text{TC}} \rangle}{Q_{\text{max}}} + \frac{N_{\text{DOMs}}}{N_{\text{DOMs}}^{\text{max}}} + \frac{N_{\text{hits}}}{N_{\text{hits}}^{\text{max}}} + \frac{N_{\text{HLC hits}}}{N_{\text{HLC hits}}^{\text{max}}}, \tag{4.12}$$

where we have defined:

- N_{DOMs}: Number of associated DOMs for the specific jet.
- $N_{\text{DOMs}}^{\text{max}}$: Maximum number of associated DOMs encountered for the jets.
- N_{hits}: Number of associated hits for the specific jet.
- $N_{\text{hits}}^{\text{max}}$: Maximum number of associated hits encountered for the jets.
- $N_{\text{HLC hits}}$: Number of associated HLC hits for the specific jet.
- $N_{\text{HLC hits}}^{\text{max}}$: Maximum number of associated HLC hits encountered for the jets.

With this definition the Q_{jet} always lies in the range $[0, 4]$ which provides an absolute quality scale. The jet Q_{jet} is then used to order the various jets with respect to decreasing Q_{jet} quality number.

In case jets are within 30 m and their opening angle is within 7.5°, jets themselves will be merged. A new quality is calculated and the order is adjusted. This process will be repeat until no more jets are merged. The remaining jets are given as the final reconstructed tracks.

4.3.1.3 IceLinefit4Dwalk

The Linefit processor can also be applied to only the hits associated to a track from a previous (in our case, IceDwalk as first guess) reconstruction. This so called "track based reconstruction" allows to obtain rather accurate results without the need of a hit cleaning procedure. In this "track based reconstruction" mode all the hits associated to the input track will be used. As the DOMs are treated separately in the IceDWalk algorithm, this leads automatically to three different types of IceLinefit4Dwalk reconstructions.

In the following of this thesis, when we will use the abbreviation DWI, DWIC or DWDC, we refer to one of these IceLinefit4Dwalk reconstructions.

4.3.2 Maximum likelihood reconstructions

The muon track reconstruction workhorse is the maximum likelihood reconstruction method. The reconstruction of IceCube events can be generalised as follows: a set of unknown parameters $\overrightarrow{a}$ has to be determined using some experimental data $\overrightarrow{x}$. The unknown parameters are determined by maximising the likelihood with respect to the measured parameters. The likelihood function is defined as follows:

$$\mathcal{L}(\overrightarrow{a}\,|\,\overrightarrow{x}) = \prod_i p(x_i|\overrightarrow{a}), \tag{4.13}$$

where $p(x_i|\overrightarrow{a})$ is the probability density function (PDF) of observing the set of measured values x_i for a given set of parameters $\overrightarrow{a}$.

To define the PDF we will describe the Cherenkov light created by a muon that forms a cone as seen in Fig. 4.3 with the following observables:

$$\overrightarrow{a} = (\overrightarrow{r_0}, t_0, \widehat{p}, E_0), \tag{4.14}$$

where r_0 is an arbitrary point along the track at time t_0, E_0 is the energy of the muon and $\widehat{p}$ is the direction of the muon at that time.

The most likely muon trajectory with parameters $\overrightarrow{a}$ is found by minimising the negative natural logarithm of the likelihood.

4.3.2.1 Single PhotoElectron Fit (SPE)

The SPE fit (for complete information, please refer to [178]) is based on the residual time, defined in Eq. 4.6. This leads to the following likelihood function constructed from the PDF for arrival times of single photons i at the locations of the hit DOMs p_1 for the SPE fit:

$$\mathcal{L}(\overrightarrow{a}|t_{\text{res},i}) = \prod_i p_1(t_{\text{res},i}|\overrightarrow{a} = d_i, \eta_i, ...), \tag{4.15}$$

Note that one DOM may contribute to this product with several hits. The function $p_1(t_{\text{res},i}|\overrightarrow{a})$ is obtained from the simulation of photon propagation through ice (see below).

The PDF, $p_1(t_{\text{res},i}|\overrightarrow{a})$, is given by the Pandel Function [179, 180]. It is a modified form of the gamma distribution and its usage is motivated by an analysis of laser light signals in the BAIKAL experiment [179]. There, it was found that for the case of an isotropic, monochromatic and point-like light source traveling into a dense medium, the time arrival PDF $p_1(t_{\text{res},i})$ is given as following:

$$p_1(t_{\text{res}}) \equiv \frac{1}{N(d_{\text{eff}})} \frac{t_{\text{res}}^{d_{\text{eff}}/\lambda - 1}}{\Gamma(d_{\text{eff}}/\lambda)} \times \exp\left[-t_{\text{res}}\left(\frac{1}{\tau} + \frac{c_{\text{medium}}}{\lambda_a}\right)\right], \tag{4.16}$$

with

$$N(d_{\text{eff}}) = \left(\frac{1}{\tau} + \frac{c_{\text{medium}}}{\lambda_a}\right)^{-d_{\text{eff}}/\lambda}. \tag{4.17}$$

For our work, d_{eff} is an empirical effective impact parameter that accounts for the relative effect of scattering depending the angle η between the unscattered light path and the PMT axis given by

$$d_{\text{eff}} = a_0 + a_1 d, \tag{4.18}$$

$$a_0 = 3.1 - 3.9\cos\eta + 4.6\cos^2\eta \tag{4.19}$$

$$a_1 = 0.84 \tag{4.20}$$

and c_{medium} is the speed of light in the ice, λ_a is the absorption length in the ice, $\Gamma(d_{\text{eff}}/\lambda)$ the gamma function while $N(d_{\text{eff}})$ is the normalisation factor. This formulation has free parameters λ and τ; which are unspecified functions of the distance d and the other geometrical parameters. They are empirically determined by a Monte Carlo model. Fig. 4.4 shows examples of the Pandel function.

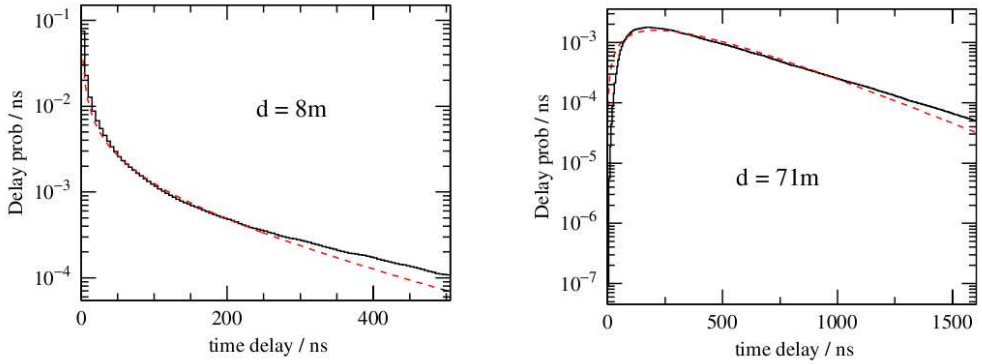

(a) (b)

Figure 4.4: Comparison of the parametrized Pandel function(dashed curves) with the detailed simulation (black histograms) at two distances d from the muon track. From [178].

As explained in [178], the Pandel function is the basis of a simple normalised likelihood but it has several deficiencies that need to be considered. First of all it is not defined for values of $t_{\text{res}} < 0$ which can arise from jitter in the PMT timing. It also has a pole at $t_{\text{res}} = 0$ both of which cause numerical difficulties. Other non-computational problems with the Pandel function also exist: it does not take into account the DOM orientation relative to the light source, nor does it take into account PMT jitter. The solution to these deficiencies is obtained by patching the Pandel function in several ways. First of all, to take into account the PMT orientation, the distance to the track d is taken to be an effective distance $d_{\text{eff}}(\eta)$, which takes into account that light is more scattered the more the PMT is facing away from the track. The PMT jitter is taken into account by convoluting the Pandel function with a Gaussian function with a width corresponding to all timing uncertainties. The interested reader can find all the detailed information in [180]. In this way, the pole at $t_{\text{res}} = 0$ is removed and negative values of t_{res} are allowed as well. Noise hits are always present in IceCube and need to be treated in the Pandel function. This is done by adding a small constant offset that corresponds to the average of all noise hits as determined through simulation.

With these ingredients, we can go back to our likelihood function, Eq. (4.15) and maximise it to find the best values of the unknown parameters. This is actually done by minimising the $-\log\left(\mathcal{L}(\overrightarrow{a}|t_{\text{res},i})\right)$. It uses LineFit as a seed track to begin the re-

construction. Track parameters are then varied until the minimum of $-\log\left(\mathcal{L}(\overrightarrow{a}|t_{\mathrm{res},i})\right)$ is reached. Advanced reconstruction techniques subsequently use the result of the first minimisation to seed the next one, which continues until a pre-set maximum of iterations is reached.

SPE Fit does not only give the reconstruction of the track but gives also quality parameters associated to the reconstruction. One of them, often used and actually used in this thesis is the *Reduced log-likelihood parameter* (Rlogl). It is the final minimised log-likelihood divided by the number of degrees of freedom, which is approximately equal to the number of DOMs participating in the event.

4.3.2.2 Multiple PhotoElectron Fit (MPE)

The SPE only considers the arrival time of the first photoelectron and ignores the subsequent others. Obviously, at high energies, DOMs will see many more than one photoelectron and hence the result could be improved if all the photoelectrons were taken into account. This is done in the MPE fit, using the pdf of the arrival time distribution of the first of N photons given by:

$$p_{\mathrm{MPE}}(t_{\mathrm{res}}) = N p_1(t_{\mathrm{res}}) \left(\int_{t_{\mathrm{res}}}^{\infty} p_1(t)\,\mathrm{d}t \right)^{N-1} \tag{4.21}$$

This is a more precise PDF and can yield better results than the SPE PDF presented above. Nevertheless, one of the issues is that the PDF function is more complex and can have more than one local minimum. Obviously, the minimisation is also more time consuming and hence running many iterations for this reconstruction is cpu time limited. Further details can be found in [178].

4.3.2.3 MuEx for MPE Fit

For a precise angular reconstruction, we use in this thesis the so-called "MuEx4MPEFit". It uses a Pandel-based log-likelihood reconstruction algorithm. At each iteration of the algorithm, only a random subsample of the pulses are used. They are resampled at each iteration (and there is also one final iteration that uses the average of all iterations, refined on the full initial pulse series). This leads, as presented in Chapter 5, to very good angular resolution.

4.3.3 Bayesian reconstructions

Additional to all previous reconstructions, this thesis also uses two other algorithms that are powerful in the background rejection process. The first one is a so-called "bayesian fit". As most of the detected signal events are actually down-going background muons ($\sim$ 75 Hz versus only $\sim$ 3-5 mHz of Northern hemisphere atmospheric neutrinos), bayesian fits allow to a *prior statement* that any given event is very likely to be down-going. This is achieved through a bayesian bias introduced in the likelihood, *i.e.* a zenith

dependent prior given by:

$$p(\theta) = A_0(\cos\theta)^{A_1} \exp\left(-\frac{A_2}{\cos\theta}\right), \tag{4.22}$$

where the numerical parameters are assigned the following values: $A_0 = 2.39655 \times 10^{-7}$, $A_1 = 1.67721$ and $A_2 = 0.778393$, which were derived from the observed distribution of down-going muons and $p(\theta) = 0$ in the Northern hemisphere.

In case of previously well-reconstructed up-going events, the bayesian fit, which "forces" a down-going behaviour, leads to a much smaller log-likelihood than the unbiased upgoing reconstruction. On the other hand, a similar log-likelihood value is assigned to a unbiased poorly-reconstructed track. This explains that the bayesian fit has a good separation power between down-going muons and up-going neutrinos.

4.3.4 Split reconstructions

Finally the last type of reconstruction that is used in this thesis, which is also useful for background rejection, is based on splitting the observed hits into two groups and repeat then the reconstruction. This procedure is aimed at identifying coincident events in the detector, which may yield incorrect reconstruction. In this analysis, we are using two types of splitting. First, the hits are divided in time where the hits are divided based on the per-DOM time into early and late hits. The other option is to split the hits based on basis of the geometrical pattern. In that case, hits are divided by a plane drawn through the centre of gravity of all hits and normal to the MPE result. After this separation, LineFit or SPE Fit are applied for each sub set of hits.

4.3.5 Angular error estimator

In this thesis, we use the so-called "Cramer-Rao" angular error estimator. It gives a lower bound on the true resolution based on the behaviour of the per-DOM PDFs near the final fit result. Specifically, it relates the covariance of each track parameter to the inverted Fisher information matrix:

$$\mathrm{cov}(\mu_m, \mu_k) \geq I_{mk}(\overrightarrow{\mu})^{-1}, \tag{4.23}$$

where $\overrightarrow{\mu}$ represents the five independent track parameters: x, y and z of the vertex position and θ and ϕ of the reconstructed direction. The Fisher information matrix is given:

$$I_{mk}(\overrightarrow{\mu}) = -\left\langle \left[\sum_i \frac{\partial^2}{\partial\mu_k \partial\mu_m}\right] \ln p(\Delta t_i|\overrightarrow{\mu}) \right\rangle, \tag{4.24}$$

where the i represents each hit DOM, $(\Delta t_i|\overrightarrow{\mu})$ is the Pandel-based MPE PDF and the angle brackets indicate an average over possible values of Δt_i, weighted by $p(\Delta t_i|\overrightarrow{\mu})$. In the follow, we make use of Cramer-Rao variance:

$$\sigma_\theta^{\mathrm{CR}} = \sqrt{(I_{\theta\theta})^{-1}}. \tag{4.25}$$

4.3.6 Energy reconstruction

Even though we are not explicitly using the energy of the particles in our analysis, it is an important variable for which it is valuable to briefly describe the method of reconstruction. First of all, it is important to have in mind that it is impossible to calculate precisely the energy incoming neutrino based on the observed muon track because location and kinematics of the interaction vertex is unknown. Moreover, as we described before, we know that the muon can travel several km through the ice and therefore lose an unknown fraction of its energy. However, we can determine the energy lost by the muon inside the detector, providing a lower bound estimation of the neutrino energy.

The energy reconstruction that is classically used in IceCube is called MuE [181]. As illustrated in Fig. 3.11, above $\sim$ 1 TeV, the muon energy loss is directly proportional to the energy of the muon. The reconstruction is based on an empirically determined parametrisation of the photon density along the reconstructed track. This estimation enters then the Pandel function and a maximisation of the likelihood is applied, taking the energy as an independent variable.

4.4 Simulations

In performing our analysis we will make use of simulated signals. These simulations are important to understand and to predict how IceCube responds to neutrinos. They obviously have to take into account the high-energy particle physics processes but also the ice properties and the IceCube hardware.

The first step in the simulation process is to generate a primary particle. Monte Carlo simulation techniques are used to properly account for the directions, locations and energy spectrum of the primaries. Three kinds of signals have to be simulated: the muon atmospheric background created by cosmic rays, performed by the so-called CORSIKA simulation, and the neutrino induced muons, meaning the actually desired signal and the neutrino background events, generated by the "neutrino-generator" (NuGen) simulation. In our analysis, we have decided to directly use real data (without observed GRB) to account for the muon atmospheric background and the only simulation used is NuGen to determine our detection efficiency of cosmic neutrinos like the ones from the GRB's. Nevertheless we will be using CORSIKA simulations in the next sections to control the various steps of our analysis and to detect any possible problem by observing discrepancies between real data and CORSIKA. Because the muon background and the atmospheric or signal neutrinos are simulated in the same way, ensuring that CORSIKA agrees with real data provides a good check of our understanding of the detector and of our simulations.

4.4.1 Neutrino simulation

NuGen simulates the neutrino interactions in the Earth and in and around the detector volume. It is based on code from ANIS [182]. The simulation starts with sampling uniformly with a power-law energy spectrum the neutrinos on the surface of the Earth. It then propagates them through the Earth, taking the interactions of the neutrinos into account. The neutrino-nucleon interactions are calculated on the basis of the cross-sections given in Fig. 3.2, calculated with CTEQ5 [183]. The structure of the Earth is taken from the Preliminary Reference Earth Model [184]. NuGen then randomly places a neutrino interaction vertex in or near the detector and calculates the probability of its interaction occurring based on the cross section and the Earth models.

With this probability (in function of the energy), the interaction products are then determined following deep inelastic scattering of Standard Model particles. Muons are created which will produce extended tracks that have to be propagated through the ice and in the detector. This part is discussed in the next section.

As this probability of interaction is an important part, we will discuss it now in more detail. The neutrino generator provides a very convenient way of taking into account all the previously described effects. The effects of cross section parameters, of the Earth modelling, of the randomised parameters of the simulation are all incorporated in a quantity called OneWeight with units $\mathrm{GeV\,cm^2\,sr}$. The simulated solid angle comprises the full sky and is therefore simulated to 4π. For any diffuse neutrino spectrum $\mathrm{d}\Phi/\mathrm{d}E\mathrm{d}\Omega$ and total number of generated events n_{gen}, each neutrino event i has a weight defined by:

$$w_i = \frac{\mathrm{OneWeight}_i}{n_{\mathrm{gen}}} \times \left.\frac{\mathrm{d}\Phi}{\mathrm{d}E\mathrm{d}\Omega}\right|_{E_i}, \tag{4.26}$$

where the weight w_i has units $\mathrm{s^{-1}}$. The sum of these weights $\sum_i w_i$ for any specific dataset gives the rate of neutrino events in Hz and the statistical error on that value is given by $(\sum_i w_i)^{1/2}$.

This expression as suited for diffuse fluxes from unresolved sources which is obviously not our situation since we are studying point source objects with given differential fluences $\mathrm{d}F/\mathrm{d}E$ $[\mathrm{GeV^{-1}\,cm^{-2}}]$. We use standard diffuse datasets to mimic pseudo-point source datasets by selecting, for each GRB, neutrino events in a zenith band of 1° around the error-integrated zenith position of the GRB, leading to a solid angle of Ω^{GRB}. Each GRB location is known with a certain angular 1σ error. To account for of this error, we first displace the GRB within the error area via a Kent distribution and then record the displaced azimuth and zenith coordinates. The Kent distribution is similar to a Gaussian distribution, but its domain is a sphere rather than an infinite plane. The event weights are then given by the following modified expression:

$$w_i = \frac{\mathrm{OneWeight}_i}{n_{\mathrm{gen}}} \times \frac{1}{\Omega_c^{\mathrm{GRB}}} \times \left.\frac{\mathrm{d}F}{\mathrm{d}E}\right|_{E_i}, \tag{4.27}$$

where Ω_c^{GRB} is the corrected zenith band opening angle, which is reduced for GRBs close enough to the horizon and where simulated events are only available for a part of the zenith band. In this case, $\sum_i w_i$ leads to the number of observed neutrinos and the statistical error is again given by $(\sum_i w_i)^{1/2}$.

As we discuss lateron, in our analysis we use two possible signal spectra to be incorporated in Eq. 4.27: a generic E^{-2} and a Waxman-Bahcall spectrum. For the muon induced atmospheric neutrinos, Eq. 4.26 is used with $\mathrm{d}\Phi/\mathrm{d}E\mathrm{d}\Omega$ given by the Honda 2006 model [185].

4.4.2 Propagation and detection simulation

As mentioned before, the CC produced muon has to be propagated through the ice. This is performed by the Muon Monte Carlo (MMC) package [173]. It assumes a baseline continuous energy loss and randomly adds stochastic energy losses based on the probabilities for the various processes to occur. As we already explained, the muon will radiate its energy as Cherenkov radiation. As shown in Fig. 3.4, the South Pole ice does not have uniform optical properties and consequently the propagation of the photons in the ice is based on non-analytical models. The propagation is simulated by a program called photonics [186] which utilises tables that describe the probability of a photon to propagate to a DOM. Discrete photon hits incident on the PMT of the DOMs are calculated from these tables and additional pulses (like e.g. noise and afterpulses) are also simulated.

The simulation then accounts for the conversion of these hits to an analog current which is propagated through the DOM's front end and electronics simulation to a voltage as measured by the DOMs. The digitisation is then simulated, as well as the DOM's triggering logic. The conditions of local coincidence are respected and the signal is then combined and evaluated by software that simulates the DAQ response. This simulated signal is then stored in the same format as real data offering the opportunity to process and to reconstruct the simulation with the same software tools as the real data.

Part III

Data Analysis

CHAPTER 5

Neutrino Selection

In the previous chapters, we have discussed the theoretical background of our research and described the hardware and software tools we will be using to analyse the data. However, we still have to address the difficult question of how we plan to detect the neutrinos from GRBs. To achieve this, we have developed a two-step approach: first a number of selections on the data are applied to remove background and identify neutrino candidate events and second a statistical tool is developed for extracting among these events, the neutrinos originating from GRBs. This Chapter focuses on the first step: the selection of the neutrino candidate events.

Our analysis aims to detect neutrinos from GRB events occurring in the Northern hemisphere. We therefore limit our search to the zenith region $> 90°$ (corresponding to declination $> 0°$). Note however that no straight zenith cut is applied on the data because misreconstruction of the track direction is possible. The choice of performing a northern sky analysis is motivated by the fact that in this zenith region band the background atmospheric muons (produced by cosmic rays interacting in the upper atmosphere) are blocked by the Earth on their way to the South Pole. The Earth is used as a shield against muons, while neutrinos (of energies $\lesssim 1\,\mathrm{PeV}$) may reach the South Pole ice without any attenuation and produce muons that travel through the detector. Restricting ourselves to this part of the sky has thus the advantage that we can be confident that any well-reconstructed event pointing back to this region is in fact a neutrino event. Nevertheless, this does not mean that the neutrino is from extraterrestrial origin: the atmospheric neutrinos represent an irreducible background for this analysis.

The trigger and filter selection, as described in Chapter 4 already reduced our data to $\sim 76\,\mathrm{Hz}$ but most of these events are still well-reconstructed down-going events. These are easily identified by their reconstructed direction. We are then left with the muons that are badly reconstructed as upgoing tracks. A series of

different cuts are performed on these events to achieve neutrino level at $\sim 4 - 5\,\mathrm{mHz}$. The most common causes of misreconstructed events are of two types: (1) muons passing just outside the detector and emitting light inwards, and (2) coincident muons from separate cosmic ray showers passing through the detector at roughly the same time.

The first section of this Chapter is devoted to a presentation of the event parameters used in this analysis to distinguish between well-reconstructed and misreconstructed events. We also describe the initial cuts which reduce the data to $\mathcal{O}(1\,\mathrm{Hz})$ by removing part of the badly reconstructed events. Finally, we will discuss the use of boosted decision tree forests, a machine learning technique that allow us to achieve a high-purity final sample consisting almost exclusively of atmospheric (and possibly astrophysical) neutrinos.

∴

5.1 Event quality and topology measures

In this section, we discuss event parameters which are used in this thesis to distinguish well-reconstructed from misreconstructed events. These selection parameters are divided into three generic categories: fit quality parameters, fit stability parameters and event topology parameters. We also use the obvious zenith distribution of the events. All the plots presented in this section describe parameter distributions consisting of IC86 data and simulation events remaining after applying the data-reduction cuts for one of the proposed pre-cuts, the "MaxFrac" pre-cut (see Section 5.2). Each plot includes simulated atmospheric neutrinos, "Honda2006" (see Section 4.4), simulated cosmic ray induced muons, "CORSIKA" (see Section 4.4), the sum of these simulated atmospheric backgrounds, "Total MC", and off-time data taken when no GRB was taking place "Experimental data". The background events are normalised to Hz per bin and plotted against the vertical axis. The off-time data sample is the referred to as *burn sample* and will not be used when the data is unblinded. The burn sample consists of off-time data used as background estimation composed of 48 data samples of 2 consecutive hours during 4 years (from May 13th, 2011 to May 18th, 2015) of real data without a known GRB. Each data sample corresponds to each month of the considered period, to account for the seasonal variations in the cosmic ray intensity. A proposed high-energy neutrino signal (E^{-2}) is shown with arbitrary normalisation to give an impression of possible cuts for signal selection.

Even though the agreement is good between the experimental testing data and the simulated backgrounds, some discriprencacies remain because the simulation does not reproduce all the tiny details of real data (noise, ice properties, *etc*). Nevertheless, there is a general agreement between these distributions which gives us confidence that our simulations are sufficiently realistic to justify tuning the analysis to accept events similar

to well-reconstructed simulated neutrinos while rejecting backgrounds characterised by the high-statistics off-time dataset.

5.1.1 Fit quality parameters

As discussed in Section 4.3, different reconstructions are performed on the data. Each of these reconstructions do not only provide a best fit track, they also give some information about how well the resulting direction hypothesis fits the observed light arrival pattern in the detector, *i.e.* they give a *quality parameter* of the reconstruction.

The charged leptons travelling the ice detected by IceCube are mostly relativistic particles. The SPE and MPE Fit algorithm assume this in reconstructing the arrival direction of the particle but the other reconstructions (LineFit, IceLineFit and the IceLineFit for DWalk family) provide an estimation of the velocity of the particle. Therefore well-reconstructed events tend to have a velocity near the speed of light, while misreconstructed events tend to have a lower velocity. The LineFit velocity is given in Fig. 5.1, while an example for the DWalk family is given in Fig. 5.2.

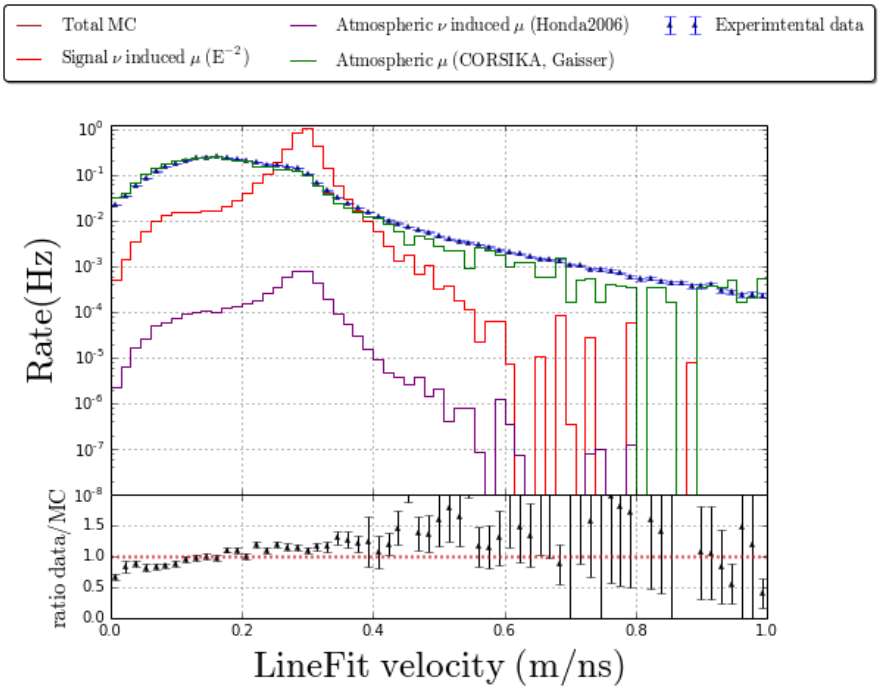

Figure 5.1: LineFit velocity distribution after MaxFrac pre-cut.

The maximum likelihood reconstructions (SPEFit and MPEFit) return the parameter logl, the negative of the log-likelihood of the fit. Although this parameter can not be used as a goodness estimator of a fit [187], it is can be used in this analysis as a measure of the

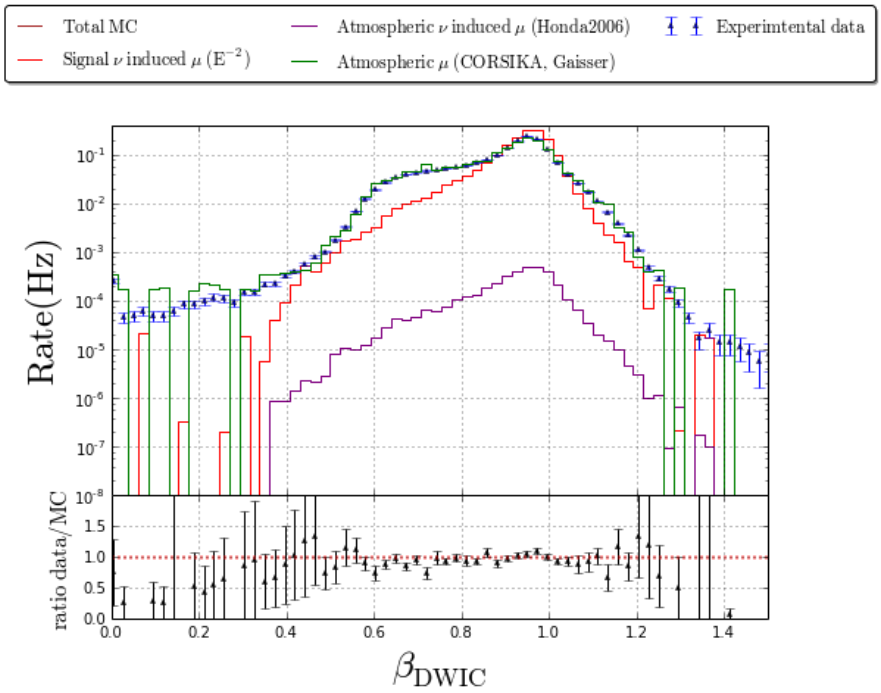

Figure 5.2: DWIC $\beta = \frac{v}{c}$ distribution after MaxFrac pre-cut.

fit quality. However, the parameter is normalised differently depending on the number of DOMs included in the fit. Therefore, we use a reduced log-likelihood parameter given by:

$$\text{rlogl} = \frac{\text{logl}}{N_{\text{dof}}} = \frac{\text{logl}}{N_{\text{ch}} - 5} \tag{5.1}$$

where N_{ch} is the number of DOMs, or channels, included in the fit, and $N_{\text{dof}} = N_{\text{ch}} - 5$ is the number of degrees of freedom in the fit. The distributions of this parameter for both the SPEFit and the MPEFit are given in Fig. 5.3 and 5.4.

In the case of MuEx4MPE (see Section 4.3.2.3), the quality parameter, σ_{MuEx4MPE}, is characterised by the spread of the various iterations of MuEx4MPE (based on HiveSplit cleaned pulses). It therefore also represents a quality parameter of the fit, smaller values indicating a more stable fit. Its distribution is given in Fig. 5.5.

Finally, as described in Section 4.3.5, we also use an angular error estimator on the zenith of the reconstruction, given by the Cramer-Rao variance on θ, calculated on the MPEFit. Again a small value of the Cramer-Rao variance indicates a smaller angular error estimation and thus a better quality of the fit . This distribution is shown in Fig. 5.6.

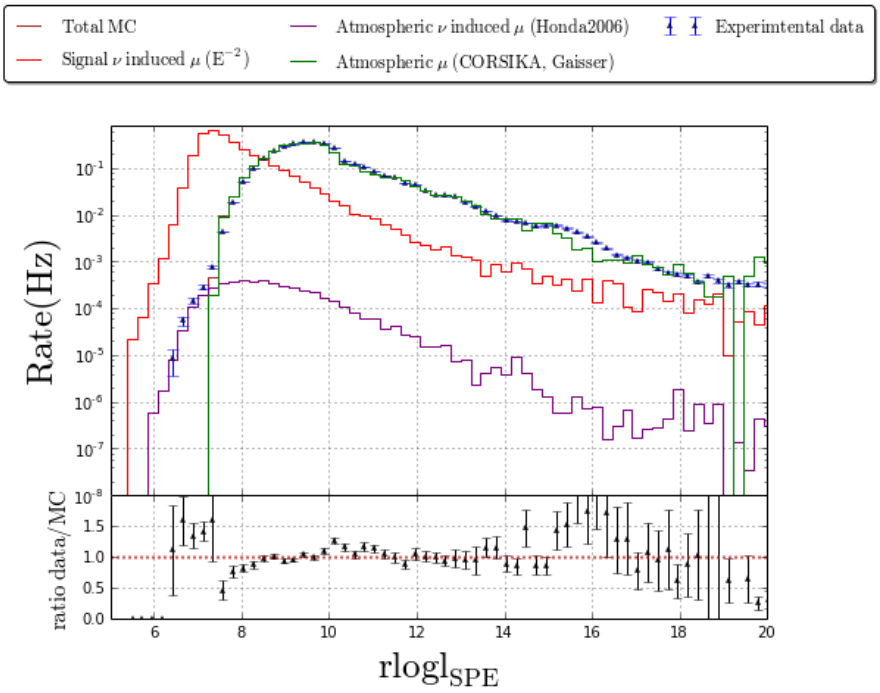

Figure 5.3: SPEFit rlogl distribution after MaxFrac pre-cut.

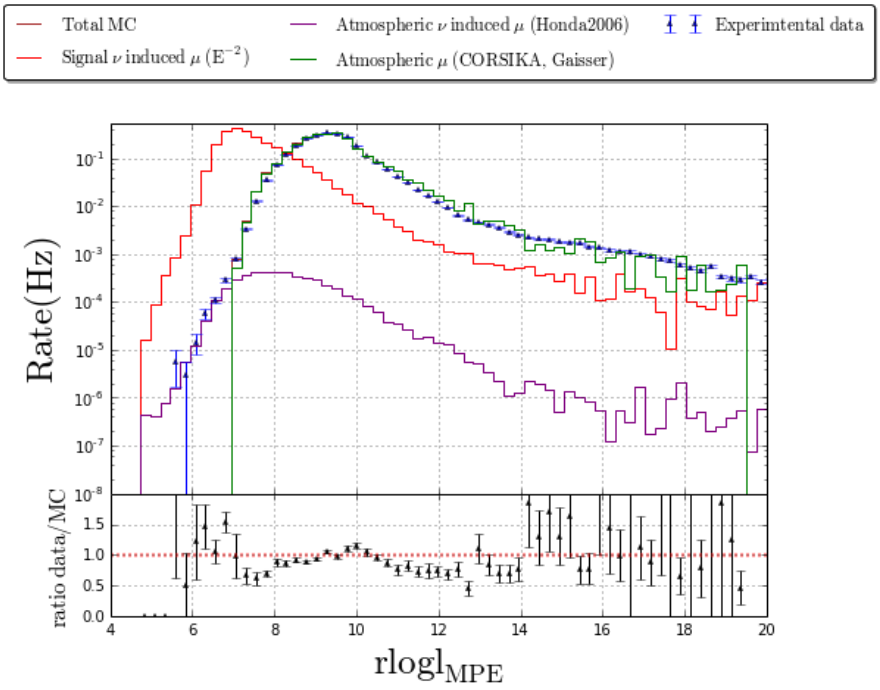

Figure 5.4: MPEFit rlogl distribution after MaxFrac pre-cut.

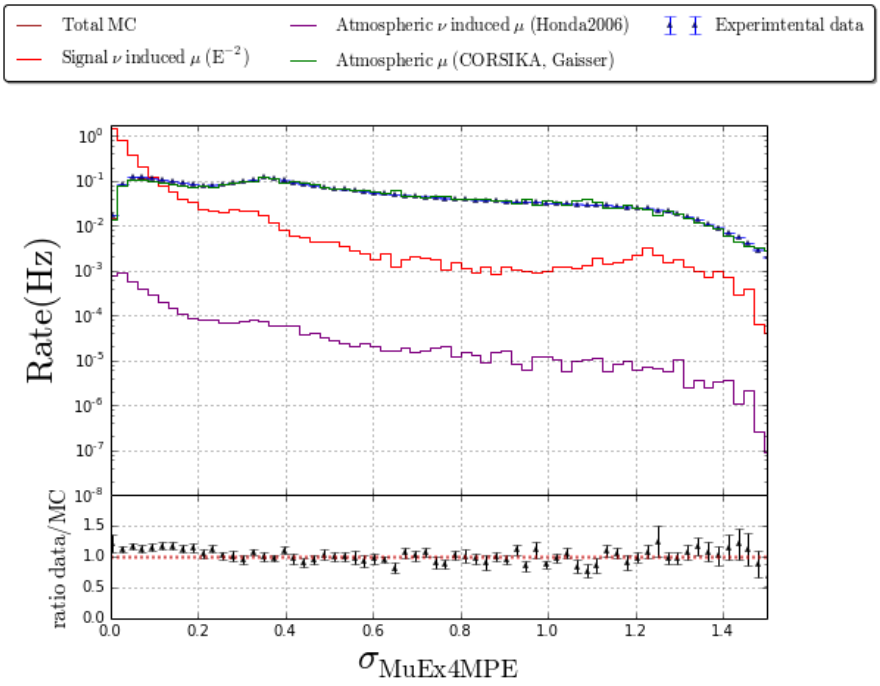

Figure 5.5: Spread estimator of the various MuEx4MPE fit, $\sigma_{\mathrm{MuEx4MPE}}$, distribution after MaxFrac pre-cut.

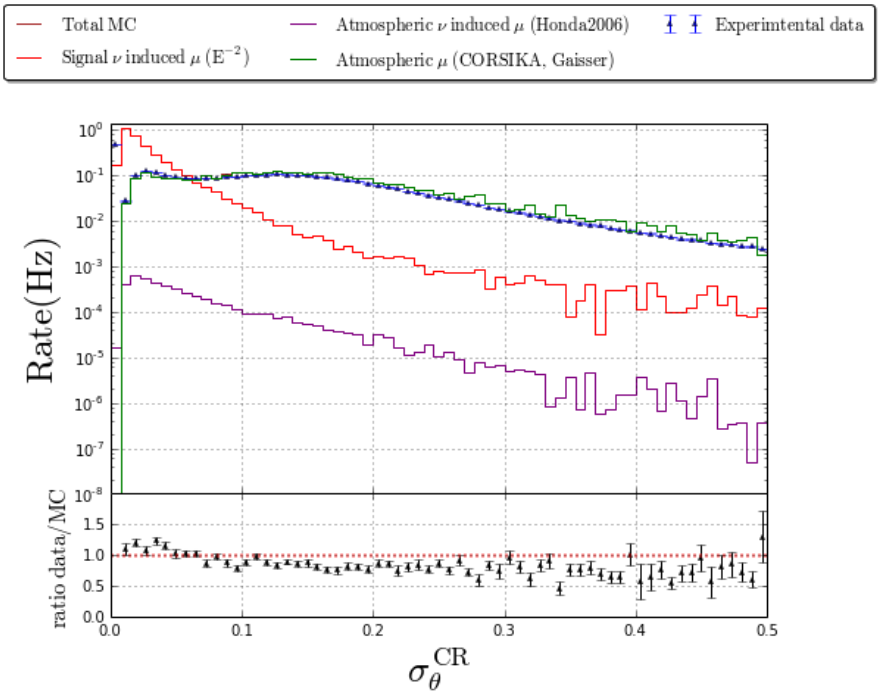

Figure 5.6: Cramer-Rao variance on θ, $\sigma_{\theta}^{\mathrm{CR}}$, distribution after MaxFrac pre-cut.

5.1.2 Zenith distribution

As discussed in the introduction of this Chapter, the zenith distribution of the events is an obvious way of separating neutrino signals and background muons. Remember however that we have decided to not apply a straight cut on this variable because of misconstruction of tracks but that we will use it as input variable of a Boosted Decision Tree procedure (see Section 5.3.2). In this analysis, we have found that the so-called MuEx4MPE reconstruction (see Section 4.3) based on HiveSplit cleaned pulses (see Section 4.1.2) was the most efficient reconstruction for separating the data based on the zenith distribution. The zenith distribution for this reconstruction is given in Fig. 5.7, where a clear turnover is observed around 90 degrees.

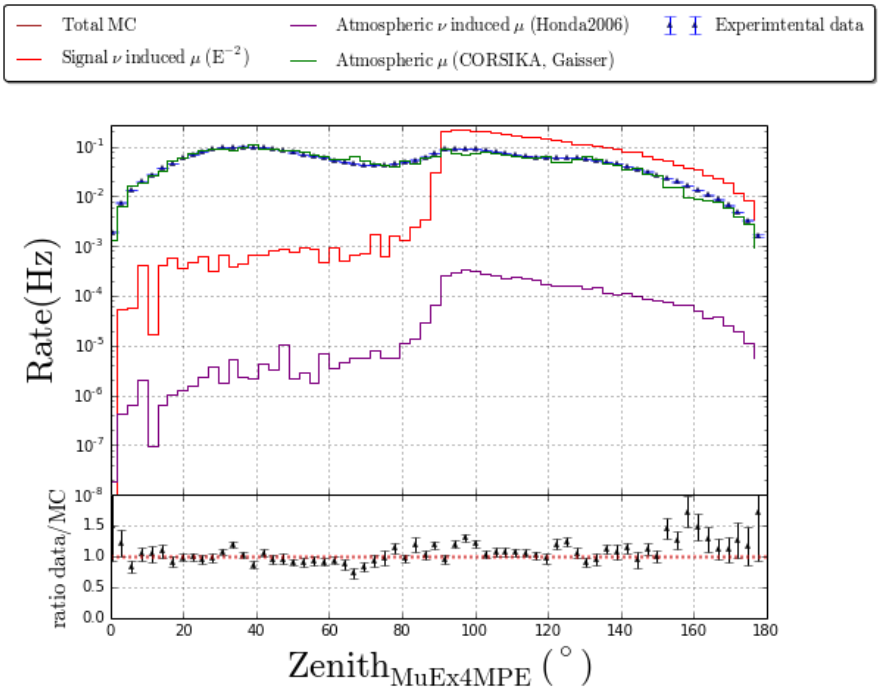

Figure 5.7: MuEx4MPEFit zenith distribution after MaxFrac pre-cut. The zenith region of $< 90°$ and $> 90°$ corresponds respectively to down and upgoing tracks.

5.1.3 Fit stability parameters

After discussing the quality of the reconstruction, we now focus on the stability of the fit result under varied reconstruction hypotheses. These parameters are powerful in separating between well-reconstructed and misreconstructed events. A first parameter is based on the biased Bayesian track reconstruction (see Section 4.3.3). This algorithm forces a downgoing reconstruction by using a Bayesian prior which greatly penalises

upgoing tracks. In case of well-reconstructed events, the log-likelihood value of this forced reconstruction will be much worse, whereas for misreconstructed events this will not be the case. The Bayes difference of $\text{rlogl}_{\text{Bayes}} - \text{rlogl}_{\text{SPE}}$ is therefore seen as an independent measure of fit stability. The distribution of this parameter is shown in Figure 5.8.

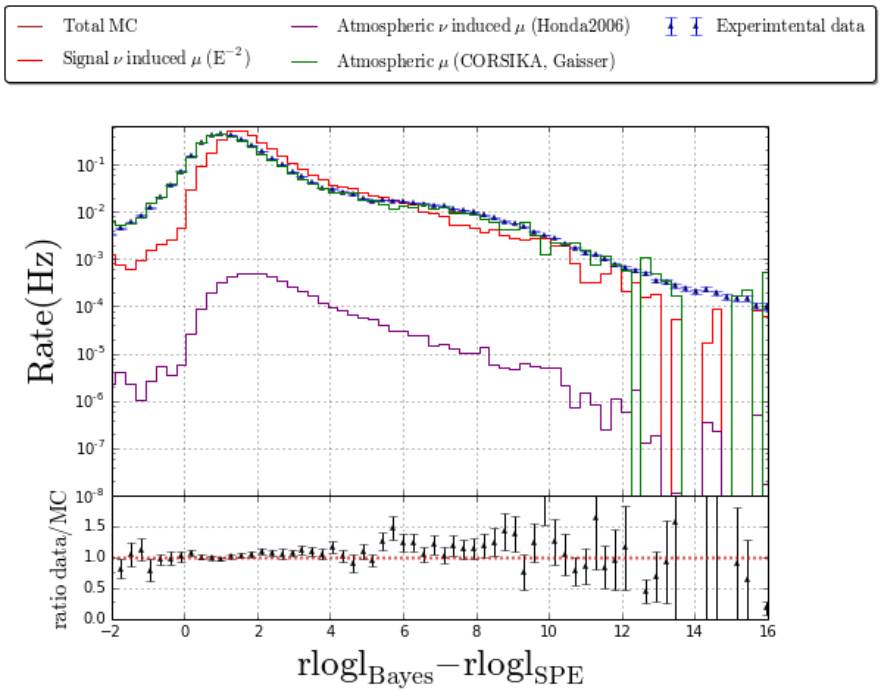

Figure 5.8: The Bayesian difference, $\text{rlogl}_{\text{Bayes}} - \text{rlogl}_{\text{SPE}}$, distribution after MaxFrac pre-cut.

We can compare the reconstruction direction achieved with the Bayesian algorithm and with a classic method. This provides a good separation of signal and background. In Fig. 5.9 we have shown the angular difference $\Delta\Psi$ between the LineFit reconstruction and the Bayesian SPEFit2 result. As the neutrino signal events are only upgoing tracks and are mostly reconstructed as upgoing tracks (see Fig. 5.7), the angular difference between the LineFit reconstruction and the forced downgoing reconstruction, Bayesian SPEFit2, will have a different behaviour for atmospheric muons or for neutrinos. We expect a peaked distribution of the angular difference for signal events with a peak at relatively high values and a more flat distribution for the background events. This expected behaviour is confirmed as can be seen in Fig. 5.9.

Finally, as presented in Section 4.3.4, we use the split reconstructions. For misreconstructed events, especially coincident events, the two pulse subseries created by these algorithms (based on time or geometry) should display a topologically diverging

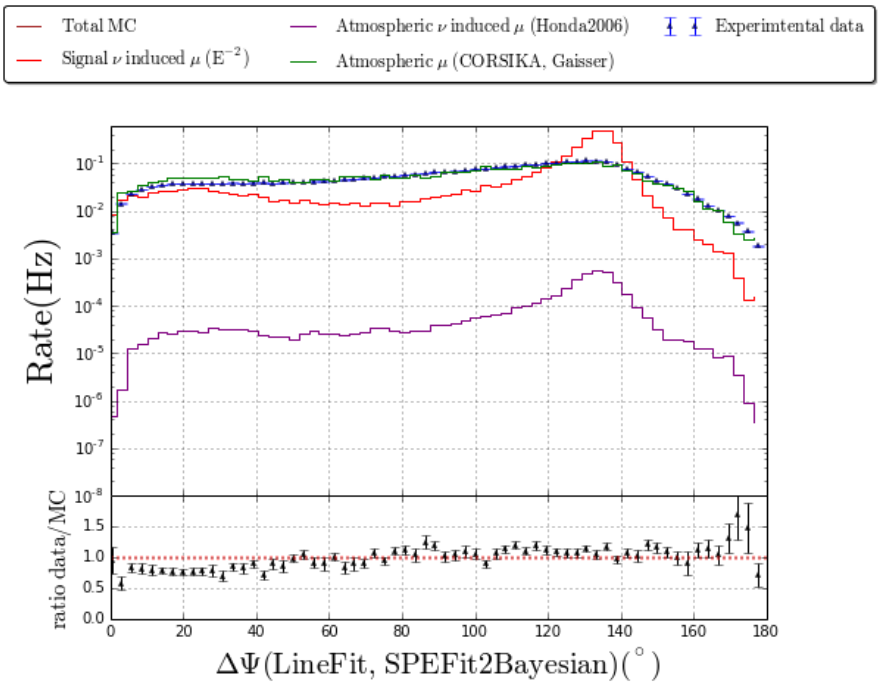

Figure 5.9: $\Delta\Psi$(LineFit,Bayes) distribution after MaxFrac pre-cut.

hit pattern leading to tracks with a different direction when compared with classic reconstructions. In this analysis, we have performed several of these calculations and the ones chosen for the MaxFrac case are presented in Fig. 5.11-5.14. As the expected hit patterns created by neutrino events and atmospheric muons are different, it is expected that these variables lead to a different behaviour for signal and for muons. This is what is visible on the following figures and is therefore of interest for the Boosted Decision Tree which will be performed.

5.1.4 Event topology parameters

We now investigate parameters that describe the topology of the event, *i.e.* the distribution of light inside the detector. One of these parameter is the so-called "smoothness" value. It analyses how uniformly (or not) the direct hit DOM projections onto the track (here MuEx4MPE) are distributed. A *direct hit* is defined as a DOM in which the first pulse arrives at approximately the expected time given by the reconstructed track [180]. In the standard processing used in this analysis, the allowed arrival time for a direct hit is $15\,\text{ns} < t_{\text{res}} < 75\,\text{ns}$, where t_{res} has been defined in Section 4.3.1.2. The distribution of the smoothness based on HiveSplit cleaned pulses is given in Fig. 5.15, where a zero value means that the direct hits are uniformly distributed. Well-reconstructed muon tracks typically have relatively smooth light patterns and thus a small value of the

smoothness parameter. We therefore expect a more uniform distribution for backgrounds events compared to the simulated signal. The last is expected to exhibit a more peaked distribution with the peak at a small value of the smoothness parameter. This theoretical behaviour is confirmed by the observed distributions. Note that the peek at zero is an artificial artefact of the algorithm.

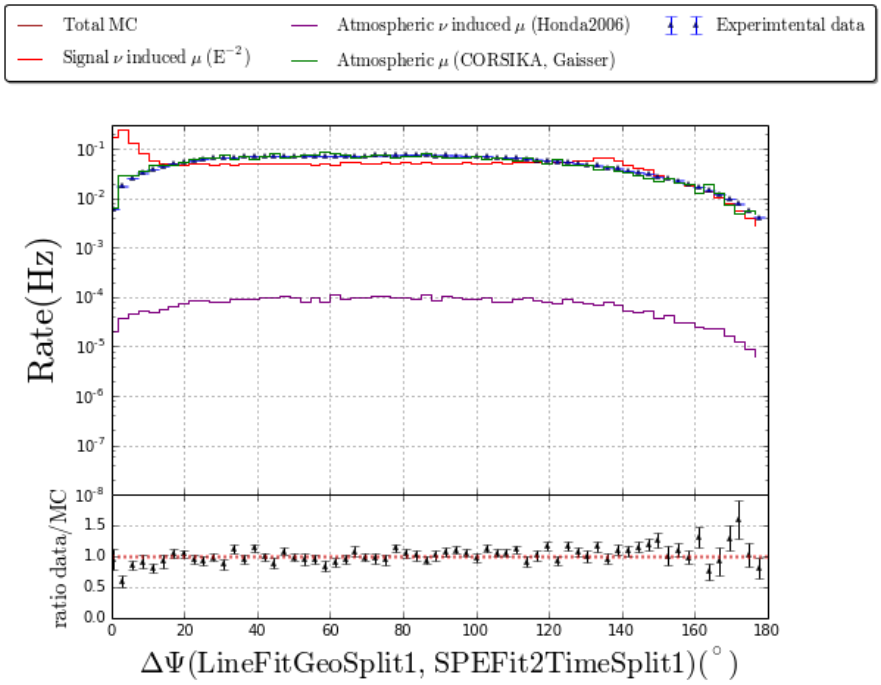

Figure 5.10: ΔΨ(LineFitGeoSplit1,SPEFitTimeSplit1) distribution after MaxFrac pre-cut.

Another powerful parameter to distinguish signal and background events is the maximum distance along the track not covered by HiveSplit cleaned hits within 150 m perpendicular distance to the track, calculated with respect to the MuEx4MPEFit. This parameter is called "l_{empty}" and its distribution is given in Fig. 5.16. As explained before, we expect smaller l_{empty} values for the signal compared to the background because of the smoothness of the light patterns.

Finally, the last topology parameter we use in this analysis is the mean value of the vertical position of the HiveSplit cleaned hits associated with the MuEx4MPE reconstruction. This parameter, called z_{mean} is shown in Fig. 5.17. As we expected the signal tracks originating from the bottom of the detector, the mean value of the vertical position of the HiveSplit cleaned hits associated to the MuEx4MPE reconstructions is expected to be lower for the signal compared to the background.

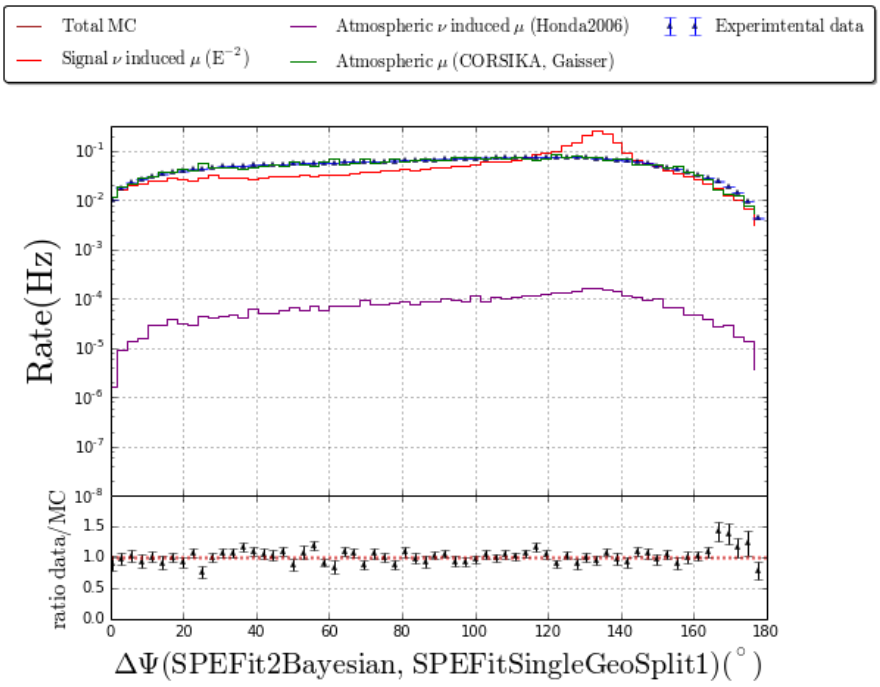

Figure 5.11: ΔΨ(Bayes,SPEFitGeoSplit1) distribution after MaxFrac pre-cut.

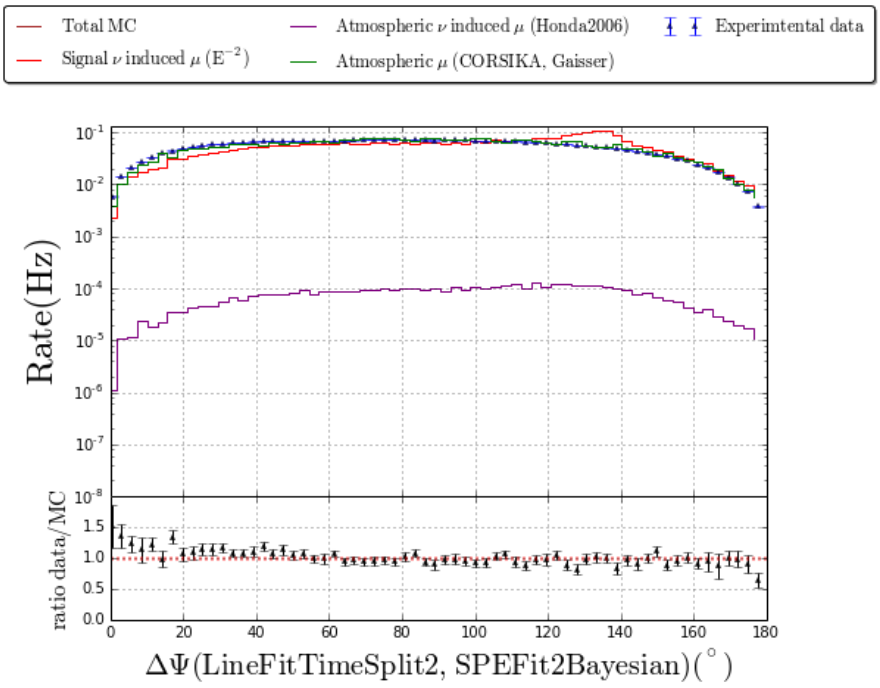

Figure 5.12: ΔΨ(LineFitTimeSplit2,Bayes) distribution after MaxFrac pre-cut.

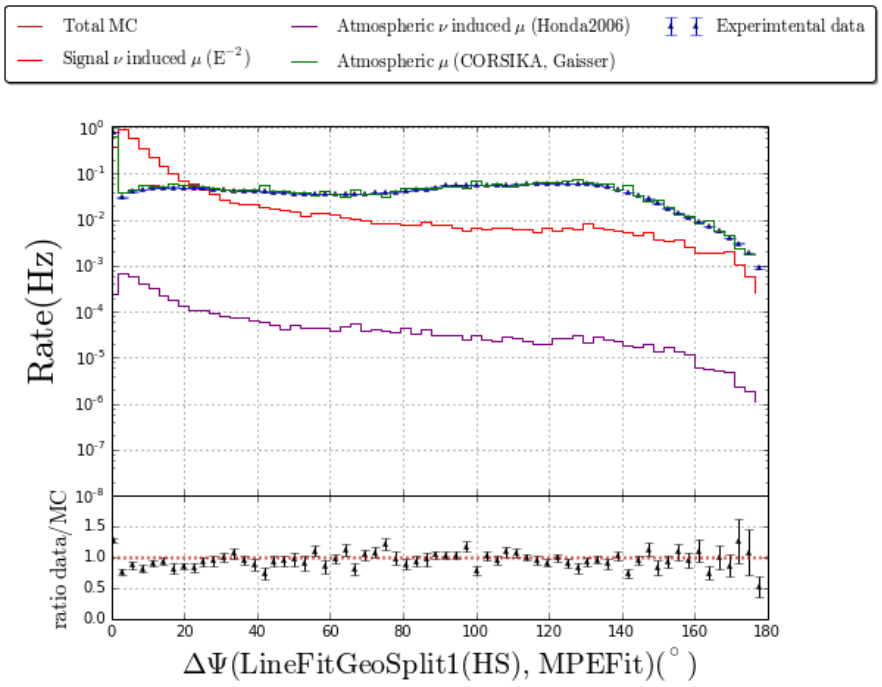

Figure 5.13: $\Delta\Psi$(LineFitGeoSplit1,MPEFit) distribution after MaxFrac pre-cut.

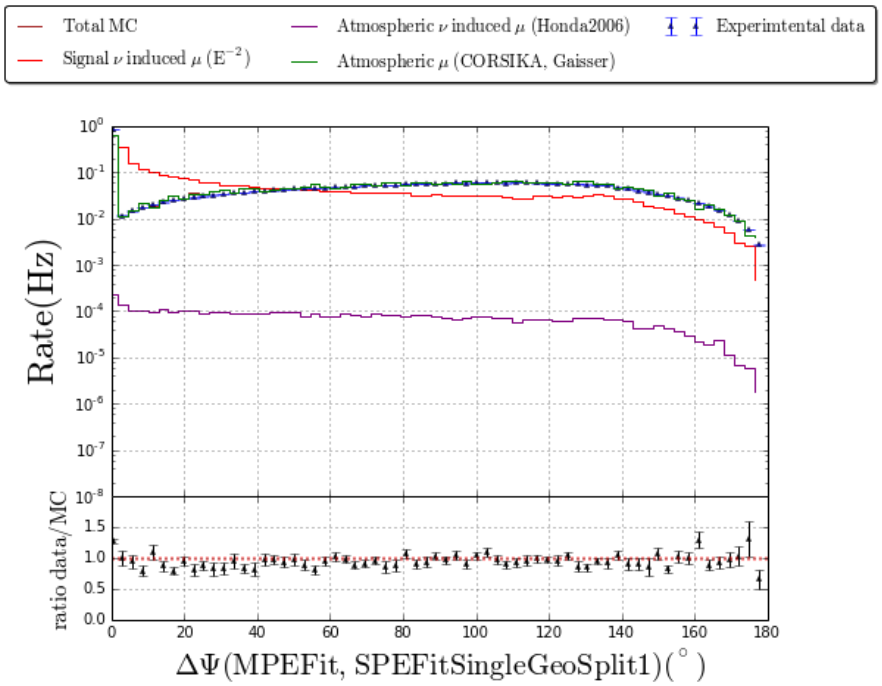

Figure 5.14: $\Delta\Psi$(MPEFit,SPEFitGeoSplit1) distribution after MaxFrac pre-cut.

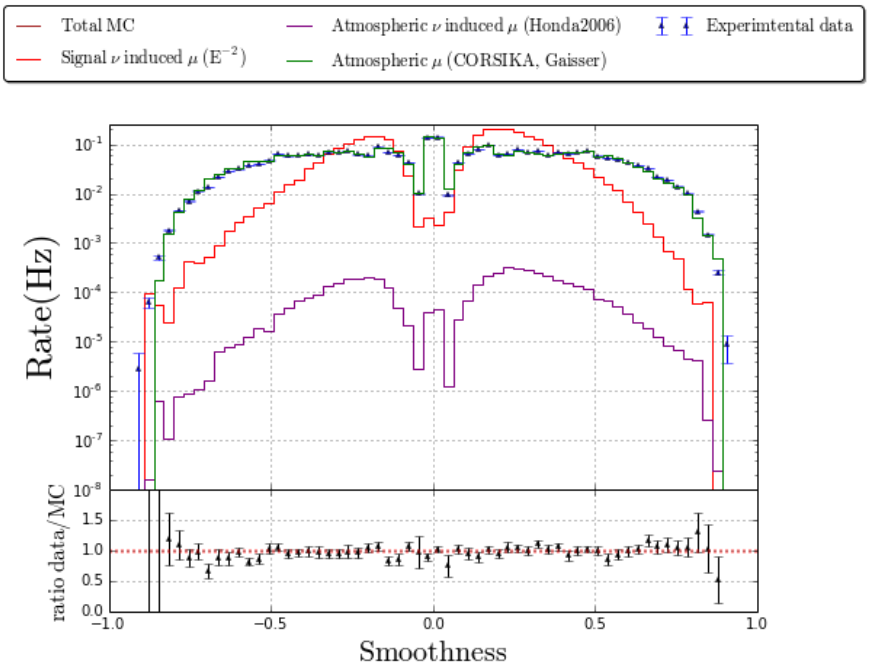

Figure 5.15: Smoothness distribution based on HiveSplit cleaned pulses wrt to MuEx4MPE after MaxFrac pre-cut.

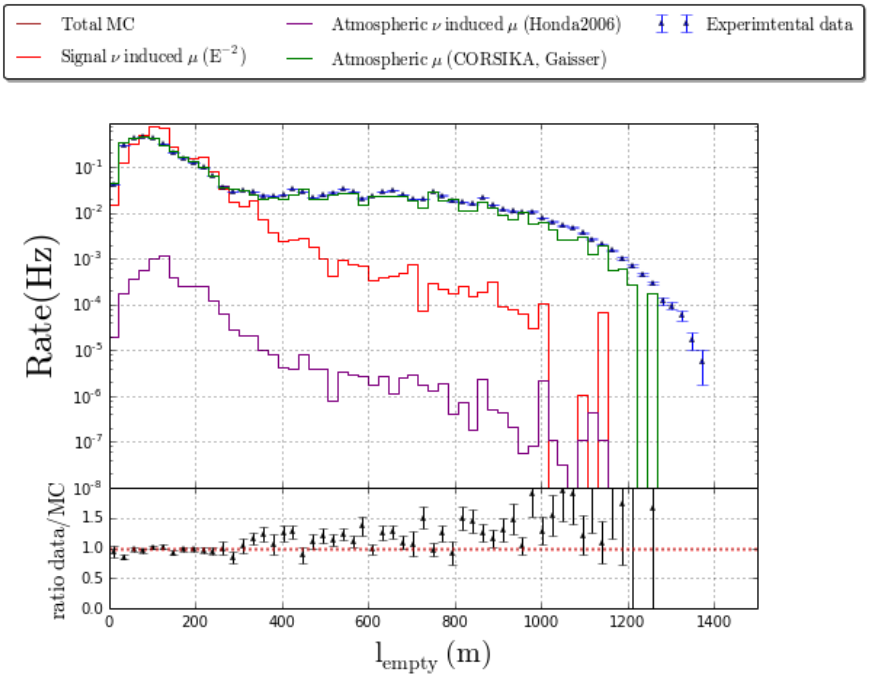

Figure 5.16: L_{empty} distribution based on HiveSplit cleaned pulses wrt to MuEx4MPE after MaxFrac pre-cut.

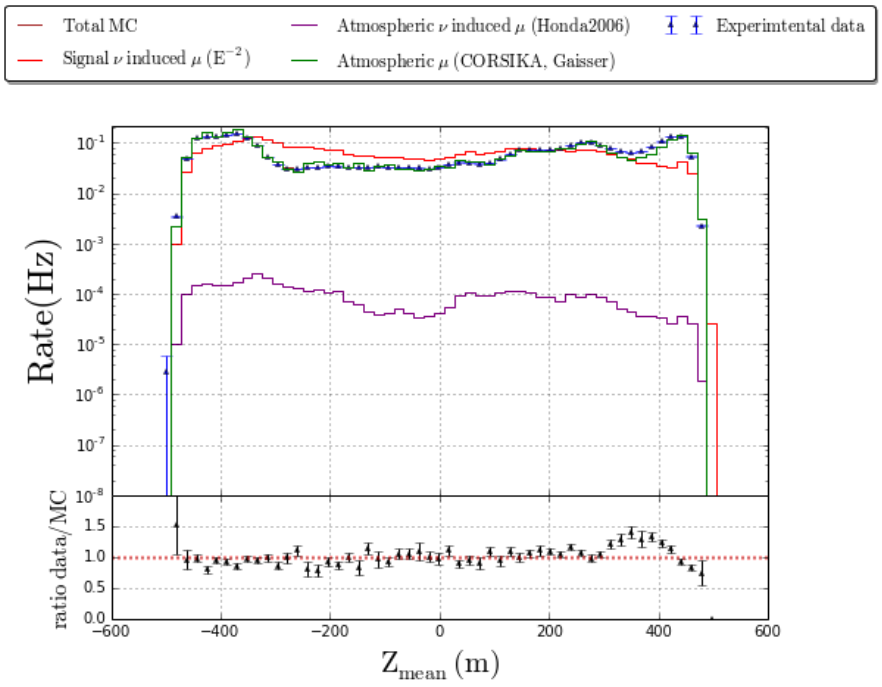

Figure 5.17: Z_{mean} distribution based on HiveSplit cleaned pulses wrt to MuEx4MPE after MaxFrac pre-cut.

5.2 Initial data-reduction cuts

In this section, we describe the method used as a pre-cut in view of a first data reduction: we start from the SMT-8 trigger which provides us data at a rate of $\gtrsim 2\,\text{kHz}$ and arrive at a rate of $\sim 3\,\text{Hz}$. As already mentioned, the first step is the application of various filters (see Section 4.2) which select muon candidate events (to be conservative, we have decided to keep Cascade like events produced by the energy loss of a ν_e induced electron). This first selection has reduced the data rate to about 76 Hz. We will now apply an innovative method developed for this analysis by our team at the *Interuniversity Institute for High Energies* (ULB-VUB), called "QualDist".

5.2.1 QualDist Method

The developed method described below aims to select muon tracks that are most likely up-going in the detector based on a sample of different reconstruction methods. To achieve this, we will assign to each reconstruction a probability of reconstructing correctly the general direction of the event (up-going or down-going) combined with the quality of the track. The quality of the fit is directly computed from the previously described variables (Section 5.1.1) and the probability of reconstructing correctly the general direction of the event is computed empirically from data and simulation. The

QualDist parameter will be computed through the bayesian defined variable "evidence" [188].

The bayesian evidence is computed from the Bayes' theorem. Let us denote $p(A, B|C)$ the probability for hypothesis A and B to be true under the condition that C is true. The product rule [188], $p(A, B|C) = p(A|C)p(B|A, C) = p(B|C)p(A|B, C)$, directly yields Bayes' theorem [189]:

$$p(A|B, C) = \frac{p(A|C)p(B|A, C)}{p(B|C)}. \tag{5.2}$$

Bayes' theorem is powerful in hypothesis testing. Consider a hypothesis H, some observed data D and prior information I. Bayes' theorem can then be rewritten as:

$$p(H|D, I) = \frac{p(H|I)p(D|H, I)}{p(D|I)}, \tag{5.3}$$

where

$$\begin{array}{lcl} p(H|D, I) & \equiv & \text{Posterior probability of hypothesis } H. \\ p(H|I) & \equiv & \text{Prior probability of hypothesis } H. \\ p(D|H, I) & \equiv & \text{Likelihood function, } \mathcal{L}(H). \\ p(D|I) & \equiv & \text{Normalization factor.} \end{array}$$

As seen in the above equation, Bayesian inference allows us to make statements about the probability of various hypotheses in the light of obtained data. Following the development made in [188], we quantify the degree to which data support a certain hypothesis and as such make an assessment of the significance. To quantify our degree of belief in a certain hypothesis H, one can use the evidence defined as:

$$e(H|D, I) = 10 \log_{10} \left[\frac{p(D|H, I)}{p(D|\overline{H}, I)} \right], \tag{5.4}$$

where $\overline{H}$ indicates hypothesis H to be false and where we have dropped the term $e(H|I)$ that mathematically arises but which only represents a fixed offset[1] In case several pieces of data D_i describe our measurements and are logically independent, the above equation becomes:

$$e(H|D, I) = \sum_i e(H|D_i, I) = 10 \sum_i \log_{10} \left[\frac{p(D_i|H, I)}{p(D_i|\overline{H}, I)} \right]. \tag{5.5}$$

For each event recorded by IceCube, we have up to seven different reconstructions of its arrival direction (see Section 4.3). If we define the probability $p(D_i = \text{up or down}|H, I)$ (respectively $p(D_i = \text{up or down}|\overline{H}, I)$) representing the probability

[1] The complete form of Eq. (5.4) is $e(H|D, I) = e(H|I) + 10 \log_{10} \left[\frac{p(D|H,I)}{p(D|\overline{H},I)} \right]$.

that reconstruction i is up or down-going knowing that the simulated track was up-going (respectively down-going), we compute a new parameter, called QualDist, given by:

$$\mathrm{QD} = 10 \sum_i \log_{10} \left[\frac{p(D_i|H,I)}{p(D_i|\overline{H},I)} \right] \times Q_i, \tag{5.6}$$

where Q_i is based on the quality factor associated to each of the considered reconstructions (see Section 5.1.1) and is given by:

$$Q = \begin{cases} \beta & \text{for} \quad 0 \leq \beta \leq 1 \\ 2-\beta & \text{for} \quad 1 < \beta < 2 \\ 0 & \text{for} \quad \beta \geq 2 \end{cases} \tag{5.7}$$

for the reconstructions where the velocity v is computed from which the relativistic $\beta = \frac{v}{c}$ is obtained and by:

$$Q = \begin{cases} \frac{6}{\mathrm{RLogL}} & \text{for} \quad \mathrm{RLogL} \geq 6 \\ 1 & \text{for} \quad 0 \leq \mathrm{RLogL} < 6 \end{cases} \tag{5.8}$$

for SPE and MPE. With these definitions, we have $0 \leq Q \leq 1$ for all the reconstructions. The probability values $p(D_i|H,I)$ and $p(D_i|\overline{H},I)$, where H represents a real upgoing track and $\overline{H}$ represents a real downgoing track, have been computed with NuGen simulation for the up-going tracks and CORSIKA for the down-going (using real data and assuming all the tracks are down-going gives, at Level2, very similar results) and are given in Table 5.1. As the track can only be down or up-going, the probabilities for

Table 5.1: Probabilities used in the QualDist method.

	LineFit	SPEFit2	MPEFit	ILF	DWI	DWIC	DWDC
$p(\mathrm{up}\|H,I)$	0.913809	0.910533	0.916546	0.862702	0.836002	0.909753	0.770321
$p(\mathrm{up}\|\overline{H},I)$	0.311406	0.288345	0.304969	0.345373	0.214998	0.0849678	0.455515

the downgoing reconstruction results are obtained by subtracting the values of Table 5.1 from 1.

With all this in mind, we can now assign to each event a QualDist value calculated as indicated above. As we do not know in advance whether the results will be optimal if we use the full sample of reconstructions or part of it, it has been chosen to try all the possible combinations of the 7 considered reconstructions. We then end up with 126 possible values of total evidence for each event. Figure 5.18 gives an example of one of the obtained results. As we can see on that figure, the obtained separation between signal and background events is good. The distribution shows a good agreement between CORSIKA and data expect for QD=0, where data exhibits an excess with respect to CORSIKA. This is due to the fact that real data contains events consisting only of noise hits leading to failing fit procedures. However this does not have a direct impact on the

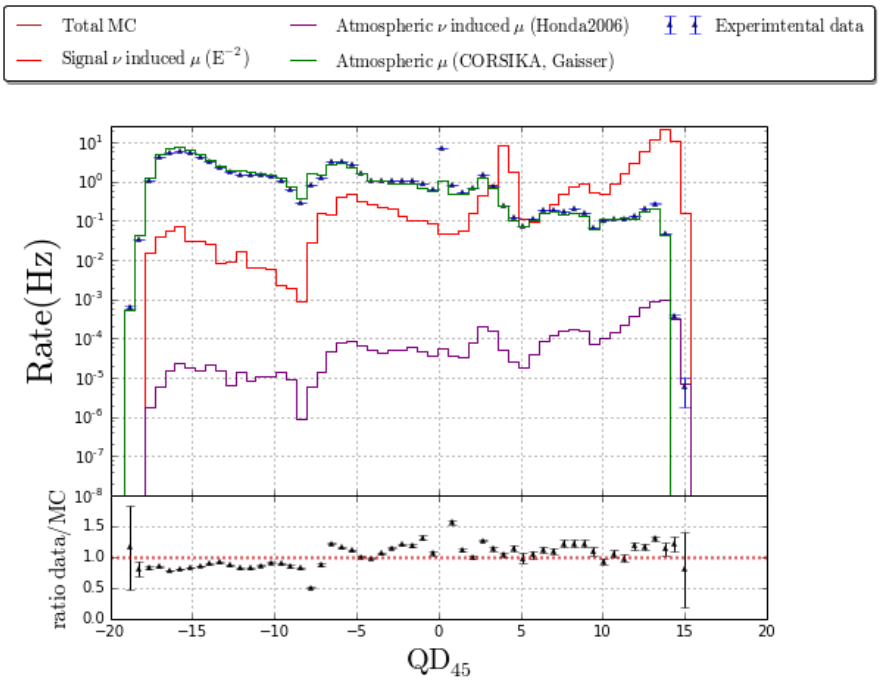

Figure 5.18: QualDist distribution for combination 45, corresponding to the combination of DWIC, DWI and SPEFit2.

analysis as the cut values are, in all cases, bigger than 0 (see next section). The "bumpy" structure of this variable arises because QD is calculated by summing fixed values that are only spread by the quality factor, which is always never bigger than one.

5.2.2 Proposed pre-cuts

We have obtained 126 possible QualDist selection modes and have to define the best combination of tracks and the actual cut point. To achieve this, we have decided to create ROC plots [190]. We therefore have calculated the ROC curves for each of the 126 possible combinations of tracks and have extracted the 4 best combinations for different background efficiency regimes. Figure 5.19 gives the result of this procedure, where we have defined the efficiency as $\epsilon_{b(s)} = \frac{N_{b(s),>\mathrm{QD_{cut}}}}{N_{b(s),\mathrm{tot}}}$, where $b(s)$ stands for background (signal), and $>\mathrm{QD_{cut}}$ refers to events passing the QD cut. As no one single "best cut point" appears, we have decided to define several possible cut points and optimise each of them separately. Two of them are "physically" motivated and are the following:

- "Maximum Significance" (MaxSign): we compute, for each possible combination while scanning different possible cut values, the significance of the signal given by Sign= $\frac{\epsilon_s}{\sqrt{\epsilon_s+\epsilon_b}}$ and record the cut maximising this observable. We finally select the

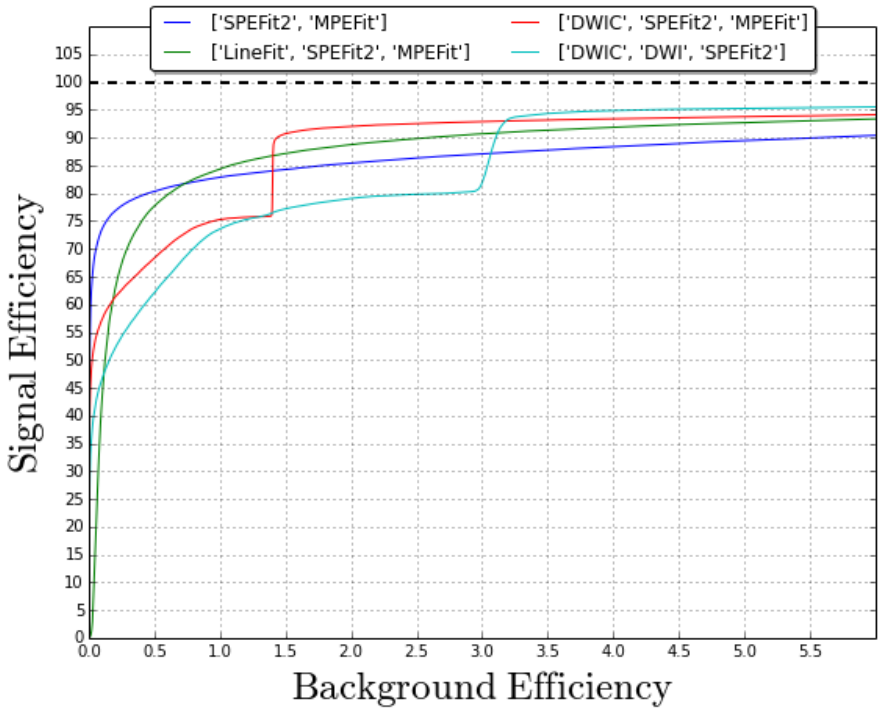

Figure 5.19: ROC curves for the 4 best combinations of various reconstructions corresponding to a certain background efficiency regime. The signal and background efficiencies are given in percent.

cut point and the combination of tracks that offers the best background rejection (minimising ϵ_b).

- "Maximum Fraction" (MaxFrac): we compute, for each possible combination while scanning different possible cut values, the fraction of the signal given by Frac= $\frac{\epsilon_s}{\epsilon_b+1}$ and record the cut maximising this observable. We finally select the cut point and the combination of tracks that corresponds to the maximum of all the maximums.

This leads to a cut at $\epsilon_b = 2.35\%$ for MaxSign, corresponding to a cut on QualDist at QD= 5.98 calculated for the combination of tracks of DWIC, SPEFit2 and MPEFit and to a second cut at $\epsilon_b = 3.78\%$ for MaxFrac, corresponding to a cut on QualDist at QD= 2.95 for the combination of DWIC, DWI and SPEFit2.

Finally we consider pre-cuts for smaller possible values of the background efficiency ranging from $\epsilon_b = 0.2\%$ to 2.2% leading to specific cuts on QD, where QD is calculated using the best combination corresponding to the considered background efficiency (see Fig. 5.19).

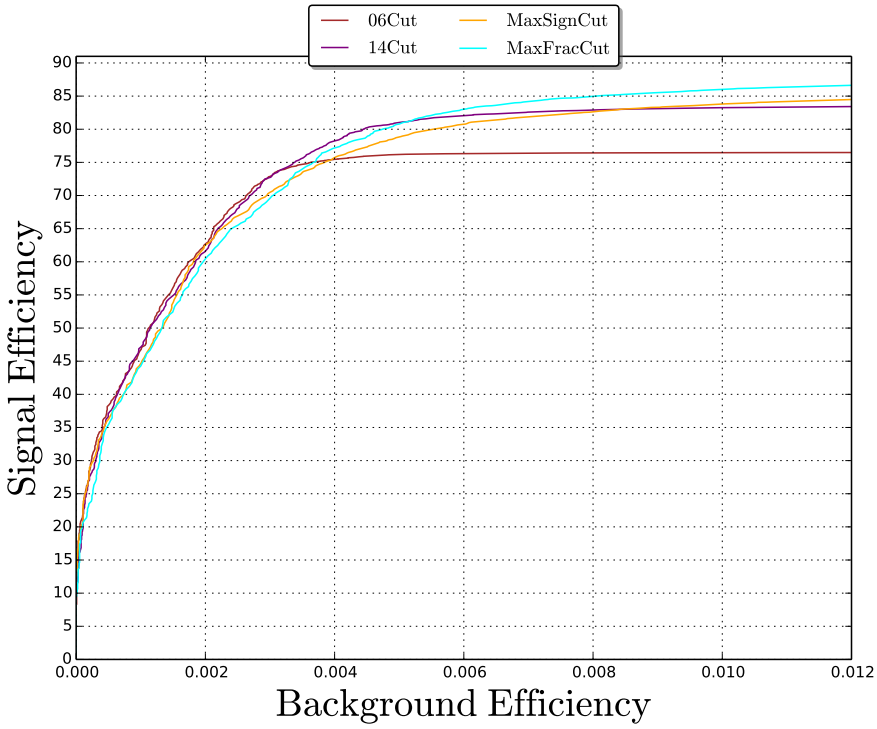

Figure 5.20: ROC curves for the 4 best cuts of each of the best combinations of various reconstructions.

Each of these 12 possible pre-cuts are then applied to the data. Based again on ROC curves, we only keep the best cut for each of the 4 best combinations and we thus end with four possible pre-cuts on the data. The final ROC plot of the 4 investigated pre-cuts is given in Fig. 5.20. To compare the performance of the different possibilities of our innovative method and with the standard IceCube selection, a signal efficiency in function of the primary energy of the track and compared to MuonLevel3 (an additional classical processing pass often used in IceCube analysis which reduces the data rate to about 1 Hz) is given on Fig. 5.21. We see that, at least for two of the proposed pre-cuts, we are improving the classical MuonLevel3 for most of the energy ranges. The final pre-cut will be defined after the BDT selection and will be determined to maximise the effective area, as defined lateron.

The following table gives the passing rates for each of these 4 proposed pre-cuts (compared to Level2 after filter selection).

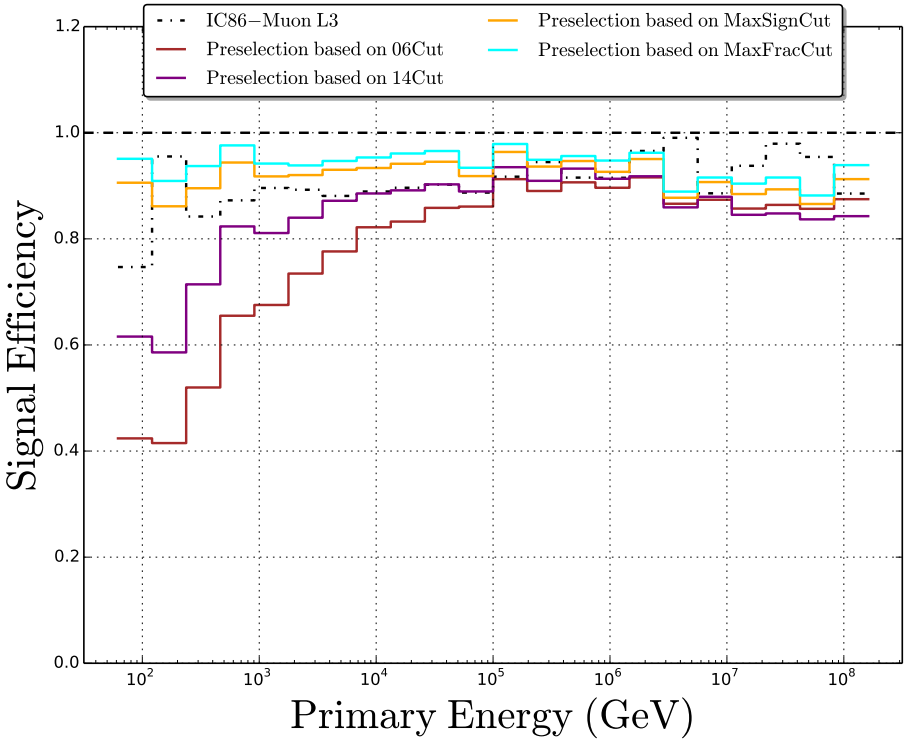

Figure 5.21: Signal Efficiency for the 4 proposed pre-cuts in function of the simulated neutrino energy.

Table 5.2: Passing rates after the appliance of the 4 possible pre-cuts.

	06 Cut	14 Cut	MaxSign Cut	MaxFrac Cut
NuGen	82.38%	88.34%	93.36%	95.14%
Burn Sample	0.66 Hz (0.87%)	1.40 Hz (1,84%)	2.93 Hz (3,86%)	3.44 Hz (4,53%)

5.3 Working towards neutrino candidate events

After the cuts described in the previous section, the data rate is about $\mathcal{O}(1\,\mathrm{Hz})$, but we are still dominated by misreconstructed cosmic ray muon events. Our aim is to retain only well-reconstructed upgoing events consisting of background atmospheric neutrinos and hopefully neutrinos from GRBs, while rejecting all others muons. In the last years, decision tree forests [191] have emerged as a popular classification strategy for resolving the kind of problem we are facing. A custom, hybrid Python-C++ decision tree forest

implementation called "pybdt", developed within the IceCube Collaboration, has been used for this analysis. A detailed presentation of this computing tool can be found in [192]. We restrict ourself to a brief presentation of the Boosted Decision Tree (BDT) working scheme.

5.3.1 Boosted Decision Tree Forests

The first element on which BDTs are built is the concept of *Decision Trees*. A decision tree is a decision support tool that uses a tree-like model of decisions and their possible consequences. It consists of a binary tree with a cut on one parameter specified at each node, called "split node", until it reaches a "leaf node", which has no more child nodes. In our analysis, the leaf node can either be *signal leaf* or a *background leaf*. An example of a decision tree is given in Fig. 5.22.

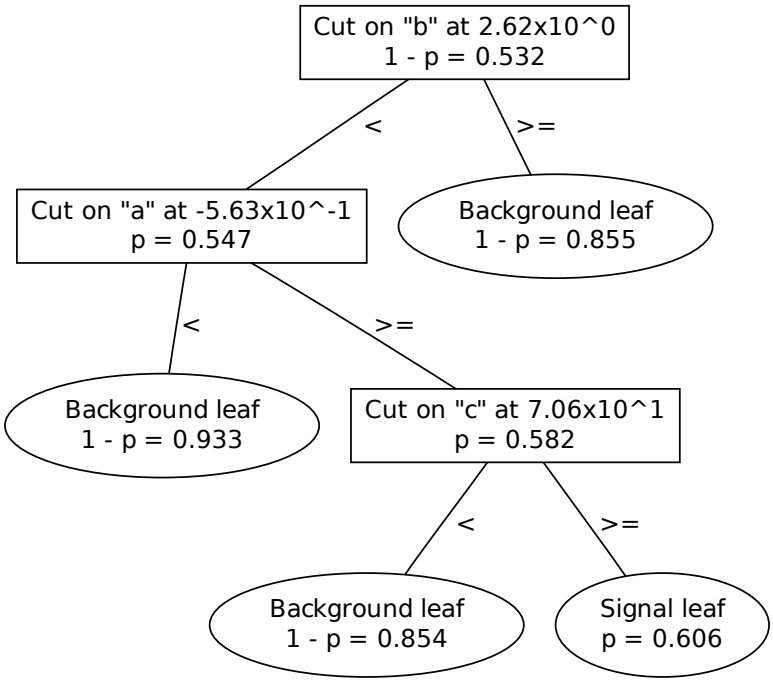

Figure 5.22: An example of a decision tree. From [192].

These trees are generated by a recursive process called training. The generic concept is to split events of known class (signal or background) into a *training* and a *testing* sample, where the former is used to construct trees and the latter is used to validate them. The training process assures that we obtain the overall maximum of the separation gain for all event parameters. Once this optimum is reached, the algorithm repeats recursively for the subsamples corresponding to a smaller or a greater parameter value than the

optimum cut on that parameter. The training process stops when it achieves one of the following criteria:

- The user-specified maximum tree depth is reached.
- A node has either only signal or only background training events remaining.
- The best available split would result in a node with less than a user-specified minimum number of events remaining.

Obviously, if we would only create one tree limited by its depth, we would misclassify less-typical events. We could then decide to increase the depth of the tree but we would then take the risk of possible overtraining the data. *Overtraining* arises when very deep trees are used because they have the drawback that they are finely tuned to the details of the less-typical events in the training sample such that their performance on testing or unknown samples is not consistent with their performance on the training sample. Basically this means that decisions are made based on statistical fluctuations of real signal events, obviously leading to a worse performance. Therefore, we use another technique called decision tree *forest*. In this method many decision trees (hundreds in our analysis) are used, each of them with a certain weight. A forest yields a score on the interval $[-1, +1]$ rather than a discrete signal or background classification. The various trees in the forest differ because they are trained under slightly different conditions. Two techniques are commonly used for this purpose: boosting and randomisation. In this thesis, we use the *boosting* procedure. The boosted decision tree forests consist of adjusting the relative weight of training sample events in between each individual tree training. This process is called boosting because it "boosts" the weights of misclassified training events.

Even with the forest method and the boosting procedure, overtraining can still appear in the classification procedure when one branch of the tree may contain additional useful splits, while the other disproportionately contains less productive splits that are overtuned to the training samples. To avoid this effect, we remove parts of trees that add little discrimination power. This is referred to as *pruning* [192].

5.3.2 Classification of events using a BDT

In this section, we apply the previously described procedure for each of our proposed pre-cuts. For each of them, we use the same BDT options, which have been chosen to optimise the BDT performance. Each forest has 400 trees, and each split was chosen by considering 20 evenly spaced cut values of each variable. A maximum depth of 3, a boost strength β of 0.7 and pruning strength of 35% has been used. A detailed presentation of all the possible options in BDT training and their impact are presented in [193].

5.3.2.1 Input variables and BDT training

As already mentioned, the resulting datasets after each of the 4 previously discussed pre-cuts are separately optimised. In Table 5.3, we give as an example the list of the variables on which the BDT has been trained for the MaxFrac pre-cut (the given values show the importance in the BDT, so the variables are ordered by importance in decreasing order from top to bottom). Each of these variables has been defined and its distribution before BDT has been shown in Section 5.1 or in Section 5.2.

Table 5.3: BDT input variables and their relative weight.

Input Variables	Relative weight in the BDT
$\mathrm{Zenith}_{\mathrm{MuEx4MPE}}$	0.193391
$\sigma_{\theta}^{\mathrm{CR}}$	0.163717
$\sigma_{\mathrm{MuEx4MPE}}$	0.122516
QD_{62}	0.106667
Smoothness	0.064155
$\Delta\Psi$(LineFitGeoSplit1,MPEFit)	0.059408
QD_{45}	0.049488
$\mathrm{l}_{\mathrm{empty}}$	0.036451
$\mathrm{rlogl}_{\mathrm{MPE}}$	0.036191
$\mathrm{Z}_{\mathrm{mean}}$	0.034340
$\mathrm{rlogl}_{\mathrm{Bayes}}-\mathrm{rlogl}_{\mathrm{SPE}}$	0.032639
$\Delta\Psi$(LineFitGeoSplit1,SPEFitTimeSplit1)	0.023033
$\Delta\Psi$(LineFitTimeSplit2,Bayes)	0.020786
$\Delta\Psi$(LineFit,Bayes)	0.020786
$\Delta\Psi$(LineFitTimeSplit2,MPEFit)	0.015918
$\Delta\Psi$(MPEFit,SPEGeoSplit1)	0.011588
$\Delta\Psi$(Bayes,SPEGeoSplit1)	0.010296

The objective of the training is, as described in Section 5.3.1, to maximise signal and background discrimination while avoiding overtraining. One test of this uses the remaining NuGen simulation data and off-time data to compare agreement between training and testing score distributions. This establishes that the BDT does not overtrain to specific events in the training samples. Figure 5.23 is the overtraining plot for this BDT. As can be seen on this figure, though there is possible overtraining to the signal at low BDT scores and background at high BDT scores, this effect is slight and according to the Kolmogorov-Smirnov test score, it is on an acceptable level. The result of applying this BDT on data can therefore be considered as trustful.

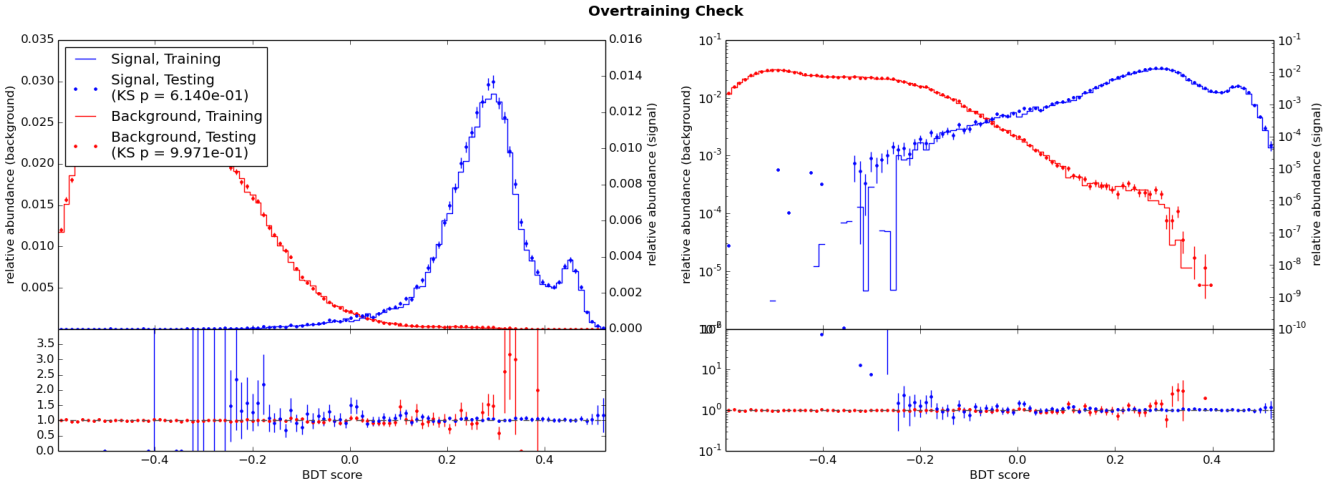

Figure 5.23: Overtraining check for the discussed BDT.

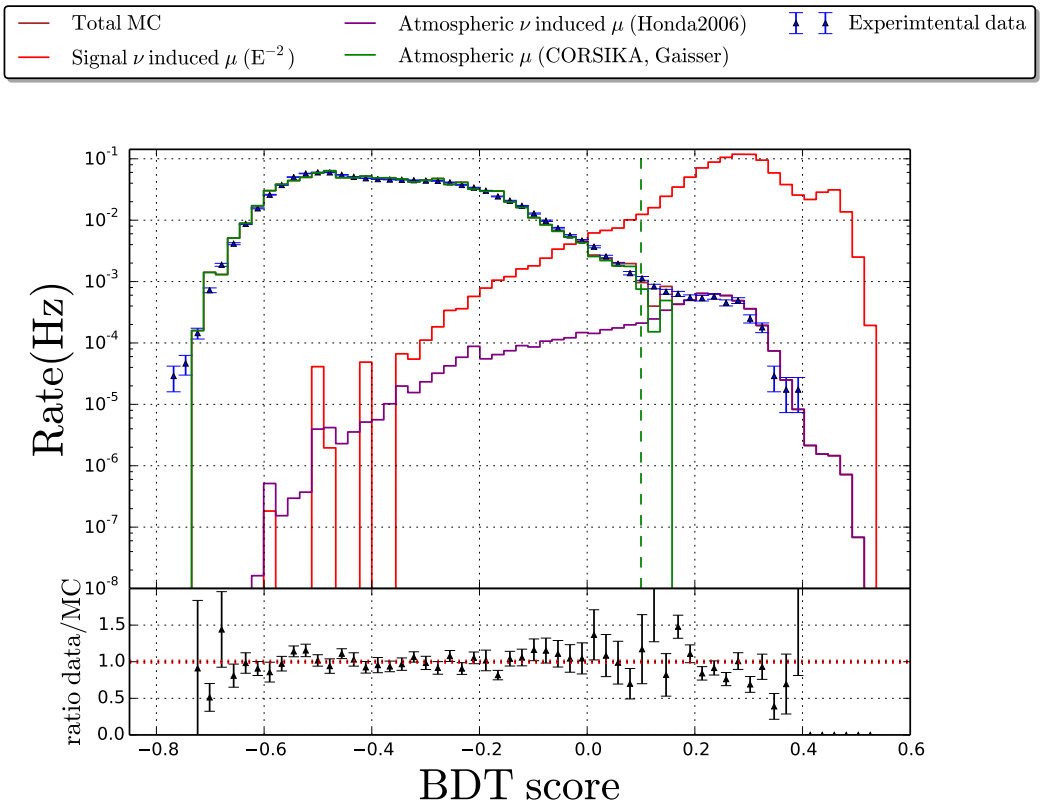

Figure 5.24: BDT performance. The green dashed line represents the proposed cut value of 0.10.

5.3.2.2 BDT performance

The final BDT score distribution for the considered datasets is given in Fig. 5.24 and a proposed cut value of 0.10, corresponding to a signal purity[2] of $\sim 85\%$, is shown as a dashed green line. As explained in next Chapter, this BDT cut value is motivated by the study of the sensitivity and the discovery potentials of our analysis.

The performance of the selected classifier can be quantified in various ways. One of these is the so-called effective area, referring to the ratio of the observed event rate and the incoming neutrino flux. As such the effective area, obtained from simulations, provides a means to relate our observations with the actual neutrino flux. Therefore, a greater effective area is a quality parameter of the event selection. We have decided to fix our pre-cut choice on this parameter (see Section 5.2). A comparison of the four pre-cuts and the previous IC86 GRB analysis performed in IceCube [34] is given in Fig. 5.25.

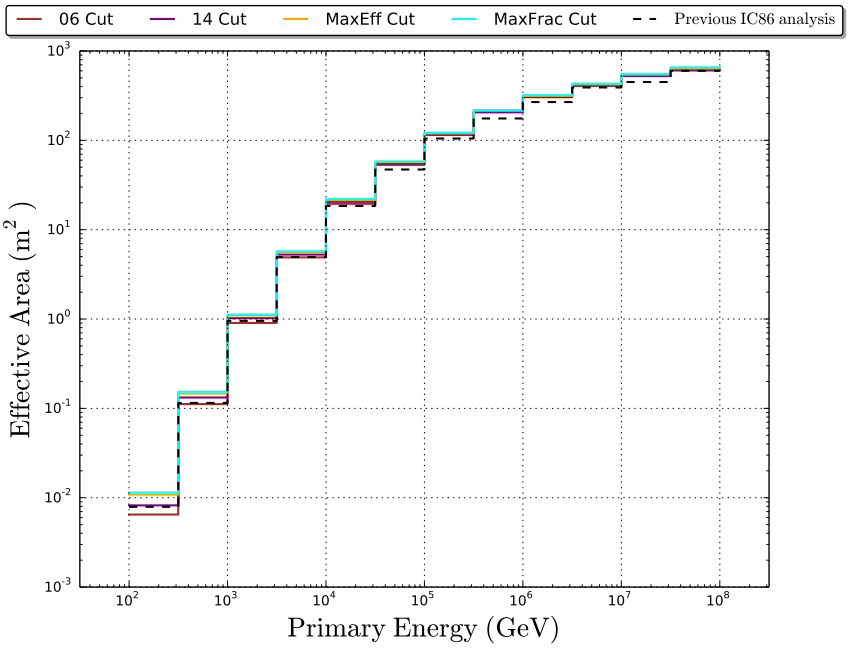

Figure 5.25: Effective areas comparison of the four pre-cuts for the same value of signal purity. The obtained effective area in a previous GRB analysis performed in IceCube [34] is also shown. The effective area in this figure has been computed for an E^{-2} signal spectrum.

[2]The signal purity is defined as the estimate of the ratio of the atmospheric neutrino rate to the total atmospheric neutrino plus atmospheric muon rate

As can be seen on Fig. 5.25, our newly developed event selection improves previous analyses made within the IceCube Collaboration. We now can determine our pre-cut value that maximises the effective area, which appears to be the MaxFrac cut. A detailed effective area for this pre-cut and for the proposed BDT cut of 0.10 is given in Fig. 5.26 as a function of the zenith arrival direction of the neutrinos.

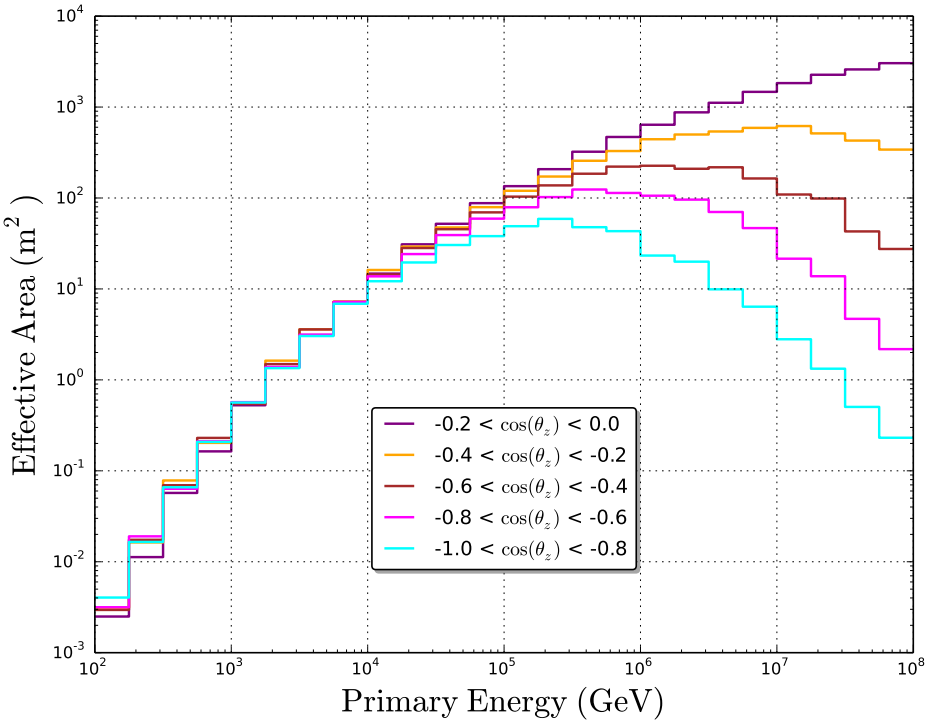

Figure 5.26: Effective area or the MaxFrac pre-cut as a function of the zenith arrival neutrino angle.

The signal efficiency as a function of the simulated neutrino energy is also a way of analysing the performance of a BDT classifier and Fig. 5.27 shows this for the MaxFrac cut for a range of BDT score cuts. As a more energetic event tends to be easier to reconstruct, an energy dependence is observed in the signal efficiency. However, we see that for the proposed final cut of 0.10, this dependence is not very strong and is not a problem for our analysis. The angular resolution of the MuEx4MPE reconstruction of the neutrino events is also an important variable for our analysis and is shown in Fig. 5.28. The same parameter as a function of energy is shown in Fig. 5.29. The overall median angular resolution amounts to 0.78° which is totally satisfying. These plots both show logically improving performance with increasing energy until 10^8 GeV.

Compared to other analyses, because the signal window is very small in time and space, our event selection tolerate more background than selections used in other analyses such as the search for clusters of northern muon neutrinos from astrophysical point sources [194]. This allows us to achieve a higher signal rate in the current analysis.

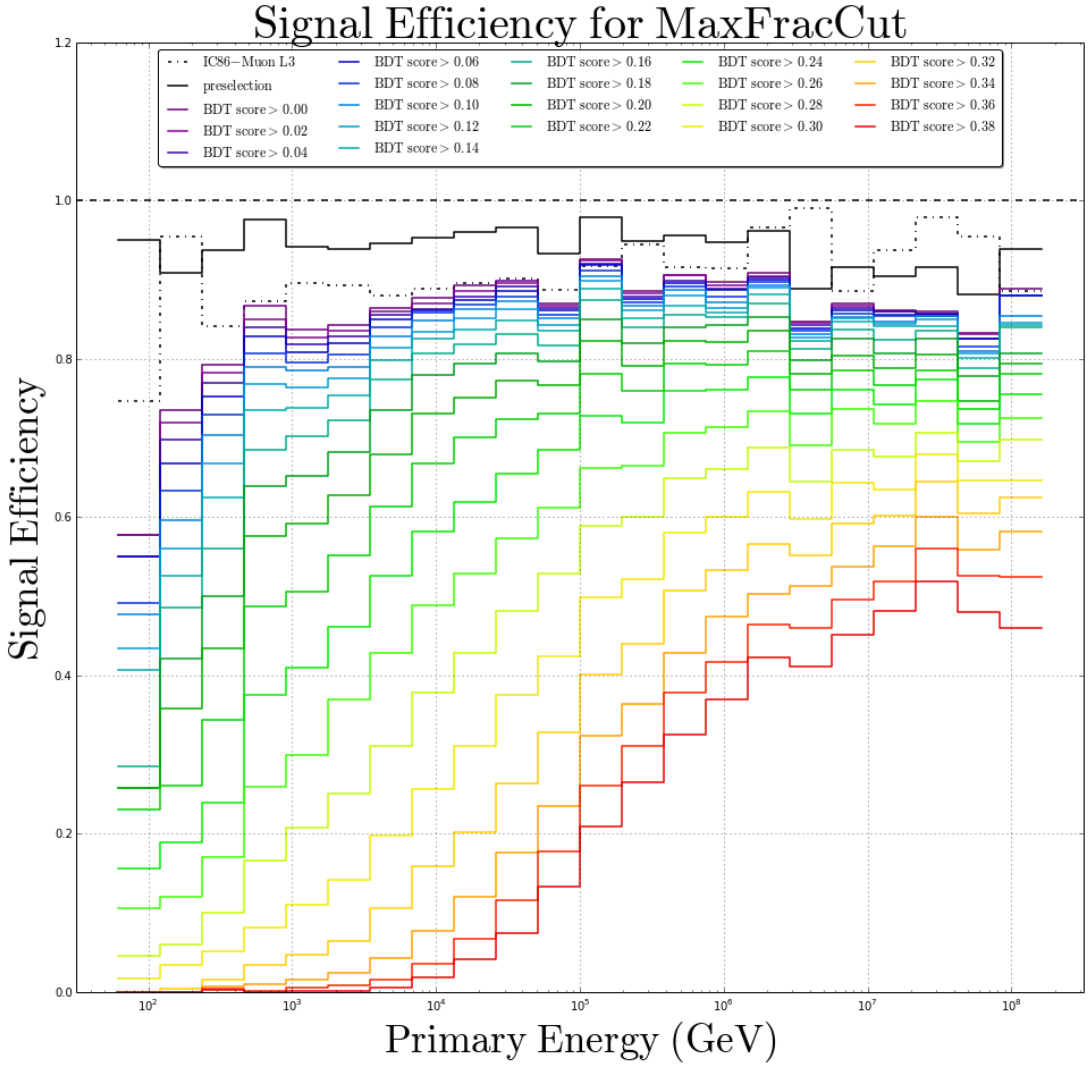

Figure 5.27: Well-reconstructed signal efficiency (for an E_ν^2 input spectrum) as a function of energy and BDT score cut for the MaxFrac pre-cut.

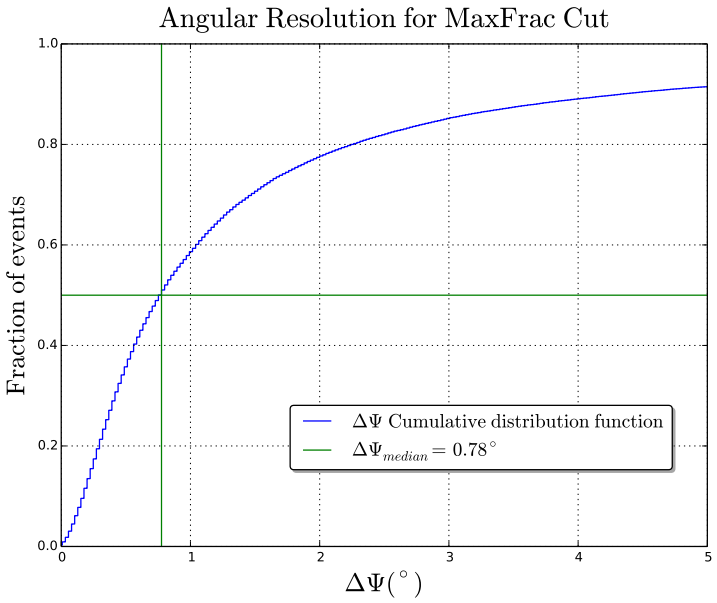

Figure 5.28: Angular resolution for the MuEx4MPE Fit at a proposed BDT score cut of 0.10 for the MaxFrac pre-cut.

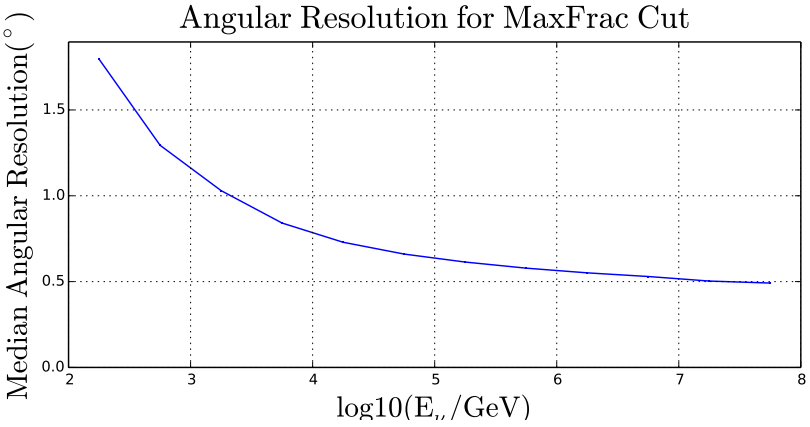

Figure 5.29: Angular resolution for the MuEx4MPE Fit as a function of the neutrino simulated energy at a proposed BDT score cut of 0.10 for the MaxFrac pre-cut.

CHAPTER 6

Statistical Tools

At the end of Chapter 5, we have obtained a final data sample that is largely composed of muon neutrinos. Unfortunately these neutrinos are mostly atmospheric events which are not related to any GRB. The goal of the statistical part of our analysis is to determine how consistent the neutrino candidate events are with being produced by GRBs. This analysis will give us access to the strength of a hypothetical signal, but because we expect occasional accidental correlations between atmospheric neutrinos and GRBs, we need a method that estimates the most likely signal strength given any particular observed ensemble of events. As we concentrate only on a subset of all the GRBs namely the ones with a short duration, we apply a different statistical analysis that the "classical" unbinned likelihood used for the GRB searches within the IceCube Collaboration [34]. As we will see this leads to very competitive results while offering a substantial gain in cpu processing time and avoids the introduction of assumptions on the energy spectrum of the neutrinos.

As we have outlined in Chapter 2, neutrinos are expected to be produced during three different phases of a GRB event: before the GRB light flash (precursor neutrinos), during the flash (prompt neutrinos) and after it (afterglow neutrinos). As we have discussed earlier, the timing signatures of these neutrinos are possibly complex and we expect a broad range of possible spectra for each of these specific phases. The prompt phase is the best theoretically predicted phase and the one for which there is the best agreement between the different models. Therefore the searches performed by the IceCube Collaboration have mostly concentrated on prompt neutrinos.

In this context, we have decided to perform two possible statistical searches. The first one has been developed for being sensitive to all possible neutrino emission phases and is based on the relative arrival time of the neutrino candidate events. The second approach consists of a simple counting experiment where signal events are counted, and the significance of the observation relative to the expectation from background

is determined using the Poisson distribution. We start this Chapter with a separate discussion presenting the method and the chosen tests statistic used for the two approaches. We then present the approach for deriving the needed observables applied for both analyses and conclude with the way the analysis will be performed on the real data sample.

∴

6.1 Methods and Test Statistics

This analysis is based on a stacking procedure for all the SGRBs in the considered period, which amounts to 84 for the 4 considered years. As we describe in the next section, we characterise the performance of the analysis and calculate fluence constraints and statistical significances of the data based on frequentist statistics. In this approach, we need to define a quantity used to compare hypothetical and actually observed experimental outcomes with each other, called *Test Statistic*. This means that we construct a variable that describes typical background in such a way that if signal events are present, the computed resulting value of this variable deviates sufficiently enough from a typical background-only value. We present below the cuts and the test statistic for the two investigated approaches in this thesis.

6.1.1 All phases search

The goal of this section is to develop a method that would not only be sensitive to prompt neutrinos but also to precursor or afterglow neutrinos. We have to keep in mind that there is an obvious lack of knowledge about the expected precursor or afterglow neutrino signal signature. Because we do not know when these neutrinos are expected and because their absolute arrival time on Earth will be affected by the redshift of their progenitor, we have decided to develop a method only based on the relative arrival time of the neutrinos on Earth.

For this approach, we perform for each GRB an angular cut on the corresponding full data sample (we thus use the full 2 hours of recorded data $[t_{\mathrm{GRB}} - 1\,\mathrm{hr}, t_{\mathrm{GRB}} + 1\,\mathrm{hr}]$). The applied angular cut consists of an angular cut around the GRB position. For this we take into account the two angular uncertainties of the analysis: the error on the GRB position and the reconstruction angular error. The 1σ error on the GRB position is given by the GCN circular and the 1σ reconstruction error has been calculated from the angular resolution of the considered reconstruction, the MuEx4MPE fit (see Fig. 5.28), which amounts to 1.352° for a BDT score cut of 0.10. These 1σ errors are quadratically added. Finally, we have chosen, after optimisation for different sigma values, to consider the total 2-sigma error. Our angular window is therefore given by

$\mathrm{err}_{\mathrm{tot}} = 2 \times \sigma_{\mathrm{tot}} = 2 \times \sqrt{\sigma^2_{\mathrm{GRB}} + \sigma^2_{\mathrm{reco}}}$.

We know that our neutrino events follow a Poissonian distribution. The probability for observing n events in a time interval Δt and with a rate of r is therefore given by:

$$\mathrm{p}(n|r, \Delta t) = \frac{(r\Delta t)^n}{n!} \exp(-r\Delta t). \tag{6.1}$$

We can now invert the question and ask ourself what would be the time needed $\mathrm{d}t$ to observe n events. This leads us to the so-called *Erlang distribution* [195] which is defined as

$$\mathrm{p}(\Delta t|n, r) = \frac{(r\Delta t)^{(n-1)}\ r}{(n-1)!} \exp(-r\Delta t). \tag{6.2}$$

The parameter n is called the shape parameter and defines the studied time interval. For $n = 1$, the time interval is computed between neighbour events and we obtain the expected exponential distribution. For $n = 2$, we consider the time interval needed to detect 2 events, *i.e.* the interval between next-to-neighbour events and so on for the following integers. As we expect that the signal events are emitted during bursts of neutrinos, we expect that the Δt of signal events are small. As the negative exponential distribution exhibits already a natural maximum at zero, the case of $n = 1$ in Eq. (6.2) is not of interest for us. We therefore concentrate on shape parameters $n > 1$. Intuitively, $n = 2$ appears to be the best choice because higher values would "dilute" the signal events and we have performed our analysis for this shape parameter. A specific study has however been performed for $n = 1$ and $n = 3$ and lead to worse sensitivity curves than the $n = 2$ case. Fig. 6.1 gives an example of the background time intervals distribution computed for next-to-neighbour events.

If signal events are present in the data set, they are expected to yield clustering of events in the stacked time windows if our GRBs contain some generic inner engine and consequently the distribution of Δt will deviate from the Erlang distribution. We use this deviation as the definition of the test statistic for this approach. Therefore, we have decided to use a simple Pearson's χ^2 test as the test statistic. As we already mentioned, for SGRBs, we expect the prompt neutrino signals to arrive with small Δt and we therefore expect a deviation from the Erlang distribution in the small Δt region. This nicely matches the fact that the Erlang PDF for background events vanishes at low Δt values, leading to a high sensitivity for signal events. If the precursor or afterglow neutrinos also arise from a "burst", they will also be depicted by small Δt between events. Therefore, we expect the deviation from the Erlang distribution in the small Δt. We have decided to compute our χ^2 test only for the Δt values smaller than the maximum value of the Erlang distribution, to avoid the natural statistical variation of the tail of the distribution. The Pearson's χ^2 test for this case is given by:

$$\chi^2 = \sum_{\mathrm{i}=1}^{n} \frac{(O_i - E_i)^2}{E_i}, \tag{6.3}$$

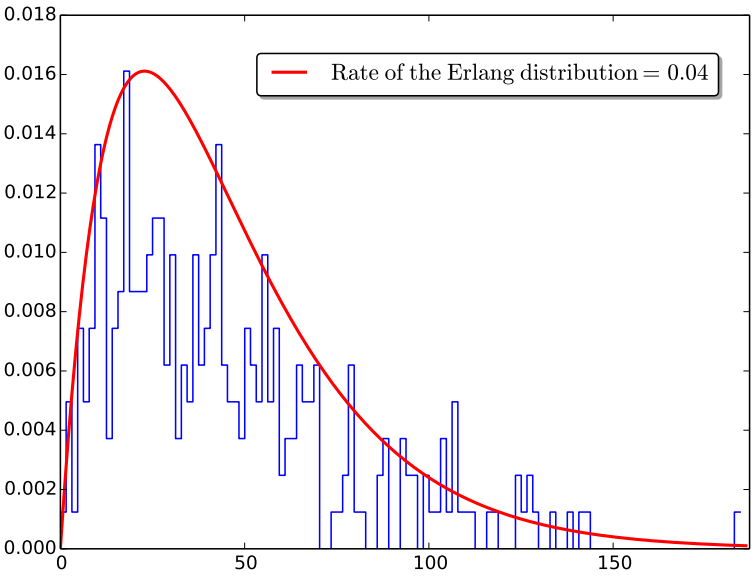

Figure 6.1: Next-to-neighbour time interval distribution for background-only (BDT score cut ≥ 0.0). The horizontal axis is Δt [s] and the vertical axis is the normalised number of events in each bin of Δt. The red line is the corresponding Erlang best fit pdf, $p(\Delta t|n = 2, r = 0.04)$.

where i refers to the bin number, n is the bin number corresponding to the maximum of the Erlang distribution, O_i is the number of observation in bin i and E_i is the corresponding value of the Erlang function. We have nevertheless tested the computation of the χ^2 test on the full distribution for stability check. This study has confirmed that the χ^2 test computed on only the small time intervals is more sensitive and does not introduce any bias.

6.1.2 Prompt search

For this approach, we have decided to apply a simple cut and count method. Two cuts are applied on the data. The first one selects events based on their timing with respect to the GRB trigger time and the second only picks up events of which the direction points back around the GRB position. After these two cuts, we simply use the Poisson statistic, see Eq. (6.1), to determine our discovery potentials and sensitivities.

- Time cut: Different time windows have been investigated, and it has been chosen to define the cut on the time so that the starting time of the events are in a time window of 4 s around the GRB trigger time of $[t_{\mathrm{GRB}} - 1\,\mathrm{s}, t_{\mathrm{GRB}} + 3\,\mathrm{s}]$ (remember

that in the current analysis, we only investigate GRBs with a total duration less than 2 seconds).

- Spatial cut: The angular cut is the same as for the all phases search and is given by $\mathrm{err}_{\mathrm{tot}} = 2 \times \sigma_{\mathrm{tot}} = 2 \times \sqrt{\sigma^2_{\mathrm{GRB}} + \sigma^2_{\mathrm{reco}}}$

6.2 Frequentist approach

We now use the previously defined test statistics for describing the possible signal strenght. For this, we use a frequentist approach and define fluence constraints and statistical significances of the data.

We therefore define the significance of an observed test statistic T_{obs} as the probability of obtaining an equal or larger value based on a distribution of background-like pseudo-experiments. These pseudo-experiments lead us to the so-called "null-hypothesis" test statistic distribution. We then study the response of the analysis to a possible signal using a Monte-Carlo based generation of pseudo-experiments containing simulated neutrino signal events mixed with the background only pseudo-event sample. For this, we compute the normalisation factor μ of the neutrino spectrum, reweighting Eq. (4.27) with an overall signal strength, needed for detecting the presence of the signal in the data. As we aim for a discovery, we apply this approach for different BDT score cut in view of optimising the BDT score cut to obtain the best discovery potential, *i.e.* the lowest possible μ.

6.2.1 Randomised background pseudo-experiments

As described above, the first step in our statistical analysis is to perform background-only pseudo-experiments. For this we use our off-time burn sample and scramble this data with assigning a random azimuth value between 0 and 2π and a random time value in the two hours time window. We then apply the cuts of the specific method (see Section 6.1.1 and 6.1.2) and compute the test statistic for each of these 10^8 randomisations.

Changes in the atmosphere temperature over the course of the year result in a seasonal variation in the down going cosmic ray air showers [196, 197] and therefore in our background estimation, see Fig 6.2. We take this effect into account by having chosen our 48 patches composing the burn sample as one patch per month in the 4 considered years.

6.2.2 Randomised signal injection

For the signal injection we use standard diffuse datasets (which contain events distributed evenly throughout the sky) to simulate pseudo-point source datasets by selecting, for each GRB, events in a zenith band of 1° around the burst location. As is described

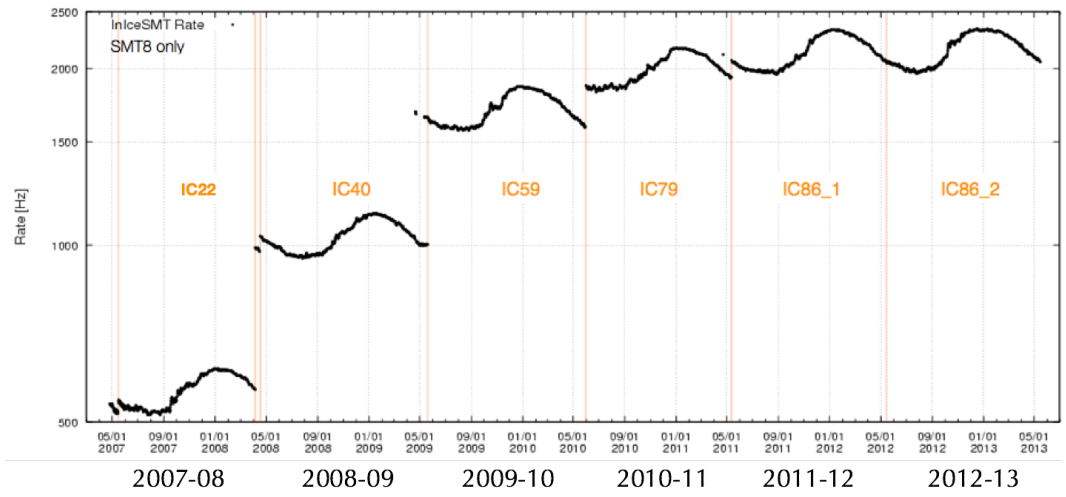

Figure 6.2: Seasonal variations of the background rate in the IceCube Observatory. With the courtesy of P. Desiati.

in Section 4.4.1, the pseudo-GRB angular resolution needed for displacing the simulated neutrino direction with the Kent distribution, is drawn randomly from the catalog of GRBs which have happened during the 4 first years of IC86. As in both methods we need a detection time of the neutrino candidate, we simulate this for each NuGen event in the 1° zenith band. For this, we generate an event starting time in the detector according to the T_{90} of the GRB following a signal time PDF. This PDF is constructed based on the actual state of theoretical knowledge of neutrino emission during GRBs. The PDF is flat during the gamma ray emission, and has Gaussian tails to avoid a hard time cut at the edges of the on-time window. The width of the Gaussian tails is given by σ_t, which is set to the GRB duration (T_{90}). The tails of the Gaussians are trunctated at $4\sigma_t$. An example of a signal time PDF is given in Fig 6.3.

For the all phases study, we have to take into account the redshift of the GRBs because it is responsible for time delay. In this case, we have fitted a function describing the known redshift distribution [198] of the GRBs and randomly generate a redshift value for each pseudo-experiments.

As discussed in Section 4.4.1, event weights from the neutrino-generator are constructed such that the sum of the weights of simulated events gives the rate of such events. The individual event weight w_i can be treated as the Poisson rate for the occurrence of that event. The probability of a signal event being injected is therefore given by:

$$p_i = \frac{w_i}{1!} e^{-w_i} \approx w_i, \tag{6.4}$$

where the approximation is valid because the individual weights are very small. Each pseudo-experiment consists then of picking a random number between 0 and 1 for each

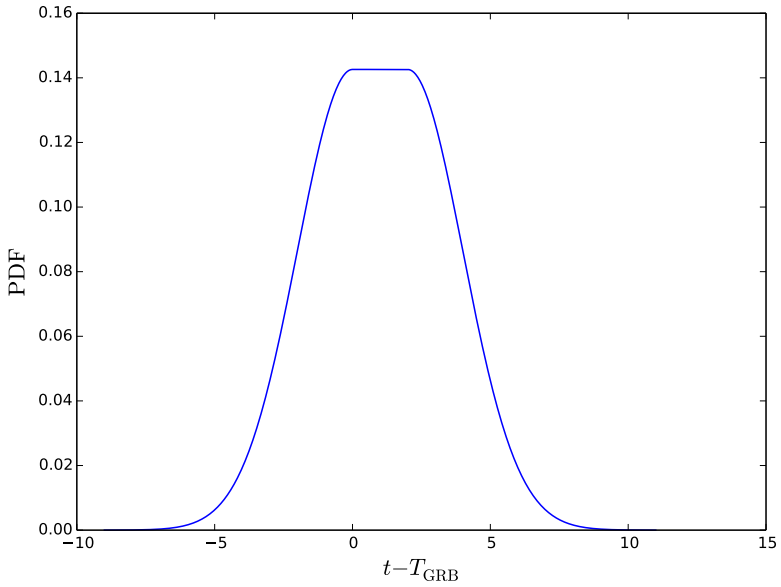

Figure 6.3: Example of the signal time PDF for $T_{90} = 2\,\mathrm{s}$.

NuGen event. If this random number is less than w_i, the event is injected for the computation of the test statistic value otherwise it is rejected.

6.2.3 Significance and Discovery Potentials

As explained above, we use the test statistic to define the significance of the analysed dataset. As outlined in [192], the significance is defined as the probability (called p-value) of obtaining an equal or greater test statistic value from background events if the true signal strength is zero. The significance is commonly expressed as a number of sigmas, which relates it to the Gaussian distribution. In particle physics, the threshold for a discovery claim is set conventionally, if somewhat arbitrarily, at 5σ corresponding to a p-value of about 10^{-7}. As we aim for a discovery we therefore need enough background-only randomisation to achieve this limit. The background-only T distribution is obtained by performing 10^8 pseudo-experiments with no signal injection. The test statistic distributions for both approaches are shown in Fig 6.4 and 6.5.

The discovery potential is a measure that quantifies the signal strength needed to obtain a significant result given the simulated signal acceptance and measured backgrounds. It is defined as the signal normalisation which yields a 5σ result with respect to the background expectation in 50% of signal-injected pseudo-experiments. This quantity is found using a minimisation routine which performs 10^4 pseudo-experiments

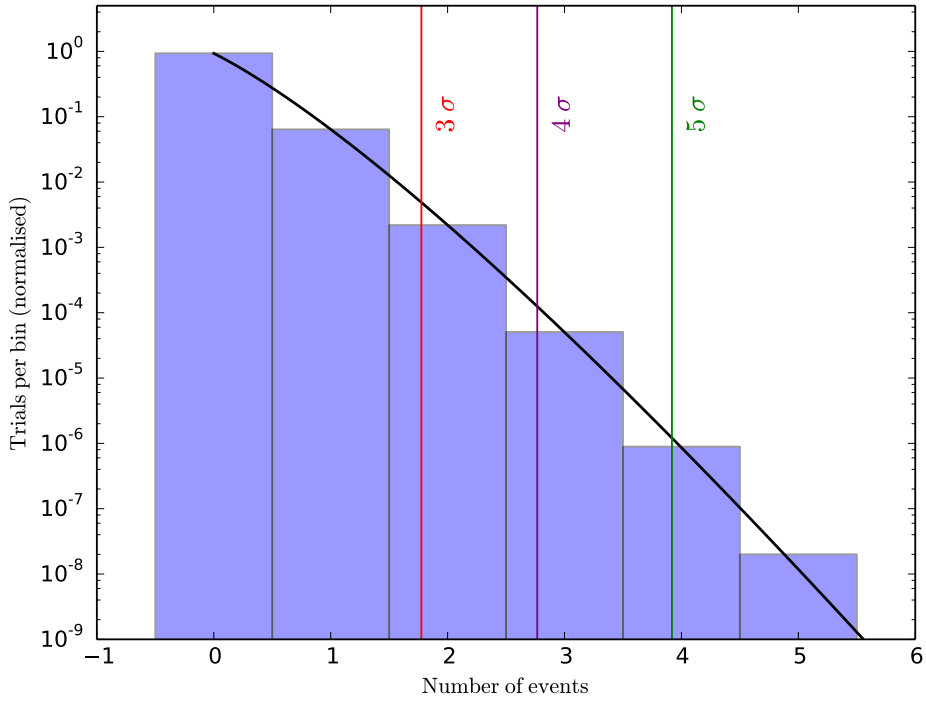

Figure 6.4: Test Statistic distribution (BDT score cut ≥ 0.10) for the prompt search. The values of the test statistic corresponding to the 3, 4 and 5 σ thresholds are respectively shown by a red, purple and green line. The black line refers to the Poisson distribution best fit.

for each signal normalisation tested until the 5σ threshold is exceeded by 50% of trials. A related quantity is the least detectable signal: the signal normalisation which yields a 5σ result in 90% of trials.

Both quantities are useful for optimising our analysis. As outlined before, the analysis is performed with the hope of observing a significant result, and the discovery potential and least detectable signal quantify the signal strength required to do so. Therefore, these are the quantities that are used for determining the optimal final classifier score cut. The optimisation curves for the prompt search are shown for a generic E^{-2} in Fig. 6.6 and for the Waxman-Bahcall flux, *cf.* Eq. (2.17), in Fig. 6.7.

For the all phases search, as the theoretical expectations are not well defined for the precursor and afterglow signatures, two options have been investigated: the first one computes the discovery potentials and least detectable signals for the only well-predicted signature, the prompt phase (Figures 6.8 and 6.9) and the second one simulates the

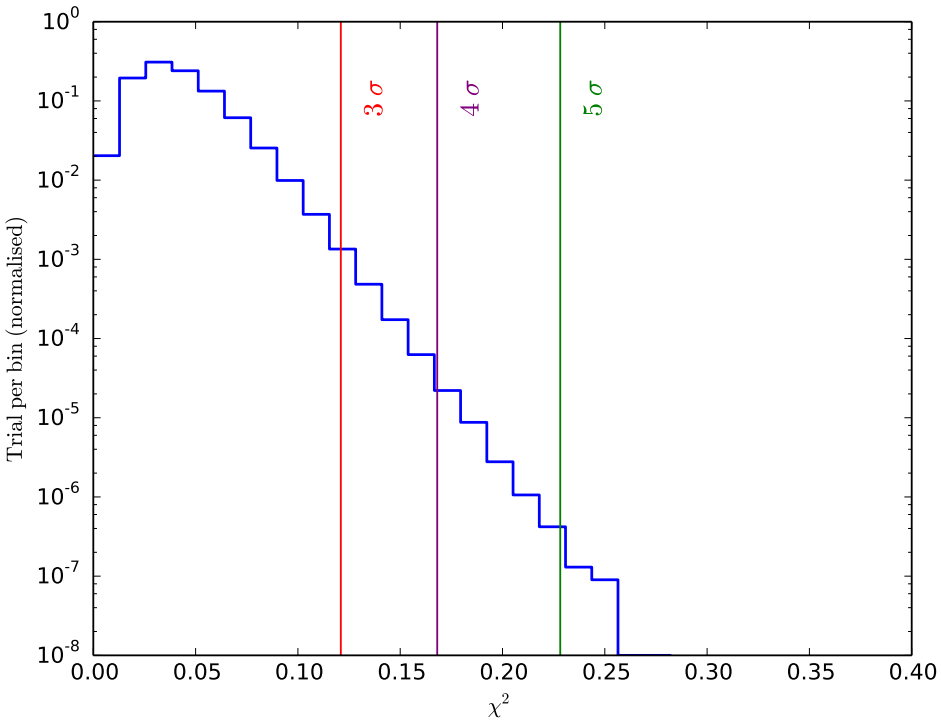

Figure 6.5: Test Statistic distribution (BDT score cut ≥ 0.10) for the all phases search. The values of the test statistic corresponding to the 3, 4 and 5 σ thresholds are respectively shown by a red, purple and green line.

analysis response for a generic and extremely simple precursor signal based on neutrinos emitted, at the source, one minute before the GRB flash and during T_{90}. This signal is then redshifted by randomly generating a redshift corresponding to the observations of the redshift distribution for the SGRBs [198]. The result for an E^{-2} spectrum for this signal simulation is given in Fig. 6.10.

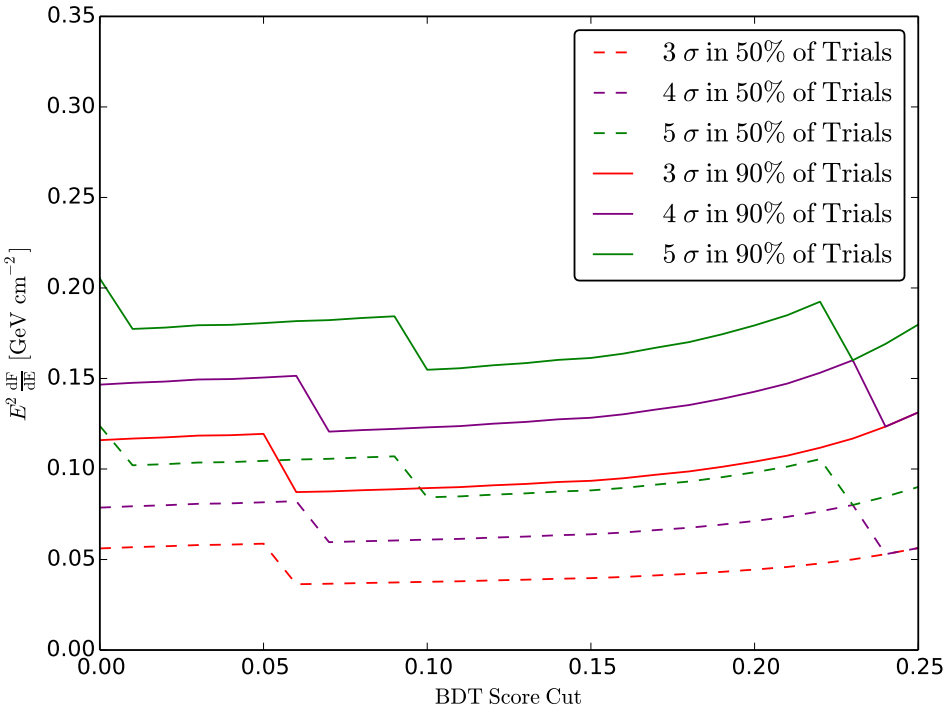

Figure 6.6: Discovery potentials and least detectable signals for the prompt search in function of BDT score cuts for a generic E^{-2} signal spectrum. The 3, 4 and 5 σ thresholds are respectively shown by a red, purple and green line. The steps visible on this plot arise because of the intrinsic integer character of the Poisson distribution.

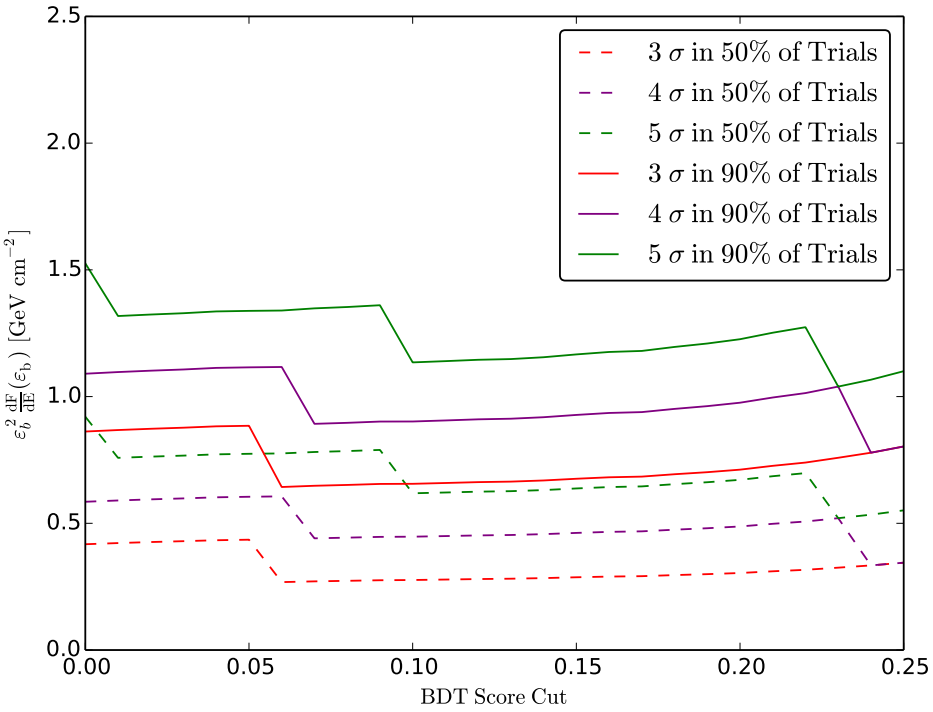

Figure 6.7: Discovery potentials and least detectable signals for the prompt search in function of BDT score cuts for the Waxman-Bahcall signal spectrum. The 3, 4 and 5 σ thresholds are respectively shown by a red, purple and green line. The steps visible on this plot arise because of the intrinsic integer character of the Poisson distribution.

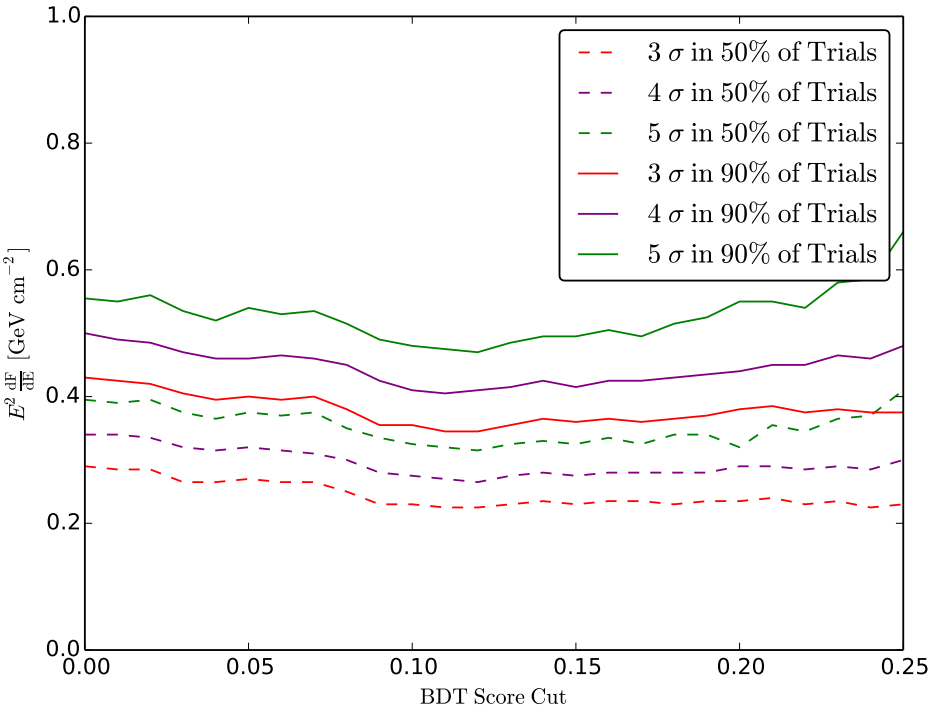

Figure 6.8: Discovery potentials and least detectable signals for the all phases search (prompt signal) in function of BDT score cuts for a generic E^{-2} signal spectrum. The 3, 4 and 5 σ thresholds are respectively shown by a red, purple and green line.

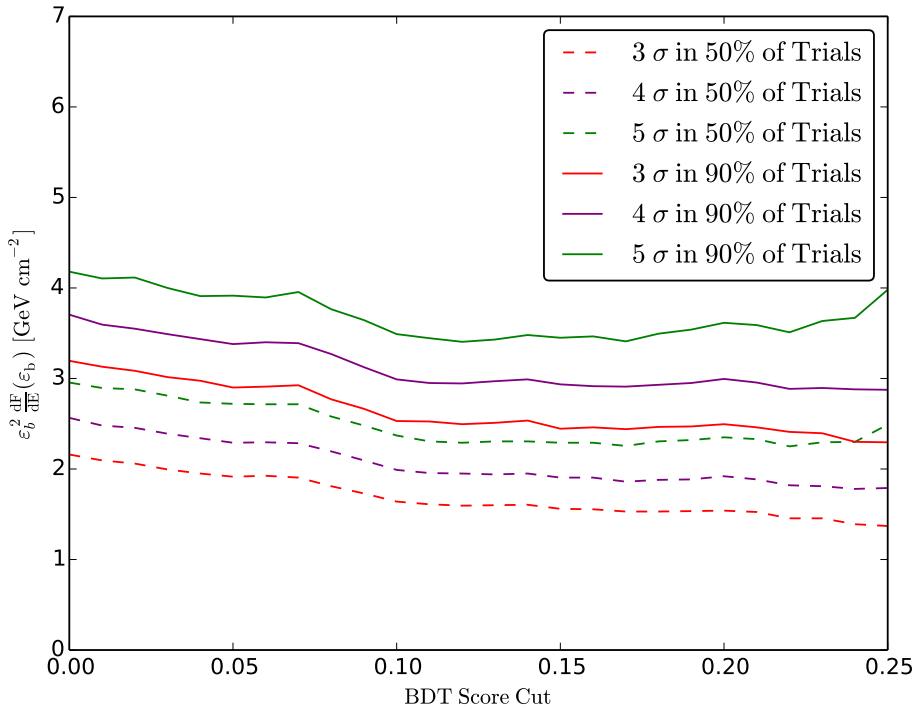

Figure 6.9: Discovery potentials and least detectable signals for the all phases search (prompt signal) in function of BDT score cuts for the Waxman-Bahcall signal spectrum. The 3, 4 and 5 σ thresholds are respectively shown by a red, purple and green line.

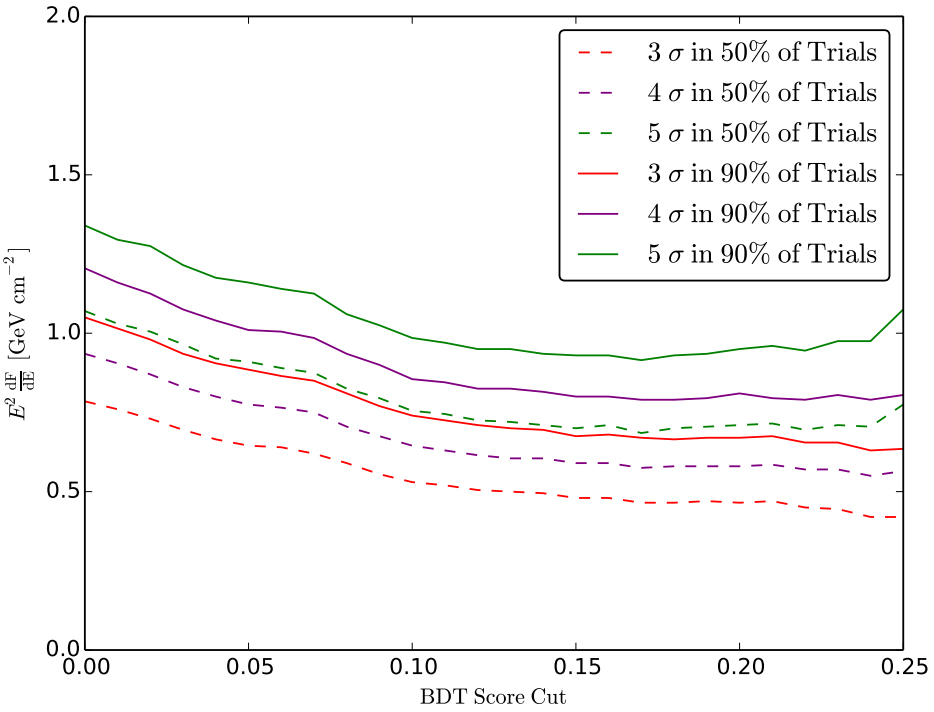

Figure 6.10: Discovery potentials and least detectable signals for the all phases search (precursor signal) in function of BDT score cuts for a generic E^{-2} signal spectrum. The 3, 4 and 5 σ thresholds are respectively shown by a red, purple and green line.

6.2.4 Upper limits and Sensitivity

As explained in [156], based on the previously defined test statistic distributions, we construct one-sided confidence intervals [199, 200, 201] as follows: for each value of μ, a confidence belt is found such that, for repeated experiments, the probability of observing a test statistic greater than $T_1(\mu)$ is some defined percentage, e.g. 90%. This function is then inverted so that $\mu_1(T)$ is a function of T such that for an observed value of T, $\mu_1(T)$ is an upper limit for μ at the 90% confidence level (CL). Practically, this means that upper limits are calculated in a similar manner as the discovery potentials. The exclusion CL for a given signal normalisation is the fraction of trials which yield $T > T_{\text{obs}}$.

For optimisation purposes, the sensitivity is defined as the average 90% CL upper limit, weighted using the background-only T distribution, *i.e.* the value of the signal normalisation which yields a test statistic value greater than the median test statistic value in 90% of trials. The results of these calculations are again given respectively for E^{-2} and Waxman-Bahcall flux in Figures 6.11 and 6.12 for the prompt search.

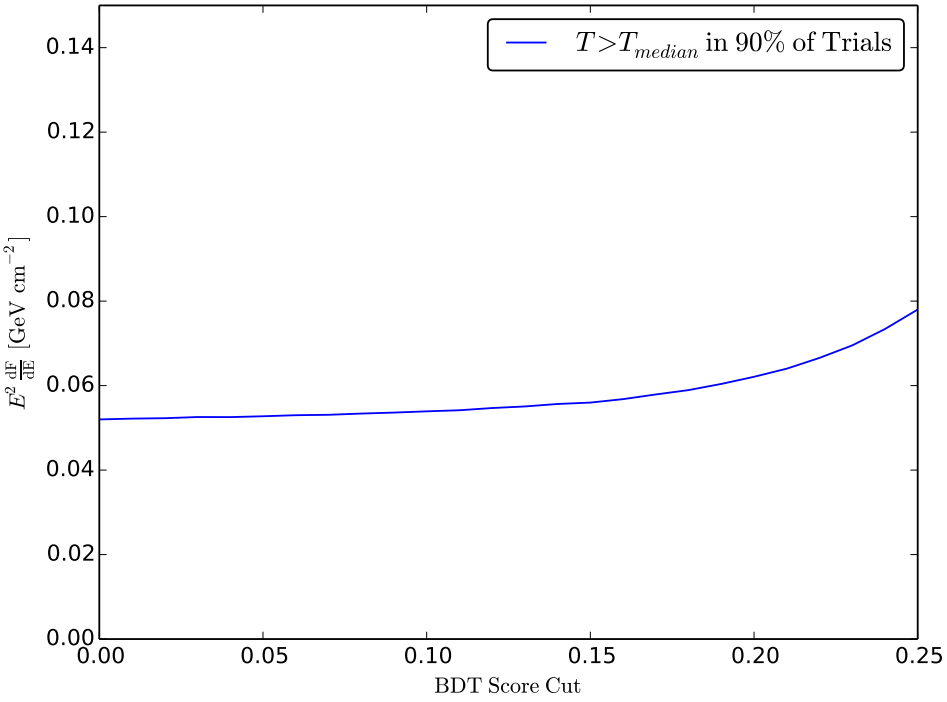

Figure 6.11: Sensitivity curve for the prompt search in function of BDT score cuts for a generic E^{-2} signal spectrum.

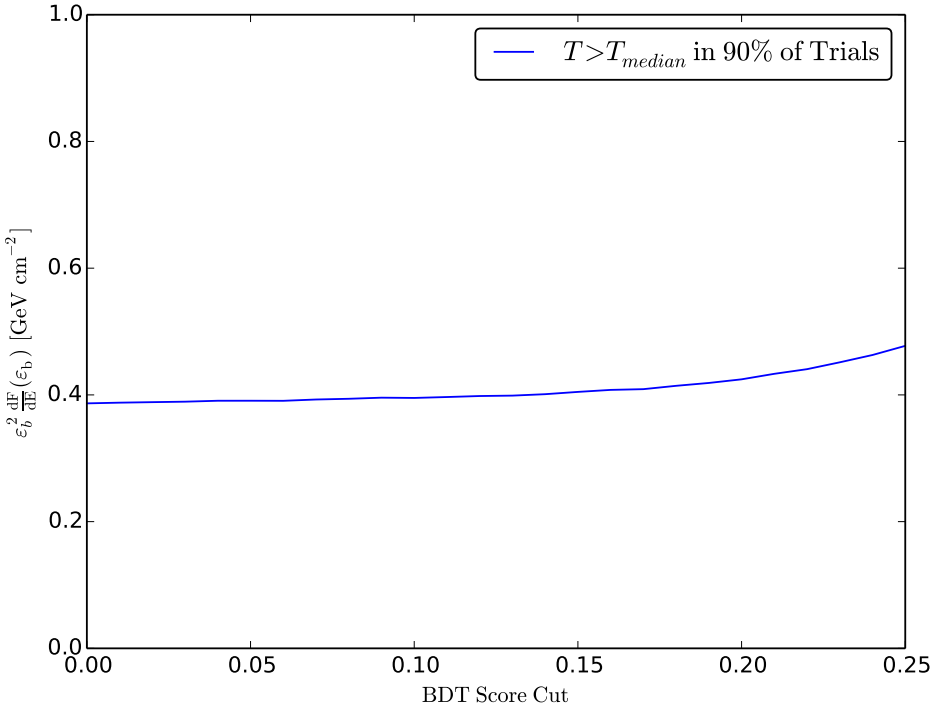

Figure 6.12: Sensitivity curve for the prompt search in function of BDT score cuts for the Waxman-Bahcall signal spectrum.

As for the discovery potentials, we present the results for two typical possible signal signatures. The analysis response for the only prompt signal is visible in Fig. 6.13 and 6.14, whereas the result for an E^{-2} typical precursor signature (see definition in previous section) is shown in Fig. 6.15.

6.3 Optimisation and final cut choice

We have shown our analysis responses to different signal signatures based on two possible statistical tools. We now have to determine which is our final statistical analysis method that will be applied on the real data and which, after optimisation, defines our final BDT score cut and finalise therefore our event selection procedure.

We have developed two possible statistical tools for analysing the data. One of these aims to analyse the data for detecting possible precursor, prompt or afterglow signal events. As the constraint on prompt neutrinos is already stringent and because our three phases search has never been performed in IceCube, we decide to use this method

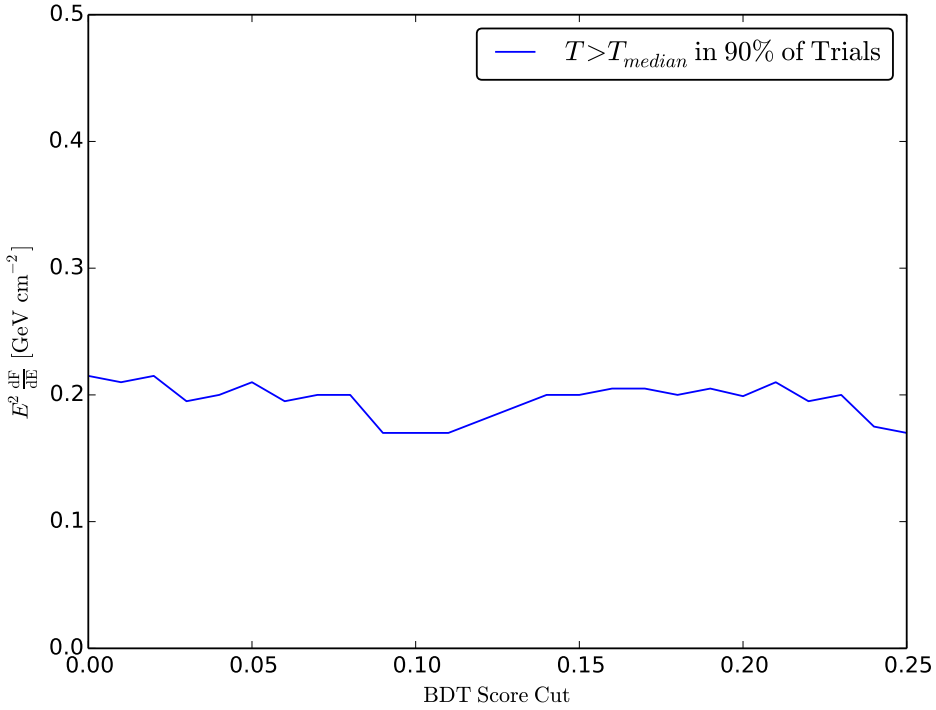

Figure 6.13: Sensitivity curve for the all phases search (prompt signal) in function of BDT score cuts for a generic E^{-2} signal spectrum.

for optimising a possible discovery. As can be seen from the corresponding discovery potential and sensitivity curves, we loose sensitivity with this method compared to the cut and count but we also investigate an unexplored region. This worse sensitivity is logical because the all phases search only analyses the data through pairs of neutrinos which obviously introduce an intrinsically lower sensitivity than a cut and count method that uses every event independently. If no discovery is made with the Δt method, we therefore will use the cut and count method for computing flux upper limits and constraining the prompt models (there is no convincing model for precursors or afterglows to constrain).

We first consider the discovery potential Fig. 6.8, 6.9 and 6.10 (and more precisely the 5σ curve for the least detectable signal) for the optimisation purpose. We see that whatever the signal spectrum and signature, it is not strongly sensitive to the exact cut value in the BDT score cut range of $[0.10, 0.15]$. The sensitivity figures for the prompt search show that optimising for limit setting would yield a looser cut. However, the sensitivity limit barely changes if the cut is tightened from 0.05 to around 0.15. In the end, choosing the final cut is a subjective decision. The statistics

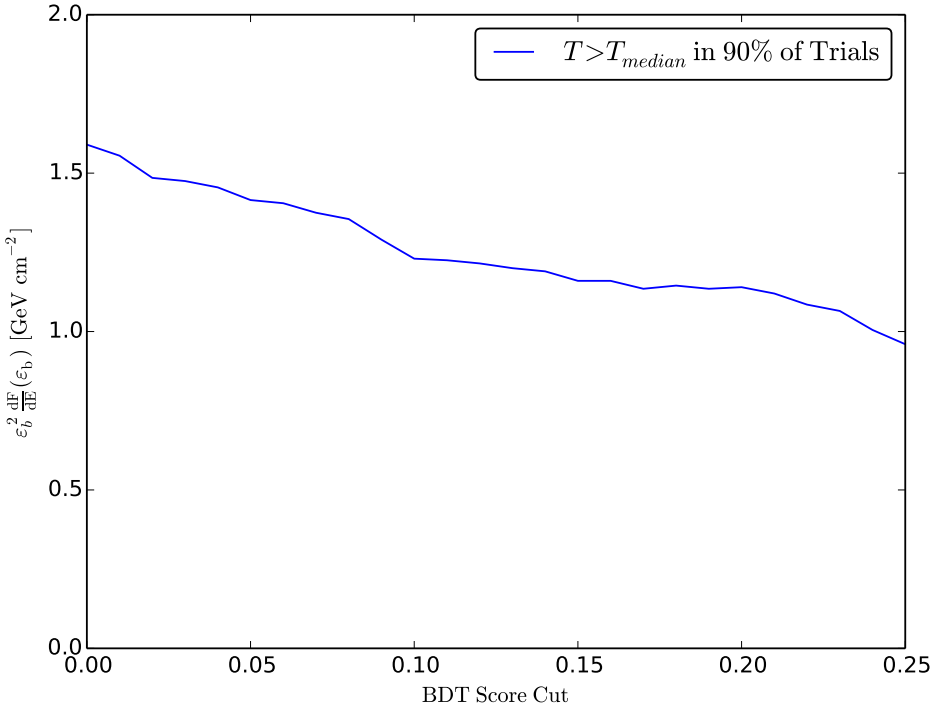

Figure 6.14: Sensitivity curve for the all phases search (prompt signal) in function of BDT score cuts for the Waxman-Bahcall signal spectrum.

analysis helps us to fix this limit, but it cannot be the last word. In our case, as can be seen in Fig. 5.27, the BDT used for the analysis is energy dependent. As the cut is tightened, first we reject mis-reconstructed events but then we begin to reject low energy neutrinos which are the least signal-like events in the atmospheric neutrino background. The plots above show that cutting away more of the low energy neutrinos slightly degrades the prompt sensitivity limit but that it is crucial to do so to arrive on the discovery potential optimum plateau and so to improve this limit. But besides these criteria, we also want to make sure we do not cut too hard and miss events that are potentially interesting. That is, we would prefer to see an intermediate-significance, low energy neutrino than to cut it out of the analysis.

Furthermore, comparing the E^{-2} and the Waxman-Bahcall optimisations, we realise that the normalisation for high BDT scores is highly dependent on the hardness of spectrum. As we do not know precisely which spectrum we are expecting, we propose to stay on the safe side and avoid too hard cuts. With all of this in mind, we propose a final cut of 0.10. This is the loosest cut which is still in the discovery potential signal optimum plateau. It is slightly tighter than the prompt sensitivity optimum, resulting

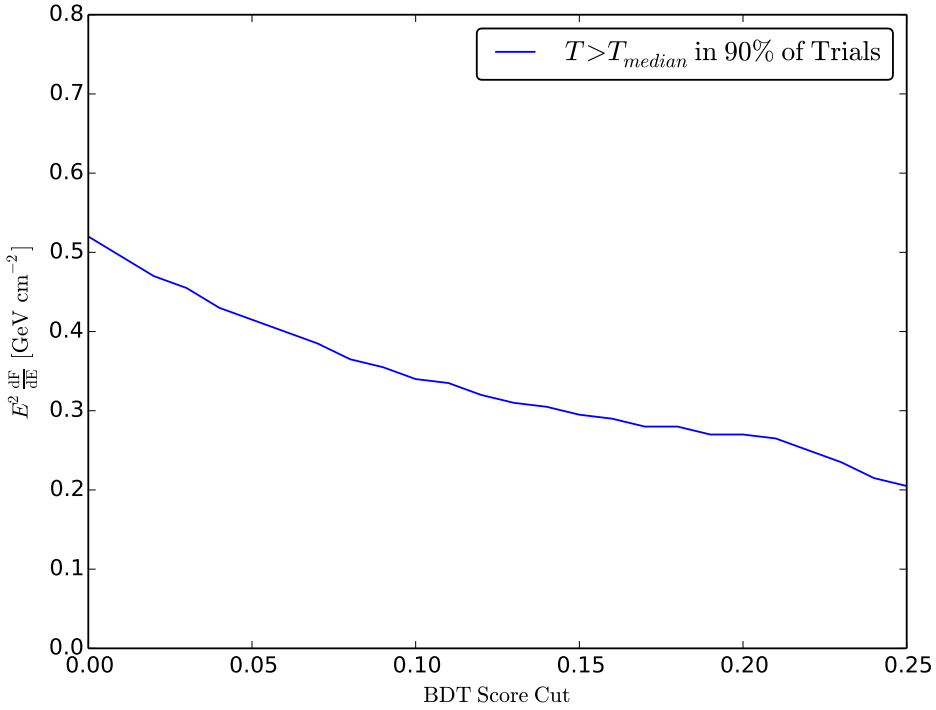

Figure 6.15: Sensitivity curve for the all phases search (precursor signal) in function of BDT score cuts for a generic E^{-2} signal spectrum.

in a slightly higher sensitivity limit.

CHAPTER 7

Results of the 4 years IC86 Search

As explained in the previous Chapters, we have performed a *blind* analysis. The concept of a blind analysis is to avoid or, at least, to reduce any experimenter's bias, the unintended biasing of a result in a particular direction. This implies that the method that is being used for analysing the data is fixed before the analyser looks at data in its final form. In our thesis, we have achieved blindness by using the hidden box method [202], which keeps the data in a defined on-source region blinded. In Chapter 5 and 6, we therefore have defined our cuts and test statistics, as well as the sensitivities and discovery potentials solely from off-source data (*i.e.* our burn samples and simulated signals) without looking into the on-source region. In the IceCube Collaboration, the unblinding of the data is only authorised after an extensive reviewing process. This analysis has received the unblinding approval on August 27th, 2015. Once approval was obtained, the on-source data have been analysed and the significance of the analysis has been computed. Unfortunately we had also to compute an upper limit of the expected flux sincee no significant signal has been observed.

This Chapter is devoted to the results of the unblinding of the on-source data. The two first sections provide the significance of the performed analyses. Section 7.3 presents the systematic errors we have to take into account in our analysis and the last section of this thesis presents, unfortunately, only the constraints we have derived on the theoretical prediction for a prompt neutrino flux orginating from Gamma Ray Bursts.

∴

7.1 Results of the all phases search

We have described in Section 6.1.1, the details of the performed cuts and the definition of the test statistic used for the all phases search. The background data we have used

to determine the rate of the Erlang distribution has been computed by considering identical sky patches as the on-source regions but at the opposite direction in the sky (180° in azimuth but keeping the declination the same). Below, we give the final result for this analysis.

The final test statistic amounts to $\chi^2_{\text{obs}} = 0.024$ which leads to an analysis significance characterised by a p-value of $p = 0.83$. The background-only test statistic distribution and the final result are shown in Fig. 7.1. This result does not lead to any discovery and

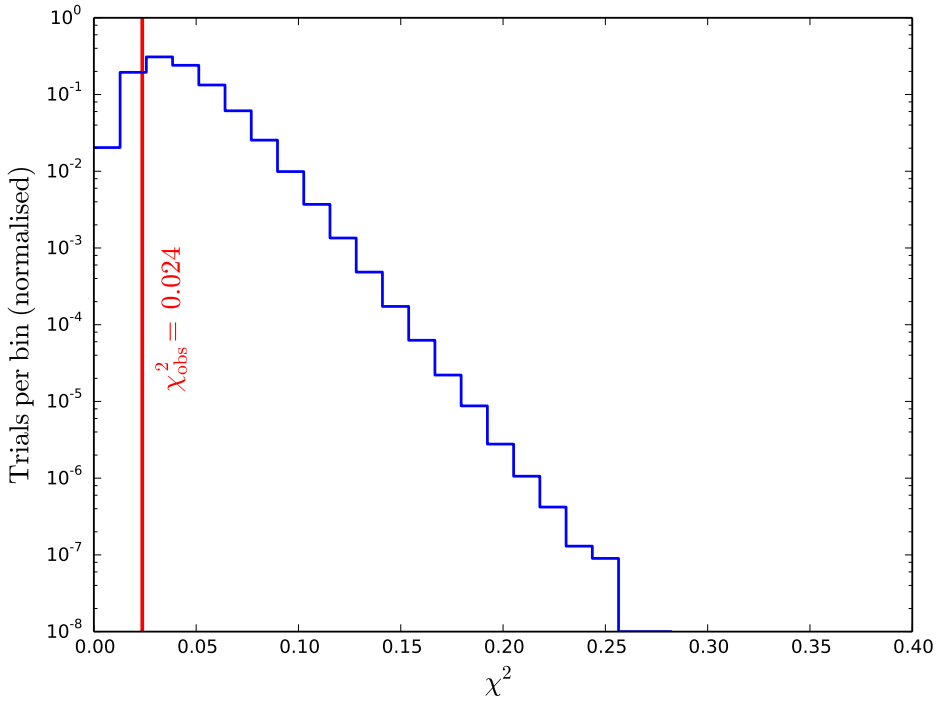

Figure 7.1: Background-only test statistic distribution for the all phases search with the observed test statistic of the unblinded on-source data shown in red.

we will therefore compute upper limits on the prompt theoretical models.

7.2 Results of the Prompt Search

As we saw in the previous section, the all phases search has not lead to any discovery and consequently we apply below the method of the prompt search, *i.e.* the cut and count analysis, in order to provide an upper limit on the neutrino fluence to restrict certain models.

After applying the two defined cuts of this search (see Section 6.1.2), the number of events passing these cuts, *i.e.* the test statistic of a cut and count experiment, amounts to $n = 0$, which corresponds to a p-value of $p = 1$. Before deriving upper-limits, we will discuss below the systematic errors of our analysis and compute constraints on the prompt neutrino emission model, parameterised in Eq. (2.17).

7.3 Systematics uncertainties

In the next section we will compute the one-sided confidence interval upper limit on the neutrino flux correlated with SGRBs. This result is obviously affected by systematic errors in the measured background and the simulated signal events. However, since this analysis is based on off-source data to describe the background, the systematic uncertainties on the final limit are minimal. The only part of the analysis that is subject to systematics errors is the signal simulation due to uncertainties in the properties of the detector, including the ice properties and properties of the Standard Model of Particle Physics. All these uncertainties impact the neutrino flux arriving at the detector but also the amount of photons detected by the DOMs composing IceCube and propagate in all the steps of our analysis through the computed flux limits.

7.3.1 Sources of uncertainties and estimation of their impact

An extensive study of these systematic errors has been performed, for the same type of analysis, in [192]. We have therefore decided to refer to that study for estimating the impact of the various errors for our analysis and will briefly resume the obtained results in the following paragraphs. It is important to keep in mind that in general, the error in the limit is dominated by effects on lower energy events, *i.e.* events with the worst reconstruction and for which the uncertainties play a relatively higher role. The impact of each of these uncertainties is therefore spectrum dependent: softer spectra are subject to larger systematic errors. In [192], the error estimation in the generic broken power law model, has been calculated for an E^{-2} spectrum and conservatively applies the resulting value to the entire range of E^{-1}/E^{-2} break energies.

Optical Module Efficiency. A first uncertainty that has to be taken into arises directly from the detection modules of IceCube, the DOMs. As presented in Section 3.3.1, the DOMs are composed of photomultiplier tubes that collect and enhance the light signal left by the particles travelling through the ice. The quantum efficiency of the DOMs is therefore an important factor of uncertainties. By scaling the recorded charge for a given amount of emitted light, it has a direct impact on the reconstructions attempts. The uncertainty of the DOM efficiency relative to the baseline simulation is conservatively estimated to be $\pm 10\%$. The impact on a E^{-2} flux limit of this error has been estimated to $^{+4.0}_{-4.3}$ [192].

Photon Propagation in the Ice. As discussed in Section 3.2, the absorption and scattering properties of the ice are an other important aspect of IceCube and has obviously an impact on the detection and timing of the produced light. The profiles of these two ice properties are measured as a function of depth using the flashers deployed on the DOMs. The errors on these fits are estimated to be ±10%. The impact on a E^{-2} flux limit of this error has been estimated to $^{+1.7}_{-5.0}$ [192].

Particle Physics and others. The neutrino simulation is also subject to various uncertainties: interaction cross section[1], muon energy losses, density profile of the Earth and the rock density near the detector. All these important variables of the simulation scale the final number of neutrinos detected in IceCube by impacting the Earth absorption, the probability of a neutrino to produce a muon in the ice and the amount of light deposited near the detector. For vertically up-going events and an E^{-2} spectrum these effects contribute a maximum $\sim 8\%$ uncertainty in the neutrino rate [203]. We choose, as in [192], a conservative approach by applying this value to all events and all model spectra.

7.3.2 Total systematic errors

The total systematic error is obtained by adding all the previously described errors in quadrature and taking the square root. As we already discussed, we compute one-sided confidence intervals. This means that we are only interested in effects which degrade the upper limit. This leads to an upper margin of error +9.1%. Systematic errors are included in the next section.

7.4 Model constraints

As we have found no signal events, we now compute constraints on the expected neutrino flux of Eq. (2.17).

This equation uses a total flux normalisation Φ_0 in units of $\mathrm{GeV}^{-1}\,\mathrm{cm}^2\,\mathrm{sr}^{-1}\,\mathrm{s}^{-1}$. Above, we have presented all our results in fluence units of $\mathrm{GeV}^{-1}\,\mathrm{cm}^2$ and for the total expected signal of the 84 SGRBs. We now need a per-burst fluence F_0 and assume that the 84 analysed bursts are representative of a total number of n_{GRB} bursts per year full sky. This n_{GRB} refers to the total number of GRBs potentially observable on Earth. This means that it does not refer to the number of detected bursts but estimates also the bursts that have not been seen because, for e.g., they were hidden by the Sun or moon or they occur outside the field of view of any satellite, *etc.* As in previous IceCube publications [31, 32], we take this total number of observable GRBs to $n_{\mathrm{GRB}} = 667$. We can then link the pur-burst fluence normalisation, used for weighting correctly Eq.

[1]For IceCube's energy range of interest, these interaction cross sections are only inferred indirectly, as these energies have not been reached in laboratory measurements.

(4.27), to the flux normalisation Φ_0 of Eq. (2.17) as follows:

$$F_0 = \frac{4\pi \cdot 365.25 \cdot 24 \cdot 3600}{n_{\mathrm{GRB}} \cdot 0.3} \Phi_0, \tag{7.1}$$

where the 0.3 factor accounts for the fact that the SGRBs population only represents 30% of the total GRBs population.

Following the method detailed in Section 6.2.4, we derive upper limits for the expected neutrino flux and present this result in Fig. 7.2. To account for various theoretical uncertainties, we present the result in a $\Phi_0 - \varepsilon_b$ plane for three exclusion contours of a confidence level of 50%, 1σ and 90%. As explained before, we take the systematic uncertainty for an E^{-2} spectrum as an approximate estimate of the uncertainty for this model. This corresponds here in a vertical shift of 9.1% upwards. As we can see, the

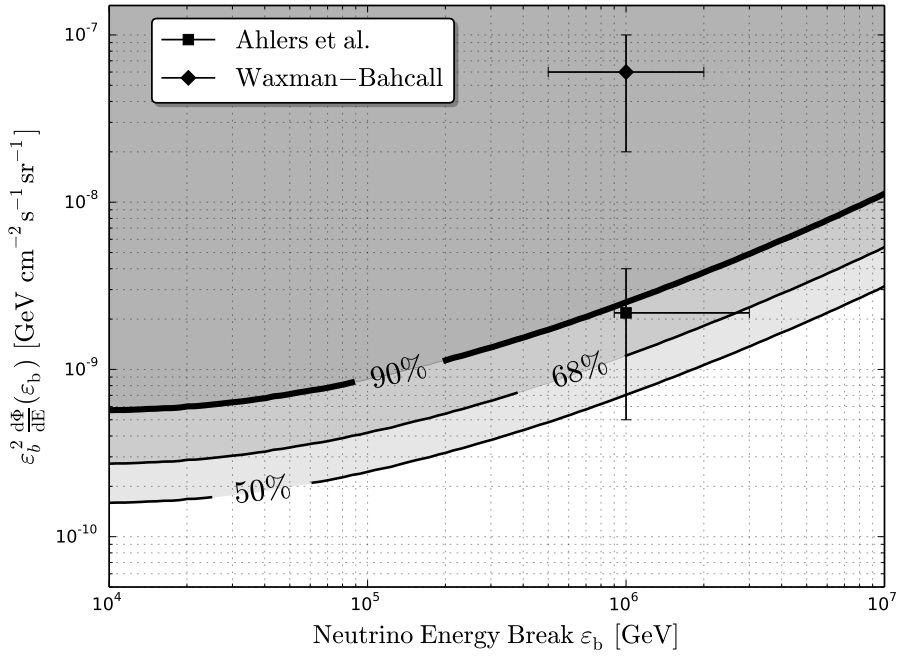

Figure 7.2: Exclusion contours showing constraints on models that predict a doubly-broken power law spectrum. Neutron escape [144] is totally excluded by our current limits; more optimistic models allowing proton escape [45] are in tension with our observations but not yet strongly excluded.

models based on neutron escape to explain the origin of the UHECRs are totally excluded by our analysis. The proton escape models are not yet strongly excluded but the range of possible variations is partly excluded and globally the model seems to be in tension with

our limits. Our results confirm previous analyses and enhance the results of the latest GRB search in IceCube, see Fig. 2.20. The less stringent limit arises from the fact that in our final search, we have analysed a drastically reduced number of GRBs compared to the previous IceCube analysis [34].

Summary and Outlook

This thesis was devoted to the study of the production of neutrinos during Gamma Ray Burst (GRBs) phenomena in the attempt to (partially) answer the question of the origin of the Ultra-High Energy Cosmic Rays (UHECRs). GRBs have been proposed as the sources of the UHECRs. Indeed, the leading model theorising the production of gamma-rays in these explosions, the Fireball Model, needs a shock mechanism that naturally accelerates protons to the desired high energies. Moreover the spectrum of these accelerated particles is compatible with the observed cosmic rays. If this model happens to be correct, the interactions between the accelerated protons and the gamma ray photons create neutrinos through the decay of photo-meson produced pions. The Fireball model predicts three possible phases of neutrinos production: prompt neutrinos, which are produced during the gamma flash, precursor neutrinos consisting of a pre-gamma ray burst and an afterglow emission. The detection of these neutrinos is therefore a smoking gun signal that GRBs are the sources of UHECRs.

GRBs are sudden, intense and non-repetitive flashes of gamma-rays. They are the most luminous and among the most energetic events in the Universe. Their energy release is measured to be as high as $\sim 10^{51}$ ergs, which is comparable with the supernovae phenomena. However, for GRBs, the energy is emitted on time scales of seconds to minutes whereas in supernovae, it can take over weeks to months. GRBs are therefore the most concentrated and brightest electromagnetic explosions in the Universe. As we have discussed in Chapter 2, GRBs are naturally divided into two subclasses based on their duration. This property seems actually to be linked to the kind of progenitors responsible for the GRBs. To take full advantage of this known physical property, we have decided to only perform our analysis on the short duration GRBs (SGRBs) which are suggested to be the visible part of the merging of two compact objects (neutron stars or black holes).

To look for neutrinos originating from SGRBs, we have used the four first years of data from the IceCube Neutrino Telescope in its final configuration composed by 86 strings of 60 optical modules each. During this period 84 workable short GRBs have been detected by the IceCube Neutrino Observatory. IceCube is an indirect neutrino detector that collects the light emitted by the charged-current created lepton travelling through the instrumented ice of the South Pole. However, independently of the produced flavour distribution at the source, the intergalactic propagation is long enough to achieve an observed flavour ratio of an approximately equal distribution for

each flavour $(e : \mu : \tau) = (1 : 1 : 1)$. Even though two muon neutrinos are produced at the source against one electron and no tau neutrino, part of the signal that has undergone a flavour change will be missed. The ongoing search for cascade-like events in the detector, the trace left by charged-current electrons, taus and by neutral current interactions will therefore complete the results obtained in our analysis.

The difficulty of observing these ν_μ resides in the enormous background of events that hide the targeted signal. The background is mainly composed of atmospheric muons and of atmospheric neutrinos. We therefore decided to only analyse SGRBs happening in the Northern sky in order to use the Earth as a natural shield against most of the atmospheric muons. However, even though IceCube has good reconstruction algorithm capabilities, the rate of misreconstructed downgoing muons as upgoing events is higher than the rate of upgoing neutrinos. In Chapter 5, we therefore developed various quality cuts, starting with a novel method called QualDist, followed by a machine learning technique. This technique allowed us to achieve a final event selection level composed of $\sim$ 85% upgoing neutrinos (mostly irreducible background consisting of upgoing atmospheric neutrinos) and $\sim$ 15% of misreconstructed downgoing atmospheric muons.

Two statistical approaches have then been performed, as described in Chapter 6, in order to identify among all these terrestrial neutrinos, possible GRB coincident neutrinos. In this context, aiming for discovery, we have developed a unique method sensitive to all possible produced neutrinos by investigating the relative arrival times of the neutrino candidate events. For this, we have used the Erlang probability distribution function that gives access to the time interval required to observe n events, based on which we have constructed a χ^2 test as test statistic. We have finally assigned significance levels and sensitivities to this statistical analysis considering only a prompt signal as it is the only emission phase that is theoretically well described. Meanwhile, we have tested a classic cut and count method to computed upper limits in case of the previous analysis does not lead to a discovery. All these testing and analysing phases have been performed as a blind analysis, meaning that the method used for analysing the data is fixed before the analyser looks at the data in their final form. The concept of a blind analysis is to avoid or, at least, to reduce any experimenter's bias, the unintended biasing of a result in a particular direction. We therefore used off-source data, composed by real observed data recorded by IceCube but captured during periods where no GRB has been detected. When the final cuts and test statistics are defined, as well as the sensitivities and discovery potentials, an extensive reviewing process inside the IceCube Collaboration has been carried out.

Finally we were allowed to unblind the real on-source data and to compute the significance of our data sample under the relative arrival time analysis. This analysis has not lead us to a discovery and we therefore conclude that this analysis of four years of IC86 data does not contain neutrinos correlated with SGRBs above the expected atmospheric backgrounds. This implies that we have set constraints on neutrino

production models using the developed cut and count method, presented in Fig. 7.2. The interpretation of this null result depends obviously on the chosen model, so we have attempted to present the results in two extreme theoretical contexts of prompt neutrino emission. We have considered a doubly-broken power law spectrum with break energies covering multiple orders of magnitude to which IceCube is sensitive. This is similar to the approach highlighted in previously IceCube published work [32, 34] but it is the first time a study is only dedicated to SGRBs. However, because SGRBs only represent 30% of the total GRB population, we have analysed a drastically reduced number of GRBs. This is also an expected behaviour as we had developed our methods aiming at a discovery and not achieving hard constraints. Nevertheless, our approach, which is totally independent from previous ones with a new event selection method and a newly developed statistical analysis, confirms previous non detection of neutrinos correlated with GRB in the context of GRB domination of UHECR production. It is clear from Fig. 7.2 that we strongly exclude models that produce the entire UHECR flux using neutrons that freely escape the GRB Fireball. Regarding the models predicting a possible flux of escaping protons, for which the escape mechanism has not been precisely specified, we observe that our results do not exclude these models but puts hard constraints on GRB dominated UHECR production. In the future, by accumulating more data, and because of the low background in this search and the generality of the models, we expect our constraints to become more stringent (almost linearly with the number of detected SGRBs in the absence of a clear emerging signal).

This work, as well as all previous GRB searches, achieves the same conclusion: the constraints become harder and harder and we may therefore assert that the probability that GRBs are important contributors of ultra high energy cosmic rays become thiner and thiner. The IceCube Collaboration is performing new searches considering new neutrino channels and the Southern sky. As it seems to be indicated at this analysis level, no signal events have been detected yet. If this is confirmed in the near future, it will become almost impossible to continue considering GRBs as the principal source of UHECRs. IceCube has started an online search for neutrinos correlated with GRBs with a latency of equal or less than one day. We should therefore in the near future be able to assert firmly if GRBs are contributors to UHECRs or not. For the beauty of science and the pleasure of physicists, let us hope that the answer will be negative...

Appendices

APPENDIX A

GRB Catalog

In this appendix, we present the GRB catalog that has been used in this thesis. Based on GRB-web (http://grbweb.icecube.wisc.edu), we provide individual GRB information. The names of the bursts are built according to the date on which the GRB occurred (in the format YYMMDD). A letter (A, B, *etc.*) indicating the order in which bursts on the same day were reported is added to this number. The positions of the GRBs are given in equatorial coordinates: α is the right ascension, δ is the declination, and σ is the 1 sigma angular error. All the angles are expressed in degrees. Next columns present the time information of the GRB. We give the trigger time T_0 in UT along with the GRB duration expressed by T_{90} in seconds relative to T_0. The remaining column gives fluence information, where f_γ is the normalisation of the fluence in erg cm^{-2}.

The presented tables do not include all the SGRBs that have happened during the search period because some of them have happened during a down time of IceCube (no run, test run or unstable run).

Table A.1: GRB Catalog for the 4 first years of IC86 used in this thesis.

Name	Position			Time		f_γ [erg cm^{-2}]
	α [°]	δ [°]	σ [°]	T_0	T_{90} [s]	
110529A	118.3300	67.9100	1.5000	00:48:40.249	0.570	2.320×10^{-6}
110705A	156.0240	40.0990	0.1610	03:37:09.942	0.250	3.300×10^{-6}
110802A	44.4550	32.5930	0.1163	15:19:16.191	0.600	1.300×10^{-5}
110916A	4.1100	40.3600	21.8600	00:23:01.648	1.790	4.230×10^{-7}
111112A	223.7200	28.8100	3.8300	21:47:48.164	0.190	7.670×10^{-7}
111113A	225.3900	2.1850	0.0957	05:10:13.625	0.160	7.700×10^{-6}
111117A	12.7020	23.0210	0.0172	12:13:41.000	0.470	6.700×10^{-7}
111126A	276.0570	51.4610	0.0304	18:57:42.000	0.800	7.000×10^{-8}
111222A	179.2200	69.0710	0.0001	14:51:55.023	0.320	7.200×10^{-6}
120205A	243.4170	25.9000	23.8333	06:51:05.307	0.580	1.110×10^{-7}
120222A	299.5500	26.4900	2.7600	00:29:36.130	1.080	1.730×10^{-6}
120302B	24.0900	9.7100	13.8700	17:19:59.082	1.600	1.190×10^{-7}
120305A	47.5360	28.4920	0.0003	19:37:30.000	0.100	2.000×10^{-7}
120323A	340.4070	29.7170	0.1180	12:10:15.970	0.500	1.080×10^{-5}
120327B	170.4100	23.7600	13.0000	10:01:49.234	0.250	1.140×10^{-7}
120415B	190.6900	4.9100	6.8800	21:23:41.026	0.960	1.310×10^{-7}
120519A	178.3660	22.4070	0.6340	17:18:14.640	0.720	3.700×10^{-6}
120603A	198.7940	4.3260	0.6427	10:32:09.854	0.380	1.000×10^{-6}
120616A	79.6900	56.4400	8.5400	15:06:50.639	0.050	2.580×10^{-7}
120617A	22.3090	33.8040	0.2510	15:02:47.025	0.500	2.100×10^{-6}
120624A	4.7730	7.1670	0.4427	07:24:22.982	0.300	6.500×10^{-6}
120630A	352.3000	42.4950	0.0274	23:17:33.000	0.600	6.100×10^{-8}
120814A	26.1900	22.4500	3.7100	04:49:12.579	0.890	3.830×10^{-7}
120814B	90.5700	33.1300	10.6800	19:16:06.746	0.190	1.280×10^{-7}
120816B	341.1550	2.1560	2.5100	23:58:18.852	0.768	9.700×10^{-5}
120822A	181.7200	80.5600	7.7000	15:03:56.399	1.540	1.090×10^{-7}
121011B	182.8090	44.1130	1.4943	22:32:20.083	0.350	2.800×10^{-6}
121012A	33.4200	14.5800	6.7800	17:22:16.386	0.450	1.150×10^{-6}
121124A	87.9300	49.5500	14.6400	14:32:07.299	0.260	5.660×10^{-8}
130204A	105.6400	41.9200	7.0700	11:36:51.704	0.190	2.810×10^{-7}
130219C	211.6000	12.2200	16.6800	15:01:13.946	1.540	2.030×10^{-7}
130307A	155.9960	22.9980	0.3643	03:01:44.471	0.380	1.430×10^{-6}
130325B	30.4400	62.0600	16.1400	00:07:46.818	0.640	5.660×10^{-8}
130404C	28.2900	56.4900	18.2300	21:02:11.029	0.960	2.200×10^{-7}
130603B	172.2010	17.0710	0.0003	15:49:14.000	0.180	6.600×10^{-6}
130622A	312.7400	24.4600	10.9100	14:45:53.204	0.960	4.320×10^{-7}

Table A.2: GRB Catalog for the 4 first years of IC86 used in this thesis (continued).

Name	Position			Time		f_γ [erg cm^{-2}]
	α [°]	δ [°]	σ [°]	T_0	T_{90} [s]	
130628B	312.8300	6.1000	4.9700	20:38:01.789	0.510	1.030×10^{-6}
130705A	156.3000	47.4100	19.3700	09:33:03.959	0.120	2.120×10^{-7}
130706A	299.3600	56.4800	10.4300	21:36:07.810	0.120	1.870×10^{-7}
130716A	179.5810	63.0570	0.0420	10:36:53.588	0.770	9.200×10^{-7}
130912A	47.5930	13.9970	0.0003	08:34:57.996	0.510	2.290×10^{-6}
130924B	78.5900	39.2600	5.8600	21:51:01.640	1.800	3.470×10^{-7}
131126A	215.4300	53.5300	0.7600	03:54:08.270	0.128	2.000×10^{-6}
131217A	86.5900	30.6000	6.4100	02:36:11.564	0.760	6.760×10^{-7}
131224A	296.8340	31.6680	0.0203	16:54:37.000	0.800	3.000×10^{-8}
140105A	208.2200	50.1700	6.0700	01:33:01.014	1.080	8.700×10^{-7}
140105B	252.8800	19.0300	3.9500	17:56:32.642	0.570	1.300×10^{-7}
140129B	326.7570	26.2060	0.0003	12:51:09.000	1.360	7.100×10^{-8}
140402A	207.5920	5.9710	0.0500	00:10:06.998	0.320	2.840×10^{-7}
140428B	2.0060	68.1720	1.2880	21:44:35.456	0.150	9.230×10^{-7}
140501A	171.8800	24.6400	10.7400	03:19:41.406	0.260	2.400×10^{-7}
140516A	252.9890	39.9630	0.0004	20:30:54.000	0.190	2.300×10^{-8}
140606A	201.7990	37.5990	0.0243	10:58:13.000	0.340	5.100×10^{-8}
140610B	199.0500	35.9100	8.1800	11:41:21.757	0.960	2.640×10^{-7}
140626B	120.8100	38.7800	6.6100	20:14:14.248	1.800	9.930×10^{-7}
140705A	293.7320	21.8970	0.0004	09:32:48.000	0.080	3.800×10^{-8}
140807A	200.1600	26.4900	2.5300	11:59:33.484	0.510	1.290×10^{-6}
140831A	280.3700	25.6400	8.9100	05:09:01.256	0.700	5.790×10^{-8}
140903A	238.0210	27.6080	0.0101	15:00:30.000	0.300	1.400×10^{-7}
140906C	314.9610	1.9390	0.1703	23:51:12.815	0.160	-
140930B	6.3480	24.2940	0.0003	19:41:42.000	0.840	8.100×10^{-6}
141020B	214.2960	7.9840	0.0608	10:31:31.155	1.600	8.470×10^{-8}
141105B	16.9100	29.1700	4.1000	09:44:47.213	1.280	8.830×10^{-7}
141113A	171.0200	80.2600	12.1500	08:17:43.503	0.440	1.470×10^{-7}
141124A	135.0700	78.1800	4.9800	06:38:20.736	0.510	5.230×10^{-7}
141126A	243.8700	59.9900	17.1200	05:35:56.536	0.890	4.050×10^{-7}
141202A	143.0730	54.1610	0.5430	11:17:05.606	1.340	4.440×10^{-6}
141205A	92.8590	37.8760	0.0203	08:05:17.490	1.500	1.100×10^{-6}
141205C	92.8590	37.8760	0.0330	08:05:17.491	1.280	1.070×10^{-6}
141208B	359.2600	26.4400	16.9800	15:09:58.319	0.960	1.910×10^{-7}
141212A	39.1240	18.1470	0.0005	12:14:01.000	0.300	7.200×10^{-8}
141213A	248.1900	18.0600	8.7200	07:12:15.429	0.760	6.580×10^{-7}

Table A.3: GRB Catalog for the 4 first years of IC86 used in this thesis (continued).

Name	Position			Time		f_γ [erg cm^{-2}]
	α [°]	δ [°]	σ [°]	T_0	T_{90} [s]	
150101A	312.6030	36.7330	0.0005	06:28:53.766	0.240	9.900×10^{-8}
150128A	127.6500	63.1500	9.0900	14:58:54.503	0.090	1.270×10^{-7}
150201B	5.6300	19.7500	13.9200	00:56:54.289	0.510	6.540×10^{-8}
150208B	350.6700	34.8900	4.1700	22:17:18.616	0.130	2.530×10^{-8}
150215A	305.6200	3.3800	14.6800	00:37:26.597	0.520	2.150×10^{-7}
150226A	63.5000	22.5100	1.2800	05:20:26.778	1.400	1.750×10^{-6}
150320A	139.9800	68.9300	10.5500	11:05:31.598	0.060	2.170×10^{-7}
150325A	133.1400	37.7500	10.1700	16:42:02.495	0.080	8.940×10^{-8}
150412A	186.7900	2.9100	17.5900	12:10:36.742	0.580	1.300×10^{-7}
150412B	220.2600	20.1300	8.1100	22:20:36.202	0.640	4.150×10^{-7}
150423A	221.5790	12.2830	0.0003	06:28:04.000	0.220	6.300×10^{-8}
150506B	76.3200	67.8100	3.2100	15:07:05.617	0.510	3.970×10^{-7}

List of Figures

List of Tables

Bibliography

[1] M. Hitary, M. Charles, and F. Shannon, "Crathes warren field," *British archaeology*, no. 107, pp. 12–18, 2009. - Cited on p. 1.

[2] T. Wulf, "About the radiation of high penetration capacity contained in the atmosphere," *Physikalische Zeitschrift 10th year*, vol. 5, pp. 152–157. - Cited on p. 2.

[3] D. Pacini, "La radiazione penetrante alla superficie ed in seno alle acque," *Il Nuovo Cimento (1911-1923)*, vol. 3, no. 1, pp. 93–100, 1912. - Cited on p. 2.

[4] C. L. Cowan *et al.*, "Detection of the free neutrino: a confirmation," *Science*, vol. 124, no. 3212, pp. 103–104, 1956. - Cited on p. 3.

[5] V. N. Aseev *et al.*, "Upper limit on the electron antineutrino mass from the troitsk experiment," *Phys. Rev. D*, vol. 84, p. 112003, 2011. - Cited on p. 3.

[6] C. Kraus *et al.*, "Final results from phase ii of the mainz neutrino mass searchin tritium β decay," *Eur. Phys. J. C*, vol. 40, no. 4, pp. 447–468, 2005. - Cited on p. 3.

[7] R. Davis, D. S. Harmer, and K. C. Hoffman, "Search for neutrinos from the sun," *Phys. Rev. Lett.*, vol. 20, pp. 1205–1209, 1968. - Cited on p. 4.

[8] Y. Fukuda *et al.*, "Solar neutrino data covering solar cycle 22," *Phys. Rev. Lett.*, vol. 77, pp. 1683–1686, 1996. - Cited on p. 4.

[9] M. G. Aartsen *et al.*, "Observation of High-Energy Astrophysical Neutrinos in Three Years of IceCube Data," *Phys. Rev. Lett.*, vol. 113, p. 101101, 2014, 1405.5303. - Cited on pp. 4, 21, and 50.

[10] V. Hess, "Über beobachtungen der durchdringenden strahlung bei sieben freiballonfehrten," *Physikalische Zeitschrift*, vol. 13, p. 1084, 1912. - Cited on p. 10.

[11] S. H. Neddermeyer and C. D. Anderson, "Note on the Nature of Cosmic Ray Particles," *Phys. Rev.*, vol. 51, pp. 884–886, 1937. - Cited on p. 10.

[12] http://www.physics.utah.edu/ whanlon/spectrum.html. - Cited on pp. 11 and 159.

[13] S. Gabriel and G. Patrick, "Solar energetic particle events: Phenomenology and prediction," *Space. Sci. Rev.*, vol. 107, no. 1-2, pp. 55–62, 2003. - Cited on p. 10.

[14] A. D. Erlykin and A. W. Wolfendale, "Structure in the cosmic ray spectrum: An update," *J. Phys.*, vol. G27, pp. 1005–1030, 2001. - Cited on p. 10.

[15] M. Ackermann *et al.*, "Detection of the Characteristic Pion-Decay Signature in Supernova Remnants," *Science*, vol. 339, p. 807, 2013, 1302.3307. - Cited on p. 10.

[16] W. Baade and F. Zwicky, "Cosmic rays from super-novae," *P. Natl. Acad. Sci. USA*, vol. 20, no. 5, pp. 259–263, 1934. - Cited on p. 10.

[17] V. Ginzburg and S. Syrovatskii, *The Origin of Cosmic Rays*. Pergamon, 1964. - Cited on p. 10.

[18] J. Wdowczyk and A. W. Wolfendale, "Implications of an extragalactic origin for the highest energy cosmic rays," *Astrophys. J.*, vol. 349, p. 35, 1990. - Cited on p. 10.

[19] K. Greisen, "End to the cosmic ray spectrum?," *Phys. Rev. Lett.*, vol. 16, pp. 748–750, 1966. - Cited on p. 10.

[20] G. T. Zatsepin and V. A. Kuzmin, "Upper limit of the spectrum of cosmic rays," *JETP Lett.*, vol. 4, pp. 78–80, 1966. - Cited on p. 10.

[21] T. K. Gaisser, T. Stanev, and S. Tilav, "Cosmic Ray Energy Spectrum from Measurements of Air Showers," *Front. Phys. China*, vol. 8, pp. 748–758, 2013, 1303.3565. - Cited on pp. 12 and 159.

[22] D. Mueller *et al.*, "Energy spectra and composition of primary cosmic rays," *Astrophys. J.*, vol. 374, 1991. - Cited on p. 12.

[23] J. Beringer *et al.*, "Review of particle physics," *Phys. Rev. D*, vol. 86, p. 010001, 2012. - Cited on pp. 13 and 159.

[24] J. Abraham *et al.*, "Properties and performance of the prototype instrument for the pierre auger observatory," *Nucl. Instrum. Meth. A*, vol. 523, no. 1–2, pp. 50 – 95, 2004. - Cited on p. 13.

[25] A. M. Hillas, "The Origin of Ultrahigh-Energy Cosmic Rays," *Ann. Rev. Astron. Astrophys.*, vol. 22, pp. 425–444, 1984. - Cited on pp. 14 and 159.

[26] E. Fermi, "On the Origin of the Cosmic Radiation," *Phys. Rev.*, vol. 75, pp. 1169–1174, 1949. - Cited on pp. 15, 39, and 43.

[27] M. Longair, *High Energy Astrophysics*. Cambridge University press, 2011. - Cited on pp. 15, 16, 17, 18, 19, 159, and 160.

[28] A. R. Bell, "The acceleration of cosmic rays in shock fronts II," *Mon. Not. Roy. Astron. Soc.*, vol. 182, pp. 443–455, 1978. - Cited on p. 18.

[29] M. Duvoort, *A search for Gamma Ray Burst neutrinos in AMANDA*. PhD thesis, Universiteit Utrecht, 2009. - Cited on pp. 20 and 160.

[30] R. W. Klebesadel, I. B. Strong, and R. A. Olson, "Observations of Gamma-Ray Bursts of Cosmic Origin," *Astrophys. J.*, vol. 182, pp. L85–L88, 1973. - Cited on pp. 21 and 24.

[31] R. Abbasi *et al.*, "Limits on Neutrino Emission from Gamma-Ray Bursts with the 40 String IceCube Detector," *Phys. Rev. Lett.*, vol. 106, pp. 141–101, 2011, 1101.1448. - Cited on pp. 22, 50, 146, and 162.

[32] R. Abbasi *et al.*, "An absence of neutrinos associated with cosmic-ray acceleration in γ-ray bursts," *Nature*, vol. 484, pp. 351–353, 2012, 1204.4219. - Cited on pp. 22, 50, 51, 52, 146, 151, and 162.

[33] S. Adrian-Martinez *et al.*, "Search for muon neutrinos from gamma-ray bursts with the ANTARES neutrino telescope using 2008 to 2011 data," *Astron. Astrophys.*, vol. 559, p. A9, 2013, 1307.0304. - Cited on p. 22.

[34] M. Aartsen *et al.*, "Search for Prompt Neutrino Emission from Gamma-Ray Bursts with IceCube," *Astrophys. J.*, vol. 805, p. L5, 2015, 1412.6510. - Cited on pp. 22, 50, 51, 119, 123, 148, 151, 162, and 165.

[35] N. Gehrels *et al.*, "The Swift Gamma-Ray Burst Mission," *AIP Conf. Proc.*, vol. 727, pp. 637–641, 2004, astro-ph/0405233. - Cited on pp. 23 and 26.

[36] C. Meegan *et al.*, "The Fermi Gamma-Ray Burst Monitor," *Astrophys. J.*, vol. 702, pp. 791–804, 2009, 0908.0450. - Cited on pp. 23 and 26.

[37] W. Atwood *et al.*, "The Large Area Telescope on the Fermi Gamma-ray Space Telescope Mission," *Astrophys. J.*, vol. 697, pp. 1071–1102, 2009, 0902.1089. - Cited on pp. 23 and 26.

[38] T. Piran, "The physics of gamma-ray bursts," *Rev. Mod. Phys.*, vol. 76, pp. 1143–1210, 2004, astro-ph/0405503. - Cited on pp. 23, 25, 29, 31, 33, 37, 40, 41, 160, and 161.

[39] P. Meszaros, "Gamma-Ray Bursts," *Rept. Prog. Phys.*, vol. 69, pp. 2259–2322, 2006, astro-ph/0605208. - Cited on pp. 23, 29, 30, 35, 39, 40, 160, and 161.

[40] N. Gehrels and S. Razzaque, "Gamma Ray Bursts in the Swift-Fermi Era," *Front. Phys. China*, vol. 8, pp. 661–678, 2013, 1301.0840. - Cited on pp. 23, 26, and 34.

[41] B. Paczynski, "Gamma-ray bursters at cosmological distances," *Astrophys. J.*, vol. 308, pp. L43–L46, 1986. - Cited on pp. 23, 25, 35, and 38.

[42] J. Goodman, "Are gamma-ray bursts optically thick?," *Astrophys. J.*, vol. 308, pp. L47–L50, 1986. - Cited on pp. 23, 25, 35, and 38.

[43] A. Shemi and T. Piran, "The appearance of cosmic fireballs," *Astrophys. J.*, vol. 365, pp. L55–L58, 1990. - Cited on pp. 23, 25, 35, and 38.

[44] E. Waxman, "Cosmological origin for cosmic rays above 10^{19} eV," *Astrophys. J.*, vol. 452, pp. L1–L4, 1995, astro-ph/9508037. - Cited on pp. 23 and 43.

[45] E. Waxman and J. N. Bahcall, "High-energy neutrinos from cosmological gamma-ray burst fireballs," *Phys. Rev. Lett.*, vol. 78, pp. 2292–2295, 1997, astro-ph/9701231. - Cited on pp. 23, 44, 48, 50, 147, 162, and 166.

[46] E. Waxman and J. N. Bahcall, "High-energy neutrinos from astrophysical sources: An Upper bound," *Phys. Rev.*, vol. D59, p. 023002, 1999, hep-ph/9807282. - Cited on pp. 23, 44, 49, and 161.

[47] A. Gomboc, "Unveiling the Secrets of Gamma Ray Bursts," *Contemp. Phys.*, vol. 53, no. 4, pp. 339–355, 2012, 1206.3127. - Cited on pp. 24, 27, 31, 32, 34, 36, 42, 160, and 161.

[48] R. Hascoet, F. Daigne, and R. Mochkovitch, "Prompt thermal emission in gamma-ray bursts," *Astron. Astrophys.*, vol. 551, p. A124, 2013, 1302.0235. - Cited on pp. 24 and 31.

[49] E. Mazets, S. Golenetskii, and V. Ilyinskii, "flare of cosmic gamma radiation as observed with "cosmos-461" satellite," *JETP Lett.*, vol. 19, p. 77, 1974. - Cited on p. 24.

[50] T. Cline *et al.*, "Energy spectra of cosmic gamma-ray bursts," *Astrophys. J. Lett.*, vol. 185, p. L1, 1973. - Cited on p. 24.

[51] G. Fishman and C. Meegan, "Gamma-ray bursts," *Ann. Rev. Astron. Astrophys.*, vol. 33, pp. 415–458, 1995. - Cited on pp. 24 and 29.

[52] C. Meegan *et al.*, "Spatial distribution of gamma-ray bursts observed by BATSE," *Nature*, vol. 355, pp. 143–145, 1992. - Cited on p. 25.

[53] P. Meszaros, P. Laguna, and M. Rees, "Gas dynamics of relativistically expanding gamma-ray burst sources: Kinematics, energetics, magnetic fields and efficiency," *Astrophys. J.*, vol. 415, pp. 181–190, 1993, astro-ph/9301007. - Cited on pp. 25, 35, and 39.

[54] M. Rees and P. Meszaros, "Relativistic fireballs - energy conversion and time - scales," *Mon. Not. Roy. Astron. Soc.*, vol. 258, pp. 41–43, 1992. - Cited on pp. 25 and 39.

[55] M. Rees and P. Meszaros, "Unsteady outflow models for cosmological gamma-ray bursts," *Astrophys. J.*, vol. 430, pp. L93–L96, 1994, astro-ph/9404038. - Cited on pp. 25 and 39.

[56] R. Narayan, B. Paczynski, and T. Piran, "Gamma-ray bursts as the death throes of massive binary stars," *Astrophys. J.*, vol. 395, pp. L83–L86, 1992, astro-ph/9204001. - Cited on p. 25.

[57] B. Paczynski and G. Xu, "Neutrino bursts from gamma-ray bursts," *Astrophys. J.*, vol. 427, pp. 708–713, 1994. - Cited on pp. 25 and 44.

[58] K. Hurley, "Gamma-Ray burst observations: Past and future," *AIP Conf. Proc.*, vol. 265, pp. 3–12, 1991. - Cited on p. 25.

[59] C. Kouveliotou *et al.*, "Identification of two classes of gamma-ray bursts," *Astrophys. J.*, vol. 413, pp. L101–104, 1993. - Cited on pp. 25, 28, 29, and 160.

[60] E. Costa *et al.*, "Discovery of an X-ray afterglow associated with the gamma-ray burst of 28 February 1997," *Nature*, vol. 387, pp. 783–785, 1997, astro-ph/9706065. - Cited on p. 25.

[61] G. Boella *et al.*, "Bepposax, the wide band mission for x-ray astronomy," *Astron. Astrophys.*, vol. 122, pp. 299–307, 1997. - Cited on p. 25.

[62] J. van Paradijs *et al.*, "Transient optical emission from the error box of the gamma-ray burst of 28 February 1997," *Nature*, vol. 386, pp. 686–689, 1997. - Cited on p. 25.

[63] J. S. Bloom *et al.*, "The Discovery and broad - band follow - up of the transient afterglow of GRB 980703," *Astrophys. J.*, vol. 508, pp. L21–L24, 1998, astro-ph/9808319. - Cited on p. 25.

[64] D. Frail *et al.*, "The Radio afterglow from the gamma-ray burst of 8 May 1997," *Nature*, vol. 389, p. 261, 1997. - Cited on p. 25.

[65] M. Metzger *et al.*, "Spectral constraints on the redshift of the optical counterpart to the gamma-ray burst of 8 May 1997," *Nature*, vol. 387, pp. 878–880, 1997. - Cited on p. 25.

[66] S. Djorgovski *et al.*, "Spectroscopy of the host galaxy of the gamma-ray burst 980703," *Astrophys. J.*, vol. 508, pp. L17–L20, 1998, astro-ph/9808188. - Cited on p. 25.

[67] S. Kulkarni *et al.*, "Identification of a host galaxy at redshift z = 3.42 for the gamma-ray burst of 14 December 1997," *Nature*, vol. 393, pp. 35–39, 1998. - Cited on p. 25.

[68] P. Meszaros and M. Rees, "Optical and long wavelength afterglow from gamma-ray bursts," *Astrophys. J.*, vol. 476, pp. 232–237, 1997, astro-ph/9606043. - Cited on p. 26.

[69] R. Wijers, M. J. Rees, and P. Meszaros, "Shocked by GRB-970228: The Afterglow of a cosmological fireball," *Mon. Not. Roy. Astron. Soc.*, vol. 288, pp. L51–L56, 1997, astro-ph/9704153. - Cited on pp. 26 and 160.

[70] M. Vietri, "The Soft X-ray afterglow of gamma-ray bursts, a stringent test for the fireball model," *Astrophys. J. Lett.*, 1997, astro-ph/9701024. - Cited on p. 26.

[71] M. Tavani, "X-Ray Afterglows from Gamma-Ray Bursts," *Astrophys. J.*, vol. 483, pp. L87–L90, 1997. - Cited on p. 26.

[72] D. E. Reichart, "Observations and Theoretical Implications of GRB 970228," *Astrophys. J.*, vol. 485, pp. L57–L60, 1997. - Cited on p. 26.

[73] J. Heise *et al.*, "X-ray flashes and X-ray rich gamma-ray bursts," *AIP Conf. Proc.*, vol. 662, pp. 229–236, 2003, astro-ph/0111246. - Cited on p. 26.

[74] T. Piran, "Gamma-ray bursts and the fireball model," *Phys. Rept.*, vol. 314, pp. 575–667, 1999, astro-ph/9810256. - Cited on pp. 27 and 31.

[75] J. K. Becker, "High-energy neutrinos in the context of multimessenger physics," *Phys. Rept.*, vol. 458, pp. 173–246, 2008, 0710.1557. - Cited on pp. 28, 45, 46, 47, 160, and 161.

[76] Y.-P. Qin *et al.*, "The hardness-duration correlation in the two classes of gamma-ray bursts," *Publ. Astron. Soc. Jpn.*, vol. 52, pp. 759–761, 2000, astro-ph/0005005. - Cited on p. 28.

[77] G. Pendleton *et al.*, "The intensity distribution for gamma-ray bursts observed with batse," *Astrophys. J.*, vol. 464, p. 606, 1996. - Cited on p. 29.

[78] E. Fenimore, C. D. Madras, and S. Nayakshin, "Expanding relativistic shells and gamma-ray burst temporal structure," *Astrophys. J.*, vol. 473, p. 998, 1996, astro-ph/9607163. - Cited on p. 29.

[79] E. Fenimore and E. Ramirez-Ruiz, "Redshifts for 220 BATSE gamma-ray bursts determined by variability and the cosmological consequences," *Astrophys. J.*, 2000, astro-ph/0004176. - Cited on p. 29.

[80] D. E. Reichart *et al.*, "A possible cepheid-like luminosity estimator for the long gamma-ray bursts," *Astrophys. J.*, vol. 552, p. 557, 2000, astro-ph/0004302. - Cited on p. 30.

[81] D. Band *et al.*, "BATSE observations of gamma-ray burst spectra. 1. Spectral diversity.," *Astrophys. J.*, vol. 413, pp. 281–292, 1993. - Cited on pp. 31 and 160.

[82] S. Iyyani *et al.*, "Variable jet properties in GRB110721A: Time resolved observations of the jet photosphere," *Mon. Not. Roy. Astron. Soc.*, vol. 433, p. 2739, 2013, 1305.3611. - Cited on pp. 31, 32, and 160.

[83] J. M. Burgess *et al.*, "Constraints on the Synchrotron Shock Model for the Fermi GBM Gamma-Ray Burst 090820A," *Astrophys. J.*, vol. 741, p. 24, 2011, 1107.6024. - Cited on p. 31.

[84] P. Meszaros *et al.*, "X-ray rich GRB, photospheres and variability," *Astrophys. J.*, vol. 578, pp. 812–817, 2002, astro-ph/0205144. - Cited on p. 31.

[85] F. A. Harrison *et al.*, "Optical and radio observations of the afterglow from GRB 990510: evidence for a jet," *Astrophys. J.*, vol. 523, pp. L121–L124, 1999, astro-ph/9905306. - Cited on p. 32.

[86] K. Stanek *et al.*, "BVRI observations of the optical afterglow of GRB 990510," *Astrophys. J.*, vol. 522, p. L39, 1999, astro-ph/9905304. - Cited on p. 32.

[87] P. Meszaros and M. Rees, "Grb 990123: reverse and internal shock flashes and late afterglow," *Mon. Not. Roy. Astron. Soc.*, vol. 306, pp. L39–L43, 1999, astro-ph/9902367. - Cited on p. 33.

[88] J. Rhoads, "How to tell a jet from a balloon: A Proposed test for beaming in gamma-ray bursts," *Astrophys. J.*, vol. 487, p. L1, 1997, astro-ph/9705163. - Cited on p. 33.

[89] J. Rhoads, "The dynamics and light curves of beamed gamma-ray burst afterglows," *Astrophys. J.*, vol. 525, pp. 737–749, 1999, astro-ph/9903399. - Cited on p. 33.

[90] R. Sari, T. Piran, and J. Halpern, "Jets in GRBs," *Astrophys. J.*, vol. 519, p. L17, 1999, astro-ph/9903339. - Cited on p. 33.

[91] A. Panaitescu and P. Kumar, "Fundamental physical parameters of collimated gamma-ray burst afterglows," *Astrophys. J.*, vol. 560, p. L49, 2001, astro-ph/0108045. - Cited on p. 33.

[92] D. A. Frail *et al.*, "Beaming in gamma-ray bursts: Evidence for a standard energy reservoir," *Astrophys. J.*, vol. 562, p. L55, 2001, astro-ph/0102282. - Cited on p. 33.

[93] S. Colgate, "Early gamma rays from supernovae," *Astrophys. J.*, vol. 187, p. 333, 1974. - Cited on p. 34.

[94] T. Galama *et al.*, "Discovery of the peculiar supernova 1998bw in the error box of GRB 980425," *Nature*, vol. 395, p. 670, 1998, astro-ph/9806175. - Cited on p. 34.

[95] S. Kulkarni *et al.*, "Radio emission from the unusual supernova 1998bw and its association with the gamma-ray burst of 25 April 1998," *Nature*, vol. 395, pp. 663–669, 1998. - Cited on p. 34.

[96] J. Hjorth *et al.*, "A very energetic supernova associated with the gamma-ray burst of 29 March 2003," *Nature*, vol. 423, pp. 847–850, 2003, astro-ph/0306347. - Cited on p. 34.

[97] K. Z. Stanek *et al.*, "Spectroscopic discovery of the supernova 2003dh associated with GRB 030329," *Astrophys. J.*, vol. 591, pp. L17–L20, 2003, astro-ph/0304173. - Cited on p. 34.

[98] S. Campana *et al.*, "The shock break-out of grb 060218/sn 2006aj," *Nature*, vol. 442, pp. 1008–1010, 2006, astro-ph/0603279. - Cited on p. 34.

[99] S. Woosley, "Gamma-ray bursts from stellar mass accretion disks around black holes," *Astrophys. J.*, vol. 405, p. 273, 1993. - Cited on pp. 35 and 42.

[100] B. Paczynski, "Are gamma-ray bursts in star forming regions?," *Astrophys. J.*, vol. 494, p. L45, 1998, astro-ph/9710086. - Cited on p. 35.

[101] D. B. Fox *et al.*, "The afterglow of grb050709 and the nature of the short-hard gamma-ray bursts," *Nature*, vol. 437, pp. 845–850, 2005, astro-ph/0510110. - Cited on p. 35.

[102] E. Berger *et al.*, "The Afterglows, redshifts, and properties of Swift gamma-ray bursts," *Astrophys. J.*, vol. 634, pp. 501–508, 2005, astro-ph/0505107. - Cited on p. 35.

[103] E. Berger *et al.*, "The afterglow and elliptical host galaxy of the short gamma-ray burst GRB 050724," *Nature*, vol. 438, pp. 988–990, 2005, astro-ph/0508115. - Cited on p. 35.

[104] D. Eichler *et al.*, "Nucleosynthesis, Neutrino Bursts and Gamma-Rays from Coalescing Neutron Stars," *Nature*, vol. 340, pp. 126–128, 1989. - Cited on pp. 35 and 43.

[105] S. Kobayashi, T. Piran, and R. Sari, "Can internal shocks produce the variability in GRBs?," *Astrophys. J.*, vol. 490, pp. 92–98, 1997, astro-ph/9705013. - Cited on p. 35.

[106] F. Daigne and R. Mochkovitch, "Gamma-ray bursts from internal shocks in a relativistic wind: temporal and spectral properties," *Mon. Not. Roy. Astron. Soc.*, vol. 296, p. 275, 1998, astro-ph/9801245. - Cited on p. 35.

[107] M. Lyutikov, "The electromagnetic model of gamma ray bursts," *New J. Phys.*, vol. 8, p. 119, 2006, astro-ph/0512342. - Cited on p. 35.

[108] G. Drenkhahn and H. Spruit, "Efficient acceleration and radiation in Poynting flux powered GRB outflows," *Astron. Astrophys.*, vol. 387, pp. 714 – 724, 2002, astro-ph/0202387. - Cited on p. 35.

[109] B. Zhang and H. Yan, "The Internal-Collision-Induced Magnetic Reconnection and Turbulence (ICMART) Model of Gamma-Ray Bursts," *Astrophys. J.*, vol. 726, p. 90, 2011, 1011.1197. - Cited on p. 35.

[110] F. Daigne and R. Mochkovitch, "The Expected thermal precursors of gamma-ray bursts in the internal shock model," *Mon. Not. Roy. Astron. Soc.*, vol. 336, p. 1271, 2002, astro-ph/0207456. - Cited on p. 36.

[111] A. K. Harding and M. G. Baring, "Escape of high-energy photons from relativistically expanding gamma-ray burst sources," *AIP Conf. Proc.*, vol. 307, no. 520, 1994. - Cited on p. 37.

[112] B. Paczynski, "Super-eddington winds from neutron stars," *Astrophys. J.*, vol. 363, p. 218, 1990. - Cited on p. 38.

[113] E. M. Rossi, A. M. Beloborodov, and M. J. Rees, "Neutron-loaded outflows in gamma-ray bursts," *Mon. Not. Roy. Astron. Soc.*, vol. 369, pp. 1797–1807, 2006, astro-ph/0512495. - Cited on p. 39.

[114] S. Razzaque and P. Meszaros, "Mev-gev emission from neutron-loaded short gamma-ray burst jets," *Astrophys. J.*, vol. 650, pp. 998–1003, 2006, astro-ph/0601652. - Cited on p. 39.

[115] E. V. Derishev, V. V. Kocharovsky, and V. V. Kocharovsky, "The neutron component in fireballs of gamma-ray bursts: Dynamics and observable imprints," *Astrophys. J.*, vol. 521, no. 2, p. 640, 1999. - Cited on p. 39.

[116] A. Pe'er *et al.*, "The connection between thermal and non-thermal emission in gamma-ray bursts: general considerations and GRB 090902B as a case study," *Mon. Not. Roy. Astron. Soc.*, vol. 1, no. 420, pp. 468–482, 2012. - Cited on p. 39.

[117] S. Guiriec *et al.*, "Detection of a Thermal Spectral Component in the Prompt Emission of GRB 100724B," *Astron. J.*, vol. 727, p. L33, 2011, 1010.4601. - Cited on p. 39.

[118] J. I. Katz, "Two populations and models of gamma-ray bursts," *Astrophys. J.*, vol. 422, p. 248, 1994, astro-ph/9212006. - Cited on p. 39.

[119] P. Meszaros and M. Rees, "Relativistic fireballs and their impact on external matter - Models for cosmological gamma-ray bursts," *Astrophys. J.*, vol. 405, p. 278, 1993. - Cited on p. 39.

[120] R. Sari and T. Piran, "Hydrodynamic time scales and temporal structure of GRBs," *Astrophys. J.*, vol. 455, p. L143, 1995, astro-ph/9508081. - Cited on p. 39.

[121] R. Blandford and D. Eichler, "Particle Acceleration at Astrophysical Shocks: A Theory of Cosmic Ray Origin," *Phys. Rept.*, vol. 154, pp. 1–75, 1987. - Cited on p. 39.

[122] A. Achterberg *et al.*, "Particle acceleration by ultrarelativistic shocks: Theory and simulations," *Mon. Not. Roy. Astron. Soc.*, vol. 328, p. 393, 2001, astro-ph/0107530. - Cited on p. 39.

[123] D. C. Ellison and G. P. Double, "Nonlinear particle acceleration in relativistic shocks," *Astropart. Phys.*, vol. 18, pp. 213–228, 2002, astro-ph/0202106. - Cited on p. 39.

[124] M. Lemoine and G. Pelletier, "Particle transport in tangled magnetic fields and Fermi acceleration at relativistic shocks," *Astrophys. J.*, vol. 589, pp. L73–L76, 2003, astro-ph/0304058. - Cited on p. 39.

[125] R. Sari and T. Piran, "Variability in GRBs: A Clue," *Astrophys. J.*, vol. 485, p. 270, 1997, astro-ph/9701002. - Cited on pp. 39 and 41.

[126] M. Ackermann *et al.*, "Fermi observations of grb 090510: A short-hard gamma-ray burst with an additional, hard power-law component from 10 kev to gev energies," *Astrophys. J.*, vol. 716, no. 2, p. 1178, 2010. - Cited on p. 41.

[127] Bošnjak, Ž., Daigne, F., and Dubus, G., "Prompt high-energy emission from gamma-ray bursts in the internal shock model," *Astron. Astrophys.*, vol. 498, no. 3, pp. 677–703, 2009. - Cited on p. 41.

[128] A. Abdo *et al.*, "Fermi Observations of High-Energy Gamma-Ray Emission from GRB 080916C," *Science*, vol. 323, pp. 1688–1693, 2009. - Cited on pp. 42 and 161.

[129] S. Razzaque, C. D. Dermer, and J. D. Finke, "Synchrotron radiation from ultra-high energy protons and the Fermi observations of GRB 080916C," *Open Astron. J.*, vol. 3, pp. 150–155, 2010, 0908.0513. - Cited on p. 41.

[130] K. Asano, S. Guiriec, and P. Meszaros, "Hadronic Models for the Extra Spectral Component in the short GRB 090510," *Astrophys. J.*, vol. 705, pp. L191–L194, 2009, 0909.0306. - Cited on p. 41.

[131] K. Murase, K. Asano, T. Terasawa, and P. Meszaros, "The Role of Stochastic Acceleration in the Prompt Emission of Gamma-Ray Bursts: Application to Hadronic Injection," *Astrophys. J.*, vol. 746, p. 164, 2012, 1107.5575. - Cited on p. 41.

[132] S. Woosley, "Models for Gamma-Ray Burst Progenitors and Central Engines," 2011, 1105.4193. - Cited on p. 42.

[133] C. Wolf and G. Rayet, "Spectroscopie stellaire," *Cr. Acad. Sci.*, vol. 65, pp. 292–296, 1867. - Cited on p. 42.

[134] J. Weisberg, J. Taylor, and L. Fowler, "Gravitational waves from an orbiting pulsar," *Sci. Am.*, vol. 245, pp. 66–74, 1981. - Cited on p. 43.

[135] E. Waxman, "Cosmological gamma-ray bursts and the highest energy cosmic rays," *Phys. Rev. Lett.*, vol. 75, pp. 386–389, 1995, astro-ph/9505082. - Cited on p. 43.

[136] M. Vietri, "On the acceleration of ultrahigh-energy cosmic rays in gamma-ray bursts," *Astrophys. J.*, vol. 453, pp. 883–889, 1995, astro-ph/9506081. - Cited on p. 43.

[137] S. Razzaque, P. Meszaros, and E. Waxman, "Neutrino tomography of gamma-ray bursts and massive stellar collapses," *Phys. Rev.*, vol. D68, p. 083001, 2003, astro-ph/0303505. - Cited on pp. 44, 46, and 47.

[138] E. Waxman and J. N. Bahcall, "Neutrino afterglow from gamma-ray bursts: Similar to 10^{18}eV," *Astrophys. J.*, vol. 541, pp. 707–711, 2000, hep-ph/9909286. - Cited on pp. 44, 48, and 49.

[139] A. Domínguez *et al.*, "Detection of the cosmic γ-ray horizon from multiwavelength observations of blazars," *Astrophys. J.*, vol. 770, p. 77, 2013, 1305.2162. - Cited on p. 45.

[140] S. Razzaque, P. Meszaros, and E. Waxman, "High energy neutrinos from gamma-ray bursts with precursor supernovae," *Phys. Rev. Lett.*, vol. 90, p. 241103, 2003, astro-ph/0212536. - Cited on p. 47.

[141] E. Waxman, S. Kulkarni, and D. Frail, "Implications of the radio afterglow from the gamma-ray burst of May 8, 1997," *Astrophys. J.*, vol. 497, pp. 288–293, 1998, astro-ph/9709199. - Cited on p. 47.

[142] B. Katz, R. Budnik, and E. Waxman, "The energy production rate & the generation spectrum of UHECRs," *J. Cosmol. Astropart. P.*, vol. 0903, p. 020, 2009, 0811.3759. - Cited on p. 48.

[143] A. Goldstein *et al.*, "The Fermi GBM Gamma-Ray Burst Spectral Catalog: The First Two Years," *Astrophys. J. Suppl.*, vol. 199, pp. 19–45, 2012, 1201.2981. - Cited on p. 48.

[144] M. Ahlers, M. Gonzalez-Garcia, and F. Halzen, "GRBs on probation: testing the UHECR paradigm with IceCube," *Astropart. Phys.*, vol. 35, pp. 87–94, 2011, 1103.3421. - Cited on pp. 48, 147, and 166.

[145] R. Abbasi *et al.*, "Search for muon neutrinos from Gamma-Ray Bursts with the IceCube neutrino telescope," *Astrophys. J.*, vol. 710, pp. 346–359, 2010, 0907.2227. - Cited on pp. 50 and 162.

[146] A. Avrorin *et al.*, "Search for neutrinos from gamma-ray bursts with the Baikal neutrino telescope NT200," *Astron. Lett.*, vol. 37, pp. 692–698, 2011. - Cited on p. 50.

[147] D. Guetta *et al.*, "Neutrinos from individual gamma-ray bursts in the BATSE catalog," *Astropart. Phys.*, vol. 20, pp. 429–455, 2004, astro-ph/0302524. - Cited on pp. 50 and 162.

[148] J. K. Becker *et al.*, "Coincident grb neutrino flux predictions: implications for experimental uhe neutrino physics," *Astropart. Phys.*, vol. 25, pp. 118–128, 2006, astro-ph/0511785. - Cited on pp. 50 and 162.

[149] G. J. Feldman and R. D. Cousins, "A Unified approach to the classical statistical analysis of small signals," *Phys. Rev.*, vol. D57, pp. 3873–3889, 1998, physics/9711021. - Cited on pp. 52 and 162.

[150] P. Baerwald, M. Bustamante, and W. Winter, "Are gamma-ray bursts the sources of ultra-high energy cosmic rays?," *Astropart. Phys.*, vol. 62, pp. 66–91, 2015, 1401.1820. - Cited on p. 51.

[151] A. Roberts, "The birth of high-energy neutrino astronomy: A personal history of the dumand project," *Rev. Mod. Phys.*, vol. 64, pp. 259–312, Jan 1992. - Cited on p. 55.

[152] T. K. Gaisser, F. Halzen, and T. Stanev, "Particle astrophysics with high energy neutrinos," *Phys. Rep.*, vol. 258, no. 3, pp. 173 – 236, 1995. - Cited on p. 55.

[153] F. Halzen and S. R. Klein, "Invited review article: Icecube: An instrument for neutrino astronomy," *Rev. Sci. Instrum.*, vol. 81, no. 8, 2010. - Cited on pp. 55, 60, 61, 63, and 163.

[154] J. A. Formaggio and G. P. Zeller, "From ev to eev: Neutrino cross sections across energy scales," *Rev. Mod. Phys.*, vol. 84, pp. 1307–1341, Sep 2012. - Cited on p. 56.

[155] R. Gandhi *et al.*, "Neutrino interactions at ultrahigh-energies," *Phys. Rev.*, vol. D58, p. 093009, 1998, hep-ph/9807264. - Cited on pp. 57 and 162.

[156] K. J. Meagher, *Limits on Neutrino Emission from Gamma-Ray Bursts with the 40 String IceCube Detector*. PhD thesis, University of Maryland, 2012. - Cited on pp. 57, 137, and 162.

[157] T. K. Gaisser and T. Stanev, "Neutrino-induced muon flux deep underground and search for neutrino oscillations," *Phys. Rev. D*, vol. 30, pp. 985–990, Sep 1984. - Cited on p. 58.

[158] P. A. Čerenkov, "Visible radiation produced by electrons moving in a medium with velocities exceeding that of light," *Phys. Rev.*, vol. 52, pp. 378–379, Aug 1937. - Cited on p. 58.

[159] C. A. Mead, "Quantum theory of the refractive index," *Phys. Rev.*, vol. 110, pp. 359–369, Apr 1958. - Cited on p. 58.

[160] M. Ackermann *et al.*, "Optical properties of deep glacial ice at the south pole," *J. Geophys. Res.-Atmos.*, vol. 111, no. D13, 2006. - Cited on pp. 59, 60, and 163.

[161] P. B. Price, K. Woschnagg, and D. Chirkin, "Age vs depth of glacial ice at south pole," *Geophys. Res. Lett.*, vol. 27, no. 14, pp. 2129–2132, 2000. - Cited on p. 59.

[162] N. E. Bramall *et al.*, "A deep high-resolution optical log of dust, ash, and stratigraphy in south pole glacial ice," *Geophys. Res. Lett.*, vol. 32, no. 21, pp. n/a–n/a, 2005. - Cited on p. 59.

[163] G. Mie, "Beiträge zur optik trüber medien, speziell kolloidaler metallösungen," *Ann. Phys.*, vol. 330, no. 3, pp. 377–445, 1908. - Cited on p. 59.

[164] M. Aartsen *et al.*, "Measurement of south pole ice transparency with the icecube led calibration system," *Nucl. Instrum. Meth. A*, vol. 711, no. 0, pp. 73 – 89, 2013. - Cited on p. 59.

[165] D. Heereman, *HitSpooling: An Improvement for the Supernova Neutrino Detection System in IceCube*. PhD thesis, Université libre de Bruxelles, 2015. - Cited on pp. 61 and 163.

[166] P. O. Hulth *et al.*, "The AMANDA experiment," in *Neutrino '96. Proceedings, 17th International Conference on Neutrino Physics and Astrophysics, Helsinki, Finland, June 13-19*, 1996, astro-ph/9612068. - Cited on pp. 60, 62, and 163.

[167] K. Hanson and O. Tarasova, "Design and production of the icecube digital optical module," *Nucl. Instrum. Meth. A*, vol. 567, no. 1, pp. 214 – 217, 2006. - Cited on p. 62.

[168] R. Abbasi *et al.*, "The icecube data acquisition system: Signal capture, digitization, and timestamping," *Nucl. Instrum. Meth. A*, vol. 601, no. 3, pp. 294 – 316, 2009. - Cited on pp. 62, 65, 66, and 163.

[169] R. Abbasi *et al.*, "Calibration and characterization of the icecube photomultiplier tube," *Nucl. Instrum. Meth. A*, vol. 618, no. 1–3, pp. 139 – 152, 2010. - Cited on p. 62.

[170] P. C. Redl, *A search for muon neutrinos coincident with Gamma-ray bursts with the IceCube 59-string detector*. PhD thesis, University of Maryland, 2011. - Cited on pp. 64 and 163.

[171] A. Achterberg *et al.*, "First year performance of the icecube neutrino telescope," *Astropart. Phys.*, vol. 26, no. 3, pp. 155 – 173, 2006. - Cited on p. 65.

[172] J. L. Kelley, "Event triggering in the icecube data acquisition system," *IceCube Internal Note*, 2014. - Cited on pp. 66, 67, and 163.

[173] D. Chirkin and W. Rhode, "Muon Monte Carlo: A High-precision tool for muon propagation through matter," 2004, hep-ph/0407075. - Cited on pp. 70, 91, and 163.

[174] W. Yao *et al.*, "Review of Particle Physics," *J. Phys.*, vol. G33, pp. 1–1232, 2006. - Cited on p. 70.

[175] J. D. Jackson, *Classical Electrodynamics*. Wiley, third ed., 1999. - Cited on pp. 71, 72, 73, 163, and 164.

[176] N. Whitehorn, *A Search for High-Energy Neutrino Emission from Gamma-Ray Bursts*. PhD thesis, University of Wisconsin-Madison, 2012. - Cited on pp. 76, 77, 78, and 164.

[177] M. Zoll, *Preparations for the next solar WIMP Analysis with IceCube - Advances in simulation, filtering, event topology identification and analysis approach*. PhD thesis, Stockhoms Universitet, 2014. - Cited on p. 77.

[178] J. Ahrens *et al.*, "Muon track reconstruction and data selection techniques in amanda," *Nucl. Instrum. Meth. A*, vol. 524, no. 1–3, pp. 169 – 194, 2004. - Cited on pp. 80, 81, 82, 85, 86, 87, and 164.

[179] D. Pandel, *Estimmung von Wasser- und Detektorparametern und Rekon- struktion von Myonen bis 100 TeV mit dem Baikal-Neutrinoteleskop NT-72.* PhD thesis, Humboldt-Universitt zu Berlin, 1996. - Cited on p. 85.

[180] N. van Eijndhoven, O. Fadiran, and G. Japaridze, "Implementation of a Gauss convoluted Pandel PDF for track reconstruction in Neutrino Telescopes," *Astropart. Phys.*, vol. 28, pp. 456–462, 2007, 0704.1706. - Cited on pp. 85, 86, and 103.

[181] M. G. Aartsen *et al.*, "Energy Reconstruction Methods in the IceCube Neutrino Telescope," *J. Instrum.*, vol. 9, p. P03009, 2014, 1311.4767. - Cited on p. 89.

[182] A. Gazizov and M. Kowalski, "Anis: High energy neutrino generator for neutrino telescopes," *Comput. Phys. Commun.*, vol. 172, p. 203, 2005. - Cited on p. 90.

[183] H. Lai *et al.*, "Global qcd analysis of parton structure of the nucleon: Cteq5 parton distributions," *Eur. Phys. J. C*, vol. 12, no. 3, pp. 375–392, 2000. - Cited on p. 90.

[184] A. M. Dziewonski and D. L. Anderson, "Preliminary reference earth model," *Phys. Earyh Planet. In.*, vol. 25, no. 4, pp. 297 – 356, 1981. - Cited on p. 90.

[185] M. Honda *et al.*, "Calculation of atmospheric neutrino flux using the interaction model calibrated with atmospheric muon data," *Phys. Rev. D*, vol. 75, p. 043006, Feb 2007. - Cited on p. 91.

[186] J. Lundberg *et al.*, "Light tracking through ice and water: Scattering and absorption in heterogeneous media with photonics," *Nucl. Instrum. Meth. A*, vol. 581, no. 3, pp. 619 – 631, 2007. - Cited on p. 91.

[187] J. Heinrich, "Pitfalls of goodness-of-fit from likelihood," in *Proceedings of the PHYSTAT Conference*, Stanford Linear Accelerator Center, 2003. - Cited on p. 97.

[188] E. Jaynes, *Probability Theory*. Cambridge University Press, 2003. - Cited on p. 109.

[189] T. Bayes and R. Price, "An essay towards solving a problem in the doctrine of chances," *Phil. Trans.*, vol. 53, p. 370, 1763. - Cited on p. 109.

[190] L. B. Lusted, "Decision-making studies in patient management," *N. Engl. J. Med.*, vol. 284, pp. 416–24, 1971. - Cited on p. 111.

[191] J. R. Quinlan, "Induction of decision trees," *Mach. Learn.*, vol. 1, p. 81, 1986. - Cited on p. 114.

[192] M. Richman, *A Search For Muon Neutrinos Coincident with Northern Gamma-Ray Bursts using IceCube*. PhD thesis, University of Maryland, 2015. - Cited on pp. 115, 116, 129, 145, 146, and 165.

[193] M. Stuckens, "IceCube Earth WIMP event selection optimistaion using machine learning techniques," Master's thesis, Vrije Universiteit Brussel, 2014. - Cited on p. 116.

[194] M. G. Aartsen *et al.*, "Searches for Extended and Point-like Neutrino Sources with Four Years of IceCube Data," *Astrophys. J.*, vol. 796, no. 2, p. 109, 2014, 1406.6757. - Cited on p. 121.

[195] A. K. Erlang, "Solution of some problems in the theory of probabilities of significance in automatic telephone exchanges," *Post Office Elec. Eng.*, vol. 13, pp. 5–13, 1917. - Cited on p. 125.

[196] S. Tilav *et al.*, "Atmospheric variations as observed by icecube," in *Proceedings of the 31st International Cosmic Ray Conference*, (Lodz, Poland), 2009. - Cited on p. 127.

[197] P. Desiati *et al.*, "Seasonal variations of high energy cosmic ray muons observed by the icecube observatory as a probe of kaon/pion ratio," in *Proceedings of the 32st International Cosmic Ray Conference*, (Beijijng, China), 2011. - Cited on p. 127.

[198] E. Berger, "Short-Duration Gamma-Ray Bursts," *Ann. Rev. Astron. Astrophys.*, vol. 52, pp. 43–105, 2014, 1311.2603. - Cited on pp. 128 and 131.

[199] J. Neyman, "Outline of a theory of statistical estimation based on the classical theory of probability," *Phil. Trans. R. Soc.*, vol. A 236, p. 333, 1937. - Cited on p. 137.

[200] A. Stuart, J. K. Ord, and A. Steven, *Classical Inference and the Linear Model*, vol. vol. 2B of *Kendall's Advanced Theory of Statistics*. London: Arnold, 6th ed ed., 1994. - Cited on p. 137.

[201] K. Nakamura and others (Particle Data Group), "Review of particle physics," *J. Phys.*, vol. G 37, 2010. - Cited on p. 137.

[202] J. R. Klein and A. Roodman, "Blind analysis in nuclear and particle physics," *Ann. Rev. Nucl. Part. Sci.*, vol. 55, pp. 141–163, 2005. - Cited on p. 143.

[203] A. Achterberg *et al.*, "Five years of searches for point sources of astrophysical neutrinos with the AMANDA-II neutrino telescope," *Phys. Rev.*, vol. D75, p. 102001, 2007, astro-ph/0611063. - Cited on p. 146.